



VCU

Virginia Commonwealth University
VCU Scholars Compass

Theses and Dissertations


Graduate School

2019

Electrostatic Networks and Mechanisms of Δ pH-Dependent Gating in the Human Voltage-Gated Proton Channel Hv1

Ashley L. Bennett
Virginia Commonwealth University

Follow this and additional works at: <https://scholarscompass.vcu.edu/etd>

 Part of the [Biochemistry Commons](#), [Biophysics Commons](#), [Cellular and Molecular Physiology Commons](#), and the [Structural Biology Commons](#)

© Ashley L. Bennett

Downloaded from

<https://scholarscompass.vcu.edu/etd/6046>

This Dissertation is brought to you for free and open access by the Graduate School at VCU Scholars Compass. It has been accepted for inclusion in Theses and Dissertations by an authorized administrator of VCU Scholars Compass. For more information, please contact libcompass@vcu.edu.

© Ashley L. Bennett 2019
All Rights Reserved

Electrostatic Networks and Mechanisms of Δ pH-Dependent Gating in the Human Voltage-Gated Proton Channel Hv1

A dissertation submitted in fulfillment of the requirements for the degree of
Doctor of Philosophy at Virginia Commonwealth University
by

Ashley Lauren Bennett

Mentor: I. Scott Ramsey, Ph.D.
Professor, Virginia Commonwealth University

Virginia Commonwealth University
Richmond, Virginia
9 September 2019

ACKNOWLEDGMENTS

I would like to thank Virginia Commonwealth University School of Medicine and the Department of Physiology and Biophysics for providing me the opportunity to pursue a graduate education. I would especially like to thank my advisor, Dr. I. Scott Ramsey, and committee members Dr. John Hackett, Dr. Lei Zhou, Dr. Phil Mosier, and Dr. Bill Barton. Their guidance and suggestions greatly improved the quality of my work and I am extremely grateful for the time they all took out of their busy schedules to teach me and critique my work. Dr. Victor de la Rosa, a former Ramsey Lab postdoctoral fellow, was a great collaborator to work with and he continues to answer my questions and provide thoughtful feedback. I would like to thank Dr. Glen Kellogg in the Department of Medicinal Chemistry for allowing me access to the GPU server and the Center for High Performance Computing core facility for letting me use the CPU server to run molecular dynamics simulations. I also like to thank Dr. Pittman for helping me customize my course work to make it more relevant to my research topic and Dr. Clive Baumgarten for pushing me to do better and nominating me for several prestigious awards at VCU. For providing the infinite support that is necessary to complete a graduate degree I would like to thank my parents Dave and Angie Bennett, my grandmothers Phyllis Harrison and Shelby Bennett, my boyfriend David Wright and his parents Andy and Sherry. I would also like to thank Jennings Bennett, Trevor Bennett, Sydney Bennett, Michelle Bullin, and Steve O'Connor. Lastly, I would like to acknowledge and thank my dog, Kepler, for forcing to get outside and get some fresh air every now and then. This dissertation was completed in memoriam of Steve D. O'Connor, William J. Bennett, Denver N. Williams, and Jesse W. Bennett.

TABLE OF CONTENTS

ACKNOWLEDGMENTS	ii
LIST OF FIGURES	vi
LIST OF TABLES	vii
LIST OF ABBREVIATIONS	viii
ABSTRACT	iii
CHAPTER 1: INTRODUCTION	1
1.1: Discovery, Classification, and Functional Properties	1
1.1.1: Classification, General Structure, and Functional Properties	1
1.1.2: Physiological Functions	3
1.1.3: The Voltage Clamp Method	6
1.2: Structure of Hv1	9
1.2.1: Coiled-Coil Domain	9
1.2.2: Voltage-Sensing Domain of Hv1	9
1.2.3: Dimer Structure of Hv1	13
1.2.4: Cooperativity in Hv1	14
1.3: Hydrated Electrostatic Networks	18
1.3.1: Hydration in the Hv1 VSD	20
1.3.2: Extracellular Electrostatic Network	22
1.3.3: Intracellular Electrostatic Network	24
1.4: The H⁺ Permeation Pathway and Mechanisms of H⁺ Permeation	27
1.4.1: Identity of the Permeating Species	27
1.4.2: Proton Conduction in Hv1	28
1.4.3: Mechanisms Proton Conduction in Hv1	29
1.5: Mechanisms of voltage sensing and voltage-dependent gating	32
1.5.1: Voltage Sensing Mechanisms in Hv1	32
1.5.2: Mechanisms of Voltage-Dependent Gating in Hv1	33
1.6: The selectivity filter and mechanisms of proton selectivity	38
1.6.1: The Hv1 Selectivity Filter	38
1.6.2: Mechanisms of Selectivity in Hv1	40
1.7: Hv1 Inhibition by Zn²⁺	43
1.7.1: The Zn²⁺ Binding Site in Hv1	43
1.7.2: Mechanisms of Zn²⁺ Inhibition of Hv1	43
1.8: The pH sensor and ΔpH-dependent gating	45
1.8.1: Hv1 ΔpH-Dependent Gating	45
1.8.2: Hv1 ΔpH Sensor Structure	46
1.8.3: The EC pH Sensor	47
1.8.4: The IC pH Sensor	49
1.8.5: Mechanisms of ΔpH-Dependent Gating in Hv1	50
1.8.6: Coupling Between Voltage- and ΔpH-Dependent Gating in Hv1	53

1.9: Homology Models of Hv1	55
1.9.1: Electrostatic Networks in Homology Models	56
1.9.2: Resting State Homology Models.....	57
1.9.3: Activated State Homology Models	59
CHAPTER 2: SPECIFIC AIMS	70
2.1: AIM I: Build Experimentally-Validated Models of Hv1.....	70
2.2: AIM II: The ECEN is Necessary for Δ pH-Dependent Gating in Hv1	71
2.3: AIM III: Residues in the ICEN Communicate with the ECEN	73
CHAPTER 3: MATERIALS AND METHODS	74
3.1: Computational Methods.....	74
3.1.1: Building a Resting State Model of Hv1 Voltage Sensor Domain	75
3.1.2: Building an Activated State Model of Hv1 Voltage Sensor Domain	78
3.1.3: Molecular Dynamics Simulations of Resting State Model Hv1F.....	79
3.1.4: Molecular Dynamics Simulations of Hv1J	83
3.1.5: Analysis of Molecular Dynamics Trajectories	87
3.2: Experimental Methods.....	90
3.2.1: Site-Directed Mutagenesis	90
3.2.2: Electrophysiology	90
CHAPTER 4: EXPERIMENTALLY-VALIDATED MODELS OF Hv1	96
4.1: Resting State Model Hv1F	96
4.2: Activated State Model Hv1J.....	98
4.3: Molecular Dynamics on Hv1J WT	99
4.3.1: Salt Bridges in the Activated State Model Hv1J.....	100
4.3.2: PROPKA3.1 pK_a Calculations in Activated State Model Hv1J	102
4.4: Molecular Dynamics on Hv1F WT	105
4.4.1: Salt Bridges in the Resting State Model Hv1F	105
4.4.2: PROPKA3.1 pK_a Calculations in Resting State Model Hv1F	106
4.4.3: Hv1F pK_a Covariance	107
4.4.4: Electrostatic Interactions and pK_a Dynamics	109
CHAPTER 5: EXPERIMENTAL MEASUREMENT OF Hv1 FUNCTION IN ECEN MUTANTS.....	131
5.1: ECEN Single Mutants	132
5.2: ECEN Double Mutants	133
5.3: ECEN Triple Mutants.....	134
5.4: MD on Hv1J and Hv1F ECEN Mutants	135
5.4.1: Hv1J ECEN Mutant MD	135
5.4.2: Hv1F ECEN Mutant MD.....	137
CHAPTER 6: Hv1 ALLOSTERY BETWEEN ECEN AND ICEN.....	155
CHAPTER 7: DISCUSSION	158
7.1: Hv1J Homology Model and Molecular Dynamics	160
7.1.1: Hv1J Homology Model	160
7.1.2: Hv1J Molecular dynamics	161
7.1.3: Hv1J PROPKA3.1 pK_a Calculations	166
7.2: Hv1F Homology Model and Molecular Dynamics	169

7.2.1: Hv1F Homology Model	169
7.2.2: Molecular Dynamics on Hv1F WT	170
7.2.3: PROPKA3.1 pK _a Calculations on Hv1F	172
7.3: Structure of the ΔpH Sensor in Hv1.....	177
7.4: Allosteric Communication Between ICEN and ECEN	189
7.5: A Refined Mechanism of ΔpH-Dependent Gating in Hv1.....	193
BIBLIOGRAPHY	202
APPENDIX A.....	215
APPENDIX B.....	219
VITA	220

LIST OF FIGURES

Figure 1.1 : Overview of Hv1 Structure	62
Figure 1.2 : Voltage-Sensor Domain Sequence Alignment	63
Figure 1.3 : The Whole-Cell Voltage Clamp Configuration	65
Figure 1.4 : Voltage-Dependent Gating in Hv1	66
Figure 1.5 : Inhibition of Hv1 by Zn ²⁺ Binding	69
Figure 3.1 : Overview of Hv1F Modeling	95
Figure 4.1 : Overview of Resting State Hv1F Model	112
Figure 4.2 : Hv1F Model Accommodates Zn ²⁺ Binding Site in ECEN	113
Figure 4.3 : The Hv1F Model has the Proper Register of S4	114
Figure 4.4 : The Hv1F Model Accommodates the K157-K221 Interaction	115
Figure 4.5 : Overview of Hv1J Activated State Model	116
Figure 4.6 : The Hv1J Model is Consistent with Experimental Data	117
Figure 4.7 : Hv1F and Hv1J are Stable in the MD Environment	118
Figure 4.8 : Salt Bridges in Hv1J	119
Figure 4.9 : PROPKA3.1 pK _a Predictions in Hv1J WT MD	120
Figure 4.10 : pK _a Covariance in Hv1J WT MD	122
Figure 4.11 : H168 pK _a and E164 pK _a Coupling in Hv1J MD	123
Figure 4.12 : Salt Bridges in Hv1F WT MD	124
Figure 4.13 : PROPKA3.1 pK _a Predictions in Hv1F WT MD	125
Figure 4.14 : pK _a Covariance in Hv1F WT MD	127
Figure 4.15 : E119 and D185 pK _a Coupling in Hv1F WT MD	128
Figure 4.16 : E119 pK _a is Largely Influence by Coulombic Interactions	129
Figure 4.17 : D185 Interacts with W207 in Hv1J WT MD	130
Figure 5.1 : Raw Voltage Clamp Data for Hv1 WT	140
Figure 5.2 : Hv1 EC pH Sensitivity of Voltage-Dependent Gating in ECEN Single Mutants	146
Figure 5.3 : Hv1 EC pH Sensitivity of Voltage-Dependent Gating in ECEN Double Mutants	147
Figure 5.4 : Hv1 EC pH Sensitivity of Voltage-Dependent Gating in ECEN Triple Mutants	148
Figure 5.5 : Salt Bridges in Hv1J ECEN Mutant Simulations	149
Figure 5.6 : ECEN Structure in Hv1J WT and ECEN Mutant MD	150
Figure 5.7 : ECEN pK _a Values in Hv1J ECEN Mutant MD	151
Figure 5.8 : ECEN pK _a Values in Hv1F ECEN Mutant MD	152
Figure 5.9 : Salt Bridges on Hv1F ECEN Mutant Simulations	153
Figure 5.10 : ECEN Structure in Hv1F WT and ECEN Mutant MD	154
Figure 6.1 : Zn ²⁺ Potency is Reduced by E153A	157
Figure 7.1 : Model of ΔpH-Dependent Gating in Hv1	199
Figure 7.2 : Predicted Titration Curves of Hv1	201
Supplementary Figure 1 : E119 pK _a in the Presence of Zn ²⁺ versus Na ⁺ in Hv1F WT MD	216
Supplementary Figure 2 : Hv1F WT MD D123 Distances	217
Supplementary Figure 3 : Groththus Proton Transfer	218

LIST OF TABLES

Table 1.1 : Experimentally Supported Electrostatic Interactions in Hv1	67
Table 1.2 : Two Sample t-Test Comparing ΔpH Sensitivity in Hv1 WT and Mutants:	68
Table 3.1 : Structural Restraints Used to Refine the Hv1F Resting State Model	93
Table 3.2 : Structural Restraints Used to Refine the Hv1J Activated State Model	94
Table 4.1 : PROPKA3.1 Average pK_a in Hv1J MD Systems	121
Table 4.2 : PROPKA3.1 Average pK_a in Hv1F MD Systems	126
Table 5.1 : Average Raw V_{thr} of Hv1 WT and ECEN Mutants	141
Table 5.2 : Average ΔV_{thr} of Hv1 WT and ECEN Mutants	143

LIST OF ABBREVIATIONS

1-palmitoyl-2-oleoylphosphatidylcholine (POPC)
2-(*N*-morpholino)ethanesulfonic acid (MES)
4-(2-hydroxyethyl)-1-piperazineethanesulfonic acid (HEPES)
50% inhibitory concentration (IC_{50})
Active state Hv1 model (Hv1J)
Alanine (A, Ala)
Alpha carbon ($C\alpha$)
Angstrom (\AA)
Apparent open probability (P_o)
Apparent open probability-voltage relationship (P_o -V)
Arginine (R, Arg)
Asparagine (N, Asn)
Bis-tris methane (Bis-tris)
Boltzmann constant (K_B)
Central processing unit (CPU)
Ciona intestinalis (*Ci*)
Chloride (Cl^-)
Conductance (G)
Conductance-voltage relationship (G-V)
Constant atom, pressure, and temperature ensemble (NPT)
Current (I)
Cysteine (C, Cys)
Density functional theory (DFT)
Disuccinimidyl suberate (DSS)
Electrostatic network (EN)
Elementary charge (e_0)
Energy minimization (EM)
Extracellular (EC)
Extracellular electrostatic network (ECEN)
Extracellular pH (pH_o)
Femtosecond (fs)
Generalized interaction analysis (GIA)
Gigabyte (GB)
Gigaohm ($G\Omega$)
Glutamate (E, Glu)
Glutamine (Q, Gln)
Graphics processing unit (GPU)
Green fluorescent protein (GFP)
Hill coefficient (n_H)
Histidine (His)
Hydrogen bonded chain (HBC)
Hydronium ion (H_3O^+)
Hydroxide ion (OH^-)
Intracellular (IC)

Intracellular electrostatic network (ICEN)
Intracellular pH (pH_i)
Kelvin (K)
Methanesulfonate (MeSO₃⁻)
Micromolar (μM)
Millimolar (mM)
Millivolts (mV)
Molecular dynamics (MD)
Mus musculus (*Mm*)
Nanosecond (ns)
N-Cyclohexyl-2-aminoethanesulfonic acid (CHES)
Open probability (P_{open})
Open probability-voltage relationship (P_{OPEN-V})
Particle mesh Ewald (PME)
Periodic boundary conditions (PBC)
Picosecond (ps)
POPC phosphate phosphorous atom (P)
Protein data bank (PDB)
Proton (H⁺)
Radial distribution function (RDF)
Random-access memory (RAM)
Resting state Hv1 model (Hv1F)
Reversal potential (E_{rev})
S1 transmembrane helix (S1)
S2 transmembrane helix (S2)
S3 transmembrane helix (S3)
S4 transmembrane helix (S4)
Tail current (I_{tail})
Temperature (T)
Terminal nitrogen atoms of arginine (NH1 and NH2)
Terminal oxygen atoms of aspartate (OD1 and OD2)
Threshold potential (V_{thr})
Total internal reflection fluorescence microscopy (TIRFM)
Transmembrane (TM)
Transmembrane electrical potential/voltage (V)
Transmembrane pH gradient (ΔpH)
Tryptophan (W, Trp)
Voltage clamp fluorometry (VCF)
Voltage-gated channel (VGC)
Voltage-gated proton channel (Hv1)
Voltage-sensor domain (VSD)
Voltage-sensitive phosphatase (VSP)
Western blot (WB)
Wild type (WT)
Zinc(II) (Zn²⁺)

ABSTRACT

Electrostatic networks and mechanisms of ΔpH -dependent gating in the human voltage-gated proton channel hv1

By Ashley Lauren Bennett, B.S. Chemistry, Biology

A dissertation submitted in partial fulfillment of the requirements for the degree of Doctor of Philosophy at Virginia Commonwealth University.

Virginia Commonwealth University, 2019

Director: I. Scott Ramsey, Ph.D.
Assistant Professor, Department of Physiology and Biophysics

The structure of the voltage-gated proton (H^+) channel Hv1 is homologous to the voltage sensor domain (VSD) of tetrameric voltage-gated Na^+ , K^+ and Ca^{2+} channels (VGCs). Unlike VGCs, Hv1 lacks a pore domain and instead adopts a homodimeric quaternary architecture in which the VSDs physically interact with one another. Similar to VGCs and other VSD proteins, Hv1 is gated by changes in membrane potential (V), but voltage-dependent gating in Hv1 is also exquisitely sensitive to changes in the transmembrane pH gradient (ΔpH). Changes in either extracellular pH (pH_o) or intracellular pH (pH_i) cause the apparent open probability (P_{OPEN})-V relation to shift ~ 40 mV per pH unit. The effect of pH changes on voltage sensitivity is a defining biophysical feature of Hv1 channels. Zn^{2+} and other divalent metal ions also affect voltage-dependent gating in Hv1, and the effect of extracellular Zn^{2+} is phenomenologically similar to lowering pH_o , suggesting that protons and Zn^{2+} may utilize a similar mechanism. Although a high resolution X-ray structure of an Hv1-like chimeric protein was previously reported, the structural basis for ΔpH -dependent gating in Hv1 remains poorly understood.

To gain insight into structural features that mediate pH-sensitive gating in Hv1, we constructed new resting- and activated-state Hv1 homology models using constraints determined from functional studies measured under voltage clamp. We then conducted all-atom molecular dynamics (MD) simulations, analyzed salt bridges, and calculated side chain pK_a values at residues that were previously shown to form intracellular or extracellular electrostatic networks (ICEN and ECEN, respectively). Correlated changes in salt bridge distances and pK_a values suggest a novel interaction between the ECEN acidic residues E119 and D185 and S4 Arg ‘gating charges’ and we hypothesized these interactions to be important in ΔpH-dependent gating. Consistent with this hypothesis, experimental data show that ΔpH-dependent gating is compromised at acidic pH_o in E119A-D185A (but not E119A or D185A single mutants), suggesting that E119 and D185 interactions are required for ΔpH-dependent gating when pH_o is altered. MD simulations conducted on activated- and resting-state E119A and D185A Hv1 model proteins permitted us to compare changes in salt bridge patterns in WT and mutant systems. We show that calculated pK_a values at E119 and D185 are sensitive to nearby electrostatic interactions, suggesting that mutations may exert their functional effects, at least in part, by altering the ECEN effective pK_a and thus influencing pH_o sensitivity. As previously reported for Zn²⁺, E119A and D185A mutations also elicit rearrangements in ICEN structure, raising the possibility that ΔpH-dependent gating requires long-range allosteric interactions between ICEN and ECEN residues. Our experimental and computational studies suggest a new model for the ΔpH-dependent gating mechanism in Hv1 in which S4 Arg residues compete with H⁺ for ECEN and ICEN interactions and voltage sensitivity is determined by ECEN and ICEN pK_a shifts.

CHAPTER 1: INTRODUCTION

1.1: Discovery, Classification, and Functional Properties

Proton (H^+) currents were first proposed by Hastings in 1972 as part of the mechanism for bioluminescence in dinoflagellates (Fogel and Hastings, 1972) and were first measured in snail neurons in 1982 using the voltage clamp method (Thomas and Meech, 1982). In the years following, H^+ currents were measured in many different cell types (for a review see Capasso et al., 2011). After many years of debate over the identity of the protein responsible for the H^+ conductance, the human HVCN1 gene was finally identified and proposed to encode the voltage-gated H^+ channel Hv1 (Ramsey et al., 2006). Mouse and *Ciona intestinalis* HVCN1 orthologues encoding Voltage Sensor Only Proteins (VSOPs) were simultaneously identified by a separate group (Sasaki et al., 2006). Hv1 remains the only voltage-gated H^+ channel discovered so far and Hv1 orthologues from fifteen different species have been reported to function as voltage-gated H^+ channels in overexpression systems (DeCoursey, 2018).

1.1.1: Classification, General Structure, and Functional Properties

The HVCN1 gene encodes a 273-residue protein that is now generally known as the voltage-gated H^+ channel Hv1. The VSDs of Hv1, tetrameric VGCs, and voltage-sensitive phosphatases (VSPs) are formed by the first four transmembrane (TM) helical segments (S1-S4), which are phylogenetically conserved (Figure 1.1A; Figure 1.2; DeCoursey, 2015; Ramsey et al., 2006; Sasaki et al., 2006). VSDs in tetrameric VGCs are structurally independent, but in Hv1 channels that lack a pore domain, the two VSDs form a homodimer; with each VSD containing a H^+ -selective permeation pathway. Functional interactions between protomers have been reported

([Figure 1.1B](#); (Gonzalez et al., 2010; Musset et al., 2010, (Gonzalez et al., 2010; Koch et al., 2008; Lee et al., 2008; Musset et al., 2010b; Qiu et al., 2013; Ramsey et al., 2006; Sasaki et al., 2006; Tombola et al., 2008).

Single-particle photobleaching and mutagenesis experiments in engineered tandem dimers strongly suggest that each protomer in the Hv1 dimer is functional (Tombola et al., 2008). For example, incorporating the N214C mutation into only one protomer resulted in ~50% reduction in H⁺ current when MTS reagents were applied to the cell, whereas constructs containing N214C in both subunits mediated little or no H⁺ current, indicating that each VSD contains its own H⁺ permeation pathway (Tombola et al., 2008). Removing the intracellular C-terminal domain coiled-coil (CC) domain from Hv1 (Hv1ΔC) construct increases the fraction of Hv1 particles that exhibit single-step photobleaching, suggesting that the CC domain is required for dimer stability (Koch et al., 2008; Lee et al., 2008). Other studies suggest that the dimer interface is also formed by residues in the extracellular S1-S2 loop (Lee et al., 2009), but other interface residues may remain to be identified. Hv1ΔC constructs are more likely to form monomers in photobleaching and biochemical assays, but retain the hallmark voltage- and ΔpH-dependent gating of wild-type (WT) Hv1, suggesting that monomeric channels are functional (Koch et al., 2008; Lee et al., 2008; Tombola et al., 2008). However, Hv1ΔC can be co-immunoprecipitated (Koch et al., 2008) and may function as dimers *in vivo* (Li et al., 2015).

Hv1 remains the only WT VSD that is known to mediate an activated-state H⁺-selective conductance. The high degree of sequence conservation and structural similarity among VSDs ([Figure 1.2](#)) suggest that the structural determinants required for H⁺ conduction are likely to be fairly subtle. ΔpH-dependent gating may also be attributable to subtle structural differences between Hv1 and other VSD-containing proteins. For example, pH_o-dependent modulation of

voltage-sensitive gating in the Slo1 (BK) K^+ channel was recently shown to be abrogated by neutralizing mutation at D153 (Zhou et al., 2018). However, the Slo1 D153-equivalent residue in Hv1 is a non-ionizable Ser (S143), suggesting that Δ pH-dependent gating in Hv1 requires different residue(s). Whereas the mechanisms of voltage-dependent gating (De La Rosa and Ramsey, 2018; Gonzalez et al., 2013) and inhibition by Zn^{2+} (De La Rosa et al., 2018; Qiu et al., 2016; Ramsey et al., 2006) are understood in some detail, mechanisms of H^+ selectivity (discussed in more detail later), H^+ permeation, pH_i and pH_o sensing, and Δ pH-dependent gating remain poorly understood.

1.1.2: Physiological Functions

Voltage-gated H^+ currents attributable to Hv1 has been measured in a variety of different cell types (for review see Table 1 in DeCoursey, 2018). In most cells, Hv1 regulates pH_i by mediating H^+ efflux (Decoursey, 2003). However, species-dependent differences in Hv1 biophysical properties (Fogel and Hastings, 1972; Rodriguez et al., 2017; Smith et al., 2011) raise the possibility that Hv1 has a different physiological role in some organisms. For example, inward H^+ currents through Hv1 are hypothesized to be necessary for the tonoplast action potential that gives rise to dinoflagellate bioluminescence (DeCoursey, 2013). Hv1 was also recently identified in snails, but snail Hv1 exhibits a weak dependence on pH_i and a hyperpolarizing shift in the conductance-voltage (G-V) relationship, which allows Hv1 to conduct an inward, depolarizing H^+ current (Thomas et al., 2018). Although it remains to be confirmed, Hv1 is thought to play an important role in action potential generation in snail neurons (DeCoursey, 2013).

In most species, however, Hv1 only conducts outward H^+ currents under steady-state conditions and thus serves to extrude acid equivalents. For example pelagic phytoplankta called coccolithophores convert bicarbonate (HCO_3^-) into calcite ($CaCO_3$) and constitute an important component of the global carbon cycle (Taylor et al., 2011). $CaCO_3$ production generates intracellular H^+ and thus causes coccolithophore acidification that is hypothesized to be compensated by H^+ efflux through Hv1 (Taylor et al., 2011). Hv1-dependent control of pH_i in coccolithophores may therefore be important for controlling global atmospheric CO_2 levels and ocean pH, and could represent a target for ameliorating challenges associated with global climate change (Taylor et al., 2011).

In mammalian cells, Hv1 also typically mediated only H^+ efflux. Perhaps the best studied role for Hv1 is in the phagocyte respiratory burst. To kill bacterial pathogens, the phagocyte NADPH oxidase (*phox*) enzyme complex mediates sustained extracellular (or intra-phagosomal) superoxide anion production (DeCoursey, 2010; Dinauer et al., 1987; Henderson et al., 1987, 1988a, 1988b; Musset et al., 2008a). *phox* activation causes profound intracellular acidification and membrane depolarization (Bánfi et al., 1999; DeCoursey, 2010; El Chemaly et al., 2010; Henderson et al., 1987, 1988a, 1988b; Musset et al., 2008a). Sustained depolarization or intracellular (IC) acidification negatively regulate *phox* activity, potentially decreasing pathogen clearance (DeCoursey, 2010). Indeed, superoxide production and bacterial killing are attenuated in Hv1-null 'knockout' mice (Ramsey et al., 2009; Sasaki et al., 2006). It is now well-accepted that Hv1 provides the charge compensation for *phox* and H^+ efflux during the phagocyte respiratory burst (DeCoursey, 2010; DeCoursey et al., 2003; El Chemaly et al., 2010; Henderson et al., 1987; Ramsey et al., 2009; Sasaki et al., 2006).

Reactive oxygen species (ROS) are reactive molecules that are produced as a byproduct of many cellular metabolism reactions and can damage cellular macromolecules, leading to disease (Thannickal and Fanburg, 2000). Hv1 is a potential therapeutic target for diseases in which ROS production negatively affects disease severity or progression, including B-cell lymphoma, inflammatory airway diseases like asthma, ischemic stroke, lupus erythematosus, neurodegeneration, traumatic brain injury, autoimmune diseases including rheumatoid arthritis, and multiple sclerosis (Capasso et al., 2010; Cho et al., 2009; Eder and DeCoursey, 2001; Fischer, 2012; Fischer et al., 2002, 2002; Morihata et al., 2000; Tian et al., 2016; Wu et al., 2012; Yu et al., 2018). However, the role of Hv1 in the pathogenesis of human diseases and therapeutic potential of Hv1 antagonists remains to be established. Hv1 may function to regulate pH of the airway surface liquid, which could have implications for the treatment of asthma and other respiratory diseases (Cho et al., 2009; Fischer, 2012; Fischer et al., 2002). In basophils, Hv1 appears to regulate histamine secretion (Musset et al., 2008a). Hv1 is expressed in human (but not mouse) sperm and is thought to be required for sperm maturation and fertility (Lishko and Kirichok, 2010). Hv1 is also upregulated in B cell lymphomas and metastatic breast cancer cells (Capasso et al., 2010; Wang et al., 2011, 2012). Hv1 physically associates with B cell receptor (BCR) complex and is required for antigen-dependent B lymphocyte signaling and proliferation (Boyd et al., 2009; Capasso et al., 2010). Taken together, the available evidence strongly suggests that the physiological requirements for Hv1 channel activity could be exploited for the development of novel therapeutic purposes.

1.1.3: The Voltage Clamp Method

Hv1 function is best studied using voltage clamp techniques that allow ion currents to be measured at fixed membrane potentials ([Figure 1.3; Hamill et al., 1981; Hille, 2001](#)). Voltage clamp is powerful because it allows researchers to both control the fraction of voltage-gated ion channels that are open and to directly measure the current carried by open channels. In voltage clamp methods, the transmembrane electrical potential (i.e., voltage) may be held constant by injecting current into the cell via a micropipette. The injected current is of opposite sign but equal magnitude to the amount of current flowing through open ion channels in the cell membrane (Hille, 2001). Voltage clamp methods can therefore be used to hyperpolarize (in which the inside of the cell is negative relative to the outside of the cell), or depolarize (in which the inside of the cell becomes more positive) the membrane. Because gating in VGCs, VSPs, and Hv1 depends on voltage, applying the appropriate voltage can be used to force a channel into either an open or closed state at the experimenter's discretion.

During a typical voltage clamp experiment, the membrane potential is sequentially stepped from a holding value to a series of different step voltages to generate a series of current traces at specified potentials ([Figure 5.1A](#)). The time course of the current during the test voltage reports gating kinetics and steady-state currents elicited during voltage steps conform to the predictions of Ohm's law ($V = IR$, where I is current and R is resistance). Returning the voltage to a more hyperpolarizing potential where channels are closed after each step voltage generates 'tail' currents (I_{tail}). Because the hyperpolarizing step is delivered fast enough such that the current direction reverses before channels can close, I_{tail} can be measured at a single fixed potential after steps to a range of potentials that elicit changes in channel open probability (P_{open}). The driving force for I_{tail} is thus constant in each record and the instantaneous I_{tail} is directly

proportional to the P_{open} at the end of the preceding voltage step. The threshold potential (V_{thr}) is defined as the minimum depolarizing voltage required to elicit I_{tail} larger than the background current as determined, somewhat arbitrarily, by the experimenter. Although arbitrary, an advantage to the use of V_{thr} determination is that only small step currents (i.e., due to channel opening at low P_{open} values) are required, and changes in pH_o or pH_i that result from H^+ movement through open Hv1 channels can be minimized, ensuring that the experimentally imposed ΔpH is intact when the measurement is made (Musset et al., 2008b).

In another type of voltage clamp experimental protocol, step voltage is constant and tail voltage is varied, allowing the experimenter to measure the ‘reversal potential’ (E_{rev}) of the instantaneous I_{tail} . E_{rev} is the voltage at which no net current flows across the membrane (i.e., the zero current potential). Comparisons between the Nernst potential, which is the calculated equilibrium potential for an ion with a known concentration gradient, and the experimentally measured E_{rev} are useful for determining the ionic selectivity of channels (Hille, 2001). For an exquisitely H^+ -selective channel I, E_{rev} is expected to equal the Nernst potential for H^+ at known pH_i and pH_o . Deviations from the Nernstian prediction can thus indicate a loss of selectivity. Intra- and extracellular recording (IC and EC, respectively) solution compositions are under experimental control in voltage clamp methods, allowing investigators to set the Nernst potential through choice of recording solution. In the whole-cell voltage clamp recording mode, the solution filling the micropipette dialyzes the cell cytoplasm, allowing control over the IC ion concentrations. The pipette solution typically remains constant during the course of a whole-cell voltage clamp experiment. In contrast, the bath solution can be easily superfused and is frequently changed during the course of a voltage clamp experiment. Voltage clamp methods thus allow for exquisite control of channel state at defined voltages and chemical gradients, and

are thus provide powerful tools for measuring the voltage dependence of gating in VGCs, VSPs, and particularly Hv1 channels.

1.2: Structure of Hv1

1.2.1: Coiled-Coil Domain

The C-terminal CC domain interacts with the CC domain of the adjacent protomer in the Hv1 dimer, ([Figure 1.1B](#); Gonzalez et al., 2010; Koch et al., 2008; Lee et al., 2008; Musset et al., 2010; Tombola et al., 2008, 2010). The structure of the CC domain is revealed by an X-ray crystal structure corresponding to residues 226-266 in Hv1 (PDB ID 3A2A), which forms a parallel, left-handed, double-helical structure (Li et al., 2010). At ~ 2.0 Å resolution, the CC domain crystal structure shows a typical CC domain with a heptad repeat pattern but which has features that are atypical of CC domains from other proteins and suggest that CC domain dimerization in Hv1 could be dynamic (Fujiwara et al., 2012; Li et al., 2010). No VSD residues are included in the crystallized proteins and CC domain functions other than serving as the main dimer interface in Hv1 remain elusive.

1.2.2: Voltage-Sensing Domain of Hv1

Like VSDs in VGCs and VSPs, the Hv1 VSD senses changes in the transmembrane voltage (De La Rosa and Ramsey, 2018). The majority of experimental and computational studies of the Hv1 VSD structure agree that the VSD contains a solvent-filled lumen that forms the pathway for H^+ permeation and gating charge movement (Banh et al., 2019; Chamberlin et al., 2014; Ramsey et al., 2010; Randolph et al., 2016; Takeshita et al., 2014). Solvent access to the center of the VSD is limited by hydrophobic side chains V109 (S1), F150 (S2), V177 (S3), and V178 (S3) that face the channel lumen and form what has been termed a ‘hydrophobic plug’

(Banh et al., 2019; Chamberlin et al., 2014; Ramsey et al., 2010; Randolph et al., 2016; Takeshita et al., 2014). The S4 segments in VGCs and VSPs typically contain four Arg residues (R1-R4), that function as gating charges, but in Hv1 R4 is replaced by an Asn (N214 or N4), and Hv1 thus contains only three canonical S4 gating charges (Ramsey et al., 2006; Sasaki et al., 2006). R205H (R1H) confers inward H⁺ currents at negative potentials where the channel is normally closed and the VSD is assumed to populate a resting-state conformation (Randolph et al., 2016). The ability for R1H to confer resting-state H⁺ currents is shared with other VSD-containing proteins and has been interpreted to mean that R1 is in register with hydrophobic plug residues in the VSD resting state (Randolph et al., 2016; Starace and Bezanilla, 2004; Starace et al., 1997; Villalba-Galea et al., 2013). N214R (N4R) reveals a voltage-dependent open-state block of the H⁺ conductance, suggesting that N214 is in register with the hydrophobic gap in the VSD activated state (Randolph et al., 2016). S1, S2 and S3 helices contain acidic residues that are thought to serve as ‘counter-charges’ that make state-dependent Coulombic interactions with the S4 gating charge Arg side chains; E153 and D174 are thought to interact with R2 and R3 to stabilize the (S4 down) resting-state conformation while E119, D123, D130 and D185 likely interact with R1 and R2 to stabilize the (S4 up) activated-state conformation of the Hv1 VSD ([Figure 1.4](#); [Table 1.1](#); [Chamberlin et al., 2014](#); [Ramsey et al., 2010](#); voltage-dependent gating explained in more detail later). D112 (S1) is thought to interact with R1 in the resting state and R3 in the activated state (Berger and Isacoff, 2011; Musset et al., 2011; Ramsey et al., 2010; Randolph et al., 2016).

The only crystal structure of an Hv1 VSD reported to date (mHv1cc; PDB 3WKV) is a chimeric construct containing mainly mouse Hv1 residues; a portion of the S2-S3 loop was taken from *Ci*-VSP and the C-terminal coiled coil was transplanted from GCN4 (Takeshita et al.,

2014). The protein was crystalized at ~ 3.5 Å resolution in what was initially interpreted to be the resting state of Hv1 (Takeshita et al., 2014); however, later studies show that mHv1cc is more likely to represent an intermediate-state conformation (Randolph et al., 2016). The mHv1cc crystal structure confirmed previous predictions that the tertiary structure of the Hv1 VSD is similar to the structures of VSDs in VGCs and VSPs (Takeshita et al., 2014). Furthermore, an electron density attributed to Zn^{2+} was observed at the extracellular entrance to the H^+ permeation pathway near the E119-, D123-, H140- and H193-equivalent (human Hv1 numbering) residues (Takeshita et al., 2014). The location of a Zn^{2+} ion bound to each mHv1cc protomer confirmed that the suspected Zn^{2+} binding site simultaneously involves E119, D123, H140 and H193 residues from the same subunit (Ramsey et al., 2006), and contradicted an alternative hypothesis that Zn^{2+} binds at two separate inter-subunit interface locations formed by H140 and H193 residues from adjacent protomers (Musset et al., 2010a; Takeshita et al., 2014). Although mHv1cc reveals general architectural features about the Hv1 VSD structure, resolution is insufficient to unambiguously assign the positions of many side chains, and fundamental questions about the structural bases of Hv1 function remained unanswered by the X-Ray structure.

Furthermore, residues in the S2-S3 loop of mHv1cc that were transplanted from *Ci*-VSP are implicated in forming Coulombic interactions that stabilize the VSD resting-state conformation in WT Hv1 (Ramsey et al., 2010), raising the possibility that the non-conserved substitutions may have resulted in a non-native structure (Takeshita et al., 2014). This interpretation is supported by the location of functionally important D185 and R1 side chains in an aliphatic crevice that is inaccessible to water in mHv1cc (Takeshita et al., 2014). Another potential caveat to interpretation of the mHv1cc structure is the replacement of the native Hv1

CC domain with the leucine zipper from GCN4, which evidently caused the protein to crystallize as a trimer (Takeshita et al., 2014). It remains unclear whether a trimer is a physiologically relevant quaternary structure. Density was not solved for potentially important residues (220 to 225) that are located between the VSD and CC, and the structural relationship between these domains remains controversial (Fujiwara et al., 2014; Li et al., 2015). Another unexpected feature of the mHv1cc structure is that solvent access to the H⁺ pore within the VSD is occluded by hydrophobic residues in two different locations (Takeshita et al., 2014), which stands in contrast to accessibility studies suggesting deep hydrated vestibules (Berger and Isacoff, 2011; Hong et al., 2013; Li et al., 2015). The absence of a solvated pathway for S4 gating charge movement is also inconsistent with the generally accepted mechanism of voltage-sensing (Vargas et al., 2012). Experimental studies in Hv1 strongly support the notion that, like other VGCs and VSPs, voltage sensing in Hv1 requires cationic S4 Arg side chain ‘gating charges’ to cross the electrical field by moving through a hydrated VSD ‘gating pore’ (Carmona et al., 2018; De La Rosa and Ramsey, 2018; Gonzalez et al., 2010).

The structure of the Hv1 N-terminal domain (residues 1-100) remains wholly unknown. Hv1 constructs lacking an N-terminal domain have fast gating kinetics suggesting that the N-terminal domain has a role in gating (Koch et al., 2008). Phosphorylation of Y29 by PKC also alters Hv1 gating properties (Musset et al., 2010c), but the molecular mechanism remains unknown. Alternative start codon usage results in expression of an N-terminally truncated form of Hv1 with altered gating properties (Hondares et al., 2014), but the structure and mechanism of the truncated peptide is not known.

1.2.3: Dimer Structure of Hv1

Based on the ability of disuccinimidyl suberate (DSS) and other reagents to readily crosslink Hv1 protomers detected in Western Blot (WB) experiments, several groups concluded that Hv1 forms a homodimer and the CC domain was immediately suspected to form the dimer interface (Koch et al., 2008; Lee et al., 2008; Tombola et al., 2008). A Cys-less Hv1 mutant protein also forms dimers and suggests that dimerization in Hv1 is independent of disulfide formation (Lee et al., 2008). However, Cys substitution at specific residue locations in the CC and S1-S2 loop is sufficient to confer chemical crosslinking, indicating that protomers interact at two distant interface locations (Lee et al., 2008). Because bifunctional maleimide-based reagents like DSS require access to solvent to catalyze crosslinking, their utility for identifying dimer interface residues within or near in hydrophobic TM regions is limited, and more studies are needed to fully describe the dimer interface in Hv1. Additional evidence for dimerization was gleaned from biochemical studies: a) HA- and Myc-tagged Hv1 proteins can be co-immunoprecipitated (Koch et al., 2008); b) inter-subunit fluorescent resonance energy transfer (FRET) is observed (Koch et al., 2008; Qiu et al., 2013); and c) two-step photobleaching events in single Hv1-green fluorescent protein (GFP) fusion protein particles observed using total internal reflection fluorescence microscopy (TIRFM) indicate that most Hv1 proteins are in dimeric assemblies (Tombola et al., 2008).

Truncating the CC domain (Hv1 Δ C) reduces indices of dimerization, suggesting that channels are expressed as a monomers (Koch et al., 2008; Lee et al., 2008; Tombola et al., 2008), as described previously in [CHAPTER 1.1.1](#). Heterologous overexpression of Hv1 Δ C yields robust H⁺ currents, consistent with the hypothesis that monomeric Hv1 channels remain functional (Koch et al., 2008; Lee et al., 2008; Tombola et al., 2008). Covalently linking two

Hv1 protomers by expression of concatenated tandem dimer cDNA constructs also yields functional Hv1 channels (Tombola et al., 2008). As previously discussed ([CHAPTER 1.1.1](#)), N214 (N4) in human Hv1 is typically occupied by an Arg (R4) residue in other VSDs. Incorporating N214C into one or both protomers of the tandem dimer construct allows expression of dimeric complexed with defined stoichiometry: WT-WT, WT-N214C, N214C-WT, or N214C-N214C. Because the introduced Cys is readily modified by MTSET, an arginine-mimetic positively charged moiety can be covalently linked to Hv1 at one or both N214C locations. In WT-N214C, MTSET application blocks ~40% of the original H⁺ current whereas in N214C-N214C the current is almost completely blocked, suggesting that Hv1 tandem dimers possess H⁺ pores in each of the two VSD protomers (Tombola et al., 2008). Although the activation and deactivation kinetics in Hv1ΔC are much faster than WT Hv1, steady-state properties including voltage- and ΔpH-dependent gating are preserved (Koch et al., 2008; Ramsey et al., 2010; Tombola et al., 2008).

1.2.4: Cooperativity in Hv1

Hv1 is gated by multiple different stimuli, including changes in voltage, ΔpH, temperature, and mechanical force, and the effects of changes in one stimulus on the open/closed equilibrium may be allosterically coupled to the effect(s) produced by changes in other stimuli. Hv1 gating is therefore characterized by strong cooperativity. The effects of various stimuli to influence Hv1 gating may be mediated by individual subunits (i.e., intrasubunit cooperativity) or may depend on interactions between protomers in the dimeric quaternary structure (i.e., intersubunit cooperativity). Intrasubunit cooperative gating is displayed by the coupling between changes in membrane potential (Ramsey et al., 2006; Sasaki et al., 2006), ΔpH (Cherny et al.,

1995; Ramsey et al., 2006; Sasaki et al., 2006), extracellular $[Zn^{2+}]$ (Cherny and DeCoursey, 1999; Ramsey et al., 2006; Sasaki et al., 2006), temperature (Fujiwara et al., 2012), and mechanical stimulus (Pathak et al., 2016). Intrasubunit cooperativity is hypothesized to be independent of physical interactions at the dimer interface (Koch et al., 2008; Lee et al., 2008; Tombola et al., 2008), but this hypothesis has not been rigorously tested and the mechanisms of intrasubunit cooperativity in Hv1 remain poorly understood.

Strong experimental evidence for the existence of intersubunit cooperativity in Hv1 gating has been reported: a combination of tandem dimer, mutagenesis, gating charge measurements, and VCF experiments in full length and Hv1 Δ C channels suggest that both S4 voltage sensors must be activated to open the H^+ permeation pathways and that gating transitions in one subunit influence the likelihood that the second subunit will subsequently open (Gonzalez et al., 2010; Tombola et al., 2008). For example, limiting slope estimates of the gating charge estimates in full length Hv1 and Hv1 Δ C constructs indicate that the Hv1 Δ C construct moves half as much gating charge as the full length channel, consistent with the idea that both VSDs must activate to open the H^+ conduction pathways and indicating the CC domain is necessary for intersubunit cooperativity (Fujiwara et al., 2012; Gonzalez et al., 2010). VCF studies show that movement of S4 precedes channel opening in the full length Hv1 channel but in the Hv1 Δ C construct, the time course of channel opening overlaps with a fluorescence signal that is correlated with the S4 movement, suggesting that the CC domain introduces a delay between S4 movement and channel opening (Gonzalez et al., 2010). However, the interpretations of studies conducted in full length and Hv1 Δ C channels is limited because the quaternary structure(s) of experimentally measured channels is not independently determined, and the monomer:dimer ratio is assumed.

Biochemical and structural studies indicate that the CC domain contributes to the intersubunit interface and is necessary for Hv1 dimerization (Koch et al., 2008; Lee et al., 2008; Li et al., 2010; Tombola et al., 2008), however the oligomeric nature of Hv1 and Hv1 Δ C channels in functional studies is unknown and it is possible that the Hv1 Δ C channels remain dimers with no cooperativity between subunits, such that each subunit functions independently from the other. Hv1 Δ C constructs can be coimmunoprecipitated together (Koch et al., 2008; Lee et al., 2008), supporting the idea that CC domain truncation does not prevent dimerization in Hv1. A single point mutation, W207X, demonstrates the rapid activation and deactivation kinetics exhibited in Hv1 Δ C constructs (Cherny et al., 2015; De La Rosa and Ramsey, 2018). W207X mutations are not known to change the monomer-dimer equilibrium in Hv1 and the finding that these mutants copy the kinetic phenotype of Hv1 Δ C constructs suggests that intersubunit cooperativity may be influenced by more subtle interactions. Interestingly, a glutamate residue in the IC end of S2, E153, has been shown to contribute to intersubunit cooperativity (Tombola et al., 2008) as well as intrasubunit cooperativity (CHAPTER 6; De La Rosa et al., 2018), suggesting that inter- and intrasubunit cooperativity may be more intimately related than previously thought. Additionally, the S4/CC linker (residue 220-222 in human Hv1) was previously shown to be necessary for intersubunit cooperativity (Fujiwara et al., 2012) and contains residue K221, which is predicted to interact with E153 in the intracellular network of Hv1 to modulate voltage-dependent gating (Figure 4.1; Figure 4.4). Taken together, the data indicating the importance of W207, E153, and K221 in Hv1 cooperative gating suggests that the electrostatic interactions responsible for intrasubunit cooperativity could also influence intersubunit cooperativity. Alternatively, the effects of Hv1 Δ C on functional properties, which have previously been attributed solely to its effect on the monomer:dimer equilibrium, may

perturb the structures of electrostatic networks and indirectly alter gating properties. The effects of Hv1 Δ C could thus either be caused by monomerization, as suggested, or by changes in intrasubunit cooperativity (or both). Going forward, it will be necessary to further distinguish intersubunit cooperativity from intrasubunit cooperativity and identify the structural components and mechanisms responsible for each.

1.3: Hydrated Electrostatic Networks

Moving the positively charged S4 arginine gating charges through the hydrophobic TM space represents an energetic challenge for VSD proteins. In studies conducted on the Shaker K⁺ channel VSD, the Bezanilla laboratory showed that R4H mutation creates an activated-state H⁺ conductance, while R1H elicits a resting-state H⁺ conductance ([Starace and Bezanilla, 2001, 2004](#); [Starace et al., 1997](#)). As mentioned previously, R1H also confers a resting-state H⁺ conductance in Hv1, and Hv1 natively mediates activated-state H⁺ currents ([Ramsey et al., 2006](#); [Randolph et al., 2016](#); [Sasaki, 2017](#)). The experimental data indicate that VSDs contain a hydrophilic, water-filled pore (through which protons may permeate) that forms a low energy pathway for S4 gating charge movement. Water-protein interactions within the VSD ‘gating pore’ are therefore likely to be integral to the gating and H⁺ permeation mechanisms in VSDs.

The VSD of human Hv1 contains 34 acidic and basic residues, about half of which face the solvent-exposed central crevice gating pore. Structural studies have postulated that these ionizable side chains form two distinct electrostatic networks (ENs): the ICEN is exposed to the cell cytoplasm and the ECEN is exposed to the extracellular milieu ([Figure 4.1](#); [Figure 4.5](#); [Ramsey et al., 2010](#)). The delineation between the IC and EC side is conferred by conserved ‘hydrophobic gasket’ residues in S1-S3 ([Banh et al., 2019](#)), consistent with F150 (in S2) serving as a steric barrier to hydration in the middle of the VSD gating pore of the K⁺ channel VSDs ([Tao et al., 2010](#)). F150 is highly conserved among VSD proteins ([Figure 1.2](#)) and has been termed a ‘gating charge transfer center’ because S4 arginine residues pass by and make transient interactions with this residue during voltage-dependent gating ([Figure 1.4](#); [Tao et al., 2010](#)). A widely accepted model of VSD activation mechanism posits that S4 arginine side chains form salt bridges (i.e. attractive Coulombic interactions) with acidic side chains in the ICEN and

ECEN to stabilize resting and activated state conformations, respectively, of the VSD (Swartz, 2008; Vargas et al., 2012)

E119, D185, and D112 are acidic counter charges in the Hv1 ECEN (Berger and Isacoff, 2011; Chamberlin et al., 2014; Ramsey et al., 2010). Based on phylogenetic conservation in Hv1 orthologues, we consider other ECEN candidates to include D112, E119, D123, D130, K131, H140, and H193; candidate ICEN residues include E153, K157, R162, E164, H167, H168, K169, D174, E171, and K221 (Chamberlin et al., 2014; Ramsey et al., 2010). Confirmatory experimental data are available for most of the identified candidate residues, indicating that structural models can identify functionally significant interactions *a priori* (Chamberlin et al., 2014; Ramsey et al., 2010). For example, an interaction between D112 (S1) and R3/R211 (S4) is known to contribute to selectivity (Berger and Isacoff, 2011; Musset et al., 2011), and demonstrates that ECEN residues are required for both gating and H⁺ selectivity mechanisms.

Titration of acidic and/or basic residues is hypothesized to be central to the Δ pH-dependent gating mechanism in Hv1, and the ‘H⁺ regulatory site’ hypothesis proposed by Cherny, et al. (1995) posited separate monoprotic H⁺ binding sites at EC and IC locations. Site-directed mutagenesis to neutralize key ECEN or ICEN residues was thus predicted to abolish pH_o or pH_i sensitivity. However, an experimental test of this hypothesis in human Hv1 failed to identify mutations that abolish either Δ pH-dependent gating or H⁺ conduction (Ramsey et al., 2010), and it seems likely that ENs probably form ‘delocalized’ H⁺ binding sites that are composed of two or more side chains. The identity of ECEN and ICEN residues that form ENs in Hv1 remains mostly unknown.

1.3.1: Hydration in the Hv1 VSD

Multiple studies have demonstrated deep, hydrated vestibules in VSDs, including Hv1, and the solvent-filled gating pore is thought to constitute the H⁺ permeation pathway in Hv1 and S4 Arg to His mutant VSDs ([Randolph et al., 2016](#); [Starace and Bezanilla, 2004](#); [Starace et al., 1997](#); [Villalba-Galea et al., 2013](#)). An experimental test of this hypothesis has proven difficult because H⁺ conduction in Hv1 is evidently resilient to abrogation by neutralizing mutagenesis of candidate acidic and basic residues that were expected to contribute to the H⁺ permeation pathway (Ramsey et al., 2010). One interpretation of the available experimental data is that H⁺ transfer utilizes a more complicated mechanism than sequential ionization of titratable side chains within the Hv1 gating pore, i.e., a ‘water wire’ (Ramsey et al., 2010). Because neutralizing mutations of candidate residues abolished neither H⁺ transfer nor ΔpH sensing, it has been speculated that the presence of water in the pore of Hv1 could be required for both functions (Ramsey et al., 2006, 2010).

Consistent with experimental and computational studies indicating that the Hv1 gating pore is especially well-hydrated among VSDs (Ramsey et al., 2010), the permeability of guanidinium (a large organic cation) and Cl⁻ (which is thought to permeate together with waters of hydration) in mutant Hv1 channels also indicate the presence of deep water-filled cavities ([Berger and Isacoff, 2011](#); [Musset et al., 2011](#)). The side chain of arginine is a large, positively charged and tethered guanidinium ion that is thought to require a large volume in the gating pore in which to move as a gating charge (Mason et al., 2003). In WT Hv1, guanidinium added to the IC solution blocks outward H⁺ currents, suggesting that it can permeate only partway through the gating pore (Berger and Isacoff, 2011; Hong et al., 2013). Indeed, decreasing side chain in the R3S (R211S) Hv1 mutant allows guanidinium to permeate through Hv1, indicating that R211

contributes to the formation of a constriction or ‘selectivity filter’ within the H⁺ pore (Berger and Isacoff, 2011). Other cations, such as lithium (Li⁺) are also permeable in R211-mutant Hv1 channels, further reinforcing the hypothesis that the pore of Hv1 is sufficiently hydrated to allow hydrated metal cations to permeate (Berger and Isacoff, 2011).

Studies of guanidinium effects on Hv1 function measured in inside-out patches indicate that the IC portion of Hv1 is likely to be hydrated up to F150 in the activated-state conformation (Hong et al., 2013). The location of a hydrophobic gasket that includes F150 at the center of the H⁺ permeation pathway is consistent with the effects of F150 mutation to produce large changes in guanidinium binding affinity of (Hong et al., 2013). The available experimental data argue that a continuous column of water extends from the bulk IC milieu to at least the F150 constriction point in the VSD activated-state conformation. If the ‘selectivity filter’ in Hv1 is formed by interactions between D112 and R211 (Berger and Isacoff, 2011; Musset et al., 2011), it is expected that this location would form the narrowest part of the H⁺ pore (Berger and Isacoff, 2011). Guanidinium accessibility to F150 suggests that the hydrophobic gasket is therefore located just below the selectivity filter ([Banh et al., 2019](#); [Hong et al., 2013](#)).

Other experimental studies also indicate that water is likely to be present throughout the length of the Hv1 gating pore. The existence of phenomenologically similar resting-state H⁺ currents in R1H mutants of other VSDs (Bayless-Edwards et al., 2018; Starace and Bezanilla, 2001, 2004; Struyk and Cannon, 2007; Struyk et al., 2000; Tombola et al., 2005; Villalba-Galea et al., 2013) reinforces the interpretation that water-filled crevices are a shared structural feature that is likely to be functionally important. Based on the size of the resting state H⁺ conductance and other considerations, channel-like resting-state H⁺ permeation in R1H mutants is interpreted to require explicit titration of the introduced histidine side chain (Starace and Bezanilla, 2004).

Ionization of R1H during resting-state H^+ conduction requires a pathway for H^+ to both reach and leave the introduced His, and studies argue that the pathway for H^+ diffusion to His is most likely provided by water-filled crevices ([Randolph et al., 2016](#); [Starace and Bezanilla, 2004](#)).

Collectively, the available experimental data strongly argue that the Hv1 ion channel contains structural plasticity and/or side chain functional redundancy (which confers tolerance to mutations) that could be at least partially explained by the existence of solvent-filled crevices. We therefore hypothesized that hydration in the Hv1 gating pore is highly dynamic, and structural perturbations caused by a variety of different mutations are similarly compensated by reorganization of water-protein interactions.

1.3.2: Extracellular Electrostatic Network

Although the precise architectures of ENs in Hv1 remain unknown, mutagenesis and thermodynamic mutant cycle analysis has identified residues that are likely to directly interact with one another, and these data can be used to impose tight spatial constraints on putative Hv1 model structures ([Table 1.1](#)). For example, neutralizing either D112 or R211 shifts the $P_{\text{OPEN}}-V$ relationship positively, indicating that these residues help stabilize the VSD activated-state (open) relative to the resting-state (closed) conformation ([Ramsey et al., 2010](#)). Astonishingly, when D112 and R211 are switched (D112R-R211D), the $P_{\text{OPEN}}-V$ relationship is restored (i.e., shifted negatively relative to either D112R or R211D) to its position in WT Hv1 ([Berger and Isacoff, 2011](#)). Together with guanidinium accessibility studies discussed previously, the data indicate that D112 and R211 directly interact and contribute to activated-state ECEN structure.

Thermodynamic mutant cycle analysis is used to estimate free energy changes resulting from single and double mutations in proteins, and has been used in a number of different protein

systems to identify interacting pairs of residues (Ackers and Smith, 1985; Di Cera, 1998; Horovitz and Fersht, 1990; Horovitz et al., 1994). Interpreting mutant cycle analysis data is straightforward: if the sum of the calculated changes in Gibbs free energies elicited by two individual mutants versus the respective double mutant is zero, then the side chain interaction either does not exist or does not substantially contribute to the measured response. However, if the calculated difference in Gibbs free energy is not equal to zero, then the interaction between the mutated residues is considered to make an important contribution to the measured parameters and the mutated residues are considered likely to participate in a direct physical interaction. E119, D185, and R208 in Hv1 were previously hypothesized to contribute to ECEN structure (Ramsey et al., 2010), and mutant cycle analysis study of voltage-dependent gating in Hv1 reveals that E119-R205, E119-R208, and D185- R208 pairs are likely to interact to stabilize the activated-state conformation ([Table 1.1](#); Chamberlin et al., 2014). We used generalized interaction analysis (GIA), which is similar in principle to mutant cycle analysis (Chowdhury et al., 2014), to perform a post-hoc analysis of previously published data (Ramsey et al., 2010). Our analysis reveals that the D185-E119 pair has a calculated Gibbs free energy value of -6.1 kcal/mol, and therefore appears to form an important stabilizing interaction in the activated Hv1 channel ([Table 1.1](#)), consistent with the hypothesis that E119 and D185 contribute to ECEN structure (Ramsey et al., 2010).

Hv1 voltage-dependent gating is modulated by EC Zn^{2+} , which is primarily coordinated by H140 and H193 (Cherny and DeCoursey, 1999; De La Rosa et al., 2018; Ramsey et al., 2006). A study designed to test which residues are in proximity to and coordinate Zn^{2+} binding tested the effects of mutating candidate His-interacting side chains on measured Zn^{2+} potency in Hv1 (De La Rosa and Ramsey, 2018). Interestingly, E119H and D185H mutations both

increased Zn^{2+} potency in Hv1, suggesting that each of these residues is close enough to directly coordinate Zn^{2+} , providing further evidence that E119 and D185 contribute to ECEN structure in the Hv1 resting-state conformation (De La Rosa and Ramsey, 2018). D123 and D130 are also in proximity to the Zn^{2+} site and thus contribute to the ECEN (De La Rosa et al., 2018). Available experimental data suggest that, in the Hv1 VSD resting state, acidic residues (D112, E119, D123, D130, D185) outnumber basic residues (H140, H193, R1/R205). Voltage-dependent movement of S4 gating charges drives R2/R208 and R3/R211 outward, allowing them to interact with residues in the ECEN. We hypothesize that voltage-dependent conformational changes in the local EC electrostatic environment are likely to undergo dramatic changes that could have important consequence on the protonation states of the ionizable side chains. Furthermore, changes in side chain charge will secondarily alter the strength of Coulombic interactions that are postulated to stabilize the VSD resting/activated or channel closed/open equilibrium.

1.3.3: Intracellular Electrostatic Network

Mutagenesis and thermodynamic mutant cycle analysis has also been used to identify pairs of interacting side chains in the ICEN ([Table 1.1](#); Chamberlin et al., 2014; Ramsey et al., 2010). E153A and D174A mutations shift the P_{OPEN} -V relationship to more negative potentials, suggesting that E153 and D174 stabilize the resting state of the channel (Ramsey et al., 2010). Because E153 and D174 are expected to function as resting-state countercharges for the S4 gating charge Arg residues R2/R208 and R3/R211, the effects of E153 and D174 neutralization to destabilize the resting state relative to the open state are consistent with model predictions that they are located on the IC side of F150 and thus contribute to ICEN structure (Ramsey et al., 2010). When S4 is in the ‘up’ position (VSD activated state), E153 and D174 do not interact

with S4 gating charges because R2 and R3 have moved to their EC location. Interacting partners of E153 and D174 in the activated state of the channel remain unknown. Our post-hoc GIA analysis of E153-D174 ([Table 1.1](#)) indicates a negative value for the change in Gibbs free energy that is interpreted to mean that these residues stabilize the activated state, and appears to be in contrast with the shifts in $P_{\text{OPEN}}-V$ relationships produced by E153A and D174A mutations. The post-hoc GIA analysis of the E153-D174 interaction was based on G-V relationships but GIA is more robust when based on gating current measurements ([Chowdhury and Chanda, 2012](#); [Chowdhury et al., 2014a, 2014b](#)) and the discrepancy between the GIA and mutagenesis results could be attributed to the use of G-V curves instead of gating current measurements to perform the analysis. Formal mutant cycle analysis has not been reported for the E153A-D174A double mutant and the post-hoc GIA analysis reported in [Table 1.1](#) might be improved by running GIA voltage clamp experiments designed to measure gating current. More rigorous study of the ICEN is needed to understand its structure.

Interestingly, the conservative mutations E153D and D174E also cause large negative shifts in the $P_{\text{OPEN}}-V$ relationships but the E153D-D174E double mutant shifted the $P_{\text{OPEN}}-V$ relationships to even more negative potentials (Ramsey et al., 2010). Our post-hoc GIA determined the free energy value for E153-D174 interaction to be -3.3kcal/mol, suggesting that this interaction contributes to the stabilizing the activated state of the Hv1 channel ([Table 1.1](#)). The large shifts in the opening of Hv1 caused by these conservative mutations suggests factors in addition to charge state are important for determining interactions between side chains at positions E153 and D174. One possibility is that other, as yet unidentified residues also interact with E153 and D174 and that ICEN structure is exquisitely sensitive to structural changes introduced by mutations.

Mutant cycle analysis confirmed that E153-R205, E153-R208, D174-R205, and D174-R208 form important interacting pairs that stabilize the resting state of Hv1 ([Table 1.1](#); [Chamberlin et al., 2014](#)). Together, mutagenesis and mutant cycle analysis reveal a complicated network of interactions in the ICEN. The effects of mutations at several other acidic and basic residues in proximity to the ICEN (E171, K157, K221, and E225) have not been previously reported. However, our preliminary data shows that K157 and K221 are likely to interact and stabilize the resting state relative to the active state ([Figure 4.4A](#)), but important structural mechanistic details remain unknown. Like the ECEN in the VSD resting state, acidic residues outnumber basic residues in the ICEN in models of the VSD activated-state conformation ([Kulleperuma et al., 2013](#); [Ramsey et al., 2010](#)). We hypothesize that voltage-dependent S4 movement leads to large changes in the local ICEN electrostatic environment, and that such changes may be important for pH_i sensitivity in Hv1.

1.4: The H⁺ Permeation Pathway and Mechanisms of H⁺ Permeation

1.4.1: Identity of the Permeating Species

While Hv1 is dubbed a H⁺ channel, the exact nature of the permeating species is not known with certainty because ionic selectivity is determined by comparing the calculated Nernst potential with the measured E_{rev} , as described previously. H⁺ and H⁺ equivalents like H₃O⁺ or hydroxide ion (OH⁻) are electrophysiologically indistinguishable because they share the same Nernst potential. This conundrum has generated confusion and debate in the field that remains the subject of active discussion ([Bennett and Ramsey, 2017a, 2017b](#); [DeCoursey, 2017](#)). Despite the difficulty in precisely identifying the ionic species, independent evidence indicates that the measured Hv1 conductance is indeed a H⁺ (and not H₃O⁺ or OH⁻). The most convincing evidence comes from deuterium (D) isotope replacement experiments in which conductance in different solutions was measured: H⁺ vs. D⁺, ⁻OH vs. ⁻OD, and H₃O⁺ vs. D₃O⁺ are decreased 41%, 3%, and 8%, respectively (DeCoursey and Cherny, 1997). Astonishingly, when H₂O is replaced by D₂O in Hv1 voltage clamp experiments, the conductance decreases about 50%, which seems to rule out ⁻OH and H₃O⁺ as the permeating species (DeCoursey and Cherny, 1997). Conversely, the isotope effect of deuterium on Hv1 is close to that expected if H⁺ permeates using a Grotthuss-type hydrogen-bonded chain (HBC; [Supplementary Figure 3](#)) and the data therefor support the hypothesis that H⁺ is the ionic species that carries current through Hv1 (DeCoursey and Cherny, 1997). In short, WT Hv1 most likely *IS* a highly H⁺-selective channel.

1.4.2: Proton Conduction in Hv1

The unitary conductance of a single ion channel protein complex is determined by structural features and can help reveal permeation mechanism. Although unitary conductance is typically measured using excised patch voltage clamp experiments in which single channel currents can be readily measured and analyzed, the small Hv1 unitary conductance prevents direct observation due to amplifier signal to noise (S/N) ratio limitations. Fluctuation analysis allows single-channel conductance to be indirectly estimated from macroscopic current measurements, and has Hv1 been estimated to generate a 30-40 femtoSiemens (fS) unitary conductance at pH 6.5 (Decoursey, 2003). In comparison to many other ion channels, this is a very small unitary conductance. However, when H^+ currents are typically measured under conditions where the concentration of the permeant H^+ species at physiological pH is low (at pH 6.5, $[H^+] = 10^{-6.5}$ molar or 130 nM). In comparison, physiological extracellular Na^+ and intracellular K^+ concentrations are in the 100-150 mM range (about 1 million times higher than H^+ at pH 6.5!). It is perhaps astonishing that H^+ currents are even measurable, suggesting that Hv1 channels are likely to be expressed at high density. Consistent with this hypothesis, a recent study estimated that HEK-293 cells transfected with human Hv1 express $>10^6$ channels per cell (De La Rosa and Ramsey, 2018). Finally, a straightforward estimate of the Hv1 unitary conductance at pH 2.0 (i.e., ~ 130 mM $[H^+]$), which was previously shown to increase ~ 2 -fold per pH unit (Decoursey, 2003), suggests that when measured under ionic conditions that are equivalent to those typically used for monovalent cation-selective channels, the Hv1 unitary conductance would be ~ 0.3 pS. By comparison, unitary conductance of voltage-gated cation channels expressed in vertebrate neurons and skeletal muscle range from 2.5-50 pS, which is within an order of magnitude of our estimate for Hv1. We conclude that the unitary conductance

of Hv1 is in fact robust, but unitary currents are difficult to measure at physiological pH due to the low concentration of its permeant ion, H^+ .

1.4.3: Mechanisms Proton Conduction in Hv1

The precise mechanism of H^+ conduction in Hv1 is debated. An early hypothesis proposed that at least one, but perhaps multiple, side chains are explicitly titrated during transmembrane H^+ transfer through Hv1; in essence, the channel protein forms a hydrogen-bonded chain allowing protons to ‘hop’ from one ionizable atom to the next until they have crossed the membrane electrical field ([Decoursey, 2003](#)). However, the side chain titration hypothesis failed an experimental test: neutralizing mutations of candidate ionizable residues do not abrogate H^+ currents carried by Hv1 (Ramsey et al., 2010). The most straightforward interpretation of the mutagenesis data seems to rule out simple side chain titration as being necessary for H^+ conduction in Hv1, but it remains possible that there is a high degree of functional redundancy among ionizable side chains in Hv1 and exotic compensation in mutant proteins can account for the reported experimental data.

Grotthuss H^+ transfer, which occurs readily in aqueous solutions at physiological pH ([Supplementary Figure 3](#); Cukierman, 2006), provides a possible explanation for the H^+ conduction mechanism in Hv1. Grotthuss-type H^+ transfer requires a series of waters (or other H^+ donor/acceptor species) to form a continuous HBC ([Nagle and Morowitz, 1978](#)). Initially a H^+ protonates the first water molecule in the HBC, forming H_3O^+ . H_3O^+ subsequently donates its excess H^+ to an adjacent H_2O , effectively moving the proton the distance of one hydrogen bond in each step, and a series of hydrogen-bonded water molecules can thus sustain vectoral H^+ transfer

([Supplementary Figure 3](#)). Grotthuss H^+ transfer is faster than diffusion, and accounts for the ‘anomalously’ high mobility of H^+ in aqueous solution ([Decoursey, 2003](#)).

In the gating pore of Hv1, acidic and basic amino acid side chains could work together with resident water HBC to mediate H^+ transfer. However, the necessity of ionizable side chains in the gating pore for H^+ transfer appears to be inconsistent with experimental data reviewed earlier ([Ramsey et al., 2010](#)). The simplest explanation is that the pore of Hv1 is sufficiently hydrated in the open state to allow H^+ conduction via an all-water HBC (i.e., a water wire or proton wire). In this interpretation, side chain residues may serve mainly to constrain water molecules within the gating pore and create a permissive environment for water wire H^+ transfer ([Ramsey et al., 2010](#)). This mechanism, sometimes referred to as an ‘aqueous’ mechanism of H^+ conduction, is consistent with the presence of deep aqueous vestibules observed in activated-state Hv1 model structures ([Berger and Isacoff, 2011](#); [Hong et al., 2013](#); [Kulleperuma et al., 2013](#); [Li et al., 2015](#); [Ramsey et al., 2010](#); [Randolph et al., 2016](#); [Wood et al., 2012](#)), the anomalous large deuterium isotope replacement effect ([DeCoursey and Cherny, 1997](#)), and the presence of robust H^+ currents in many measured mutants ([Ramsey et al., 2010](#)). Because the water wire mechanism is a type of Grotthuss proton transfer, it is intrinsically H^+ selective and therefore can confer exquisite H^+ selectivity. While the water wire mechanism has been supported by some MD studies ([Ramsey et al., 2010](#); [Wood et al., 2012](#)), it is not yet possible to differentiate a HBC formed of waters versus that formed from side chains in a voltage clamp experiment and therefore, the water wire structure cannot be differentiated from a HBC formed exclusively of amino acid side chains. It is also possible that the HBC is formed from both water molecules and amino acid side chains and this possibility is supported by several MD studies ([Chamberlin et al.,](#)

2014; Kulleperuma et al., 2013; Li et al., 2015). But again this HBC composition cannot be differentiated from a side chain exclusive or water exclusive HBC.

Acidic, basic, and polar amino acids are expected to be crucial for shaping the exact geometry of the HBC, if not directly involved in conduction themselves, and thus dictate H⁺ permeation properties. Although a HBC made of only protein residues seems to be ruled out, the major contributors to the HBC and the architecture of the HBC remain to be worked out. Much work is left to be done to identify these crucial components of Hv1 but the work to differentiate the different type of HBCs will be difficult.

1.5: Mechanisms of voltage sensing and voltage-dependent gating

1.5.1: Voltage Sensing Mechanisms in Hv1

A consensus mechanism of voltage sensing in VSD containing proteins was recently proposed (Vargas et al., 2012). Arg side chains in the S4 helix of VSDs are located every three residues apart along the length of the helix (Figure 1.2), creating a positively charged helical face that faces the solvent-exposed gating pore; the S4 gating charges thus lie fully or partially within the transmembrane electric field. Changes in membrane potential act on the S4 gating charges to elicit upward (extracellular) movement upon depolarization and downward (intracellular) movement upon hyperpolarization (Figure 1.4). As the gating charges move within the electric field, they generate a small but measurable gating current. Most VSDs contain four S4 gating charge residues (R1 – R4), as exemplified by the *Shaker* K⁺ channel (Figure 1.2; Aggarwal and MacKinnon, 1996; Seoh et al., 1996). In Hv1, there are only three: R1/R205, R2/R208, and R3/R211; R4 is replaced by N4/N214 (Ramsey et al., 2006; Sasaki et al., 2006).

The earliest studies to investigate gating charges in Hv1 used mutagenesis and voltage clamp methods to examine the effects of neutralizing S4 Arg residues on voltage-dependent gating (Gonzalez et al., 2013; Ramsey et al., 2006; Sasaki et al., 2006). One study showed that R1A decreased the steepness of a Boltzmann fit to the apparent P_{OPEN}-V relation, suggesting that the equivalent gating charge valence (z_G) was reduced as expected (Ramsey et al., 2006). Another study utilized the limiting slope method to estimate gating charge valence and found that in WT (presumably dimeric) *Ciona intestinalis* Hv1, $z_G \approx 6$ elementary charges (e_0) (Gonzalez et al., 2010). The $z_G \approx 6 e_0$ is consistent with a model in which each Hv1 protomer contributes 3 e_0 and both VSDs must be activated before Hv1 can open and conduct H⁺

(Gonzalez et al., 2010). Congruous with predictions, $z_G \approx 3 e_0$ in (presumably monomeric) Hv1 Δ C and neutralizing each S4 Arg reduces the effective gating charge by $\sim 2 e_0$ in full length channels (Gonzalez et al., 2010, 2013). Gating currents were reported in mutant Hv1 channels (Carmona et al., 2018; De La Rosa and Ramsey, 2018) and integrating the gating current yields a direct estimate of the gating charge. Integration of gating current is the gold standard for measuring VSD activation. As in limiting slope measurements, S4 Arg neutralization decreases the quantity of gating charge as expected (De La Rosa and Ramsey, 2018). Voltage sensing in Hv1, therefore, appears to utilize a mechanism that is highly conserved in VGCs and VSPs from, bacteria, archaea and eukaryotes (Vargas et al., 2012).

1.5.2: Mechanisms of Voltage-Dependent Gating in Hv1

Although the notion that changes in membrane potential drive movement of the S4 helix is now well-accepted (Gonzalez et al., 2010, 2013; Larsson et al., 1996; Mannuzzu et al., 1996; Vargas et al., 2012; Yusaf et al., 1996), there is no consensus about the exact trajectory or extent of S4 movement during gating (for a review see Fig. 4 in Tombola et al., 2006). Although we can now measure electrical readouts of Hv1 gating charge movement, interpreting how S4 itself moves during gating is more difficult. This problem is exacerbated by the fact that the shape of the electrical field drop across a membrane in which the Hv1 VSD is embedded is not known, and field shape is likely to change in response to voltage-dependent conformational reorganization of VSD structure during gating. In fact, rearrangement of the transmembrane electric field around the gating charges (without any movement of the gating charges themselves) can explain observed gating currents. However, site-specific accessibility and

voltage clamp fluorometry (VCF) studies are almost universally consistent with the hypothesis that S4 undergoes major conformational changes during voltage-dependent gating.

Like gating currents, chemical accessibility and VCF studies in Hv1 are similar to previous results in VSDs from other VGC and VSPs, suggesting a shared mechanism (Gonzalez et al., 2010, 2013). For example, Cys residues introduced along the S4 helix in Hv1 exhibit conformation-dependent accessibility to [2-(trimethylammonium)ethyl] methanethiosulfonate (MTSET) and (2-sulfonatoethyl) methanethiosulfonate (MTSES), indicating that solvent accessibility to S4 is state-dependent (Gonzalez et al., 2010). The pattern of MTSES reactivity in Cys mutants introduced along the S4 helix in Hv1 strongly suggests that, just as in other VSDs, S4 moves from a down (IC solvent-exposed) position at hyperpolarizing voltages where Hv1 is closed, to an up (EC solvent-exposed) position at depolarizing potentials where Hv1 is more likely to be open (Gonzalez et al., 2010, 2013). Consistent with MTSES accessibility studies, a VCF study demonstrated that an Alexa488-maleimide fluorophore, which is highly sensitive to changes in local electrostatic environments, incorporated into an S4 Cys mutant in *Ciona* Hv1 exhibits drastic changes in fluorescence during depolarizing steps (Gonzalez et al., 2010). The kinetics of the fluorescence changes closely match the kinetics of the H⁺ current activation time course, supporting the idea that S4 undergoes a conformational change that alters environmental quenching of the Alexa488 dye during channel gating. Despite the fact that most studies are consistent with the consensus model of voltage sensor activation (Vargas et al., 2012), precise descriptions of S4 motion during gating remain a topic of debate.

Models of S4 helix movement in Hv1 include the moving orifice model, in which S4 simply moves up and down during gating, and the helix screw model, in which S4 moves up and down while also rotating (Bezanilla, 2008; Chanda and Bezanilla, 2008; Tombola et al., 2006).

MTSES accessibility reveals that L198C (on the EC end of S4) is selectively accessible at depolarizing potentials (where Hv1 is open) and N214C is selectively accessible at hyperpolarizing potentials where the channel is closed (Gonzalez et al., 2010). Taken together, MTSES accessibility experiments suggest that at least two, but possibly all three, of the S4 Arg side chains in Hv1 are moved across the field during voltage-dependent gating (Gonzalez et al., 2010).

Resting-state H⁺ currents in Hv1 R1H suggest that R1 normally prevents H⁺ permeation in the VSD resting-state conformation, implying that the introduced His is located at constriction point in the Hv1 pore (i.e., within the hydrophobic gasket) and simultaneously accessible to protons in both IC and EC solvent-filled crevices (Randolph et al., 2016). Conversely, N4R voltage-dependently blocks the outward H⁺ current, suggesting that the positive charge introduced at this position also lies near or within the solvent-filled hydrophobic constriction that forms the H⁺ pore, and can thus block the passage of H⁺ in a state-dependent fashion (Ramsey et al., 2010). Taken together, the aforementioned studies seem to rule out a one-click model (in which only one S4 arginine residue is moved across the electric field) that was proposed based on structural studies in Hv1 and *Ci*VSP (Li et al., 2014, 2015). Instead, S4 is estimated to move vertically by 10-14 Å during voltage-dependent gating (Randolph et al., 2016).

Previous studies in VCGs and VSPs suggested that S4 may also undergo a partial or full transition alpha- to 3₁₀-helical back bone structure during voltage-dependent gating (Kubota et al., 2014; Schwaiger et al., 2011; Vargas et al., 2012; Villalba-Galea et al., 2008, 2013). The first suggestion that structural reorganization in the Hv1 VSD during gating mechanisms might be more complicated than a simple up/down movement of S4 helix came from a kinetic analysis of H⁺ current time courses, where a minimum of four states were required to accommodate the

observed current transitions measured under voltage clamp (Villalba-Galea, 2014). Interestingly, the final rate-limiting transition preceding the opening of Hv1 channel is modeled to be voltage-independent, but the voltage-independent step is evidently not observed during deactivation gating (Villalba-Galea, 2014). More recent chemical accessibility and VCF studies raise the possibility that the EC end of S1 also undergoes voltage-dependent movement (Mony et al., 2015). Another study suggests that S3 residues could move during gating (Sakata et al., 2016). Together, experimental data imply that VSD conformational rearrangements during gating may be more complicated than has been previously thought, but atomic simulations that model such transitions have so far only been investigated in VGCs (Delemotte et al., 2011; Gosselin-Badaroudine et al., 2012; Jensen et al., 2012). The characteristically steep ΔpH -dependence of voltage-dependent gating in Hv1 suggests that the VSD activation mechanism could be more complicated in Hv1 than it is in other VGCs and VSPs. Voltage- and ΔpH -dependent gating in Hv1 are tightly coupled (Cherny et al., 1995; Musset et al., 2011; Ramsey et al., 2006, 2010), but the mechanism of such coupling remains essentially unknown. It is interesting to speculate that voltage-independent transitions may be key to understanding how pH changes, trigger protonation or deprotonation events outside of the electrical field, and thereby influence voltage-dependent gating in Hv1.

In summary, the mechanism of voltage-dependent gating in Hv1 is likely to be similar, but not identical to that in other VGCs and VSPs: positively charged S4 Arg gating charge residues move in response to changes in voltage and require acidic countercharges to form Coulombic interactions that stabilize resting- and activated-state conformations (Figure 1.4). Gating charge movement requires a hydrophilic pathway (the gating pore), which is also used for activated-state H^+ -selective conduction in Hv1, possibly via an intra-protein water wire. ΔpH -

dependent modulation of voltage-sensitive gating is likely to require ionizable side chains that are accessible to EC and IC solutions, and proposed H^+ regulatory sites are likely to be formed by groups of side chains that interact in electrostatic networks. Identifying the amino acids that are necessary for ΔpH -dependent gating in Hv1 remains a major challenge in the field and is crucial to developing a more complete understanding of gating mechanisms in Hv1.

1.6: The selectivity filter and mechanisms of proton selectivity

1.6.1: The Hv1 Selectivity Filter

Hv1 boasts the greatest selectivity among ion channels and transporters with no reports of ions, other than H^+ , permeating the WT channel (DeCoursey, 2015). Mutagenesis experiments have identified two residues as being required for exquisite proton selectivity in Hv1: D112 (S1) and R3/R211 (S4) (Berger and Isacoff, 2011; Musset et al., 2011). Mutating D112 to any of several side chains other than Asp (D112X) erodes the normally high H^+ selectivity in Hv1 and allows anions (e.g., Cl^- and methanesulfonate ($MeSO_3^-$)) to permeate (Musset et al., 2011). One interpretation of the Musset et al., (2011) data is that a tethered anion (i.e., Asp^- or Glu^-) is required to prevent anions in solution from permeating through the hydrated gating pore in Hv1, and suggests that D112 remains ionized in the open state conformation. In the R3S (R211S) mutant, Hv1 becomes permeable to monovalent cations other than H^+ (i.e., Li^+ and guanidinium⁺) but other Hv1 biophysical properties are evidently unaffected (Berger and Isacoff, 2011). Analogous to the effect of N4R/N214R to block the Hv1 pore, discussed previously, R3/R211 appears to be necessary for excluding cation in solution from permeating in the WT protein. Surprisingly, pH_o sensitivity is intact in both D112X and R3S mutants, indicating that H^+ selectivity and ΔpH -dependent gating are separable phenomena that are likely to utilize distinct mechanisms (Berger and Isacoff, 2011; Musset et al., 2011).

Although D112X mutants allow anion permeation, E_{rev} analyses indicate that they also permit H^+ (or a H^+ equivalent like OH^- or H_3O^+) to permeate (Musset et al., 2011). Stated differently, D112X channels do not appear to be highly selective for Cl^- over H^+ , but it remains unclear whether these mutant channels select for protons over other acid equivalent species.

Although Hv1 appears to have a long and narrow solvent-filled gating pore (Kulleperuma et al.,

2013; Ramsey et al., 2010; Wood et al., 2012), other amino acid side chains that influence H^+ selectivity have not yet been identified. However, transplanting an Asp into the position normally occupied by V116, which is predicted to be one helical turn above D112, is sufficient to reconstitute H^+ conductance and H^+ -selectivity when incorporated into the background of the otherwise nonfunctional D112V mutant (i.e., D112V-V116D) (Morgan et al., 2013). Selectivity filter ‘peregrination’ is consistent with the notion that other side chains in the Hv1 gating pore may have important roles in determining ionic selectivity, unitary conductance, or pH_o -dependent gating, but their roles have not yet been elucidated. Nonetheless, the available data unequivocally indicate that both D112 and R211 are critical components of what may be a complex selectivity filter apparatus.

Although the ‘hydrophobic gasket’ is located immediately below the selectivity-determining residues D112 and R3/R211 in activated-state Hv1 models (Kulleperuma et al., 2013; Ramsey et al., 2010; Wood et al., 2012), F150 mutations do not alter H^+ selectivity, indicating that gating and selectivity mechanisms are separable (Hong et al., 2013). Interestingly, W207 has been argued to influence selectivity in Hv1, but the effects of this mutation are only observed at $pH_o > 8$ (Cherny et al., 2015), further supporting the hypothesis that residues other than D112 and R211 are required for exquisite H^+ selectivity in WT Hv1. In contrast to D112X and R3S mutations, W207X mutants do affect pH_o sensitivity, but only at high EC pH, suggesting that W207 could contribute to both selectivity and ΔpH -dependent gating mechanisms (Cherny et al., 2015). To act as an EC pH sensor, W207 presumably needs to be in contact with the EC solution and therefore, to contribute to H^+ selectivity, W207 would most likely be located within the channel pore. However, activated-state Hv1 model structures universally place W207 in a membrane-exposed position that is shielded from solvent in the

gating pore ([Kulleperuma et al., 2013](#); [Li et al., 2015](#); [Ramsey et al., 2010](#); [Takeshita et al., 2014](#); [Wood et al., 2012](#)), and are unable to explain the functional effects of W207 mutations on selectivity and pH_o sensitivity. New, structural models that are fully consistent with experimental data are therefore needed.

1.6.2: Mechanisms of Selectivity in Hv1

D112, R3/R211, and W207 are implicated as determinants of H^+ selectivity in Hv1, but the atomic mechanism by which Hv1 achieves exquisite proton selectivity are under debate. A theoretical study employing density functional theory (DFT), a computer simulation technique based on quantum mechanics (QM) calculations that calculate putative electronic structures within molecular models was applied to the Hv1 problem ([Dudev et al., 2015](#)). The authors postulates that DFT might help determine the plausibility of bond-making and bond-breaking events, such as might occur during titration events associated with H^+ transfer via explicit ionization of Hv1 residue side chains ([Cramer, 2004](#); [Dudev et al., 2015](#)). DFT calculations were performed on a minimal Hv1-like model system containing only 2 side chains (Asp and Arg) tethered in apposition by a synthetic ring structure and a single H_2O or H_3O^+ ([Dudev et al., 2015](#)). Despite the fact that their system is highly artificial and abstracted from activated-state Hv1 model structures, the authors interpret their result as evidence in favor of a H^+ transfer event that neutralizes D112 ([Dudev et al., 2015](#)). After protonation of Asp, hydrogen bonds involving Asp and Arg in the model ring structure are disrupted and the residues move apart, allowing Asp to donate a proton to water, creating H_3O^+ and resetting the negative charge on Asp ([Dudev et al., 2015](#)). Although the Asp-titration model is intriguing, it is inconsistent with prior experimental and computational data in the literature.

Because the results of energetic calculations based on DFT are highly dependent on atomic distance, the initial coordinates of any model will significantly influence outcomes. Asp/Arg coordinates used in the ring model structure as input for DFT calculations differ substantially from the positions that these side chains occupy in Hv1 model and X-ray structures ([Chamberlin et al., 2014](#); [Kulleperuma et al., 2013](#); [Li et al., 2015](#); [Ramsey et al., 2010](#); [Randolph et al., 2016](#); [Wood et al., 2012](#)). For example, helices containing D112 and R2 (S1 and S4, respectively) are adjacent in Hv1 and all other VSD structures; in the simple ring model, however, the residues directly face one another (i.e., as if they are on S1 and S3 or S3 and S4 helices), and both distance and geometric measures are thus dramatically different. Unfortunately, structural disagreements between the model used for DFT-based calculations and experimental and computational Hv1 VSD model structures suggest that the conclusions of this study should be interpreted with caution. Furthermore, it remains unclear how Hv1 would retain H⁺ selectivity if D112 is protonated (neutralized) during H⁺ transfer; this would not only break the D112-R211 Coulombic interaction that stabilizes the activated-state structure but structurally mimic anion-permeable D112X mutants. Although [Dudev et al. \(2015\)](#) argue that Cl⁻ does not permeate in their system, the paucity of hydrating water for Cl⁻ raises suspicion about the robustness of this claim. Furthermore, the DFT study cannot address why D112X mutants evidently remain permeable to H⁺ ([Musset et al., 2011](#); [Ramsey et al., 2010](#)). Finally, the 2-residue ring omits other side chains, such as W207, that are implicated in the selectivity mechanism by experimental data ([Cherny et al., 2015](#)).

An alternative hypothesis posits that H⁺ selectivity in Hv1 is achieved by virtue of a water wire ([Ramsey et al., 2010](#)), and side chains that line the pore of Hv1 are responsible for

structuring water to facilitate HBCs between and among water molecules that support Grotthuss-type H^+ transfer ([Supplementary Figure 3](#); Ramsey et al., 2010). Because $^1H^+$, $^2H^+$ and $^3H^+$ are the only ions known to utilize the Grotthuss transfer mechanism, the pathway is inaccessible to other cations and HBC are intrinsically H^+ selective, provided that the pore is long and sufficiently charged to deny entrance to other ions (Cukierman, 2003, 2006; Pomès and Yu, 2003). It is important to note that the HBC could be formed of water molecules, acidic and basic residues, or a combination of side chains and waters; water-wire and side chain ionization mechanisms are not mutually exclusive, and exotic structural possibilities for H^+ transfer mechanism in Hv1 abound. However, a water wire model (Ramsey et al., 2010) is simple and seems able to account for all known experimental data to date ([Bennett and Ramsey, 2017a](#), [2017b](#)). Water wires can utilize a large number of possible HBC structures embedded in dynamic intra-protein reservoirs and this structural plasticity could also help explain why Hv1 is so tolerant of mutations ([Berger and Isacoff, 2011](#); [Chamberlin et al., 2014](#); [Cherny et al., 2015](#); [Morgan et al., 2013](#); [Musset et al., 2011](#); [Ramsey et al., 2010](#)). Depending on the actual number of water molecules in the Hv1 gating pore, Hv1 could contain multiple different HBCs that are simultaneously competent for H^+ transfer, allowing the water wire to conduct H^+ at a high enough rate to support a substantial unitary conductance. Critical experimental tests of the water wire hypothesis are daunting, however, due to technical limitations. Techniques that can discriminate between H^+ and OH^- permeation or detect Asp protonation events (i.e., nuclear magnetic resonance spectroscopy) are currently incompatible with the need to control transmembrane voltage and pH gradients in studies of Hv1 function.

1.7: Hv1 Inhibition by Zn²⁺

1.7.1: The Zn²⁺ Binding Site in Hv1

Inhibition of voltage-dependent gating of native H⁺ currents by Zn²⁺ was documented long before the Hv1 channel was cloned (Cherny and DeCoursey, 1999). EC Zn²⁺ causes large depolarizing shifts in the Hv1 apparent P_{OPEN}-V relation, thus keeping the channel closed at voltages it would typically be open and necessitating a larger depolarization voltage to drive the channel to the open state. Hv1 is sensitive to micromolar concentrations of EC Zn²⁺. When Hv1 was first cloned, two EC histidine residues, H140 and H193, were found to be necessary for inhibition of Hv1 by Zn²⁺, with H140A and H193A causing approximately a 30- and 10-fold, reduction in Zn²⁺ potency, respectively (Ramsey et al., 2006). Deletion of both H140 and H193 in the Hv1 H140A-H193A further reduces the Zn²⁺ potency to the millimolar concentration range (Ramsey et al., 2006). This data argues that H140 and H193 are primary coordination sites for Zn²⁺ in Hv1. However, because the H140A-H193A mutant retains millimolar Zn²⁺ potency, other residues may also contribute to Zn²⁺ coordination.

1.7.2: Mechanisms of Zn²⁺ Inhibition of Hv1

The identification of H140 and H193 as primary Zn²⁺ sites suggested a straightforward mechanism: Zn²⁺ tethers H140 (S2) and H193 (S4) restricting S4 movement and stabilizing the resting-state conformation to cause a rightward shift of the P_{OPEN}-V relation ([Figure 1.5](#); Ramsey et al., 2006). A recent investigation into more detailed mechanistic descriptions of Zn²⁺ revealed that additional residues and binding modes are involved and put forth a more detailed description of how Zn²⁺ could inhibit the Hv1 channel. VCF conducted in *Ci*-Hv1 channels labeled at the EC

end of S4 (S242C *Ci*-Hv1 numbering) labeled with the Alexa488 fluorophore suggested that Zn^{2+} can interact with several other Hv1 residues, possibly resulting in multiple Zn^{2+} binding modes in Hv1 (Qiu et al., 2016). E119 was found to play a role in coordinating Zn^{2+} (Qiu et al., 2016), consistent with the mHv1cc X-ray structure (Takeshita et al., 2014) and another mutagenesis study (De La Rosa et al., 2018). E119 was previously shown to stabilize the activated-state conformation in Hv1 by acting as a counter charge for one of the S4 gating charges (Ramsey et al., 2010), and therefore S4 counter charges were hypothesized to compete with Zn^{2+} for binding at E119. However, in *Ci*-Hv1, His is replaced by Glu at the (human Hv1) 192-equivalent amino acid position, indicating that the mechanism for Zn^{2+} coordination in *Ci*-Hv1 may be subtly but importantly different from that in human Hv1. Additionally, many of the mechanistic conclusions in the VCF study were drawn from QM studies of a *Ci*-Hv1 model that were not fully verified by experimental results, and it remains possible that the conclusions are not applicable to understanding Zn^{2+} mechanisms in human Hv1. We hypothesized that the mechanism of Zn^{2+} inhibition of Hv1 might be more complicated than a simple immobilization of S4 and showed that Zn^{2+} triggers long-range conformational changes in the ICEN that foster Coulombic interactions which stabilize the resting-state conformation (De La Rosa et al., 2018). Because the depolarizing shift in the voltage dependence of Hv1 gating elicited by Zn^{2+} is phenomenologically similar to that produced by EC acidification, their mechanisms could be mechanistically conserved.

1.8: The pH sensor and Δ pH-dependent gating

1.8.1: Hv1 Δ pH-Dependent Gating

Hv1 voltage-dependent gating is modulated by changes in Δ pH, as illustrated by studies of native voltage-gated H^+ currents (now attributed to Hv1) in rat alveolar epithelial cells (Cherny et al., 1995). Δ pH-dependent gating is considered a hallmark biophysical feature of Hv1 and indicates that Δ pH sensitivity is coupled to voltage-dependent gating; this coupling allows Hv1 to accomplish its main goal of extruding acid from the cell by only opening at potentials positive to the Nernst potential for H^+ (DeCoursey, 2015). Hv1 gating is sensitive to changes in the pH of both the EC and IC solution and changes in either pH_o or pH_i elicit equivalent shifts in the apparent P_{OPEN} -V relation when they result in the same net change in Δ pH. As a consequence, Hv1 appears to be sensitive to changes in the pH gradient (Δ pH) rather than the absolute pH of IC or EC solutions (Cherny et al., 1995; Ramsey et al., 2006; Sasaki et al., 2006). The apparent P_{OPEN} -V relation characteristically shifts about 40mv/pH unit, and this measure of coupling between pH- and voltage-dependent gating is considered to be the steepest among VGCs and VSPs (Cherny et al., 1995; Ramsey et al., 2006; Sasaki et al., 2006). Little is presently known about the identities of residues that are required for Δ pH-dependent gating in Hv1 and the mechanisms of pH_o , pH_i , and Δ pH-dependent gating and its coupling to voltage-dependent gating remain poorly understood. Several mechanisms of Δ pH-dependent gating in Hv1 have been proposed (Cherny et al., 1995; DeCoursey, 2018). Models containing either a single H^+ ‘regulatory site’ (‘butterfly’ model) that is alternately accessible to proton in either the EC or IC solutions (Cherny et al., 1995) or distinct EC and IC H^+ binding sites (‘counter-charge’ model) have been proposed (Cherny et al., 1995; DeCoursey, 2018). Until recently, experimental data

did not clearly differentiate between the two models, but the identification of H168 as a contributor to the IC site (Cherny et al., 2015, 2018) more strongly supports the ‘counter-charge’ model. One weakness of the ‘counter-charge’ model, however, is that it does not identify specific side chains other than H168 and the mechanism(s) responsible for coupling ΔpH sensing and voltage sensing remain unexplained.

1.8.2: Hv1 ΔpH Sensor Structure

As described in the ‘butterfly’ model, a simple way to construct a ΔpH sensor in Hv1 would be to have an ionizable site (or sites) with alternating access to IC and EC solution interact with the voltage sensor (Cherny et al., 1995). In that model, a single H^+ binding site either moves across or experiences changes in the transmembrane electric field, to transduce changes in IC or EC solution pH. In order to sense both IC pH and EC pH, studies have hypothesized that Hv1 contains at least two distinct H^+ binding sites that function as pH sensors: one is exposed to the EC solution and another is exposed to the IC solution (Cherny et al., 1995, 2015, 2018; DeCoursey, 2018). In the two-site model, H^+ binding at either the IC or EC site is mutually exclusive with H^+ binding at the other site (Cherny et al., 1995). The butterfly model necessitates mutual exclusivity of H^+ binding due to the movement of the binding site from the IC side of membrane to the EC side of membrane. However, the means by which the two-site model would exhibit mutual exclusivity of H^+ binding between the IC and EC sites remains unknown, but could involve allosteric communication between the two H^+ binding sites (Cherny et al., 1995).

In the first mutagenesis experiments designed to identify residues that function as pH_o sensors, each candidate ionizable residue was neutralized by mutation to Ala and the effects of pH_o changes on shifts in V_{thr} were used to determine whether mutations altered voltage- or pH-

dependent gating (Ramsey et al., 2010). Mutations (D112A, E119A, E153A, D174A, D185A and R211A) were shown to cause large positive or negative shifts in on the position of the apparent $P_{\text{OPEN}}-V$ relation, but none of the mutations tested appeared to alter ΔpH -dependent gating (i.e., the $\sim 40\text{mV/pH}$ shift seen in WT Hv1 was not substantially perturbed), suggesting that the mechanism of ΔpH sensitivity in Hv1 requires titration of more than one amino acid side chain (Ramsey et al., 2010).

A closer look at this early mutagenesis study reveals small differences in ΔpH -dependent gating between WT Hv1 and mutant Hv1, which could indicate residues that contribute to ΔpH sensing that, when mutated simultaneously, would reveal a Hv1 channel with obviously altered ΔpH -dependent gating. A two-way t-test recently performed on the mutagenesis data revealed that some residues may indeed cause small perturbations in Hv1 ΔpH sensitivity ([Table 1.2](#)). Residues of note from this analysis are E119, D123, and D185, which mutagenesis and mutant cycle analysis studies predict to contribute to the ECEN, and E153 and D174, which are predicted to contribute to the ICEN ([Figure 4.1](#); [Figure 4.5](#); Chamberlin et al., 2014; Ramsey et al., 2010). There may be insight yet to gain from these mutagenesis studies, however, so far they have not revealed the residues necessary for EC, IC, or ΔpH sensing.

1.8.3: The EC pH Sensor

A more recent mutagenesis study divulged the identity of an aromatic residue that seems to be important for pH sensing in Hv1. W207 is located in S4 adjacent to R2 (R208) and is conserved in the primary sequences of Hv1 orthologues that are known to function as voltage-gated H^+ channels; mutating W207 appears to alter functional properties that are considered defining features of Hv1 channels (Smith et al., 2011). In VSDs from related VGCs and VSPs,

W207 is replaced by another hydrophobic residue ([Figure 1.2](#)). A role for W207 in ΔpH -dependent gating was proposed based on the results of W207 mutagenesis and voltage clamp studies: W207X mutants retained ΔpH -dependent gating up to EC pH 7.5, at which point pH-dependent gating is apparently described by a slope < 40 mV/pH unit; in contrast, WT Hv1 retains quasi-linear ΔpH -dependent gating (~ 40 mV/pH unit) to at least EC pH 8.5 (Cherny et al., 2015). Importantly, W207X mutants displayed altered sensitivity to changes in pH_o but not pH_i , indicating that W207 may function as part of the EC pH sensor (Cherny et al., 2015). The demonstration that there are Hv1 mutants that can alter EC pH sensing without altering IC pH sensing is an important advance because it strongly argues that there are likely to be two physically distinct H^+ binding sites, and thus supports the two-site model for pH sensor structure in Hv1 (Cherny et al., 2015). However, W207 does not have an explicitly ionizable side chain, and mutants must therefore influence pH_o sensing mechanism in a manner that remains to be determined.

Other residues that form the EC H^+ binding site and are required for pH_o sensing at more acidic (and physiologically relevant) remain to be identified. Although residues that directly interact with W207 to form the EC pH sensor remain unknown, mutagenesis studies (Ramsey et al., 2010) provide a starting point for new, experimentally testable hypotheses about the mechanism(s) of pH_o sensing. As discussed previously, a post-hoc t-test performed in the single-mutants reported previously (Ramsey et al., 2010) revealed that ΔpH -dependent gating in E119A, D123A, and D185A mutants is subtly different from WT Hv1. We hypothesize that E119, D123, and D185 may interact directly or indirectly with W207 to form the EC H^+ binding site.

1.8.4: The IC pH Sensor

H168, was recently identified as an IC pH-sensing residue (Cherny et al., 2018). In a previous study, H168 was mutated together with two adjacent residues (H167N-H168V-K169N) which evidently has WT-like Δ pH-dependent gating when pH_o is altered (Ramsey et al., 2010). However, if H168 is located intracellularly and only senses pH_i , H168 mutations might not affect responses to pH_o changes, and Δ pH sensitivity might therefore appear normal. Therefore, the Ramsey et al., (2010) study may have overlooked H168, and potentially other residues, as contributors to the Δ pH sensing mechanism. Identifying components of the Δ pH sensor in Hv1 is thus a nontrivial task as it requires that responses to both pH_i and pH_o changes be measured in mutant proteins. This fact presents an additional technical burden because, only the IC or EC solution can be easily changed during the course of a given voltage clamp experiment.

In the more recent study on H168, various Hv1 H168 mutants (H168X) were constructed and pH_i was varied in excised inside-out patch clamp experiments (Cherny et al., 2018). The selection of H168X mutants was guided by the fact that *Helisoma trivolvis* Hv1 (htHv1) displays EC pH sensitivity that is similar to human (Hv1) (hHv1) (~40 mV/pH units), but htHv1 IC pH sensitivity is less steep (~15 mV/pH unit) than hHv1. In htHv1, the hHv1 H168-equivalent residue is replaced by Gln, and hHv1 H168Q attenuates IC pH sensitivity, resulting in an IC pH sensitivity that is more similar to htHv1 (Cherny et al., 2018). However, the reciprocal experiment (replacing Gln with His at the equivalent position in) evidently failed to reconstitute hHv1-like IC pH sensitivity, demonstrating that while H168 is a contributor to the IC pH sensor, other still-unknown are also required (Cherny et al., 2018). Because H168 is evidently not required for sensing changes in EC pH, two-site models of pH sensing mechanism in which changes in pH_i and pH_o are separately sensed but both coupled the voltage sensor are attractive.

It therefore seems likely that the EC pH sensor may also be formed by more than one side chain. Furthermore, it remains possible that interactions between and amongst ICEN and ECEN residues and long-range interactions between the networks are involved in the ΔpH -dependent gating mechanism.

1.8.5: Mechanisms of ΔpH -Dependent Gating in Hv1

Titration of explicit acidic and/or basic residues is still thought to be a primary feature of the underlying pH-dependent chemistry in Hv1. Titration events of amino acid side chains involves protonation or deprotonation, and the pH at which the numbers of ionized vs. non-ionized forms are equal is indicated by the equilibrium constant (pK_a). The pK_a is thus a measure of the tendency of an ionizable side chain to accept or give up a H^+ (Lehninger et al., 2013). Residues with pK_a values higher than the ambient pH will tend to remain H^+ -bound, and residues with pK_a values below the ambient pH will tend to give up a H^+ . Aqueous solution pK_a values for the 20 naturally occurring amino acids in are available (Lehninger et al., 2013). However, the effective pK_a of any side chain in the context of a folded protein environment may deviate substantially from the solution value (Pace et al., 2009). Electrostatic (i.e., Coulombic) interactions and solvation are major determinants of the effective side chain pK_a value in the protein environments (Pace et al., 2009). If the pK_a shifts towards the more neutral pH found in the cell, the side chain becomes more likely to engage in titration behavior at physiological pH; if the pK_a shifts away from the ambient pH, then the side chain is less likely to be titrated. By this means, pK_a shifts and the change in charge resulting from the gain or loss of H^+ can contribute significantly to the function of specific residues, and thereby influence protein function.

The ‘butterfly’ model originally proposed by Cherny et al. (1995) predicts one H⁺ binding site with alternate accessibility to IC solution and pH solution. However, W207X and H168X mutagenesis studies insinuate that Hv1 contains two separate IC and EC pH sensors (Cherny et al., 2015, 2018). Experimental studies also suggest that each pH sensor is composed of at least two residues that interact. In the two-site ‘counter-charge’ model of ΔpH-dependent gating, H⁺ occupancy at the IC pH sensor and the EC pH sensor is proposed to be mutually exclusive (Cherny et al., 1995). The ‘counter-charge’ model of ΔpH-dependent gating is designed to account for mutual exclusivity of H⁺ occupancy at IC and EC pH sensors and to accommodate the large movements of S4 that are central to the widely-accepted hypothesis for voltage sensing (DeCoursey, 2018; Vargas et al., 2012). S4 Arg residues are assumed to have a high and invariant pK_a values, and therefore remain positively charged. Cationic S4 Arg side chains make electrostatic interactions with acidic residues located on S1-S3 helices. In the activated-state VSD conformation, S4 Arg residues will interact with acidic ECEN residues, rendering the ECEN unavailable to bind a H⁺. In the resting-state conformation, S4 Arg side chains interact with the ICEN acidic groups, and the ICEN is therefore unavailable to bind H⁺. Movement of S4 alters Arg occupancy of the ICEN or ECEN in a voltage-dependent fashion, and thus determines H⁺ binding. The ‘counter-charge’ model thus allows for mutually exclusive H⁺ binding to IC or EC pH sensors and potentially explains coupling between ΔpH- and voltage-dependent gating.

S4 Arg side chains can potentially interact with a number of different acidic groups in S1-S3 that face the hydrated gating pore. When cationic S4 Arg side chains are in close proximity, acidic (and presumably negatively charged) side chains may engage in Coulombic interactions (i.e., salt bridges) with the S4 gating charges. However, when S4 moves away from

those acidic groups, the density of acidic residues without compensating positive charges remains, potentially resulting in an energetically unfavorable situation in which the protein contains a high density of negative charge. The problem of uncompensated negative charge is inherent to the two-site ‘counter-charge’ model, and represents an unsolved issue for the feasibility of the model.

To address the problem of high densities of uncompensated negative charge in the ‘counter-charge’ model, we hypothesize that S4 Arg side chain movement triggers functionally relevant shifts in side chain pK_a values that form the ICEN and ECEN. Furthermore, we posit that voltage-dependent pK_a shifts are a necessary component of the ΔpH -dependent gating mechanism in Hv1. We consider that electrostatic interactions between residues can not only cause shifts in pK_a values, but can also cause the pK_a values of the nearby interacting residues to become coupled. pK_a coupling occurs when increased H^+ occupancy at one side chain is associated with a reciprocal decrease in H^+ occupancy at another interacting side chain. Although side chain pK_a values in folded proteins can be measured using spectroscopic methods such as nuclear magnetic resonance ([Pahari et al., 2019](#)), this technique has not yet been adapted to the study of functional Hv1 channels, which requires experimental control of the transmembrane voltage and pH gradients. pK_a shifts and pK_a coupling remain difficult to measure in Hv1, and our hypothesis therefore remains untested. However, recent advancements in computational algorithms that accurately predict side chain pK_a values in folded protein structures hold promise as tools to facilitate a deeper understanding of the pH sensor structure and mechanisms of ΔpH -dependent gating in Hv1 and other VSD proteins.

Constant pH molecular dynamics (CpHMD) simulations use a set of algorithms to predict titration curves, and therefore the pK_a values, of specified side chain residues (Wallace and Shen,

2009). This can be a powerful technique because it generates titration curves for the indicated residues, allowing the pK_a for the residues to be calculated. However, performing CpHMD calculations is computationally nontrivial; CpHMD requires substantially larger computational resources than conventional MD, and achieving convergence is reported to be more difficult with the current CpHMD algorithms ([Radak et al., 2018](#); [Wallace and Shen, 2011](#)). Fortunately, empirical algorithms have also been developed, and some have been shown to successfully predict side chain pK_a values in proteins ([Alexov et al., 2011](#)). One example is PROPKA3.1, an empirical algorithm that is designed to calculate pK_a values and predict pK_a coupling in model proteins (Olsson et al., 2011). A preliminary PROPKA3.1 analysis of ionizable residues in the Hv1B model structure ([Ramsey et al., 2010](#)) predicts that pK_a values of E119, D123, D185, E153, and D174 are coupled, and may be useful for identifying residues and network interactions that are required for ΔpH -dependent gating. Hypotheses developed using pK_a analyses may be useful in guiding experimental strategies to determine whether particular residues or sets of residues are required for Hv1 function measured under voltage clamp.

1.8.6: Coupling Between Voltage- and ΔpH -Dependent Gating in Hv1

Coupling between voltage- and ΔpH -dependent gating in Hv1 is revealed by the ~ 40 mV/pH unit slope of the V_{thr} vs. ΔpH relation (Cherny et al., 1995; Ramsey et al., 2006; Sasaki et al., 2006). The simplest model to explain coupling between voltage- and ΔpH -dependent gating is competition between H^+ and S4 Arg occupancy for interactions with acidic ICEN or ECEN side chains as outlined in the ‘counter-charge’ model. Before describing our efforts to elucidate mechanisms of coupling between voltage- and ΔpH -dependent gating, we will briefly review

progress toward understanding which residues are required for ΔpH -dependent gating in Hv1.

1.9: Homology Models of Hv1

In the absence of a reliable high-resolution experimentally-determined structure of the Hv1 channel, homology modeling and MD simulations are deemed necessary. Several Hv1 model structures have been developed using a variety of computational methods and structural templates, and MD studies of Hv1 VSD models have helped guide the development of hypotheses and experiments (Chamberlin et al., 2014; Kulleperuma et al., 2013; Li et al., 2015; Ramsey et al., 2010; Randolph et al., 2016; Wood et al., 2012). So far, eight activated- or open-state models have been reported: one is based on *Ci*Hv1 (Chamberlin et al., 2014) while the others are based on hHv1: R2D and R3D (Kulleperuma et al., 2013), Hv1A and Hv1B (Ramsey et al., 2010), Hv1C (Randolph et al., 2016), and R1VZ and R2VZ (Wood et al., 2012). Four resting- or closed-state models have been reported: one model is based on *Ci*-Hv1 (denoted *Ci*-Hv1 resting here; Chamberlin et al., 2014), one model is derived from X-ray diffraction of a chimeric *Mus musculus* (*Mm*) Hv1, *Ci*VSP, and the coiled-coil from the transcription factor GCN4 and denoted mHv1cc (Takeshita et al., 2014), and two are based on hHv1: Hv1FL (Li et al., 2015) and Hv1D (Randolph et al., 2016). mHv1CC is an X-ray crystal structure (Takeshita et al., 2014) and the remaining models are homology models that are variously constrained by experimental data. *Ci*-Hv1 active (Chamberlin et al., 2014), R1VZ (Wood et al., 2012), R2VZ (Wood et al., 2012), and Hv1B (Ramsey et al., 2010) are all based on the Kv1.2-2.1 chimera X-ray structure (PDB: 2R9R; Long et al., 2007). The Hv1A homology model (Ramsey et al., 2010) was constructed using KvAP crystal structure as a template (Jiang et al., 2003) and Hv1C was built using Kv1.2 crystal structure (PDB: 3LUT; Chen et al., 2010). Hv1D (Ramsey et al., 2010) was built based on a Rosetta Homology model of the *Shaker* K⁺ channel (Pathak et al., 2007). A structural alignment between KvAP (PDB: 1ORS; Jiang et al., 2003), the Kv1.2-2.1 paddle

chimera (PDB: 2R9R; Long et al., 2007), and VSD chain A from NavAb (PDB: 3RVY; Payandeh et al., 2011) crystal structures were used as the template for building R2D and R3D (Kulleperuma et al., 2013).

1.9.1: Electrostatic Networks in Homology Models

The various models are generally consistent with the widely-accepted models of voltage sensing mechanism and voltage sensor structure (Vargas et al., 2012). For example, the available Hv1 models all contain an EN on each side of the ‘hydrophobic gasket’ near F150 (Figure 4.1; Figure 4.5), and are thus consistent with experimental data indicating the presence of such networks (Table 1.1; Chamberlin et al., 2014; Ramsey et al., 2010). Although the precise architecture of ICEN and ECEN varies, the models generally agree that E153, K157, H168, E171, D174 are the primary contributors of the ICEN and that the ECEN is composed primarily of D112, E119, D123, H140, D185, and H193. The position of S4 relative to S1-S3 appears to be highly variable in different models. The position, or register, of S4 has important mechanistic consequences because it determines how EC side chains may interact with S4 Arg side chains that are known to be required for voltage sensing.

The site-directed mutagenesis and mutant cycle analysis studies described earlier indicate that ICEN residues E153 and D174 interact with R1/R205 and R2/R208 and D112 interacts with R1/R205 in the resting-state conformation and that activated-state ECEN interactions include D112-R3/R211, E119-R1/R205, E119-R2/R208 and D185-R2/R208 (Table 1.1; CHAPTER 1.3; Chamberlin et al., 2014; Ramsey et al., 2010). Other residue pairs have not been experimentally verified, but other candidate acidic side chains have been identified and may make important contributors to EC or IC network structure. The paucity of experimental data that constrain

possible side chain interactions complicates the model-building process and results in investigator bias. Additional experimental studies that identify specific molecular interactions are needed for the development of new or refined model structures that are less biased.

1.9.2: Resting State Homology Models

One of the major discrepancies among currently-available resting-state Hv1 model structures is S4 register. The widely-accepted model posits that the S4 helix moves from a ‘down’ position, where the Arg gating charge side chains interact with anionic acidic ICEN side chains in the resting state, to an ‘up’ position in the activated state, where the S4 Arg side chains interact with acidic groups in the ECEN ([Figure 1.4](#), Aggarwal and MacKinnon, 1996; Ramsey et al., 2006; Sasaki et al., 2006; Seoh et al., 1996). S4 mobility is likely to allow for many possible S4 registers that reflect possible intermediate-state conformations that are visited only briefly during the gating process. The difficulty lies in determining which S4 positions are most likely to represent the major activated- (or open, H⁺-conducting) and resting- (or closed, non-conducting) state conformations. As previously discussed, experimental evidence places tight constraints on S4 position in the resting-state conformation, where R1/R205 is in register with F150 at the ‘hydrophobic gasket’ constriction point (Randolph et al., 2016). In both mHv1cc X-Ray structure and Hv1FL model, the register of S4 is such that R2/R208, is in register with residues making up the ‘hydrophobic gasket’ near F150; these structures seem to be incompatible with experimental data (Randolph et al., 2016). Hv1D is therefore the only published resting-state Hv1 model that is compatible with the resting state H⁺ conductance measured in R1H/R205H ([Randolph et al., 2016](#)).

The resting-state H^+ conductance in VSD R1H mutants appears to require that the introduced His be accessible to water (and thus H^+) on both the EC and IC side of the ‘hydrophobic gasket’ (Randolph et al., 2016; Starace and Bezanilla, 2004; Starace et al., 1997; Villalba-Galea et al., 2013). In the *CiHv1* resting-state model, the gating pore is only intermittently hydrated between IC and EC solutions; indeed, hydrophobic side chains intrude into the gating pore and effectively prevent R1 from interacting with solvent on either side of the membrane (Chamberlin et al., 2014). We therefore conclude that the *CiHv1* resting-state model is model inconsistent with key experimental data that constrain the Hv1 VSD resting-state structure. In contrast to the *CiHv1* resting-state model, a pathway for water to reach R1 from both the IC and EC sides of the membrane is evident the MD-equilibrated Hv1D R1H model (Randolph et al., 2016).

Although Hv1D is the only reported Hv1 resting-state model that is consistent with H^+ currents in R1H, other features of the model may require additional refinement. As discussed previously, EC Zn^{2+} modulates voltage-dependent gating in Hv1 by interacting with ECEN residues, including H140 and H193 (De La Rosa et al., 2018; Qiu et al., 2016; Ramsey et al., 2006). However, H193 and H140 are too far apart (20 Å) to simultaneously coordinate a single Zn^{2+} ion in Hv1D (De La Rosa et al., 2018). Hv1 D was developed prior to the identification of the probable Zn^{2+} coordination sphere in Hv1, and loop structures where H140 and H193 are located are notoriously difficult to accurately predict using standard *ab initio* molecular modelling approaches; in short, Hv1 D was not designed to accommodate structural constraints inferred from Zn^{2+} experimental data. Hv1D represents a reasonable starting point for the development of refined models that are consistent with what has been learned about Zn^{2+} coordination since it was first reported.

1.9.3: Activated State Homology Models

Like resting-state Hv1 models, a comparison of published activated-state models reveals a range of S4 registers relative to the S1-S3 helices. In R2VZ (Wood et al., 2012) and R3D (Kulleperuma et al., 2013), R3/R211, is in register with F150. In R1VZ (Wood et al., 2012), *Ci*Hv1 active (Chamberlin et al., 2014), Hv1A (Ramsey et al., 2010), Hv1B (Ramsey et al., 2010), and Hv1C (Randolph et al., 2016) however, the R3 side chain is on the EC side of F150, and N4/N214 is in register with F150. Finally, R2D places R3/R211 on the IC of F150 and R208 in register with F150.

Experimental data in Hv1 N4R/N214R may help to constrain the activated-state register of S4 helix. N4/N214 occupies the position of R4, the fourth gating charge in other VGCs and VSPs structures ([Figure 1.2](#)). Outward H⁺ currents in N4R are voltage-dependently blocked but the normal inward I_{tail} is measured upon hyperpolarization (Ramsey et al., 2010; Sakata et al., 2010). The data in Hv1 N4R is strongly reminiscent of pore block in tetrameric cation channels by impermeant cation species ([Hille, 2001](#)), and is interpreted to indicate that the introduced Arg is located just below the ‘hydrophobic gasket’ constriction point in the Hv1 gating pore, such that its positive charge prevents the passage of H⁺ (Randolph et al., 2016). Although Arg and Lys exhibit a potentially large degree of side chain flexibility that prevents unambiguous assignment of side chain position based on experimental data alone, a reasonable deduction is that at the level of backbone structure, N4 is approximately in register with F150 and other ‘hydrophobic gasket’ residues ([Li et al., 2014, 2015](#); [Randolph et al., 2016](#)). The experimental data appears to rule out the *Ci*-Hv1 activated-state model (Chamberlin et al., 2014) as a useful predictor of Hv1 VSD structure, but do not discriminate among other models (R1VZ, Hv1A, Hv1B, and Hv1C).

Electrophysiological data indicate that D185 is an important contributor to gating and likely interacts with R2/R208 in the activated-state VSD conformation ([Table 1.1](#); Chamberlin et al., 2014; Ramsey et al., 2010; Randolph et al., 2016). In R1VZ (Wood et al., 2012), the terminal oxygen atoms of D185 (OD1 and OD2) are $>8.5\text{\AA}$ away from the terminal nitrogen atoms (NH1 and NH1) of R2/R208 and $>7.5\text{\AA}$ away from NH1 and NH2 of R3/R211, suggesting that the D185 side chain is too distant to engage in salt bridges with S4 gating charge side chains. Similarly large ($>10\text{\AA}$ between OD1/OD2 of D185 and NH1/NH2 of R2/R208 and 9.5\AA between OD1/OD2 of D185 and NH1/NH2 of R3/R211), distances are observed in the Hv1C model (Randolph et al., 2016). R1VZ and Hv1C therefore seem inconsistent with D185 experimental data, and will not be considered further. In Hv1A, the top of S4 is splayed outward, away from the gating pore, more prominently than is seen in other models (Ramsey et al., 2010), causing the R2/R208 side chain to be distant from the D185 side chain. D185 is also not close enough to R2/R208 to form a salt bridge in Hv1B ([Table 1.1](#); [Chamberlin et al., 2014](#); [Ramsey et al., 2010](#)), but the top of S4 is not splayed out as much in Hv1B as in Hv1A, so Hv1B is deemed to be a better model for structural refinements (i.e., through side chain repositioning rather than backbone reorganization) that may make the model more consistent with experimental data and mutant cycle analysis.

Experimental data indicate that W207 contributes to both H^+ selectivity and ΔpH -dependent gating mechanisms, but the positions of W207 in currently available activated-state Hv1 models does not appear to account for the proposed functions of W207 ([Cherny et al., 2015](#)). To contribute to ion selectivity and pH_o sensing, W207 would need to be accessible to the EC solvent, and therefore probably in close proximity to, or a contributor of, the ECEN. In existing Hv1 model structures described above, the W207 side chain faces the membrane lipid

and away from the hydrated gating pore and other ECEN side chains (Chamberlin et al., 2014; Kulleperuma et al., 2013; Ramsey et al., 2010; Randolph et al., 2016; Wood et al., 2012). New or refined models that can account for W207 experimental data are therefore needed.

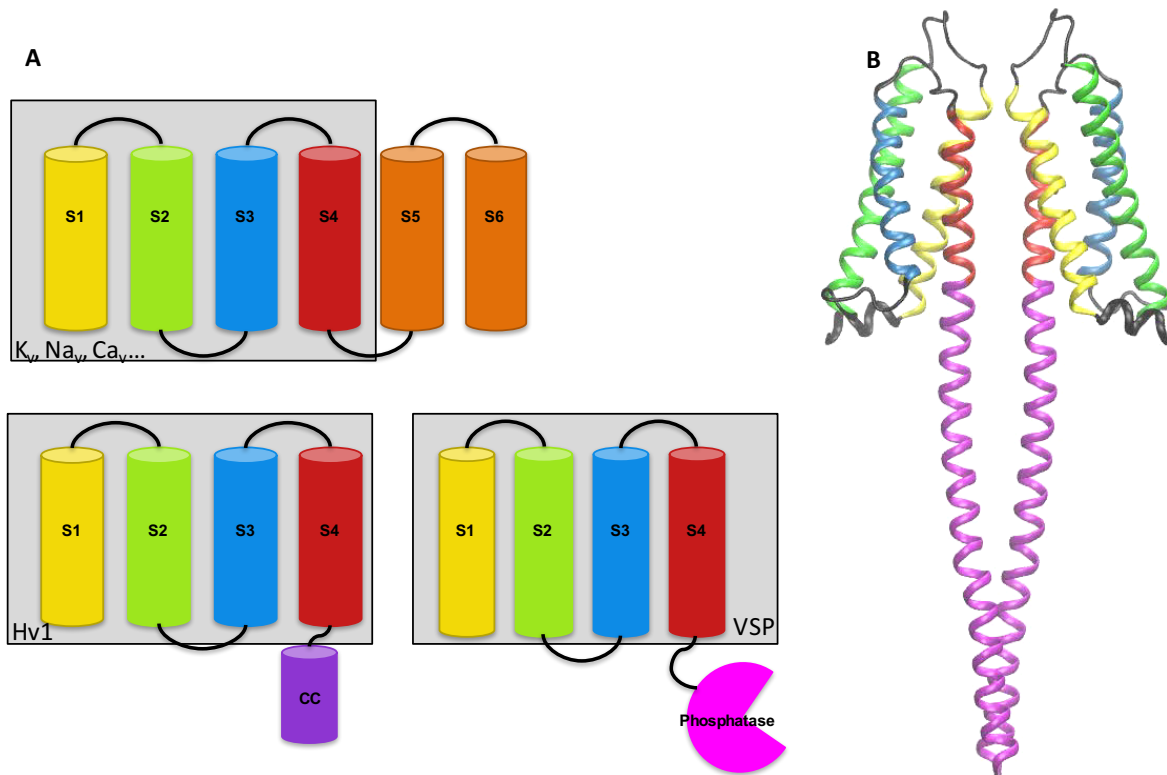


Figure 1.1: Overview of Hv1 Structure

A: Cartoon diagrams of the typical voltage-gated ion channel (VGC, top), Hv1 (bottom left), and voltage-sensitive phosphatase (VSP, bottom right). All three structures consist of the voltage sensor domain (VSD), highlighted by the grey box, made up of S1 (yellow), S2 (green), S3 (blue), and S4 (red) TM helices. In VGCs, the VSD is connected to a pore domain (orange helices), which contains the conduction pathway. In Hv1 the pore domain is replaced with the coiled-coil domain (purple), and in VSP the pore domain is replaced with a phosphatase (pink).

B: A model structure of the Hv1 dimer, Hv1FL (Li et al., 2015). The helices are colored the same way as in (A). The pore of Hv1 is contained within the VSD itself and there is one pore in each protomer

S1

	1.51	1.58	
62	RYYFIFTRLDLIWSLNYFALLFLNFFEQP-----LWCE		At TPC1 DI
430	PNFGYAISFILIIINFIAVVVETTLDIE-----		At TPC1 DII
30	SFFTGFIIYLIVLNGITMGLNETSKTFM-----		Ab Nav
12	RIFQFTVVSIIILNAVLI-ATTYELD-----		Rh Nav
189	KILAIISIMFIVLSTIALSLNTLPELQ-----SLD		Hs Kv2.1
163	RIIAIVSVMVILISIVSFCLNETLPIFRDENEDMHGSGVTFHT		Hs Kv1.2
227	RVVAIISVVFVILLSIVIFCLNETLPEFK----HYK----VFNT		Dm Shaker
	241	247	
116	LGMRVFGVFLIFLDIILMII DLSLPGK-----		Ci VSP
147	KPIHVAIIVLVVLD SFLVVGELLIDLK-----VII		Ci Hv1
42	HRFQVIIICLVVLDALLVLAELLIDLK-----IIE		mHv1cc
95	HRFQVIIICLVVLDALLVLAELLIDLK-----IIE		Mm Hv1
99	HRFQVIIICLVVLDALLVLAELLIDLK-----IIQ		Hs Hv1
	112	119	

S2

	2.43	2.50	2.57	
95	KNPKPSCKDRDYYYL GELPYLTNAESIIYEVITLAILLVHTF			At TPC1 DI
457	-----ESSAQKPWQVAE FVFGWIYVLE MALKIYT--			At TPC1 DII
57	-----QSGVYTTLFNQIVITIFTIEIILRIY---			Ab Nav
38	-----PLFLETIHLLDYGITIFFVIEILIRFIG--			Rh Nav
219	EFG-----QSTDNPQLAHVEAVCIAWFTMEYLLRFLS--			Hs Kv2.1
205	YSN-STIGYQQSTSFTDPFFIVETLCCIWFSEFLVRFFA--			Hs Kv1.2
261	TTNGTKIEEDEVPDITDPFFLIETLCIIWTFELTVRFLA--			Dm Shaker
	283	287	293	
143	-----SESSQSFYDGMALALSCYFMLDLGLRIFA--			Ci VSP
177	VPH-----GNPAPEILHGFSLSILSIFMVEIALKIIA--			Ci Hv1
72	PDE-----QDYAVTAFHYMSFAILVFFMMLDLGLRIFA--			mHv1cc
125	PDE-----QDYAVTAFHYMSFAILVFFMLEIFFKIFV--			Mm Hv1
129	PKD-----NNYAAMVFHYMSITILVFFEMMEIFFKLFV--			Hs Hv1
	150			

S3

	3.50	3.61	
137	FPISYEGSRIFWTSRLNLV KVACVVILFVDVLDVDFLYLS---		At TPC1 DI
486	----YG-FENYWREGANRFDFLVTWVIVIGETATFITP----		At TPC1 DII
84	----VHRISFFKDPWSLFDFFVVA---ISLVPTS-----		Ab Nav
66	----EKQKADFFKSGWNIFDTVIVA---ISLIPIPN-----		Rh Nav
251	----SPKKWKFFKGPLNAIDLLAILPYVVTIFLTESNK----		Hs Kv2.1
244	----CPSKAGFFTNIIMNIIDIVAIIPYFITLGTAEK----		Hs Kv1.2
301	----CPNKLNFCDVMNVIDIIAIIIPYFITLATVVAEEEDTL		Dm Shaker
	316		
172	----YGP-KNFFTNPWEVADGLIIVVTFVVVTIFYTVLDEY--		Ci VSP
209	----DH--RHFIHKKVEVLDAVVVISFGVDIALIFVG----		Ci Hv1
104	----YGP-KNFFTNPWEVADGLIVVVSFVLDLVLLFK-----		mHv1cc
157	----FR--LEFFHKKFEILD AFVVVVSFVLDLVLLFK-----		Mm Hv1
161	----FR--LEFFHKKFEILD AVVVVVSFILDIVLLFQ-----		Hs Hv1
	174	185	

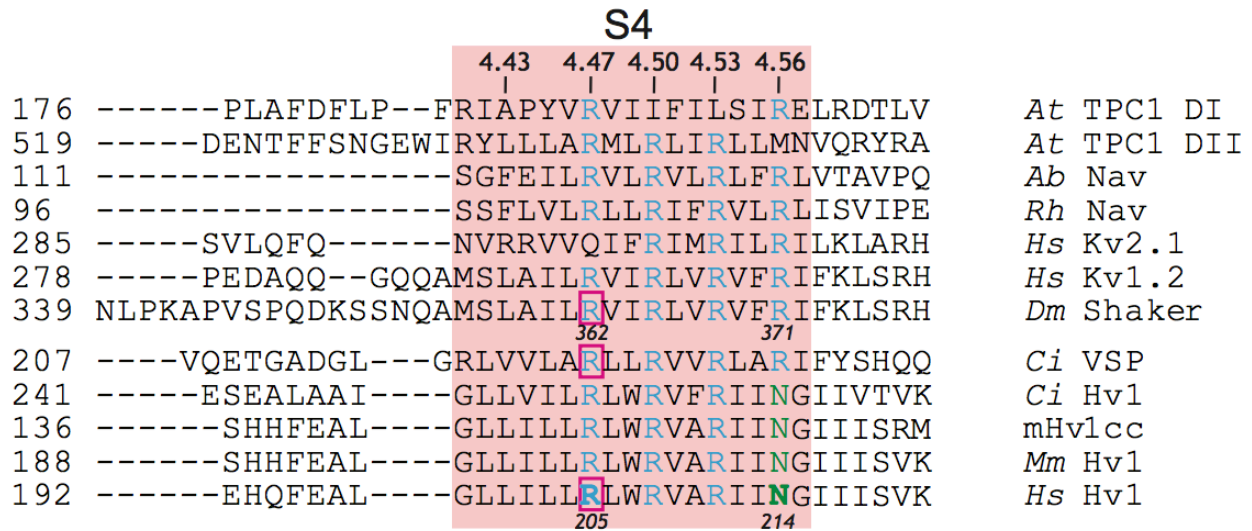


Figure 1.2: VSD Sequence Alignment

An alignment (Clustal V; DNASTar Lasergene) of amino acid sequences in VSDs from *Arabidopsis thaliana* TPC1 domain II (*AT*-TPC1-DII; pdb: 5E1J and 5DQQ; GI: 75166464), *Arcobacter butzleri* Nav (*Ab* Nav; pdb: 3RVZ; GI:339961375); *alpha proteobacterium HIMB114* Nav (*Rh* Nav; pdb: 4DXW; GI:388326718), *Homo sapiens* Kv1.2 (*Hs* Kv1.2; NP_004966; GI: 4826784), *Homo sapiens* Kv2.1 (*Hs* Kv2.1; NP_004965; GI:4826782), *Drosophila melanogaster* Shaker (*Dm* Shaker; CAA29917; GI:288442), *Ciona intestinalis* VSP (*Ci* VSP; NP_001028998; GI:76253898) and Hv1 channels from *Ciona intestinalis* (*Ci* Hv1; NP_001071937; GI:118344228), *Mus musculus* (*Mm* Hv1; NP_001035954; GI:109809757), *Homo sapiens* (*Hs* Hv1; NP_115745; GI:91992155), and a chimeric sequence composed of *Mm* Hv1 and *Ci* VSP, for which an x-ray structure of the closed state exists (Takeshita et al., 2014, *mHv1cc*; pdb: 3WKV). *Hs* Hv1 (*hHv1*) residue numbering is shown below the sequence alignment and that for *Dm* Shaker is shown above the alignment. Residues indicated with red arrows are the residues of focus for this project. This figure is reprinted from Randolph et al., 2016.

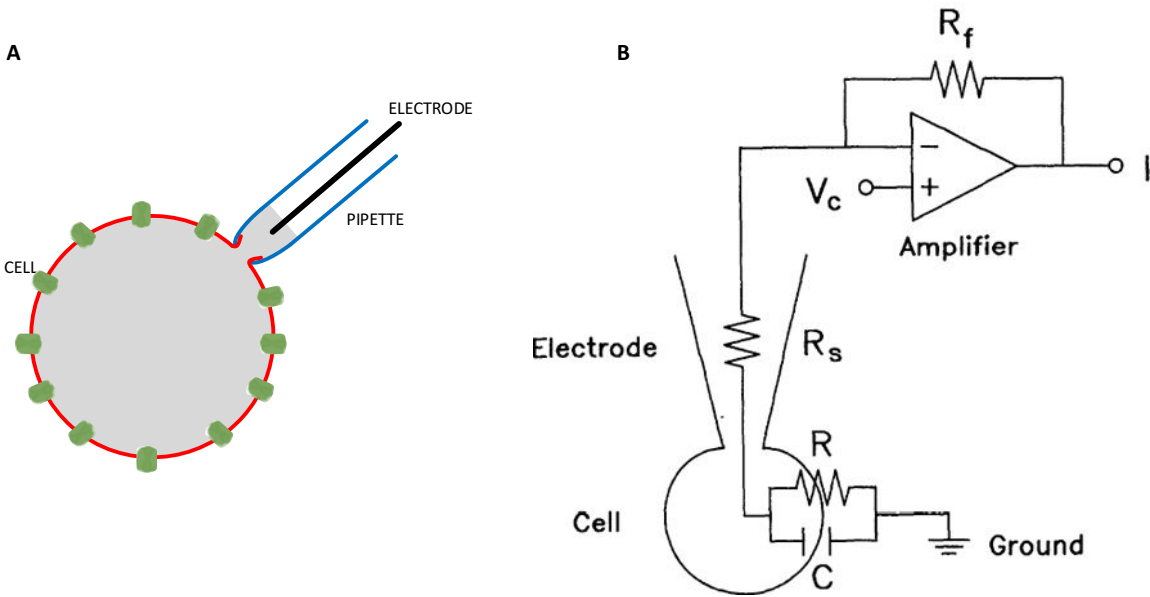


Figure 1.3: The Whole-Cell Voltage Clamp Configuration

A: Cartoon representation of the whole-cell voltage clamp mode. In whole-cell mode, the ion channel of study (green) is expressed in the cell membrane and the cytosolic solution (grey) is dialyzed using a micropipette (blue) containing an electrode (black), which has a series resistance R_s . A ground electrode is in the bath solution outside the cell. The cell membrane (red) has measurable resistance (R) and capacitance (C) as well.

B: A simplified circuit diagram of the whole-cell voltage clamp set up. The diagram is labeled the same as in (A). This diagram is from Jones, 1990.

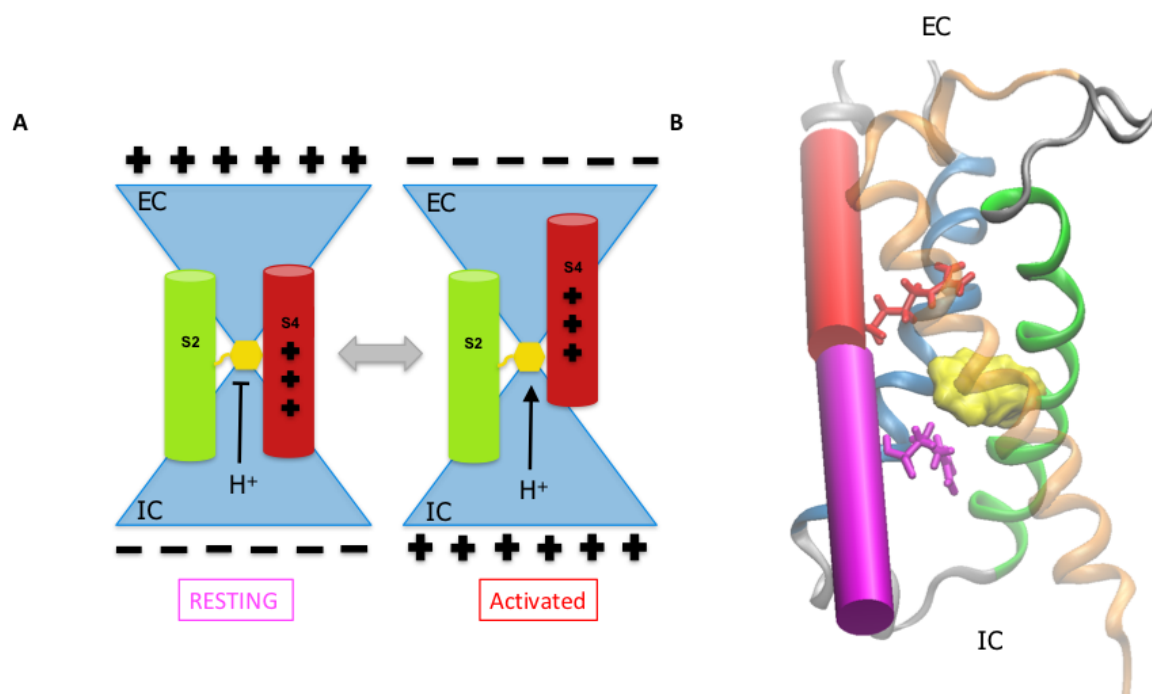


Figure 1.4: Voltage-Dependent Gating in Hv1

A: Cartoon representation of voltage-dependent gating in Hv1. Blue triangles represent aqueous filled vestibules. Yellow hexagon represents F150. The '+' signs represent the three S4 arginine gating charges on S4 (from top to bottom, R205, R208, and R211). The flathead arrow indicates that the proton (H^+) conduction pathway is closed (left) and triangle-tipped arrow indicates that the the H^+ conduction pathway is open (right). The transition between the resting (left) and activated (right) state is represented by the grey arrow in between the two cartoons.

B: Molecular representations of helix movement in Hv1. The resting state (pink S4) is represented by the Hv1D (Randolph et al., 2016) structure and the activated state structure (red S4) is represented by Hv1B (Ramsey et al., 2010).

Table 1.1: Experimentally Supported Electrostatic Interactions in Hv1

Interacting pairs in the Hv1 VSD as indicated by mutant cycle and generalized interaction analysis applied to voltage clamp experiments. These analyses show that the ECEN is composed of E119, D185, R205, and R208 and stabilizes the activated state of the channel. The ICEN is composed of E153, D174, R205, and R208 and stabilizes the resting state of the channel. Reciprocal double mutagenesis studies also demonstrate an interaction between D112 and R211 in the activated state (Berger and Isacoff, 2011).

*Data taken from Chamberlin, A., Qiu, F., Rebolledo, S., Wang, Y., Noskov, S.Y., and Larsson, H.P. (2014). Hydrophobic plug functions as a gate in voltage-gated proton channels. Proc. Natl. Acad. Sci. U.S.A. *111*, E273-282.

†Data not published

‡ GIA calculations were performed using $V_{1/2}$ data taken from Chamberlin, A., Qiu, F., Rebolledo, S., Wang, Y., Noskov, S.Y., and Larsson, H.P. (2014). Hydrophobic plug functions as a gate in voltage-gated proton channels. Proc. Natl. Acad. Sci. U.S.A. *111*, E273-282.

Table 1.1: Experimentally Supported Electrostatic Interactions in Hv1			
Interaction Pair	Relevant State	Mutant Cycle Analysis (kcal/mol)	Generalized Interaction Analysis (kcal/mol)
E153-R205	Resting	-2.44*	11.57†
E153-R208	Resting	-3.71*	18.03‡
D174-R205	Resting	-2.61*	6.44‡
D174-R208	Resting	-5.61*	14.61‡
E119-R205	Activated	1.49*	-2.30‡
E119-R208	Activated	1.05*	-5.6‡
D185-R208	Activated	1.38*	-7.6‡
E153-D174	Activated	N/A	-3.3†
E119-D185	Activated	N/A	-6.1†

Table 1.2: Two-Sample t-Test Comparing Δ pH Sensitivity in WT Hv1 and Hv1 Single Mutants

Results of a post hoc two sample t-test comparing the Δ pH sensitivity in WT and select single mutants. Residues in black show significance at $\alpha = 0.05$ (*) or $\alpha = 0.01$ (**) and residues in grey are not different from WT. D123A, E119A, and D185A are all ECEN mutants that appear to have slightly different Δ pH sensitivity from WT. Likewise, E153A and D174A are both ICEN mutants with slightly different Δ pH sensitivity from WT.

[†]Data used to run t-test was from Ramsey, I.S., Mokrab, Y., Carvacho, I., Sands, Z.A., Sansom, M.S.P., and Clapham, D.E. (2010). An aqueous H⁺ permeation pathway in the voltage-gated proton channel Hv1. *Nat. Struct. Mol. Biol.* 17, 869–875.

Table 1.2: Two-sample t-test comparing ΔpH sensitivity in WT hHv1 and hHv1 mutants			
Residue	ΔpH sensitivity (mV/pH unit)[†]	ΔpH sensitivity SEM (mV/pH unit)[†]	p-value
WT	-38	2	N/A
D112A	-38	2	1
D123A	-48	2	0.001939**
E119A	-47	2	0.000288**
N214R	-40	2	0.16798
D185A	-47	2	0.000288**
E153A	-42	2	0.018788*
D174E	-46	1	0.000097**

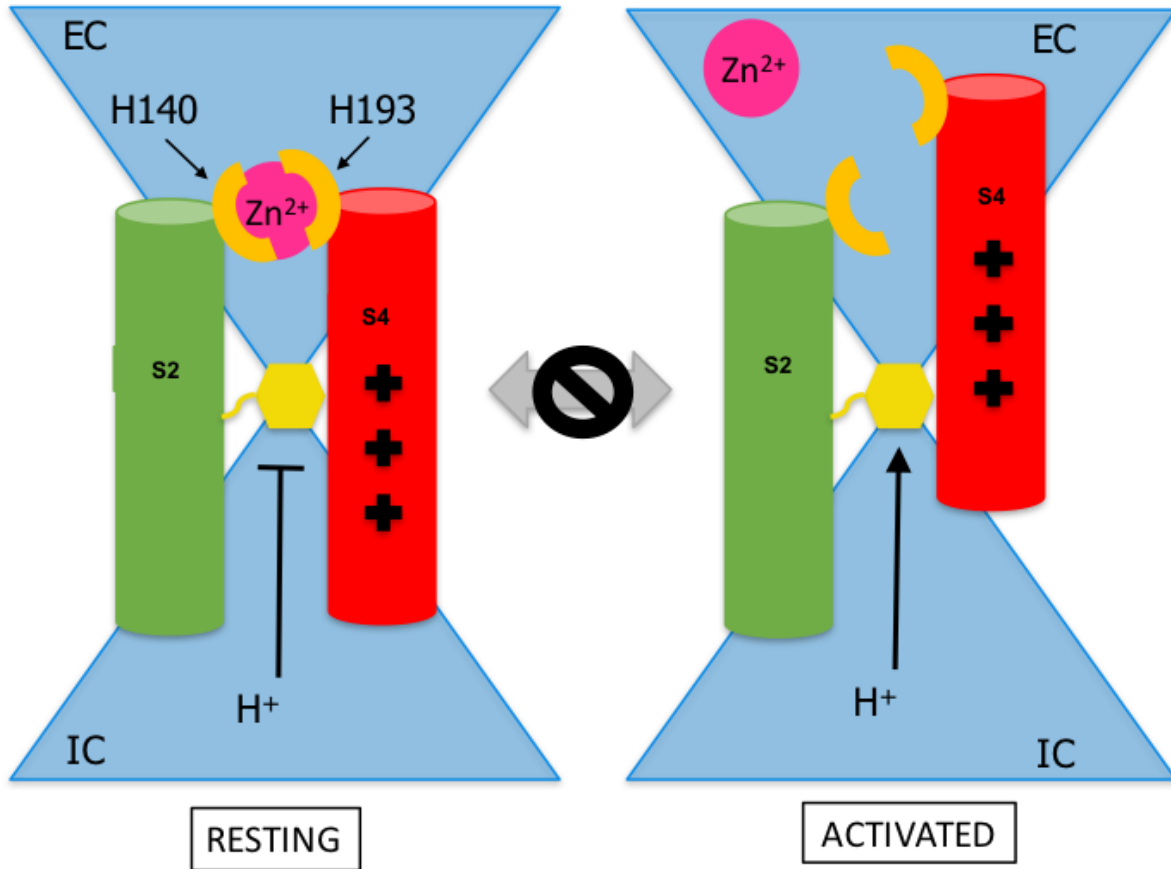


Figure 1.5: Inhibition of Hv1 by Zn²⁺ Binding

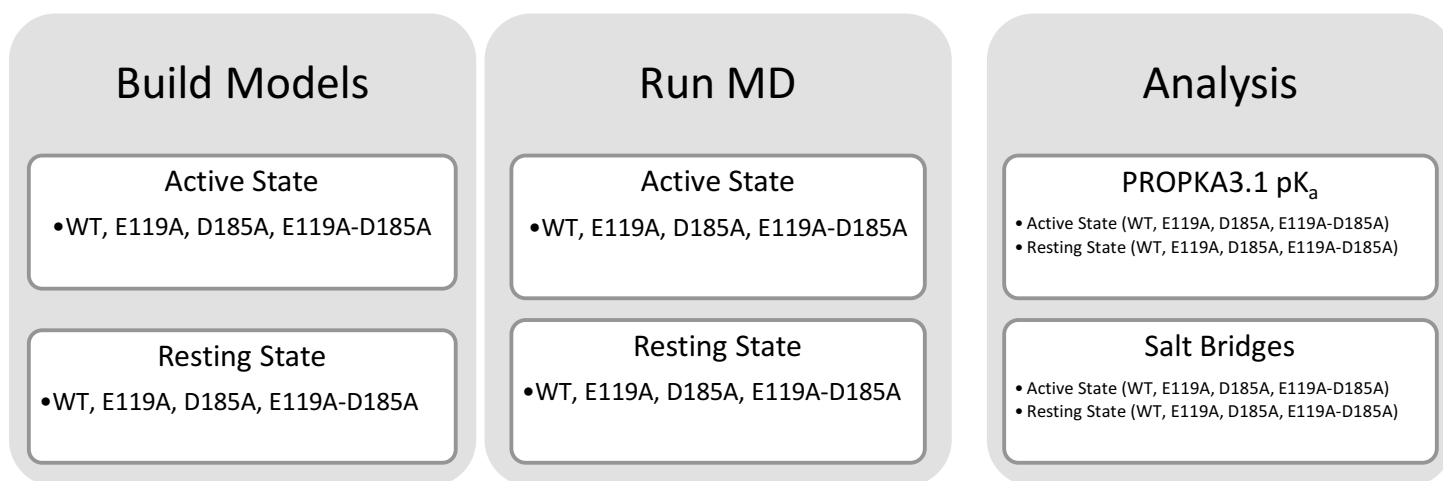
A cartoon representation of the effects of Zn²⁺ binding in the Hv1 ECEN. Blue triangles represent aqueous filled vestibules. Yellow crescents represent H140 in S2 (green cylinder) and H193 in S4 (red cylinder), the residues primarily responsible for binding Zn²⁺ (Ramsey et al., 2006). S1 and S3 are not depicted for clarity. The pink sphere represents Zn²⁺ and the yellow hexagon represents F150. The '+' signs represent the three S4 arginine gating charges on S4 (from top to bottom, R205, R208, and R211). The flathead arrow indicates that the proton (H⁺) conduction pathway is closed (left) and triangle tip arrow indicates that the the H⁺ conduction pathway is open (right). The transition between the closed (left) and open (right) state is represented by the grey arrow in between the two cartoons. The black crossed circle indicates that Zn²⁺ binding to H140 and H193 inhibits the voltage-dependent gating transition of the S4 helix, thus shifting the P_{OPEN}-V relationships to more depolarized potentials.

CHAPTER 2: SPECIFIC AIMS

The existence of at least two ENs, ICEN and the ECEN, has been clearly demonstrated. However, the exact architecture of these networks and their functions remain elusive. The overall goal is to utilize homology modeling and molecular dynamics (MD) simulations to explore the potential structures of the ENs and integrate these computational studies with site-specific mutagenesis and voltage clamp experiments in order to better understand the function of electrostatic networks in Hv1 Δ pH-dependent gating.

2.1: AIM I: Build Experimentally-Validated Models of Hv1

The first aim is to use data from voltage clamp studies to constrain models of Hv1, in both the active and resting states, such that side chain positions are consistent with the results from these various experimental methods ([Table 1.1](#); [Berger and Isacoff, 2011](#); [Chamberlin et al., 2014](#); [Randolph et al., 2016](#)). These resting and activated state models of Hv1 will then be subjected to MD simulations to investigate the dynamic behavior of the ENs. This same process will be repeated for mutant Hv1 models as well.



2.2: AIM II: The ECEN is Necessary for Δ pH-Dependent Gating in Hv1

T-tests on the Δ pH sensitivity of the mutants from early mutagenesis studies (Ramsey et al., 2010) reveal that E119A, D123A, and D185A mutants all have a Δ pH sensitivity that is faintly, but statistically, different from that of WT Hv1 ([Table 1.2](#)). Generalized interaction analysis (GIA) is an analytic method that can be performed on functional data in order to identify electrostatic interactions that contribute to channel gating (Chowdhury et al., 2014). A GIA value of zero indicates that the interaction does not contribute to channel gating, whereas GIA values not equal to zero indicates that the interaction may make a thermodynamic contribution to channel gating by stabilizing activated- vs. resting-state VSD conformations (Chowdhury et al., 2014). A preliminary GIA of Δ pH sensitivity in WT and mutant Hv1 channels reported previously (Ramsey et al., 2010) suggests that E119 and D185 interactions contribute to stabilization of the activated-state conformation ([Table 1.1](#)). The second aim of this study will use site-directed PCR mutagenesis and whole-cell voltage clamp to test if E119, D123, and D185 interact to form the EC pH sensor that is necessary for Δ pH-dependent gating in Hv1. If E119, D123, and D185 interactions are necessary for Hv1 Δ pH-dependent gating, then the $V_{\text{thr-pH}}$ and $V_{\text{thr-}\Delta\text{pH}}$ curves should saturate at acidic EC pH values.

Site-Directed PCR Mutagenesis

Single Mutants

- E119A, D123A, D130A, D185A

Double Mutants

- E119A-D123A, E119A-D185A, D123A-D185A

Triple Mutants

- E119A-D123A-D185A, E119A-D123A-D130A, D123A-D130A-D185A

Voltage-Clamp

$$pH_i = 5.5$$

$$pH_o = 4.5, 5.5, 6.5, 7.5$$

WT

Single Mutants

Double Mutants

Triple Mutants

Analysis

I_{tail} -V Curves

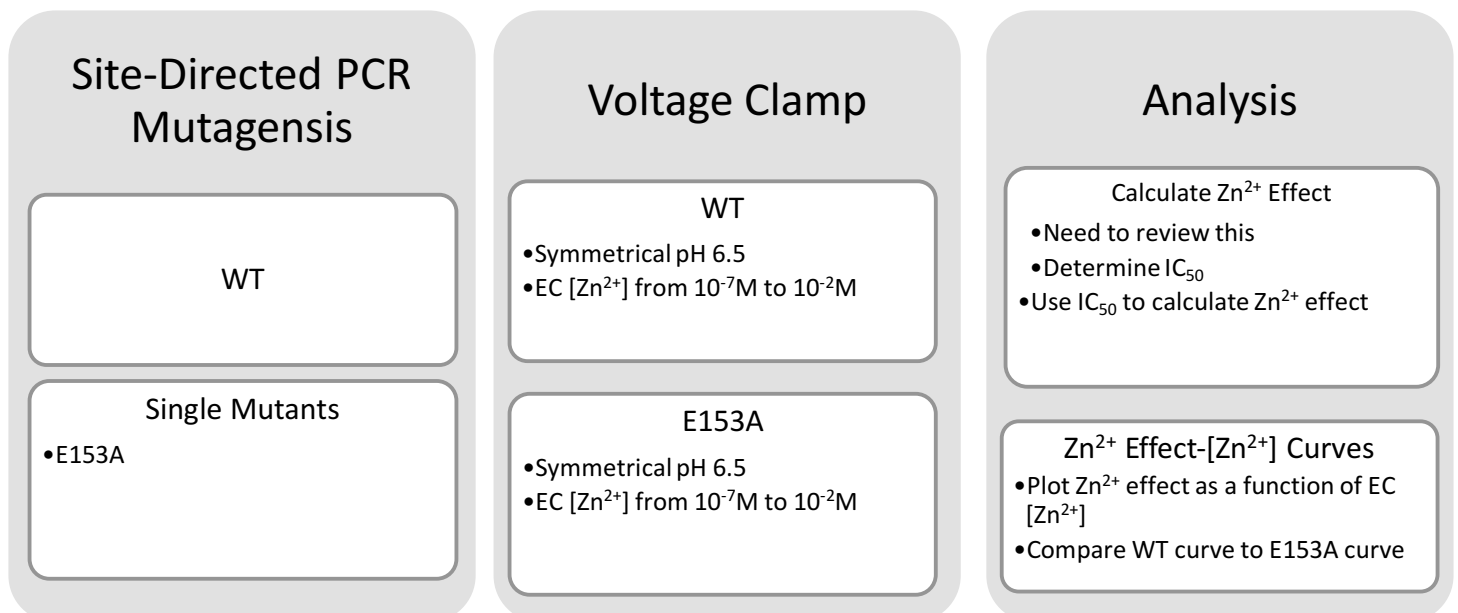
- Plot the steady state tail current (I_{tail}) as a function of voltage
- Determine threshold potential (V_{thr})

V_{thr} -pH Curves

- Plot V_{thr} as a function of pH_o
- Determine slope of curves, which is pH_o sensitivity

2.3: AIM III: Residues in the ICEN Communicate with the ECEN

Hv1 voltage-dependent gating is strongly coupled to ΔpH -dependent gating. Identification of residues that sense pH_i that do not sense pH_o (Cherny et al., 2018) and an pH_o sensor that does not sense pH_i (Cherny et al., 2015) suggests that there are two independent pH sensors and Hv1 ΔpH -dependent gating appears to be an emergent property of communication between the EC pH sensor and IC pH sensor. The ECEN contains the Zn^{2+} binding site and increasing EC Zn^{2+} concentration has the same effect on Hv1 as decreasing pH_o , indicating that H^+ and Zn^{2+} may share similar mechanisms of gating modulation in Hv1 channels. We hypothesize that if allostery between the ICEN and ECEN is required for Zn^{2+} effects on voltage-dependent gating in Hv1, then E153 mutation could alter Zn^{2+} potency relative to Hv1 WT. Consistent with this hypothesis, we showed that the E153-R208 salt bridge in the ICEN is strongly correlated with Zn^{2+} -His distances in the ECEN and E153A decreases Zn^{2+} potency (De La Rosa et al., 2018). Experimental and computational support for accomplishment of Aim III can be found in our publication entitled “Coupling between an electrostatic network and the Zn^{2+} binding site modulates Hv1 activation” (De La Rosa et al., 2018).



CHAPTER 3: MATERIALS AND METHODS

3.1: Computational Methods

Homology modeling was carried out on a 2013 MacBook Pro (2.3 GHz Intel Core i7 CPU, 16 GB 1600 MHz DDR3) running macOS Sierra using custom Python (<https://www.python.org>) scripts executed using a local install of Modeller9.16 (<https://salilab.org/modeller/>, Fiser et al., 2000; Martí-Renom et al., 2000; Sali and Blundell, 1993; Sali et al., 2016; Webb and Sali, 2014). The CHARMM36 force field naming conventions were used for residue and atom names (Best et al., 2012; Klauda et al., 2010, 2012; MacKerell et al., 1998, 2004). Only the backbone atoms of the template structures were used in the construction of Hv1 models.

Molecular dynamics (MD) simulations were carried out on a combination of GPU workstations, GPU servers, and CPU servers using NAMD (Phillips et al., 2005) in the CHARMM36 force field with TIP3P water (Jorgensen et al., 1983) using custom configuration scripts. The GPU workstation is a HP Z800 (two 3.33 GHz Intel W5590 CPUs, 1 NVIDIA Quadro 2000, 2 NVIDIA Tesla C2075) running CentOS 7.6 and Cuda 10.0 and molecular dynamics (MD) was carried out using eight CPUs and two GPUs with NAMD2.11. The head node for the GPU server is one 8-core 64-bit Intel Xeon CPU with 4 GB RAM and shared RAID 6 storage (11 TB total). The compute nodes on the GPU server are composed of three 12-core Intel Xeon CPUs with 2-3 GB RAM, three NVIDIA Tesla M2075 GPUs, and one 32-core Intel Xeon CPU with 4GB RAM and 2 NVIDIA Tesla K80 GPUs. High-speed network infrastructure is provided by an Infiniband architecture. MD on the GPU server was carried using NAMD 2.9 with 18 nodes (2 physical nodes). The CPU server (<https://rampages.us/chipc/research/facilities/>) has about 5040 64-bit Intel and AMD compute cores, each with 2–4 GB RAM/core, 10.2 TB of

total RAM, 180 TB of home space, and tmp space of between 360 and 787 GB per node. High-speed network infrastructure is provided by a 20 Gb/second Infiniband architecture. MD was carried out using 64 nodes (8 physical nodes) with NAMD2.10 on the CPU server. A summary of the workstations is provided in [Appendix B](#). Analysis of models and MD was carried out using custom Python scripts on the previously mentioned MacBook Pro and GPU workstation.

3.1.1: Building a Resting State Model of Hv1 Voltage Sensor Domain

Histidine 140 (H140) and histidine 193 (H193) in human Hv1 have been identified as the primary contributors to Zn^{2+} binding and potency (Ramsey et al., 2006). All the current models fail to recapitulate a structure that would allow H140 and H193 to simultaneously coordinate a Zn^{2+} ion. In order to generate a model that is consistent with the Zn^{2+} binding data, Modeller9.16 ([Sali and Blundell, 1993](#)) was used to make minor alterations, in an iterative manner, to a previously published Hv1 homology model. Experimental data on Hv1 Zn^{2+} binding and potency was used to derive structural restraints for the model building process ([Table 3.1](#)). Four iterations of modeling were required to produce the final resting state model. In each iteration of modeling, 100 models were produced and the best model was selected based on a combination of Modeller9.16 molpdf (<https://salilab.org/modeller/9.11/manual/node468.html>) and DOPE_HR (<https://salilab.org/modeller/9.11/manual/node253.html>) scoring functions and a structure in agreement with the experimentally defined structural restraints confirmed by visual assessment in VMD1.9.3 or VMD1.9.2 (Humphrey et al., 1996).

An overview of the resting-state Hv1 model construction is shown in [Figure 3.1](#). Hv1D was chosen as a template because the register of S4 has been shown previously to be consistent with the R1H mutant closed-state H^+ conduction (Randolph et al., 2016). The first step of

modeling involved adding the coiled-coiled (CC) domain to the VSD. Hv1D was used as the template for the VSD residues 98-225 and the X-ray structure of the CC domain (PDB 3A2A; Li et al., 2010) was used as the template for the CC domain residues 226-266. To ensure a helix structure for S4 and the CC domain, alpha helical restraints (Sali et al., 2016) were applied from residues 197-266. In the resulting intermediate model S4 is continuous with the CC domain with no breaks.

The second round of modeling was used to make minor alterations to accommodate electrostatic interactions that are indicated by electrophysiological data ([Table 1.1](#); [Table 3.1](#)). In order to allow H140 and H193 to be close enough to one another to be capable of simultaneously coordinating a single Zn^{2+} ion, the `dopehr_loopmodel` class of Modeller9.16 (Sali et al., 2016) was used to remodel the S3/S4 loop from residues 185-194. To ensure that S3 reformed a helix, alpha helical restraints were applied to residues 165-184. To create the Zn^{2+} binding site in the ECEN, upper and lower bound distance restraints were used to confine the distance between the delta nitrogen of H140 and H193 to be close enough to bind a Zn^{2+} but not too close as to preclude a Zn^{2+} from entering the binding site. The ionic radius of Zn^{2+} is approximately 0.60 Å (Haynes, 2014, 12-12) and the distance of Zn^{2+} to nitrogen interactions are about 2.044 Å (Haynes, 2014, 9-18) adding up to a minimum distance of 4.69 Å needed between the delta nitrogen of H140 and H193. Therefore, a lower bound value of 6 Å was selected to accommodate for the ionic radius of Zn^{2+} and two Zn^{2+} -nitrogen interactions. In the radial distribution function (RDF) of Zn^{2+} -oxygen bonds, the second peak usually occurs around 3-4 Å with interactions occurring beyond 4 Å being negligible (Stote and Karplus, 1995). Therefore, the upper bound distance value was selected as 10 Å to accommodate longer range interactions.

Electrophysiological data also indicates an interaction between K157 and K221 that stabilizes the closed state relative to the open state ([Figure 4.4](#)). In the model with S4 continuous with the CC domain, K157 and K221 are too far apart to accommodate any kind of interaction. Therefore, the second round of modeling also included engineering a linker helix in between S4 and the CC domain to allow for the K157-K221 interaction in the resting state. Residues 215-225 were remodeled in Modeller9.16 using the `dopehr_loopmodel` class and alpha helical restraints were applied to residues 216-221, to create the linker helix, and from residues 223-266 to ensure that the CC domain remained helical. To ensure the register of S4 was not altered the second iteration of modelling also included Coulomb restraints (<https://salilab.org/modeller/9.16/manual/node491.html#eq:coulomb>) between S4 arginine residues and their acidic countercharges in the ICEN ([Table 1.1](#); [Table 3.1](#)).

The third iteration of modeling was used to refine the newly created Zn^{2+} binding site in the ECEN. In addition to H140 and H193, E119, D123, and D185 all appear to be a part of the Zn^{2+} binding network (De La Rosa et al., 2018). After two iterations of modeling, H140, H193, and E119 are all a part of the ECEN, however D123 and D185 are left out. In order to accommodate D123 and D185 in the ECEN the `dopehr_loopmodel` class was used to remodel the backbone of S1/S2 residues 124-139 and the S3/S4 loop residues 184-186. To ensure that the helices reformed properly, alpha helical restraints were applied to residues 132-158 for the S2 helix, residue 165-185 for S3, residues 216-221 for the linker helix, and residues 223-266 for the CC domain. Additional spatial restraints derived from electrophysiological data were placed between specific residues ([Table 3.1](#)).

The fourth iteration of modeling was used to slightly refine the ICEN to allow E171 to participate. The same `dopehr_loopmodel` protocols and alpha helical restraints over the same

residue ranges were used as in round three of modeling. The spatial restraints between residues derived from electrophysiological data, however, were different ([Table 3.1](#)). The resting state model was truncated at residue 230 prior to MD simulation to reduce the amount of bulk water necessary to carry out MD and thus improve computational efficiency. This resulting model is depicted in [Figure 4.1](#). This method of Hv1F construction and the Hv1F model itself have been published (De La Rosa et al., 2018).

3.1.2: Building an Activated State Model of Hv1 Voltage Sensor Domain

There are no X-ray structures of Hv1 in the active state, so structure has to be derived from other experimental sources. In the activated state it is well accepted that D112-R211 make a salt bridge in Hv1, which forms a part of the selectivity filter (Berger and Isacoff, 2011; Musset et al., 2011). D185 has been shown to stabilize the activated state relative to the closed state (Ramsey et al., 2010) and therefore should be able to interact with the S4 arginine residues in the active state. However, in the currently available active state models of Hv1 D185 is not a part of the ECEN where the S4 arginine residues would be in the active state. Additionally, data indicates that N4R/N214R mutation produces a block of the outward current at depolarized voltages and therefore, indicates that N214 is located close to the constriction of the pore (Berger and Isacoff, 2011; Randolph et al., 2016). To accommodate these functional features into a structural model, Modeller9.16 ([Sali and Blundell, 1993](#)) was again used to modify an existing homology model of Hv1.

Only one iteration of modeling was required to produce an open state model consistent with all known experimental data. The structural restraints used to build Hv1J are shown in [Table 3.2](#). In Hv1B (Ramsey et al., 2010) the register of S4 is consistent with the N214R block

data (Randolph et al., 2016) and therefore was chosen as the template for the VSD residues 94-225. The CC domain X-ray structure (PDB 3A2A) was used as the template for the CC domain residues 226-266. To accommodate D185 in the ECEN, the S1/S2 and S3/S4 loop backbone was remodeled using `dopehr_loopmodel` class in Modeller9.16. The S3/S4 paddle structure inherited from the K_v chimera template (Long et al., 2007) present in the Hv1B model (Ramsey et al., 2010) was removed by using the `dopehr_loopmodel` class to remodel the S4 helix backbone. Additional Coulomb spatial restraints of 3 Å were applied between OD2 atom of D185 and NH2 atom of R208, OE2 atom of E119 and NH2 atom of R205, and OD2 atom of D112 and NH2 atom of R211 (Table 3.2). To ensure that the helices reformed the helical structure, alpha helical secondary structure constraints were applied to 98-124 for S1, 131-158 for S2, 170-190 for S3, and 199-266 for a S4 helix continuous with the CC domain (Table 3.2). 100 models were generated and the best model was selected based on a combination of Modeller9.16 energy rankings and visual assessment to confirm compatibility with the desired spatial restraints. The resulting model has all the desired structure features that are compatible with the functional data (Figure 4.5) and is referred to as Hv1J. Again, in order to reduce the amount of bulk water required to carry out MD, Hv1J was truncated after residue 230 prior to MD simulations.

3.1.3: Molecular Dynamics Simulations of Resting State Model Hv1F

Wild Type Simulations

To reduce the amount of bulk water required, and increase MD efficiency, the CC domain was removed by truncating Hv1F after residue 230. The truncated Hv1F was then embedded in a pre-solvated and pre-equilibrated 1-Palmitoyl-2-oleoylphosphatidylcholine (POPC) membrane in VMD1.9.2 (Humphrey et al., 1996) using a custom Tcl script. Lipid

residues with backbone atoms 0.7 Å or closer to protein backbone were deleted to prevent overlapping atoms. The system was solvated with TIP3P waters (Jorgensen et al., 1983), and, because the resting state of Hv1 is stabilized in the presence of Zn^{2+} , $ZnCl_2$ was added to the system using VMD1.9.2 AutoIonize plugin (<https://www.ks.uiuc.edu/Research/vmd/plugins/autoionize/>). The resulting system had 34 Zn^{2+} ions, 69 Cl^- ions for a total $ZnCl_2$ concentration of 150 mM, 11,954 TIP3P waters, 132 POPC lipids, and 55,959 total atoms.

Energy minimization (EM) was carried out using 5,000 steps of conjugate gradient descent EM in NAMD. After successful EM, the POPC lipid tails were equilibrated around the backbone of Hv1F for 50 ps. During this lipid equilibration the phosphate phosphorous (P) atoms of POPC groups were fixed in space, as were the TIP3P waters. After lipid equilibration, the system was subjected to a final round of equilibration, which consisted of applying 5 kcal/mol/Å² harmonic constraints to alpha carbon ($C\alpha$) atoms of Hv1F backbone and simulating under constant atom number, pressure and temperature (NPT) conditions for 1 ns. A custom Tcl forces script was used to keep water out of the membrane. Production runs in the NPT ensemble were then conducted for 150 ns to ensure sufficient sampling in the equilibrated portion of the MD trajectory. The uncertainty over the entire 150 ns trajectory is 0.6 kcal/mol. Production runs were stopped, assessed, and restarted every 10 ns.

EM, equilibration, and production runs were all carried out under standard conditions. The temperature was kept at 300K using Langevin dynamics (Phillips et al., 2005), the pressure was kept at 1 atm and coupled to temperature using a Langevin piston method (Phillips et al., 2005), with a 2 fs time step. Periodic boundary conditions (PBC; [Phillips et al., 2005](#)) were applied with PBC size 88 Å x 92 Å x 93 Å. The particle mesh Ewald (PME; [Phillips et al., 2005](#))

grid size was 125 Å x 125 Å x 125 Å. A switching distance of 10 Å, a cutoff of 12 Å, and a pair list distance of 13.5 Å was used to calculate electrostatics. A margin of 2.5 Å was added to prevent the PBC cell from becoming too small for the original patch grid. For the initial conditions, atomic velocities were determined by a random number generator and scaled to be compatible with the temperature, 300 K. For simulation restart, atomic velocities were taken from the previous run. For EM and the lipid tail equilibration around Hv1F backbone, the pressure coupling was turned off. EM, lipid equilibration, and harmonic constraint NPT were performed on the GPU server in NAMD2.9. Production runs were carried out on a CPU server using NAMD2.10.

During equilibration and throughout the entirety of production runs, the Hv1F MD system was assessed to verify maintenance of the equilibrium state by multiple methods. All the output NAMD energy terms and RMSD for backbone atoms of Hv1F were confirmed to be stably fluctuating about a mean value. Additionally, the uncertainty in the total energy was confirmed to be within the realm of thermal fluctuations with a value less than 1 $k_B T$. To verify the system was sampling equilibrium, the distribution of atomic kinetic energies was confirmed to fit the Maxwell-Boltzmann distribution. After 60 ns of production run, the Hv1F system was confirmed to be sampling equilibrium with the uncertainty in total energy below the desired threshold value (reported above).

Hv1F E119A Mutant Simulations

The Hv1F E119A model was made using the VMD1.9.3 Mutator plugin (<https://www.ks.uiuc.edu/Research/vmd/plugins/mutator/>) by converting E119 to alanine in the initial coordinates for the WT Hv1F-POPC-TIP3P-ZnCl₂ system. EM, lipid equilibration, NPT

harmonic constraint simulation, and production runs were performed in an identical manner to that used for the Hv1F WT system except that during EM and lipid equilibration the backbone atoms of Hv1F E119A were fixed to prevent kinks from forming in the S1 helix and with PME automatic grid spacing turned on and grid spacing set to 1.0 Å. For the initial conditions, atomic velocities were determined by specifying the same seed as was used for the Hv1F WT simulations. For simulation restart, atomic velocities were taken from the previous run. The equilibrium state was assessed and verified in a manner equivalent to that used for the Hv1F WT system. Production runs were carried out for 150 ns. The uncertainty in total energy for the entire trajectory was 0.6 kcal/mol.

Hv1F D185A Mutant Simulations

The Hv1F D185A model was made and simulated using the same method as for the Hv1F E119A simulations. Using the VMD1.9.3 Mutator plugin, D185 was converted to alanine in the initial coordinates for the WT Hv1F-POPC-TIP3P-ZnCl₂ system. EM, lipid equilibration, NPT harmonic constraint simulation, and production runs were performed in an identical manner to that used for the Hv1F E119A system. For the initial conditions, atomic velocities were determined by specifying the same seed as was used for the Hv1F WT and Hv1F E119A simulations. For simulation restart, atomic velocities were taken from the previous run. The equilibrium state was assessed and verified in a manner equivalent to that used for the other model simulations. Production runs were carried out for 155 ns. The Hv1F D185A the uncertainty in total energy for the entire trajectory was 0.4 kcal/mol.

Hv1F E119A-D185A Mutant Simulations

The Hv1F E119A-D185A model was made and simulated using the same method as for the Hv1F single mutant simulations. Using the VMD1.9.3 Mutator plugin, E119 was converted to alanine in the initial coordinates for the Hv1F-D185A-POPC-TIP3P-ZnCl₂ system. EM, lipid equilibration, NPT harmonic constraint simulation, and production runs were performed in an identical manner to that used for the Hv1F single mutant simulations. For the initial conditions, atomic velocities were determined by specifying the same seed as was used for the Hv1F WT simulations and for simulation restart, atomic velocities were taken from the previous run. The equilibrium state was assessed and verified in a manner equivalent to that used for the other model simulations. Production runs were carried out for 150 ns. The the uncertainty in total energy for the entire trajectory was 0.6 kcal/mol.

3.1.4: Molecular Dynamics Simulations of Hv1J

Wild Type Simulations

Simulations of Hv1J WT were carried out in a manner very similar to that used for the Hv1F WT system. Again, Hv1J was truncated after residue 230 to remove the CC domain and reduce the amount of bulk water required for MD. This truncated Hv1J model was then embedded into the same pre-solvated, pre-equilibrated POPC membrane as was used for the Hv1F WT simulation, using a custom Tcl script executed in VMD1.9.3 (Humphrey et al., 1996). Again, lipid residues with backbone atoms 0.7 Å or closer to protein backbone were deleted to prevent overlapping atoms. This system was then neutralized using VMD1.9.3 AutoIonize plugin by adding just enough KCl to neutralize the total charge on the system. The resulting system had 134 POPC lipids, 2 Cl⁻ ions, 12,055 TIP3P water molecules, and 56,501 total atoms.

MD for Hv1J system was carried out in an almost identical way to the method used for Hv1F, with the only difference being some of the force field and integrator parameters used. EM was carried out using 5,000 steps of conjugate gradient descent EM, after which the POPC lipid tails were equilibrated around the backbone of Hv1J for 50 ps. During this lipid equilibration the P atoms of POPC groups were fixed in space, as were the TIP3P waters. Just as before, the Hv1J system was subjected to a final round of equilibration, which consisted of applying 5 kcal/mol/Å² harmonic constraints to C α atoms of Hv1F backbone and simulating under NPT conditions for 1 ns after lipid equilibration. A custom Tcl forces script was used to keep water out of the membrane during the harmonic constraint MD. Production runs in the NPT ensemble were then conducted for 140 ns to ensure sufficient sampling in equilibrium conditions. Production runs were stopped, assessed, and restarted every 10 ns.

EM, equilibration, and production runs were all carried out under standard conditions, just as was done for the Hv1F system. The temperature was kept at 300K using Langevin dynamics, the pressure was kept at 1 atm and coupled to temperature using the Langevin piston method, using a 2 fs time step. PBC were applied with PBC size 81 Å x 78 Å x 94 Å. A PME grid of 125Å x 125Å x 125Å with a switching distance of 10 Å, a cutoff of 12 Å, and a pair list distance of 16 Å was used to calculate electrostatics. A margin of 2.5 Å was added to prevent the PBC cell from becoming too small for the original patch grid. For the initial conditions, atomic velocities were determined by a random number generator. For simulation restart, atomic velocities were taken from the previous run. For EM and the lipid tail equilibration around Hv1J backbone, the pressure coupling was turned off. EM, lipid equilibration, harmonic constraint NPT, and production runs were performed on the GPU workstation in NAMD2.11.

Hv1J WT Production runs were carried out for 140 ns. The equilibrium state was assessed and verified in a manner identical to that used to assess equilibrium in the Hv1F system. After 30 ns of production run, the Hv1J system was confirmed to be sampling equilibrium with the uncertainty in total energy below the desired threshold value. The uncertainty in total energy over the entire trajectory is 0.3 kcal/mol.

Hv1J E119A Mutant Simulations

The Hv1J E119A model was made using the VMD1.9.3 Mutator plugin by converting E119 to alanine in the initial coordinates for the WT Hv1J-POPC-TIP3P-KCl system. EM, lipid equilibration, NPT harmonic constraint simulation, and production runs were performed in an identical manner to that used for the Hv1J WT system except that during EM and lipid equilibration the backbone atoms of Hv1J were fixed to prevent kinks from forming in the S4 helix and the PME grid spacing was determined automatically with grid spacing set to 1.0 Å. For the initial conditions, atomic velocities were determined by specifying the same seed as was used for the Hv1J WT simulations. For simulation restart, atomic velocities were taken from the previous run. The equilibrium state was assessed and verified in a manner equivalent to that used for the Hv1J WT and Hv1F systems. Production runs were carried out for 150 ns. The Hv1J E119A systems was confirmed to be sampling equilibrium with an uncertainty in total energy for the entire trajectory of 0.9 kcal/mol.

Hv1J D185A Mutant Simulations

The Hv1J D185A model was made and simulated using the same method as for the Hv1J E119A simulations. Using the VMD1.9.3 Mutator plugin, D185 was converted to alanine in the

initial coordinates for the WT Hv1J-POPC-TIP3P-KCl system. EM, lipid equilibration, NPT harmonic constraint simulation, and production runs were performed in an identical manner to that used for the Hv1J D185A system. For the initial conditions, atomic velocities were determined by specifying the same seed as was used for the Hv1J WT simulations. For simulation restart, atomic velocities were taken from the previous run. The equilibrium state was assessed and verified in a manner equivalent to that used for the other model simulations. Production runs were carried out for 150 ns. The Hv1J D185A system was confirmed to be sampling equilibrium with an uncertainty in total energy for the entire trajectory of 1.2 kcal/mol.

Hv1J E119A-D185A Mutant Simulations

The Hv1J E119A-D185A model was made and simulated using the same method as for the Hv1J single mutant simulations. Using the VMD1.9.3 Mutator plugin, E119 was converted to alanine in the initial coordinates for the Hv1J-D185A-POPC-TIP3P-KCl system. EM, lipid equilibration, NPT harmonic constraint simulation, and production runs were performed in an identical manner to that used for the Hv1J single mutant simulations. For the initial conditions, atomic velocities were determined by specifying the same seed as was used for the Hv1J WT simulations and for simulation restart, atomic velocities were taken from the previous run. The equilibrium state was assessed and verified in a manner equivalent to that used for the other model simulations. Production runs were carried out for 220 ns. The Hv1J D185A system was confirmed to be sampling equilibrium with the uncertainty in total energy for the entire trajectory of 0.3 kcal/mol.

3.1.5: Analysis of Molecular Dynamics Trajectories

PROPKA3.1 Calculations

As discussed earlier, the pK_a of specific residues is considered to be crucial to ΔpH sensing in Hv1. While making experimental measurements of the pK_a values for specific residues in Hv1 remains a formidable challenge, predicating the pK_a values using commonly available algorithms is straightforward. PROPKA3.1 is an empirically-derived algorithm (Bas et al., 2008; Li et al., 2005; Olsson et al., 2011; Søndergaard et al., 2011) that has been shown to make accurate predictions for side chain pK_a values in proteins (Alexov et al., 2011). PROPKA3.1 is accessible via a webserver (http://nbc222.ucsd.edu/pdb2pqr_2.0.0/), can be installed locally from GitHub (<https://github.com/jensengroup>), or can be imported as a module and executed from within Python. Typically, PROPKA3.1 is run on a single PDB structure to determine the probable protonation states of various ionizable side chains. However, in Hv1, it is speculated that the pK_a values of the acidic residues that serve as countercharges for the S4 arginine residues may be shifted relative to solution values. In addition to shifting, pK_a values in Hv1 may exhibit more than one value that depends on the conformational state of Hv1 and the applied voltage. These shifts and dynamic behavior in pK_a values could allow for acidic residues, which would normally be negatively charged, to undergo titration events in physiological pH range, and therefore be essential to the pH sensing mechanism in Hv1. Using a novel adaptation of PROPKA3.1, the pK_a values of Hv1 residues were calculated on all 8 MD systems with PROPKA3.1 being carried out at every single time step (every 2 fs) during the trajectory. Bonds stretching and angle bending have the fastest vibrational period, typically occurring between 10 fs and 100 fs (Isgro et al., 2017). In MD performed by NAMD, it is ideal to sample 10x as frequently as the fastest molecular motion (Isgro et al., 2017) and therefore we sampled the pK_a

calculations every time step. Performing PROPKA3.1 over long MD trajectories allows for the fluctuations in pK_a values to be investigated. This PROPKA3.1 analysis was carried out locally using a custom python2.7 script utilizing the MDAnalysis library (Gowers et al., 2016; Michaud-Agrawal et al., 2011; <https://www.mdanalysis.org>) executed within iPython (<https://ipython.org>) on the previously described 2013 MacBook Pro.

In order to visualize the predicted pK_a values, the custom Python script mentioned above included several plotting features. In order to make plotting and data manipulation easier, pK_a values for each residue at every frame were imported into a Pandas DataFrame (<https://pandas.pydata.org/pandas-docs/stable/reference/api/pandas.DataFrame.html>). The Pandas DataFrame boxplot method (<https://pandas.pydata.org/pandas-docs/stable/reference/api/pandas.DataFrame.boxplot.html>) was used to calculate statistics for boxplots of pK_a values and the plot method (https://matplotlib.org/3.1.0/api/_as_gen/matplotlib.pyplot.plot.html) of PyPlot (https://matplotlib.org/api/plt_api.html) was used to plot the boxplots for each residue. To calculate histograms of the pK_a data, the distplot method (<https://seaborn.pydata.org/generated/seaborn.distplot.html>) of Seaborn (<https://seaborn.pydata.org/index.html>) was used. Time series of pK_a values for every residue were plotted using PyPlot (https://matplotlib.org/api/plt_api.html).

pK_a Covariance Calculations

Electrostatic interactions are a significant factor in determining pK_a values for residues in a protein environment (Alexov et al., 2011). Electrostatic interactions not only determine the pK_a values of the interacting partners, but may also cause the pK_a values of the interacting residues to

be coupled, in which the pK_a values of the interacting residues will vary together in time. To investigate if fluctuations between various residue pK_a values were correlated, a custom Python3.6 script was used to calculate a residue-by-residue covariance matrix for the pK_a values for all eight MD systems. The script loads the pK_a data for each residue at every time step into a Pandas DataFrame and then uses the `cov` method of the Pandas DataFrame (<https://pandas.pydata.org/pandas-docs/stable/reference/api/pandas.DataFrame.cov.html>) to calculate residue-by-residue pK_a covariance values. The heatmap method of Seaborn (<https://seaborn.pydata.org/generated/seaborn.heatmap.html>) was used to construct heat maps of the covariance data and the regplot method of Seaborn (<https://seaborn.pydata.org/generated/seaborn.regplot.html>) was used to make scatter plots with linear regressions for each residue-residue pair in the system.

3.2: Experimental Methods

3.2.1: Site-Directed Mutagenesis

Standard PCR-based site-directed mutagenesis described previously ([De La Rosa et al., 2018](#); [Ramsey et al., 2006, 2010](#)) on GFP- or Venus-tagged human Hv1 (hHv1) in pQBI25-fC3 or pcDNA5/FRT/TO vector was used to create E119A, D123A, E153A, and D185A single mutants, E119A-D185A, D123A-D130A, and E119A-D123A double mutants, and E119A-D123A-D185A, D123A-D130A-D185A, and E119A-D123A-D185A triple mutants. The Hv1 coding sequence for each mutant was confirmed by Sanger sequencing of cDNA using specific oligonucleotide primers (Genewiz).

3.2.2: Electrophysiology

FlpIn293-TREx cells (Life Technologies), an HEK-293 based cell line that is engineered for site-specific incorporation of genes of interest by the activity of Flp recombinase ([De La Rosa et al., 2018](#)), were transfected with either mutant or WT GFP-hHv1. 24-48 hours after transfection, whole cell voltage clamp was performed as previously has been described ([De La Rosa and Ramsey, 2018](#); [Ramsey et al., 2010](#); [Randolph et al., 2016](#); [Villalba-Galea, 2014](#)). Voltage clamp experiments were performed at multiple pH gradients, with pH_i set to 5.5 and pH_o ranging from 4.5 to 7.5. EC pH was altered by gravity-fed perfusion of the bath recording chamber.

Both bath and pipette solutions contained ~80 mM H-MeSO₃, ~80 mM TMA-OH, 8 mM HCl, 1 mM EGTA, and were adjusted to ~285 mOsm by addition of H-MeSO₃ and TMA-OH to maintain the desired pH. For pH 4.5 solutions, 100 mM citric acid was used as buffer, for pH 5.5 solutions, 100 mM MES was used, for pH 6.5 solutions, 100 mM 6.5 bis-Tris was used as buffer,

and for pH 7.5 solutions, 100 mM of HEPES was used as buffer. Ionic currents were measured with an A-M systems model 2400 patch clamp amplifier, analog filtered at 2 kHz, and digitized at 10-20 kHz using a USB-2551 A/D interface. Voltage clamp commands are controlled by custom LabView software (National Instruments) as described previously ([Villalba-Galea, 2014](#)) and no correction for liquid junction potentials or series resistance compensation was applied. Cells were held at -40 mV or -50 mV and 1000-4000 ms voltage pulses to potentials ranging from -100mV to +200 mV were applied at 0.1-0.2 Hz; holding potential and range of test potentials tested were adjusted as necessary to accurately measure the threshold potential (V_{thr}) at different pH_o . At the end of the test potential step, the voltage is stepped to -80 mV for 200-500 ms to generate inward tail currents (I_{tail}). I_{tail} was plotted as a function of the test voltage and V_{thr} was estimated by visual inspection of raw current records and I_{tail} -V relationships as previously described ([Morgan et al., 2009](#); [Ramsey et al., 2006, 2010](#)).

3.2.3: Analysis of Electrophysiology Data

A custom Java script (JustAnalysis 14.04) and Clampfit10 (Molecular Devices), described previously ([De La Rosa and Ramsey, 2018](#); [De La Rosa et al., 2018](#); [Villalba-Galea, 2014](#)), together with Microsoft Excel for Mac version 15.9.1, were used to analyze recorded I_{tail} currents and create I_{tail} -V plots. The I_{tail} currents were extrapolated to $t=0$ and the I_{tail} -V data were fit to a single exponential, as previously described ([Ramsey et al., 2006](#)). V_{thr} - pH_o relationships are constructed and fit to linear equations using custom Python scripts.

3.2.4: Zn^{2+} Potency Experiments

The Zn^{2+} potency experiments using Hv1 E153A mutants have been previously published (De La Rosa et al., 2018). Briefly, FlpIn293-TREx cells were transfected with GFP-Hv1 E153A and subjected to whole cell voltage clamp. I_{tail} was measured in EC solutions containing the indicated concentrations of Zn^{2+} and the Zn^{2+} -dependent shift in V_{thr} was used to estimate Zn^{2+} potency as described (De La Rosa et al., 2018).

Table 3.1: Structural Restraints Used to Refine Hv1F Resting State Model
Upper and lower bound forms were used to restrain either XY distances (physical.xy_distance) or the Coulomb point-point electrostatic potential (physical.coulomb) between defined atoms. Alpha helical structural restraints were also applied as described in the text. The upper and lower bound restraints are presented as mean \pm standard deviation. Atom types are defined by the CHARMM36 force field.

Table 3.1: Structural Restraints Used to Refine Hv1F Resting State Model				
Modeling Round	Atom 1	Atom 2	Mean Bound Distance	Modeller Protocol
2	H140ND1	H193ND1	Upper: 10 ± 0.1 Å Lower: 6 ± 0.1 Å	physical.xy_distance
2	K157NZ	K221NZ	Upper: 5 ± 0.1 Å	physical.coulomb
2	D174OD1	R208NH1	Upper: 5 ± 0.1 Å	physical.coulomb
2	E171OE1	R211NH1	Upper: 5 ± 0.1 Å	physical.coulomb
2	E153OE1	R205NH1	Upper: 5 ± 0.1 Å	physical.coulomb
3	H140NE2	H193NE2	Upper: 10 ± 0.1 Å Lower: 6 ± 0.1 Å	physical.xy_distance
3	K157NZ	K221NZ	Upper: 5 ± 0.1 Å	physical.coulomb
3	D174OD1	R208NH1	Upper: 5 ± 0.1 Å	physical.coulomb
3	E171OE1	R211NH1	Upper: 5 ± 0.1 Å	physical.coulomb
3	E153OE1	R208NH1	Upper: 5 ± 0.1 Å	physical.coulomb
3	E119OE1	D185OD2	Upper: 15 ± 0.1 Å	physical.coulomb
3	D123OD1	D185OD1	Upper: 15 ± 0.1 Å	physical.coulomb
3	D130OD1	H193NE2	Upper: 15 ± 0.1 Å	physical.coulomb
4	H140ND1	H193ND1	Upper: 3 ± 0.01 Å Lower: 3 ± 0.01 Å	physical.xy_distance
4	H140NE2	D185CG	Upper: 4 ± 0.01 Å	physical.xy_distance
4	H193NE2	D185CG	Upper: 4 ± 0.01 Å	physical.xy_distance
4	H140ND1	E119CG	Upper: 5 ± 0.01 Å	physical.xy_distance
4	H193ND1	E119CG	Lower: 5 ± 0.01 Å	physical.xy_distance
4	E171OE1	K157NZ	Upper: 5 ± 0.01 Å	physical.coulomb

Table 3.2: Structural Restraints Used to Refine the Hv1J Activated State Model

Upper and lower bound forms were used to restrain the Coulomb point-point electrostatic potential (physical.coulomb) between defined atoms. The upper and lower bound restraints are presented as mean \pm standard deviation. Additional alpha helical secondary structural restraints were applied to residue 98-124 for S1, 131-158 for S2, 170-190 for S3, and 199-266 for S4 and the CC domain. Atom types are defined by the CHARMM36 force field.

Table 3.2: Structural Restraints Used to Refine the Hv1J Activated State Model			
Atom 1	Atom 2	Mean Bound Distance	Modeller Protocol
D185OD2	R208NH2	Upper: $3 \pm 0.1 \text{ \AA}$	physical.coulomb
E119OE2	R205NH2	Upper: $3 \pm 0.1 \text{ \AA}$	physical.coulomb
D112OD2	R211NH2	Upper: $3 \pm 0.1 \text{ \AA}$	physical.coulomb

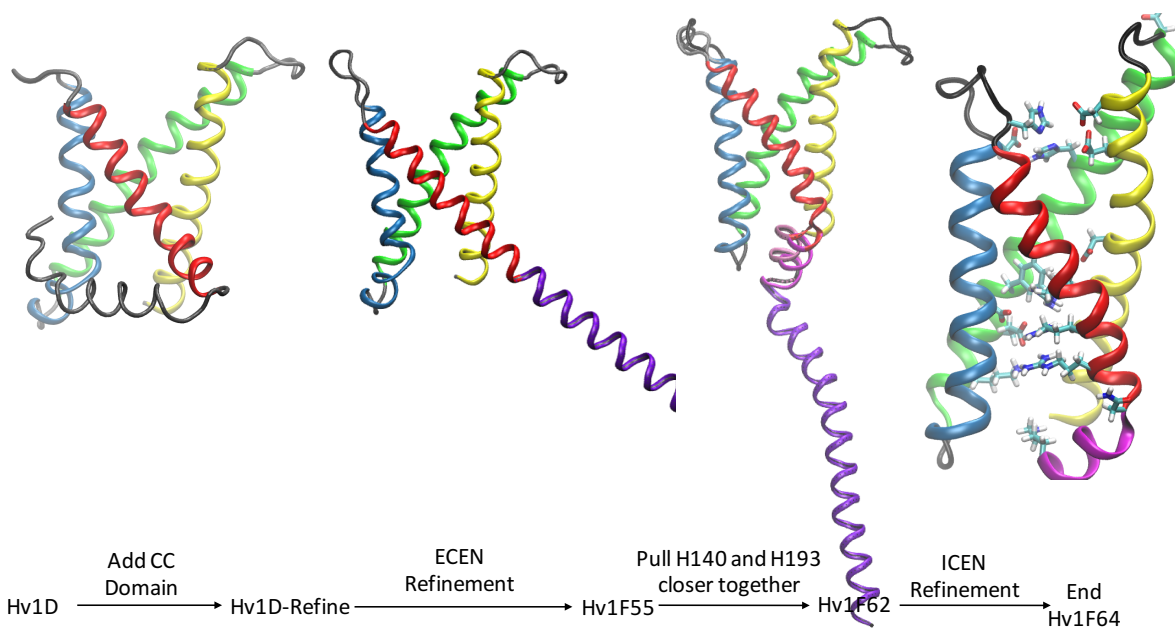


Figure 3.1: Overview of Hv1F Modeling

The template for creation of the Hv1F model (right) was Hv1D (left), which was validated by resting-state currents in the R1H mutant ([Randolph et al., 2016](#)). First, the CC domain was added to the Hv1D model to make the Hv1D-Refine model (center left). Second, H140 and H193 were pulled closer as indicated by the data to make the Hv1F55 model, and then the rest of the ECEN was refined to make the Hv1F62 model (center right). In the fourth and last step, ICEN of Hv1F62 was refined to produce Hv1F. Hv1 VSD helices are color coded for convenience: S1, yellow; S2, green; S3, blue; S4, red.

CHAPTER 4: EXPERIMENTALLY-VALIDATED MODELS OF Hv1

As previously discussed, the currently existing models of Hv1 are not entirely consistent with all known experimental data. In order to create a model that is parsimonious with all the experimental data, Modeller9.16 was used to modify existing models by incorporating interacting pairs ([Table 3.1](#), [Table 3.2](#)), as suggested by voltage clamp experimental data ([Table 1.1](#)). These new models were subsequently subjected to about 150 ns of MD and the analysis of these trajectories was used to inform hypotheses and experiments to investigate Δ pH-dependent gating in Hv1.

4.1: Resting State Model Hv1F

Using structural restraints derived from voltage clamp data ([Table 3.1](#)) to refine the resting state Hv1D model proved to be successful ([Figure 4.1](#)). The resulting resting state model, denoted Hv1F, allows for both H140 and H193 to simultaneously bind a single Zn^{2+} ion with H140-N δ and H193-N δ 3.40 Å apart from each other ([Figure 4.2](#)). In the final Hv1F model, the H140-N δ to Zn^{2+} distance is 2.39Å and that for the H193-N δ and Zn^{2+} is 2.23Å, which is consistent with the voltage clamp data demonstrating that H140 and H193 are predominately responsible for coordinating Zn^{2+} in Hv1 ([Figure 4.2](#)). Zn^{2+} potency data indicates that E119 and D185 are in vicinity of Zn^{2+} and contribute to the Zn^{2+} binding site (De La Rosa et al., 2018), suggesting that these residues are close to H140, H193 and Zn^{2+} ([Figure 4.2](#)).

An important aspect of Hv1 resting state models is the register of the S4 helix. The closed-state, inward H^+ conductance exhibited by the Hv1 R205H mutant strongly argues that the first S4 Arg, R205, is in register with hydrophobic gasket residues including F150 in the resting-state conformation (Randolph et al., 2016). Consistent with the experimental data, R1/R205 is in apposition to F150, in the resulting Hv1F model ([Figure 4.3](#)). The register of the S4 helix is stabilized by extensive electrostatic interactions amongst residues in the ICEN ([Figure 4.1C](#)). Due to the lack of positively charged residues, the ECEN is devoid of salt bridges to S4 Arg side chains and acidic residues in close proximity to one another do not interact with balancing countercharges ([Figure 4.1B](#)).

Voltage clamp on K157A-K221A mutant revealed a superadditive effect on V_{thr} in the double mutant ([Figure 4.4A](#)), indicating that K157-K221 indeed interact to stabilize the resting state relative to the active state. The terminal nitrogen atoms (NZ) for K157 and K221 are 5.55 Å apart in the Hv1F model, allowing for weak a K157-K221 interaction in the ICEN as indicated by electrophysiological data ([Figure 4.4](#)). Mutant cycle analysis proposed interactions between D174, E153, and the S4 arginine residues ([Table 1.1](#); Chamberlin et al., 2014) and the Hv1F model recapitulates these interactions as well ([Table 1.1](#), [Figure 4.1A,C](#), [Figure 4.12](#)). Overall, Hv1F is consistent with the known experimental data and shows that when lacking a high quality crystal structure, structural constraints can be successfully derived from other types of experiments and used to construct reasonable models. These results also demonstrate that minor, experimentally-informed refinements can be used to improve existing models rather than creating an entirely new model from scratch every time new data becomes available. This allows for an iterative approach where experimental data can be easily incorporated into an existing model and may be more efficient in elucidation of structure-function relationships.

4.2: Activated State Model Hv1J

The voltage clamp derived structural restraints were also successful at producing an activated state model, Hv1J, that is consistent with the known experimental data ([Figure 4.5](#)). One of the most important structural features of the active state Hv1 is the D112-R211 interaction that forms the selectivity filter (Berger and Isacoff, 2011). Hv1J exhibits a strong interaction between D112 and R211 ([Figure 4.6A](#)). Furthermore, the D112-R211 selectivity filter lies to the EC side of the F150 hydrophobic gate in the Hv1J model, which is also indicated by the voltage clamp data ([Figure 4.16A](#); Berger and Isacoff, 2011). Another critical component of the active state Hv1 model is the register of S4 relative to the S1-S3 helices. Guanidinium accessibility (Berger and Isacoff, 2011; Hong et al., 2013) and N214R block data (Randolph et al., 2016) strongly argue that N214 is in register with F150 in the active state, and the Hv1J model clearly demonstrates this ([Figure 4.5C](#)).

The new active state Hv1J model demonstrates E119-R205, E119-R208, and D185-R208 salt bridges ([Figure 4.6B](#)), which is consistent with early mutagenesis studies demonstrating that D185 and E119 stabilize the active state of the Hv1 channel (Ramsey et al., 2010) and mutant cycle analysis showing that both E119 and D185 interact with S4 arginine residues ([Table 1.1](#); Chamberlin et al., 2014). Hv1J also exhibits a D185-R211 interaction ([Figure 4.6B](#)) that has not yet been experimentally confirmed, but is consistent with the observation that D185 stabilizes the activated state of the channel (Ramsey et al., 2010). In Hv1J, W207 is facing the pore and interacting with residues of the ECEN ([Figure 4.6C](#)), which is potentially consistent with data showing that W207 appears to modulate EC pH sensing at alkaline pH_o (Cherny et al., 2015). Hv1J is the only active state Hv1 model described so far in which W207 is positioned to

participate in ECEN structure, and is therefore the most compatible with experimental data implicating this residue in Δ pH-dependent gating.

4.3: Molecular Dynamics on Hv1J WT

As for Hv1F, the Hv1J model was truncated after residue 230 to reduce the amount of bulk water necessary in the MD simulation system. The truncated, Hv1J WT VSD model was simulated for a total of 140 ns. The fluctuations in total energy of the Hv1J WT system were <1 k_bT by 30 ns (data not shown). The RMSD of the Hv1J WT model vs. the active state crystal structure of *Ci*-VSP (PDB 4G7V; Li et al., 2014), the most homologous VSD to Hv1 ([Figure 1.2](#)), stabilizes by 60 ns ([Figure 4.7A](#)). The RMSD stabilizes around 12.5 Å, which is quite high. *Ci*-VSP only has about 30% sequence identity to human Hv1 and so a higher RMSD is not surprising. Furthermore, in the crystal structure of *Ci*-VSP the alignment of S4 relative to the S1-S3 helices is much different than that found in Hv1J. In the active state *Ci*-VSP crystal structure, the second gating charge of S4 is in proximity to F150 and makes a salt bridge with the residue equivalent to D112 in Hv1. However, this register of S4 relative to S1-S3 observed in the active state VSP is compatible with neither the D112-R211 selectivity filter data (Berger and Isacoff, 2011) nor the closed-stated H^+ conductance data (Randolph et al., 2016). Therefore, the Hv1J model has a S4 register that is moved two helical turns towards the EC side relative to S1-S3 helices and places N214, the fourth S4 gating charge position, in close proximity to F150. This translation of S4 contributes significantly to the large RMSD between Hv1J and 4G7V crystal structure. The time range from 30 ns to 140 ns was used to analyze the properties of the Hv1J WT system because the system seems to have reached an equilibrium state by this point.

4.3.1: Salt Bridges in the Activated State Model Hv1J

The VMD Salt Bridges plugin with default settings was used to perform a salt bridge analysis on the Hv1J WT MD to investigate potential active state electrostatic interactions. Importantly, the D112-R211 interaction that is known to contribute to H⁺ selectivity (Berger and Isacoff, 2011), and is a crucial component of any Hv1 active state model, remains strong and stable throughout the 140 ns simulation ([Figure 4.8A](#)), demonstrating that the Hv1J model is consistent with the experimental data regarding H⁺ selectivity. D112 is also engaged in a weaker electrostatic interaction with R208, which is consistent with some data suggesting that it is R208 that interacts with D112 in the active state ([Figure 4.8A](#); Kulleperuma et al., 2013). Initially, it seemed that the experimental data showing D112-R208 interactions (Kulleperuma et al., 2013) was in conflict with data showing D112-R211 interactions (Berger and Isacoff, 2011). However, as the Hv1J MD shows, it may be that D112 can engage both R211 and R208 in electrostatic interactions and therefore the previously collected data may not be as contradictory as originally thought.

Hv1J manifests extensive interactions in both the ECEN and ICEN. Both E119 and D185 were shown to stabilize the activated state of Hv1, likely through interactions with S4 arginine residues (Ramsey et al., 2010). Mutant cycle analysis confirms that E119 engages in electrostatic interactions with both R205 and R208 and D185 engages R208 ([Table 1.1](#); Chamberlin et al., 2014). Consistent with the voltage clamp and mutant cycle analysis data, E119 was found to engage in electrostatic interactions with both R205 and R208 ([Figure 4.8B](#)). The E119-R208 interaction is stronger than the E119-R205 interaction in the Hv1J model ([Figure 4.8B](#)), which is opposite of the mutant cycle analysis but consistent with GIA ([Table 1.1](#)). The discrepancy in the experimental data obtained from different methods makes it difficult to compare Hv1J

electrostatic interactions to experimental data. GIA is considered to be a more thermodynamically robust analytic method so, preliminarily, it appears that Hv1J is consistent with the GIA interaction data. D185-R211 also makes a weaker, but still stable, electrostatic interaction during the course of the Hv1J MD trajectory ([Figure 4.8B](#)). This is slightly different when compared to the mutant cycle analysis, which indicates that D185 makes a salt bridge to R208 instead ([Table 1.1](#); Chamberlin et al., 2014). D123-R205 makes a stable but weak interaction, while D130-K131 makes a relatively dynamic interaction, which fluctuates frequently between close and long range ([Figure 4.8B](#)). D123 and D130 interactions cannot be compared to experimental data sets because no experiments have verified interacting partners for these residues. While detailed comparisons to experimental data is not yet possible, more general comparisons can be made. S4 gating charges have previously been suggested to interact with both E119 and D185 to stabilize the active state of the channel (Chamberlin et al., 2014; Ramsey et al., 2010), a feature that is recapitulated in the new Hv1J model.

There is also an extensive EN in the ICEN in the active state Hv1J model ([Figure 4.8C](#)). In the Hv1J WT MD, D174 makes a strong and stable interaction with both K157 and K221 ([Figure 4.8C](#)), but these interactions have not been experimentally validated. Additionally, E153 and K157 make a strong and stable interaction, whereas E171-K221 make a weaker, but still stable interaction ([Figure 4.8C](#)). These interactions have not yet been experimentally investigated either. Other, seemingly less important, interactions were found to contribute to the CC domain as well ([Figure 4.8D](#)), but there is not experimental data to compare to. Overall, the electrostatic interactions detected in the Hv1J model seem to be generally consistent with the known experimental data, but more experiments are necessary to verify and improve the Hv1J model.

4.3.2: PROPKA3.1 pK_a Calculations in Activated State Model Hv1J

To investigate how pK_a values of various residues fluctuate in Hv1, PROPKA3.1 calculations were carried out every 20 fs from 30-140 ns. This is the first time the PROPKA3.1 has been used to investigate pK_a fluctuations during the course of MD simulation. Surprisingly, many acidic and basic residues have pK_a values that deviate largely from what would be expected from solution pK_a values ([Figure 4.9](#); [Table 4.1](#)). With no experimental data on individual residue pK_a values, these average PROPKA3.1 pK_a values are difficult to interpret. Single mutants all appear to have ΔpH-dependent gating similar to WT, so it appears interactions between residues are necessary for Hv1 ΔpH sensitivity. Therefore, correlations between residue pK_a values may be more useful than the average pK_a values.

A pK_a covariance analysis was performed on the Hv1J pK_a time series data to identify if any residue pK_a values appeared to covary together ([Figure 4.10](#)). Quite interestingly, the pK_a of residue H168 is predicted to be highly covaried with that of E171 as well as E164 ([Figure 4.10](#)). The identification of H168 pK_a being highly covaried to another residue is exceedingly interesting as H168 was recently identified as an IC pH sensor (Cherny et al., 2018). The ability of the PROPKA3.1 covariance analysis to identify a residue known to be necessary for Hv1 ΔpH-dependent gating validates this method for identifying functionally important residues. While no functional role has yet been determined for E171 or E164, the mutagenesis studies on H168 revealed that, while H168 is necessary for Hv1 ΔpH-dependent gating, it is not sufficient, and indicates that H168 must interact with other residues to elicit the unique ΔpH-dependent gating properties of Hv1. These other residues have yet to be identified and E171 and E164 are good initial candidates.

A more in depth analysis on H168 and E164 pK_a fluctuations revealed that these pK_a values vary simultaneously in time such that when the pK_a of H168 drops, that of E164 rises and vice versa, an example of coupled pK_a values ([Figure 4.11A](#)). Consequently, there is a strong correlation ($r^2 = -0.7$) between the pK_a values of H168 and E164 ([Figure 4.11B](#)). While there is no functional information available for E164, the identification of H168 using this novel PROPKA3.1 pK_a analysis is promising and indicates that this method is useful for identifying functionally relevant residues in Hv1, especially as it pertains to ΔpH-dependent gating.

Electrostatic interactions are known to be significant contributors to residue pK_a values in proteins ([Pace et al., 2009](#)). Electrostatic interactions between H168 and E164 were examined to investigate the possibility that these interactions are related to pK_a values of E164 and H168. An overlay of the time series for H168 pK_a and H168-E164 distance shows that the distance between the Nδ atom of H168 and the terminal oxygen atoms of E164 is highly dynamic and fluctuates between making strong and weak electrostatic interactions ([Figure 4.11C](#)). The H168-E164 distance fluctuations are associated with corresponding fluctuations in the H168 pK_a value ([Figure 4.11C](#)). When H168 and E164 become closer, the pK_a value of H168 is raised such that H168 is more likely to bear a positive charge when in close proximity to the partial negative oxygen atoms of E164, promoting salt bridge formation ([Figure 4.11C](#)). Despite that there are other variables influencing the H168 pK_a, there is a moderate correlation ($r^2 = -0.5$) between the H168-E164 distance and H168 pK_a, with H168 only taking values over 6 only when the H168-E164 distances is less than 8 Å ([Figure 4.11D](#)). This analysis supports the idea that electrostatic interactions are important in influencing the residue pK_a values in Hv1.

Overall, the Hv1J model features seem to reliably reflect what is currently known from experimental data. The analysis on Hv1J presented here already provides some fascinating

insights into structure-function relationships, an establishes a new method to identify and investigate residues with important functional implications. Furthermore, this initial analysis immediately suggested some rather interesting experiments and should be useful in generating more insights and testable hypotheses of channel structure and function.

4.4: Molecular Dynamics on Hv1F WT

Just as was done for Hv1J, the amount of bulk water and overall system size for MD was minimized by truncating the resting state model Hv1F after residue 230 to remove the CC domain. The resulting Hv1F WT VSD model was simulated for 150 ns. The fluctuations in total energy of the Hv1F WT system fall below 1 $k_B T$ by 60 ns (data not shown). The RMSD of the Hv1F WT model vs. the crystal structure of *Ci*-VSP in the resting state (PDB 4G80; Li et al., 2014), the mostly closely related VSD with a solved structure, stabilizes by 80 ns ([Figure 4.7B](#)). The RMSD stabilizes around 8 Å, which is somewhat high. However, *Ci*-VSP only has about 30% sequence identity to human Hv1 ([Figure 1.2](#)) and therefore some differences between the two structures can be expected. The time ranges from 60 ns to 150 ns was used to analyze the properties of the Hv1F WT system because the system seems to have reached an equilibrium state by this point.

4.4.1: Salt Bridges in the Resting State Model Hv1F

A salt bridge analysis was used to examine potential electrostatic interactions in the resting state of Hv1. [Figure 4.12](#) shows every salt bridge detected by VMD Salt Bridges plugin using default settings in the Hv1F WT MD. As the GIA and mutant cycle analysis data suggests ([Table 1.1](#); Chamberlin et al., 2014), D174 forms a strong and stable salt bridge with R208 during the Hv1F WT MD ([Figure 4.12A](#)). Mutant cycle analysis suggests that D174 also engages in electrostatic interactions with R205 ([Table 1.1](#); Chamberlin et al., 2014), however, in the Hv1F WT model D112 forms an interaction pair with R205 instead ([Figure 4.12A](#)). Interactions that D112 may engage in the resting state has not yet been experimentally investigated and so the presence of D112-R205 interaction in the Hv1F WT MD cannot be compared to experimental

results at this time. The free energy value calculated for the the D174-R205 interaction is smaller than that for the D174-R208 interaction (Chamberlin et al., 2014), suggesting that D174-R205 may be a longer range interaction. Consistently, when the O-N cutoff distances in the VMD Salt Bridges plugin are increased to 10 Å, D174-R205 are shown to engage in a longer-range electrostatic interaction with an average roughly around 6.5 Å over the last 50 ns of MD (data not shown). Until about 110 ns E171 forms a weak but stable salt bridge with R208, but after 110 ns this interaction starts fluctuating rapidly between a strong and weak salt bridge ([Figure 4.12A](#)). Interactions involving E171 have not been investigated experimentally and therefore cannot be compared to experiments.

The ICEN has been proposed as important for stabilizing the resting state of the channel (Ramsey et al., 2010) and, consistent with this idea, almost every single salt bridge detected by the VMD Salt Bridges plugin in the resting state Hv1F WT MD is located in the ICEN ([Figure 4.12](#)). Unfortunately, there is not enough experimental data on the specific interactions in the ICEN to compare the specific interactions to experimental results. Generally speaking, however, the resting state Hv1F WT model shows a strong and stable ICEN, which is consistent with this network helping to stabilize the resting state of the channel.

4.4.2: PROPKA3.1 pK_a Calculations in Resting State Model Hv1F

Interestingly, only one weak electrostatic interaction in the ECEN, between D130 and K131, is present during the course of the Hv1F WT MD ([Figure 4.12D](#)). In fact, the ECEN has no positively charged basic residues located within range to act as countercharges to the several, negatively, charged acidic residues in the region ([Figure 4.1B](#)). Because electrostatic interactions can largely influence the pK_a value of an amino acid residue ([Pace et al., 2009](#)), PROPKA3.1

pK_a calculations were carried out on every time step (every 2 fs) of the Hv1F WT trajectory to investigate the possibility of ECEN residues with pK_a values shifted from the solution value. Similar to what was seen in the Hv1J PROPKA3.1 calculations, most of the acidic residues have pK_a values much higher than would be expected and many basic residues have pK_a values that are somewhat lower than expected ([Figure 4.13](#); [Table 4.2](#)). A few residues, with a large range of pK_a fluctuations and no outliers, such as E119, stand out and may prove to be interesting candidates for ΔpH-dependent gating experiments, however not much else can be gleaned from the average pK_a values calculated by PROPKA3.1. In order to further narrow down experimental candidates, a covariance analysis was performed on the Hv1F pK_a data to investigate the possibility that some residues have pK_a values that are coupled.

4.4.3: Hv1F pK_a Covariance

The pK_a covariance analysis of Hv1F showed that, of all residue-residue pairs, that with the highest degree of covariance is the pK_a of residue E119 and D185 ([Figure 4.14](#)). E119 and D185 are also predicted by PROPKA3.1 to be important coupling partners (data not shown), suggesting that covariance between residue pK_a values is indicative of pK_a coupling. Interestingly, E119A and D185A were two of the single mutants tested that have a ΔpH-dependent gating different from WT ([Table 1.2](#); Ramsey et al., 2010). As has been mentioned, electrostatic interactions can affect pK_a values of residues in protein environments ([Pace et al., 2009](#)), but there are no basic residues in the vicinity of E119 or D185 to form salt bridges. Repulsive electrostatic interactions can also shift pK_a values and so the distance between E119 and D185 terminal oxygen atoms was measured to assess the possibility of E119-D185 interactions.

Consistent with the preliminary GIA results suggesting an interaction between E119 and D185 ([Table 1.1](#)), the distance between the terminal oxygen atoms of E119 and D185 are quite close together throughout the Hv1F WT trajectory, during the last 40 ns of which the terminal oxygen atoms are within distance for strong Coulombic interactions ([Figure 4.15A](#)). The stable proximity of the partially negative oxygen atoms of E119 and D185 in the MD simulation is surprising. Shortly before the E119 and D185 distance shortens, a Zn^{2+} ion spontaneously diffuses into the Zn^{2+} binding site from bulk solution ([Supplementary Figure 1A](#)). The presence of the Zn^{2+} in the ECEN provides a countercharge for both E119 and D185 and helps keep the terminal oxygen atoms of these two residues close together. The coordinates of the Zn^{2+} ion are not input into PROPKA3.1 calculations and the pK_a predictions are blind to the presence of Zn^{2+} in the ECEN ([Supplementary Figure 1B-D](#)) and therefore are still useful in exploring how E119-D185 distance influences the pK_a values of these residues.

The PROPKA3.1 calculations on Hv1F revealed that both E119 and D185 pK_a values are shifted substantially upward relative to solution values ([Figure 4.13](#); [Table 4.2](#)). The pK_a distribution for both E119 and D185 exhibit a bimodal pattern with the peaks for E119 occurring around 9 and 12 and the peaks for D185 occurring around 7 and 8 ([Figure 4.15B](#)). All of the values are significant upward shifts from the solution values of 4.5 for E119 and 3.8 for D185 (Olsson et al., 2011). A time series plot of the E119 and D185 pK_a value reveals that the pK_a values of residues in protein environments are not static, they are in fact highly dynamic ([Figure 4.15C](#)), somewhat contrary to how residue pK_a values are typically viewed. Furthermore, the time series plot reveals that at about 110 ns, the time when the E119-D185 distance shortens and a repulsive E119-D185 Coulombic interaction forms ([Figure 4.15A](#)), the pK_a of both E119 and D185 shift away from one another, and become coupled to each other, fluctuating

simultaneously in time ([Figure 4.15C](#)). The pK_a of E119 and D185 are quite similar, around a value of 8, from 60 ns to 110 ns, after which E119 shifts to a pK_a of about 12 and D185 shifts to that of about 7 ([Figure 4.15C](#)), which is consistent with the peaks observed in the pK_a distributions of both E119 and D185. Additionally, a linear regression analysis demonstrates a strong and negative correlation ($r^2 = -0.9$) between the pK_a value of E119 and the E119-D185 terminal oxygen atom distance ([Figure 4.15D](#)). This analysis argues that the distance between E119 and D185 strongly influences the pK_a of the residues, but it is merely correlational and needs further supporting evidence.

4.4.4: Electrostatic Interactions and pK_a Dynamics

Unlike in the Hv1F model, E119 and D185 have countercharges that they interact with during the course of MD in the Hv1J model. If, as was suggested for the Hv1F analysis, E119 and D185 have shifted and coupled pK_a values because of their close proximity and lack of countercharges, then the E119 and D185 pK_a shifts should not be present in the Hv1J model because these residues indeed have countercharges. A comparison of E119 pK_a values in resting state model Hv1F vs. activated state model Hv1J revealed that, as expected, in Hv1J, the pK_a of E119 is shifted down significantly to take on the typical solution value of 4.5 for a glutamate, demonstrating that electrostatic interactions are important in modulating the pK_a value of E119 ([Figure 4.16A](#)).

An overlay of the E119 pK_a time series with the E119-R208 salt bridge distance shows that stability of the E119-R208 salt bridge is associated with the E119 pK_a fluctuating stably around a typical glutamate solution pK_a value ([Figure 4.16B](#)). Interestingly, during the last 20 ns of simulation, the E119-R208 distance slightly increases and, simultaneously, the E119 pK_a

shifts up slightly to about 5.5 ([Figure 4.16B](#)), which seems to account for the small peak around 5.5 in the E119 pK_a distribution ([Figure 4.16A](#)). The association of a strong electrostatic interaction involving E119 and the absence of dramatic E119 pK_a shifts is consistent with the previously proposed idea that the lack of countercharges in the ECEN in the Hv1F model contributes to the large pK_a shifts of both E119 and D185. The presence of the S4 gating charge arginine residues in the ECEN in the Hv1J model also breaks the coupling between E119 and D185 ([Figure 4.16C-D](#)). This analysis shows that, as has been previously considered, the movement of S4 between ICEN and ECEN during the gating process can cause shifts in residue pK_a values.

Curiously, the pK_a value for D185 shifts to 7 in the Hv1J MD, about the same value as was found for D185 after it started interacting with E119 for Hv1F ([Figure 4.17A](#)). The terminal oxygen atoms of D185, in fact, seem to have a rather robust interaction with the nitrogen atoms of W207 ([Figure 4.17B](#)), which is shielding D185 from engaging in interactions with the positively charged S4 arginine residues ([Figure 4.17C](#)). D185 shielding by W207 prevents the strong electrostatic interactions with Arg countercharges necessary to maintain solution pK_a values for D185 and is associated with the robust shift in the D185 pK_a value in Hv1J, similar to the case in Hv1F. This data further supports the idea that the lack of countercharges for E119 and D185 in the Hv1F model contributes to the shifted pK_a values of these residues.

Because pK_a values are crucial to titration chemistry, which is thought to be a core process in Hv1 ΔpH-dependent gating, all this data taken together suggests that E119 and D185 contribute to the ΔpH-dependent gating in Hv1. Indeed, t-tests run on early mutagenesis experiments showed that E119A and D185A single mutants both have slightly altered ΔpH-dependent gating relative to WT ([Table 1.2](#)), suggesting that indeed these two residues have an

important role in play in Δ pH-dependent gating in Hv1. There are other acidic residues (D123 and D130; [Figure 4.1](#)) in the vicinity of E119 and D185 in the ECEN that could engage in compensatory interactions in the absence of E119 or D185, and these compensatory interactions could potentially account for the small differences in Δ pH-dependent gating between WT and E119A or D185A single mutants. It is possible that an interaction between E119 and D185 is necessary for Δ pH-dependent gating in Hv1 and it therefore may be necessary to mutate both E119 and D185 to elicit a more robust perturbation in Hv1 Δ pH-dependent gating.

Explicit electrostatic interactions between residues influencing Δ pH-dependent gating was only first hinted at when H168 was identified as a IC pH sensor, and so the idea that two residues may interact to form a pH sensing unit remains relatively novel and untested. The PROPKA3.1 analysis presented here was successful at identifying H168 as a IC pH sensor and, in hopes of identifying EC pH sensors in Hv1, we performed voltage clamp experiments on E119A and D185A mutants. As these experiments were designed based on the results of the PROPKA3.1 covariance analysis, the voltage clamp experiments will also help to establish this analytic method as a valuable tool in understanding Δ pH-dependent gating mechanisms in Hv1.

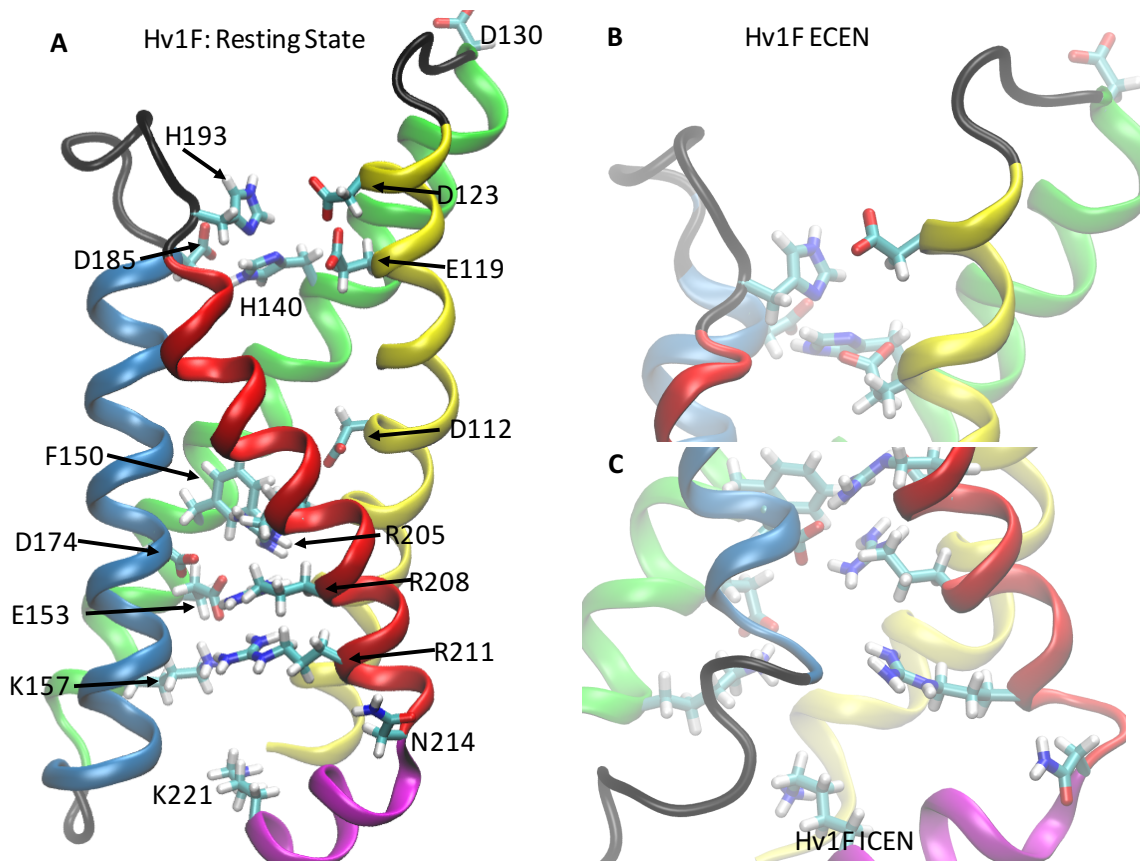


Figure 4.1: Overview of Resting State Model Hv1F.

A: Overview of full resting state Hv1F VSD structure with relevant residues indicated. The coordinates are the final output coordinates from Modeller9.16 after hydrogens were added using VMD1.9.2 AutoPSF plugin and were used as the initial coordinates for MD. The S1 helix (residues 97-125), S2 helix (residues 130-160), S3 helix (residues 170-187), S4 helix (residues 195-214), and S4-CC linker helix (residues 215-225) are represented in yellow, green, blue, red, and magenta, respectively. The extracellular (EC) side is at the top and the intracellular side (IC) is at the bottom.

B: Magnified view of the ECEN from the same coordinates and coloring scheme as shown in (A).

C: Magnified view of the ICEN from the same coordinates and coloring scheme as shown in (A) and (B).

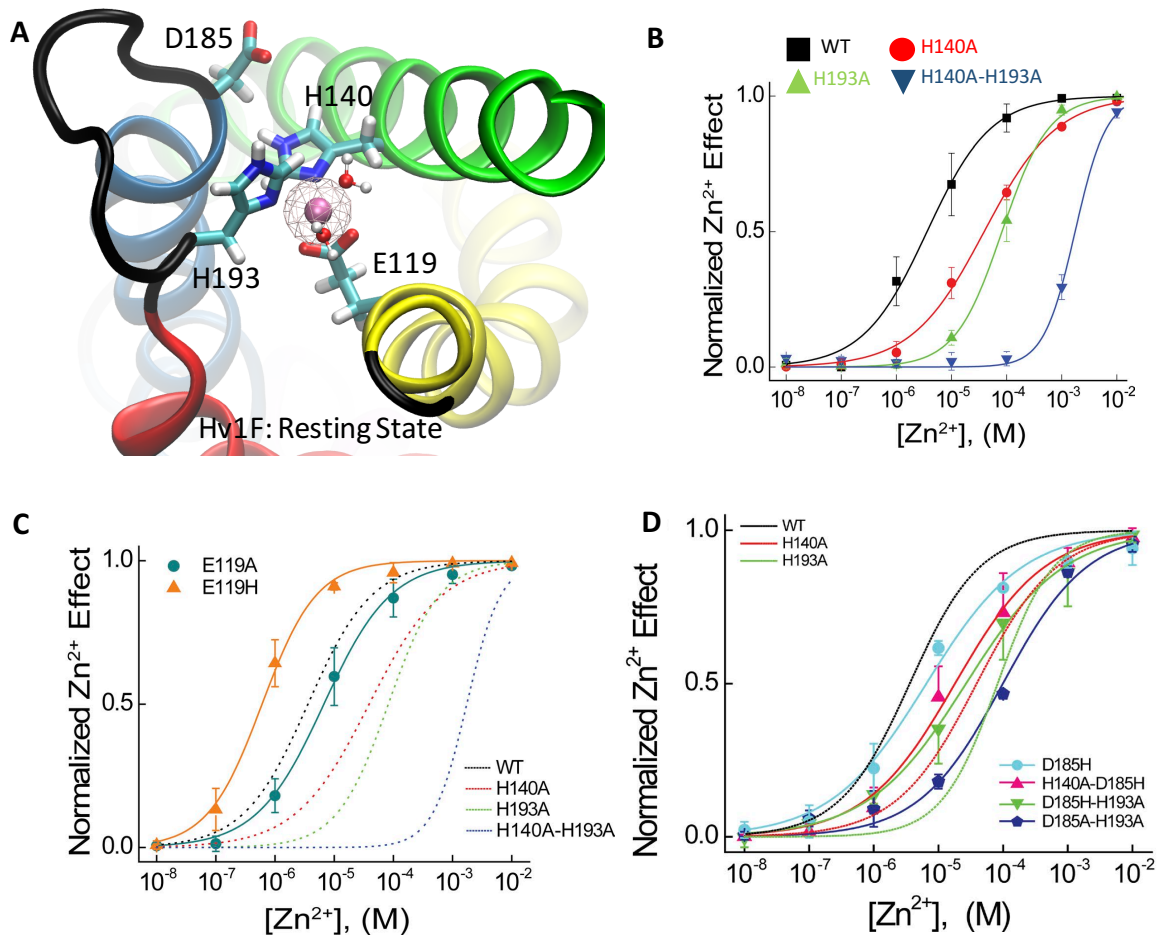


Figure 4.2: Hv1F Model Accommodates the Zn^{2+} -Binding Site in ECEN

A: Same coordinates and coloring scheme of the Hv1F model as shown in [Figure 4.1](#). In the Hv1F model, H140, H193, and E119 form the Zn^{2+} binding site in the ECEN and directly coordinate Zn^{2+} , as indicated by the voltage clamp data (B-C). D185 is capable of coordinating Zn^{2+} when H140 and/or H193 is mutated (D).

B: The Zn^{2+} dose response for Hv1 WT (black squares), H140A (red circles), H193A (green triangles), and H140A-H193A (navy triangles). H140 and H193 are both major contributors to the Zn^{2+} binding site. Figure reprinted from De La Rosa et al., 2018.

C: The Zn^{2+} dose response for Hv1 WT (black dotted line), E119A (teal circles), and E119H (orange triangles). H140A, H193A, and H140A-H193A are also plotted for comparison in red, green, and navy dotted lines, respectively. E119 appears to be a contributor to the Hv1 Zn^{2+} binding site. Figure reprinted from De La Rosa et al., 2018.

D: The Zn^{2+} dose response in Hv1 WT (black dotted line), D185H (light blue circles), and H140A-D185H (magenta triangles), D185H-H193A (green triangles), and D185A-H193A (navy pentagons). H140A and H193A are also plotted for comparison in red and green dotted lines, respectively. D185 appears to be a contributor to the Hv1 Zn^{2+} binding site. Figure reprinted from De La Rosa et al., 2018.

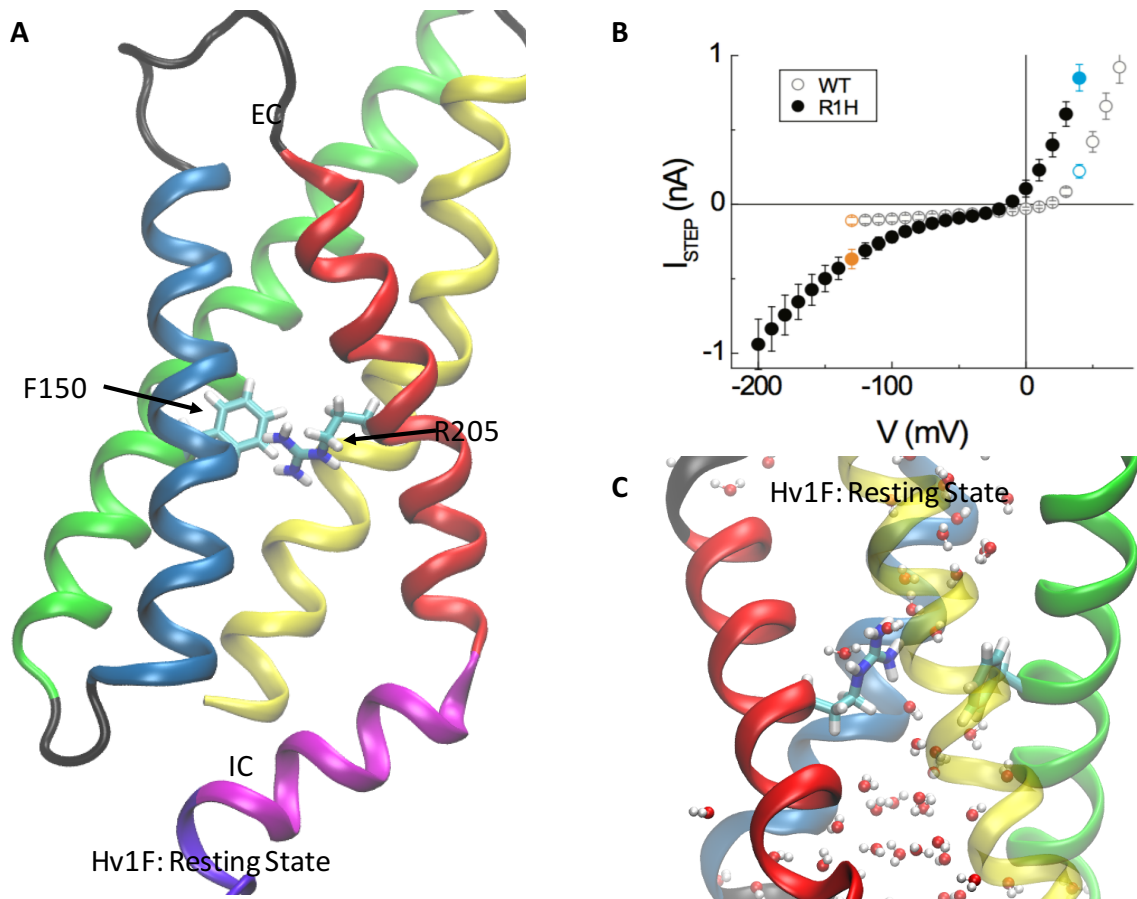


Figure 4.3: The Hv1F Model has the Proper Register of S4

A: Same coordinates and coloring scheme of the Hv1F model as depicted in [Figure 4.1](#) with F150 and R205 indicated. The relative positions of F150 and R205 are consistent with the closed state H^+ conductance in the Hv1-R205H mutant (Randolph et al., 2016).

B: The step current (I_{step}) in Hv1 WT (open circles) and Hv1 R205H (closed circles). The R205H mutation introduces a closed-state, inward H^+ conduction that is not exhibited by the WT Hv1 channel. This data suggests that R205H must be in close proximity to F150 to allow such a short circuit of the closed state. Figure reprinted from (Randolph et al., 2016).

C: At the end of 150 ns of unconstrained MD, R205 has access to both the EC and IC waters, as implied by the experimental data shown in (B; Randolph et al., 2016).

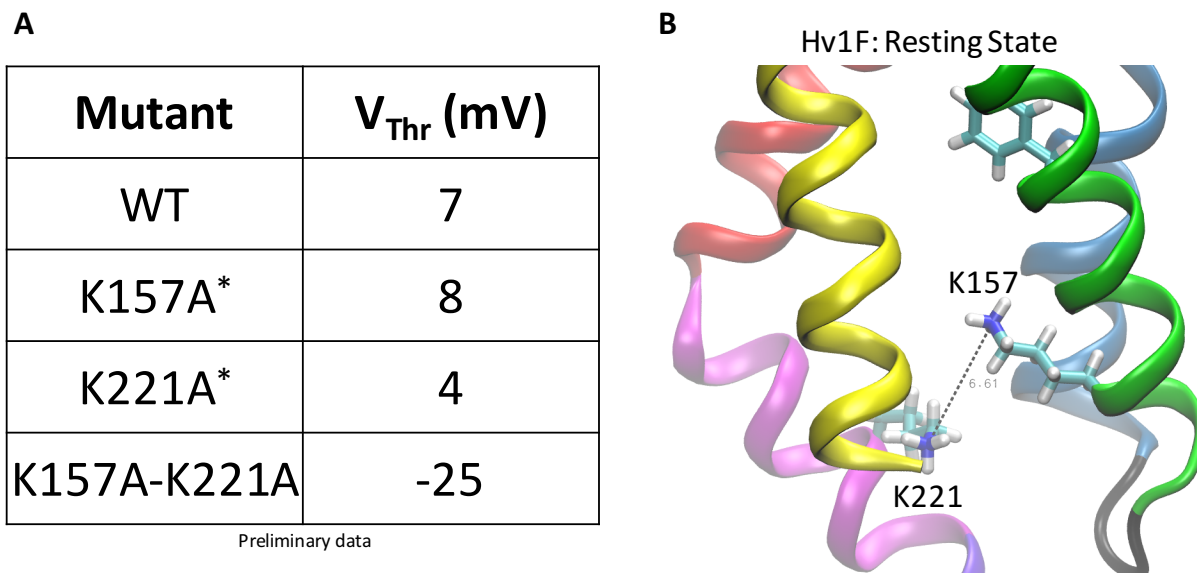


Figure 4.4: The Hv1F Model Accommodates the K157-K221 Interaction.

A: Table showing that even though the K157A and K221A single mutants do not alter voltage-dependent gating relative to WT Hv1, the K157A-K221A double mutant did. This result indicates that there is some kind of interaction between these two residues that contributes to voltage-dependent gating. When GIA is applied to this data set, the value for K157-K221 is -3.7 kcal/mol. The asterisks indicate that in the old activated state model, Hv1B (Ramsey et al., 2010), the PROPKA3.1-predicted pK_a of these two residues are coupled to each other, as well as other residues.

B: The Hv1F model includes a weak K157-K221 interaction (distance = 6.61 Å), consistent with the voltage clamp data. The coordinates and coloring schemes are the same as those depicted in [Figures 4.1-4.3](#).

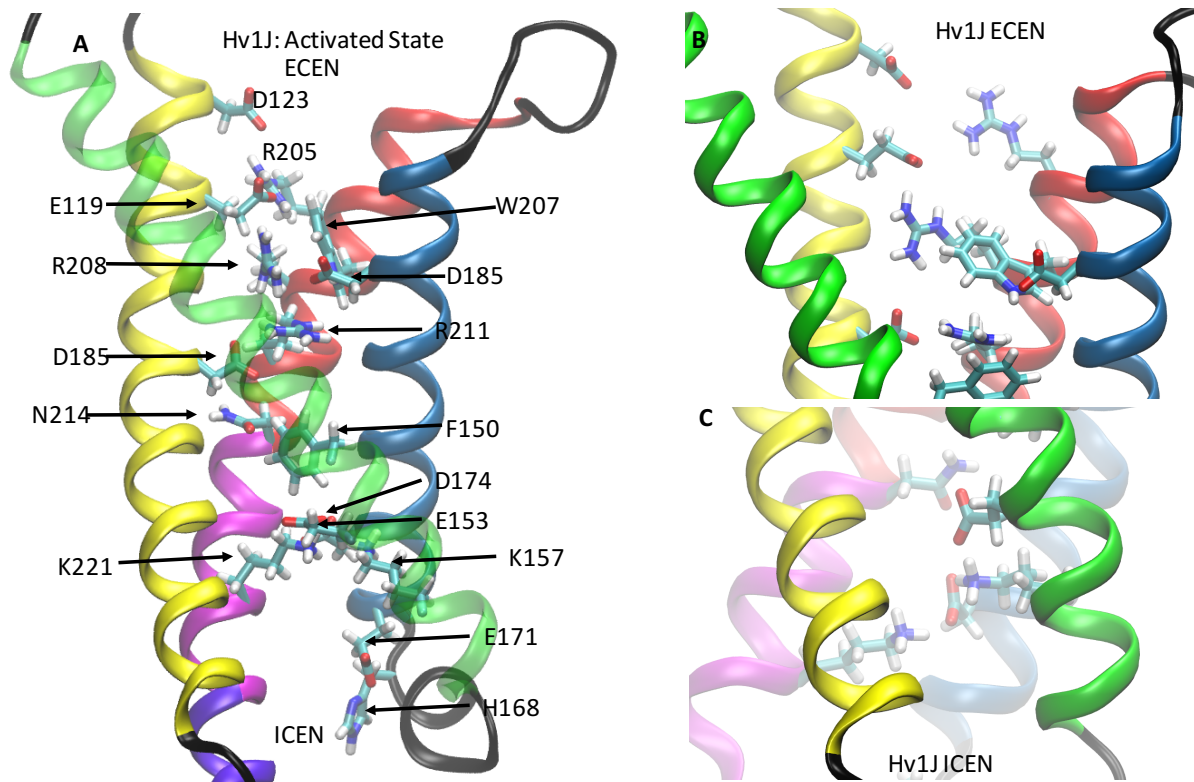


Figure 4.5: Overview of Activated State Model Hv1J

A: Overview of full Hv1J VSD structure with relevant residues indicated in licorice. The coordinates are the final output coordinates from Modeller9.16 after hydrogens were added using VMD1.9.3 AutoPSF plugin and were used as the initial coordinates for MD. The S1 helix (residues 97-125), S2 helix (residues 131-161), S3 helix (residues 170-190), S4 helix (residues 200-214), S4-CC linker helix (residues 215-225), and the CC domain are represented in yellow, green transparent, blue, red, magenta, and purple, respectively.

B: Magnified view of the ECEN from the same coordinates and coloring schemes as in (A).

C: Magnified view of the ICEN from the same coordinates and coloring schemes as in (A) and (B).

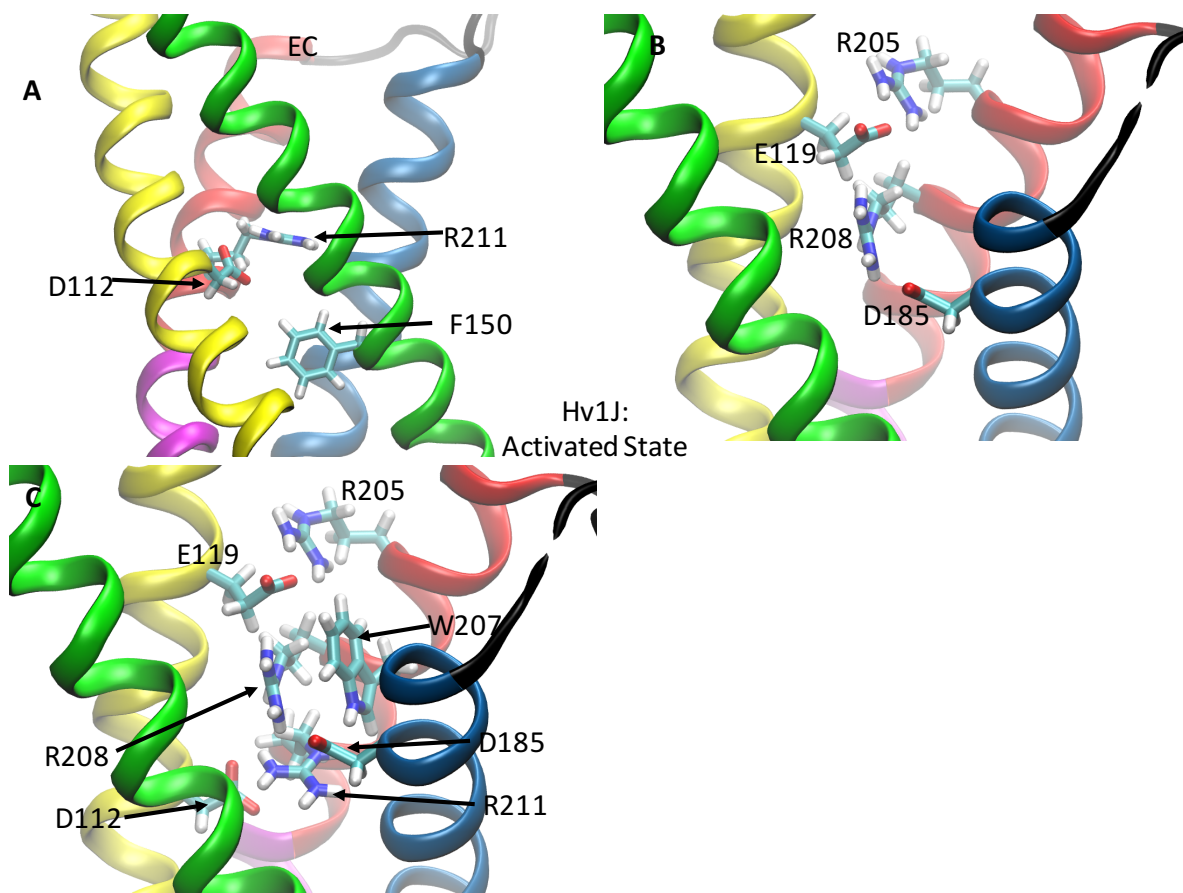


Figure 4.6: The Hv1J Model is Consistent with Published Experimental Data

A: A D112-R211 salt bridge is present on EC side of F150 in the Hv1J model, consistent with the voltage clamp data demonstrating this interaction pair serving as the selectivity filter in Hv1 (Berger and Isacoff, 2011). Same coordinates and coloring scheme as used in [Figure 4.5](#).

B: Zoomed in view of the ECEN from the same coordinates and coloring schemes as in (A). As indicated by mutant cycle analysis data, E119 forms a salt bridge with both R205 and R208 while D185 forms a salt bridge with R208 ([Table 1.1](#); Chamberlin et al., 2014).

C: Zoomed in view of the ECEN from the same coordinates and coloring schemes as in (A) and (B). Hv1J includes W207 in the ECEN as implied by the altered EC pH sensitivity of W207X mutants (Cherny et al., 2015).

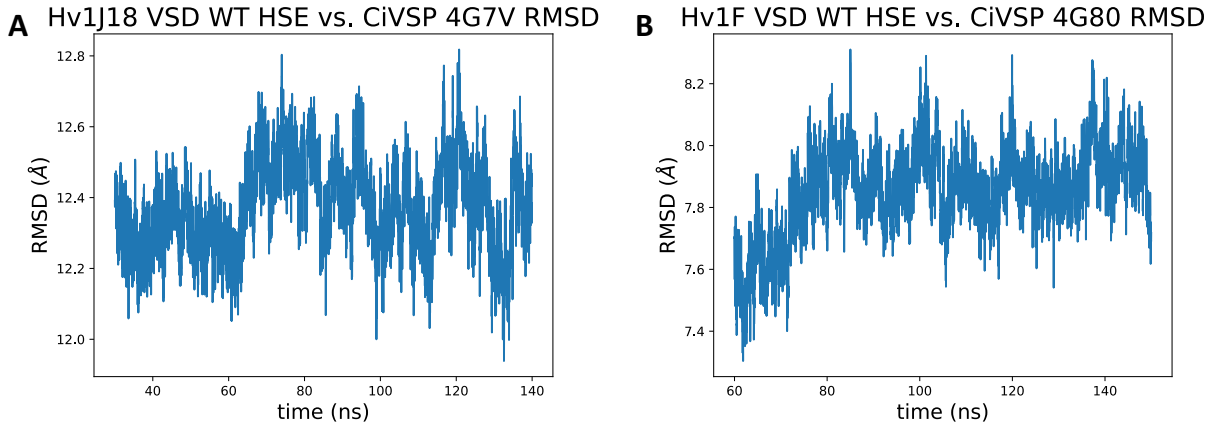


Figure 4.7: Hv1F and Hv1J models are Stable in the MD Environment.

A: The Hv1J model was truncated after residue 230 and the resulting Hv1J VSD model was subjected to 140 ns of MD. Uncertainty analysis suggests that the Hv1J WT system reaches equilibrium by 30 ns, which is confirmed by the stabilization of the RMSD vs. the open state crystal structure of *Ci*-VSP (Li et al., 2014). 30-140 ns is the time range used for analysis of the Hv1J MD trajectory.

B: The Hv1F model was truncated after residue 230 and the resulting Hv1F VSD model was subjected to 150 ns of MD. Uncertainty analysis suggests that the Hv1F WT system reaches equilibrium by 60 ns, which is confirmed by the stabilization of the RMSD vs. the closed-state crystal structure of *Ci*-VSP (Li et al., 2014). 60-150 ns is the time range used for analysis of the Hv1F MD trajectory.

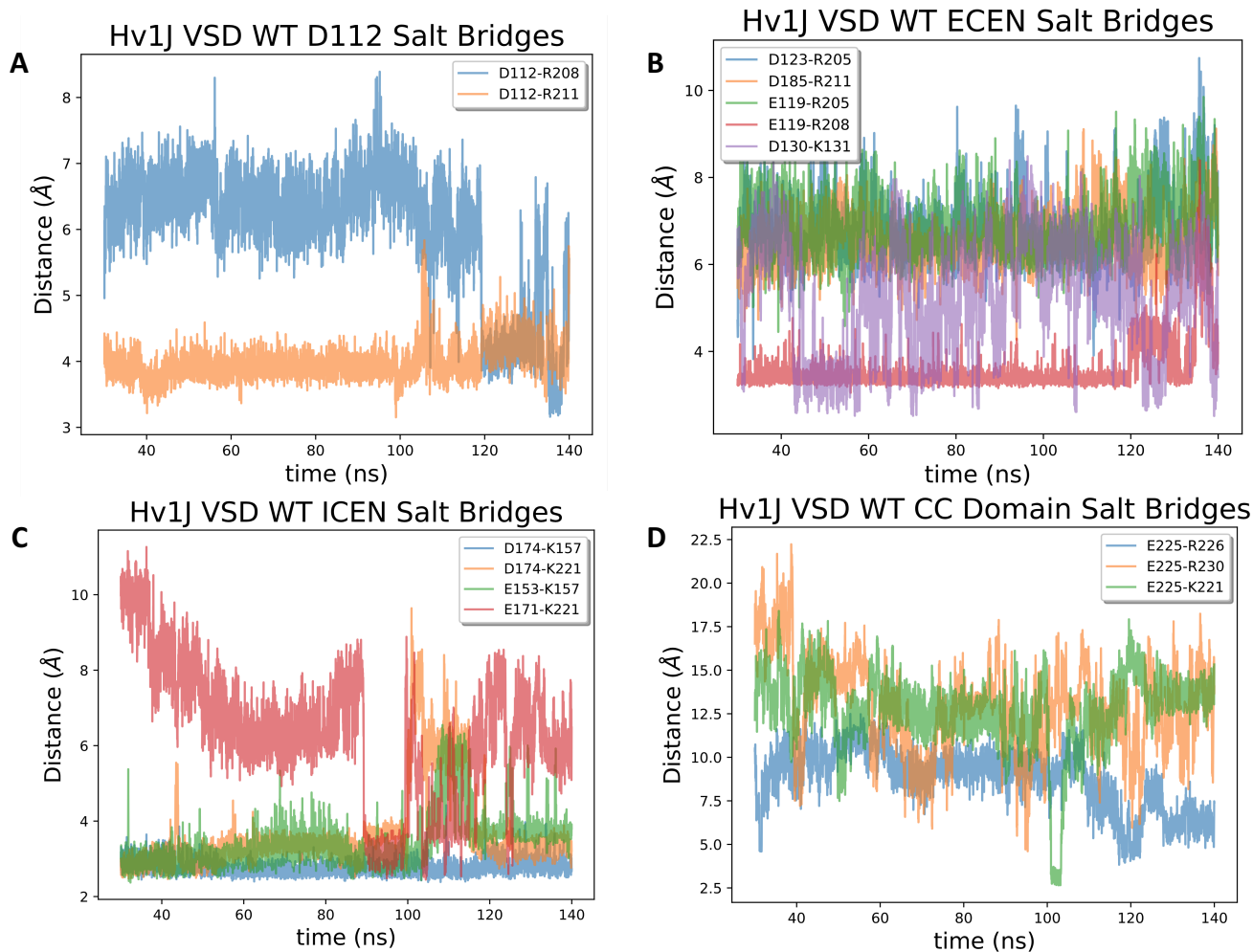


Figure 4.8: Salt Bridges in Hv1J

Salt bridges were calculated using VMD1.9.3 or VMD1.9.4 Salt Bridges plugin with default settings every 2 fs. Both the ECEN and ICEN have multiple salt bridges.

A: Salt bridges formed with the D112 are shown. D112-R208 (blue) make a stable but weak salt bridge until the last 20 ns, for which D112-R208 form a strong salt bridge. D112-R211 (orange) make a strong and stable salt bridge.

B: Salt bridges formed in the ECEN during the Hv1J WT simulation. D123-R205 (blue), D185-R211 (orange), and E119-R205 (green) all form weak salt bridges for the duration of the trajectory. E119-R208 (red) forms a strong and stable salt bridge during the course of the simulation. D130-K131 (purple) forms a highly dynamic salt bridge, fluctuating between strong and weak

C: Salt bridges formed in the ICEN during the Hv1J WT MD simulation. D174-K157 (blue), D1740-K221 (orange), and E153-K157 (green) make strong stable salt bridges throughout the simulation with the exception of a 20 ns period where they relax to weak salt bridges, only to return back to strong salt bridges. E171-K221 (red) forms a stable but weak salt bridge, and for a brief, approximately 10 ns period (90 ns-100 ns), forms a strong salt bridge.

D: Salt bridges formed in the CC domain during Hv1J WT MD simulations. E225-R226 (blue), E225-R230 (orange), and E225-K221 (green) all form very weak interactions that would best be classified as long range electrostatic interactions. While these interactions are weak, they are also stable throughout the course of the trajectory.

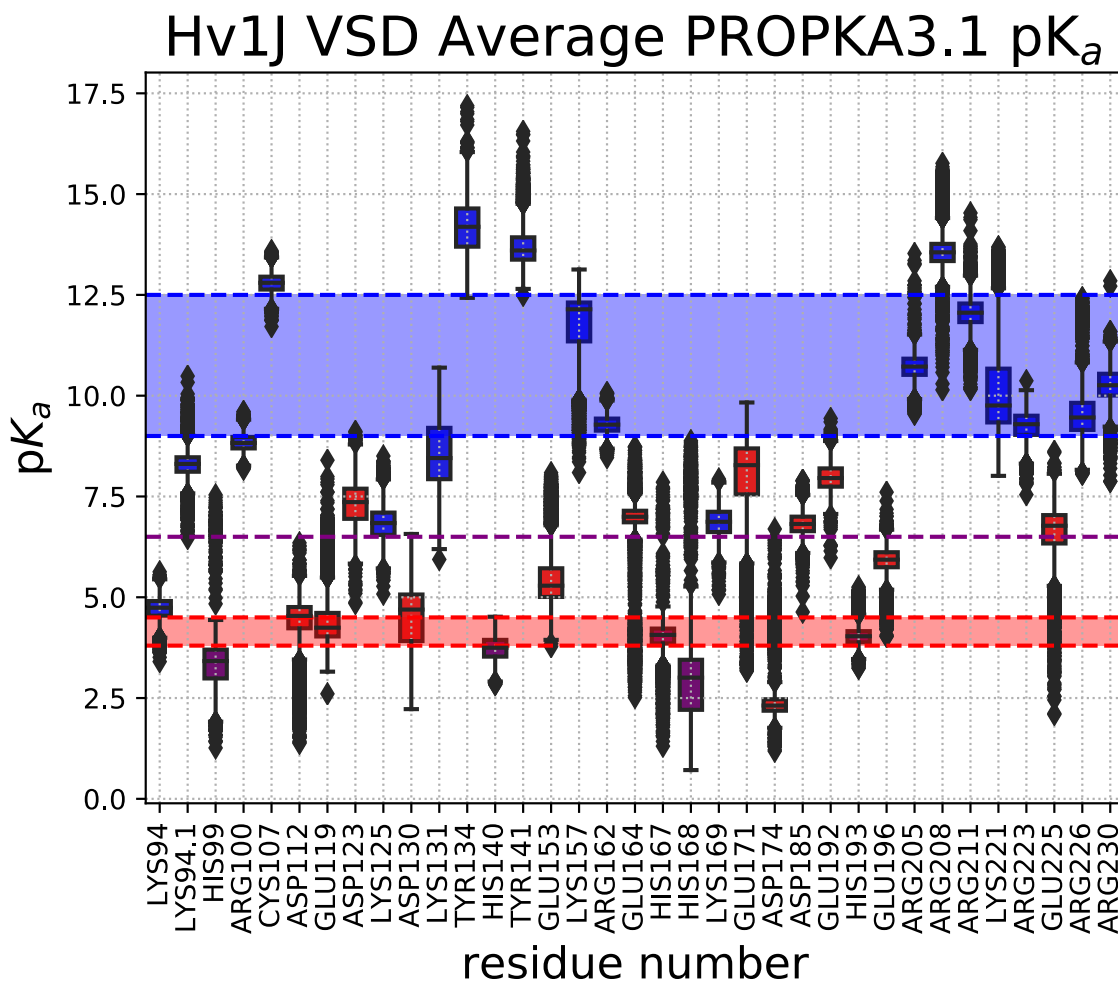


Figure 4.9: PROPKA3.1 pK_a Predictions in Hv1J WT MD

PROPKA3.1 analysis was performed every 2 fs from 30 ns to 150 ns. The median pK_a predicted, with the first and third quartiles as calculated by sns.boxplot (<https://seaborn.pydata.org/generated/seaborn.boxplot.html>), is presented as a colored rectangle for each residue. Red bars are acidic residues and the expected pK_a values for these residues fall in the shaded red region. Blue bars are basic residues and the expected pK_a values for these residues fall within the shaded blue region. Histidine residues are shown as purple bars, and the expected pK_a for histidine is indicated by the dashed purple line. The whiskers of each boxplot represent the range of the calculated pK_a values, excluding outliers, which are represented as diamond points.

Table 4.1: PROPKA3.1 Average pK_a in Hv1J MD Systems

PROPKA3.1 analysis was performed on every frame (2 fs time steps) of the Hv1J WT and mutant MD trajectories from 30 ns to end of the trajectory (see [CHAPTER 3.1.3](#)). The mean PROPKA3.1-calculated pK_a for each residue is listed. The solution pK_a is the expected pK_a for the residue in aqueous solution and is taken from the model value used in PROPKA3.1 calculations (Olsson et al., 2011).

Table 4.1: PROPKA3.1 Average pK_a for Hv1J MD Systems					
Residue	WT pK _a	E119A pK _a	D185A pK _a	E119A-D185A pK _a	Solution pK _a *
ARG100	8.84	9.35	9.46	9.29	12.5
ARG162	9.28	8.80	11.95	15.32	12.5
ARG205	10.71	9.29	10.90	8.81	12.5
ARG208	13.58	9.46	13.96	11.74	12.5
ARG211	12.05	14.38	10.81	11.77	12.5
ARG223	9.24	10.51	10.10	8.57	12.5
ARG226	9.56	10.71	11.23	9.89	12.5
ARG230	10.27	10.61	10.97	10.97	12.5
ASP112	4.30	4.91	1.76	4.97	3.8
ASP123	7.34	7.34	6.65	5.15	3.8
ASP130	4.47	5.51	5.45	5.87	3.8
ASP174	2.58	3.07	2.29	3.37	3.8
ASP185	6.82	4.97	N/A	N/A	3.8
CYS107	12.79	12.80	12.77	12.65	9
GLU119	4.42	N/A	6.69	N/A	4.5
GLU153	5.46	5.19	6.02	5.24	4.5
GLU164	6.77	5.98	3.72	4.42	4.5
GLU171	7.79	7.02	3.90	4.48	4.5
GLU192	7.98	7.46	7.63	7.49	4.5
GLU196	5.91	6.79	6.34	6.99	4.5
GLU225	6.59	7.23	4.56	6.26	4.5
HIS140	3.73	3.68	3.62	2.91	6.5
HIS167	4.00	4.45	3.62	4.07	6.5
HIS168	3.17	2.21	3.33	3.47	6.5
HIS193	4.03	3.67	3.57	3.51	6.5
HIS99	3.36	2.51	2.43	2.88	6.5
LYS125	6.83	7.26	8.03	7.18	10.5
LYS131	8.57	9.24	8.66	8.21	10.5
LYS157	11.78	10.84	12.26	11.41	10.5
LYS169	6.86	6.95	7.38	6.83	10.5
LYS221	10.23	9.92	11.16	9.67	10.5
LYS94	4.71	5.75	4.72	5.25	10.5
LYS94	8.29	7.77	9.07	8.04	10.5
TYR134	14.18	13.43	13.18	13.62	10
TYR141	13.71	13.82	13.55	13.66	10

Hv1J VSD WT PROPKA3.1 pK_a Covariance

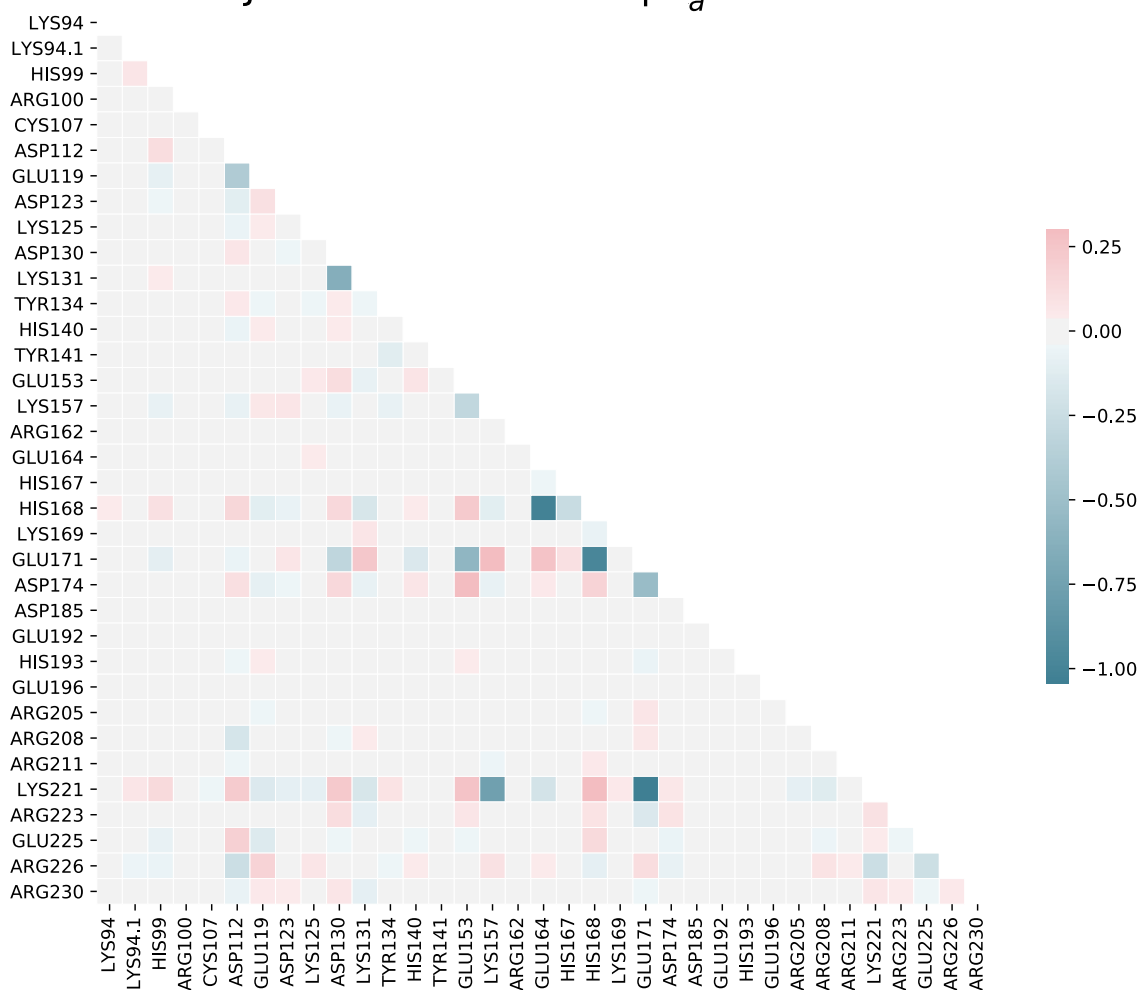


Figure 4.10: pK_a Covariance in Hv1J WT MD

Covariance results are plotted as a heat map for easier visualization of residues with larger covariance values. As indicated by the legend on the right, the more saturated the color, the larger the covariance, with pink residue pairs having positive covariance and blue residue pairs having negative covariance. A mask is applied so that the self-covariance and duplicate covariance values are not depicted.

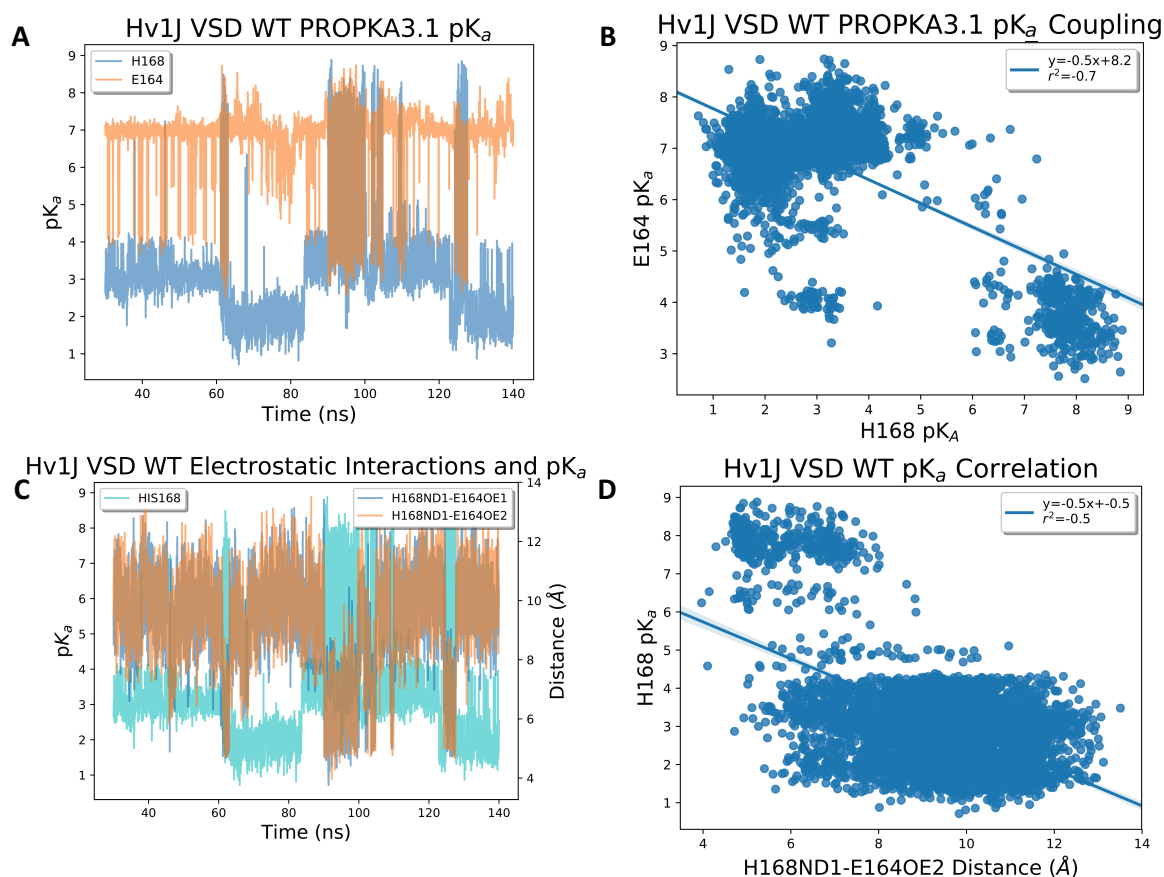


Figure 4.11: H168 pK_a and E164 pK_a Coupling in Hv1J WT MD

A: The time series overlay of H168 pK_a (blue) and E171 pK_a (orange). The fluctuations in H168 pK_a are mirrored by the fluctuations in E164 pK_a, demonstrating that the PROPKA3.1 covariance analysis identifies residues with coupled pK_a values.

B: A linear regression analysis between H168 pK_a and E164 pK_a reveals that the two are moderately correlated with one another ($y = 0.5x + 8.2$; $r^2 = -0.7$).

C: Time series overlay of H168 pK_a (cyan; left y-axis) and H168 Nδ to E164 terminal oxygen distances (blue and orange; right y-axis). When H168 and E164 become closer, the pK_a of H168 is shifted higher.

D: A linear regression analysis between H168 pK_a and H168-E164 distance shows a moderate correlation between H168-E164 distance and H168 pK_a ($y = 0.5x + 0.5$; $r^2 = -0.5$). The grey circle highlights a population of points that show that H168 only has a high pK_a when the H168Nδ-E164OE2 distance is relatively short ($< 8 \text{ \AA}$).

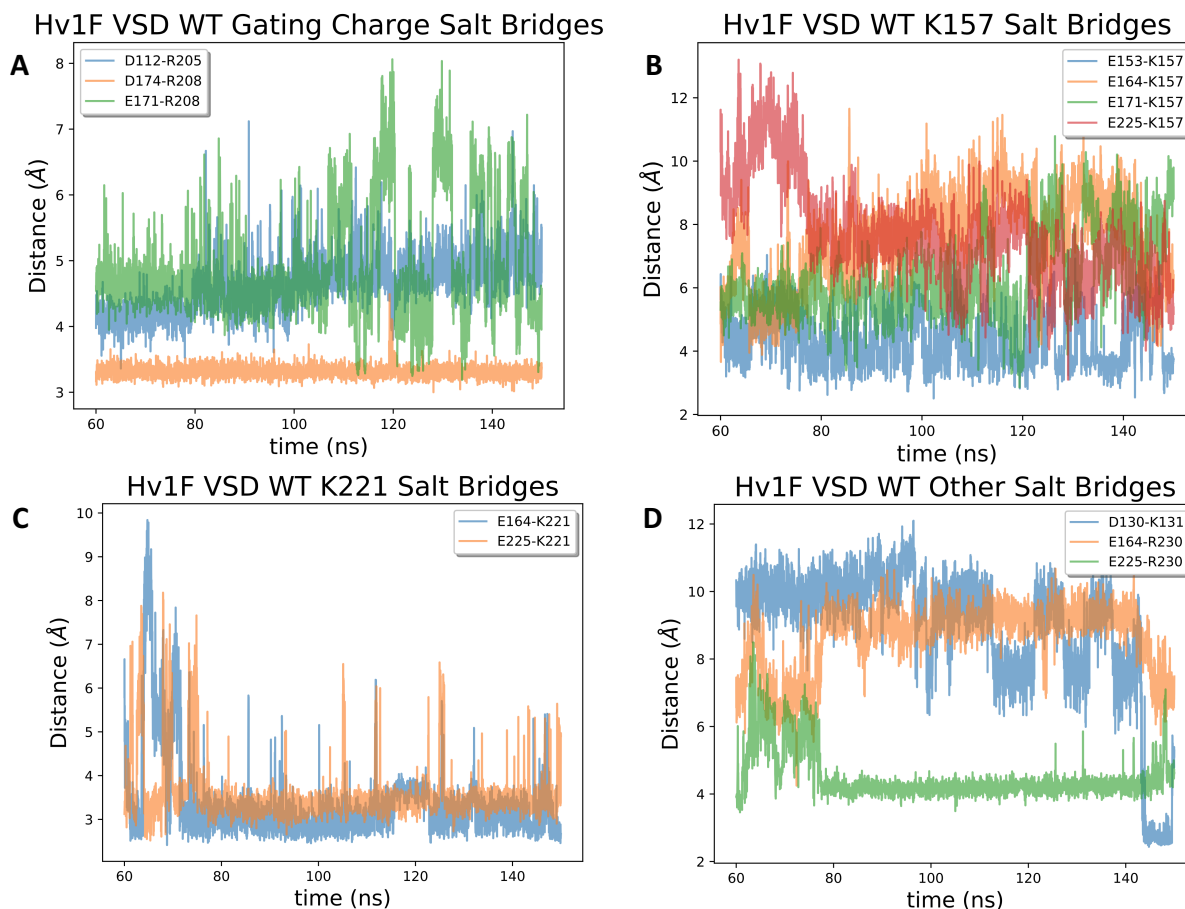


Figure 4.12: Salt Bridges in Hv1F WT MD

Salt bridges were calculated every 2 fs using VMD1.9.3 or VMD1.9.4 Salt Bridges plugin with default settings. There are no salt bridges in the ECEN in Hv1F WT MD.

A: Salt bridges formed with the S4 arginine residues are shown. R205 makes a stable but weak salt bridge with D112 (blue). R208 makes a strong and stable salt bridge with D174 (orange) and forms a weaker interaction with E171 (green), which is highly dynamic and rapidly fluctuates. R211 does not form any strong salt bridges during the course of the Hv1F WT simulation.

B: Salt bridges formed with K157 during the course of Hv1F WT simulations. K157 forms a stable and strong salt bridge with E153 (blue). Weaker and more dynamic interactions are formed between K157 and E164 (orange), E171 (green), and E225 (red).

C: Salt bridges formed with K221 during Hv1F WT MD simulation. K221 forms two strong and stable salt bridges, one with E164 (blue), and the other with E225 (orange).

D: Other salt bridges formed during Hv1F WT MD simulations. D130-K131 only begin to make a salt bridge at the end of the simulation. Likewise, E164 and R230 only seem to engage in long range electrostatic interactions. However, E225 and R230 make a relatively strong and stable salt bridge throughout the Hv1F WT MD simulation.

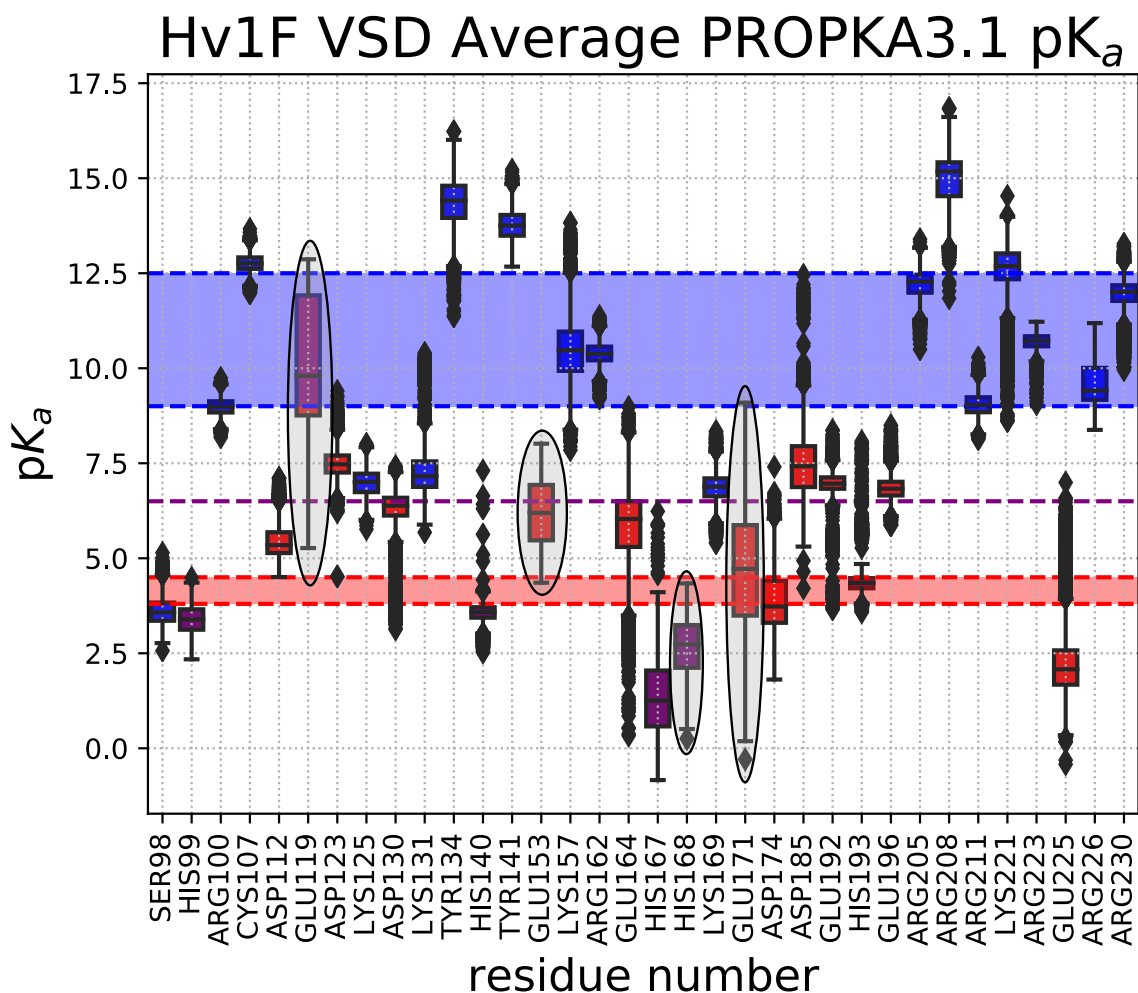


Figure 4.13: PROPKA3.1 pK_a Predictions in Hv1F WT MD

PROPKA3.1 analysis was performed every 2 fs from 60 ns to 150 ns. The median pK_a predicted, with the first and third quartiles as determined by `sns.boxplot` (<https://seaborn.pydata.org/generated/seaborn.boxplot.html>), is presented as a colored rectangle for each residue. Red bars are acidic residues and the expected pK_a values for these residues fall in the shaded red region. Blue bars are basic residues and the expected pK_a values for these residues fall within the shaded blue region. Histidine residues are shown as purple bars, and the expected pK_a for histidine is indicated by the dashed purple line. The whiskers of each boxplot represent the range of the calculated pK_a values, excluding outliers. The outliers are represented as diamond points. Grey circles indicate residues that have a pK_a range of over 2.0 units, with very few or no outliers, during the course of MD.

Table 4.2: PROPKA3.1 Average pK_a in Hv1F MD Systems

PROPKA3.1 analysis was performed every 2 fs from 60 ns to 150 ns. The mean pK_a predicted for each residue is listed. The solution pK_a is the expected pK_a for the residue in aqueous solution and is taken from the model value used in PROPKA3.1 calculations (Olsson et al., 2011).

Table 4.2: PROPKA3.1 Average pK _a for Hv1F MD Systems					
Residue	WT	E119A	D185A	E119A-D185A	Solution pK _a *
ARG100	8.98	9.56	9.33	9.30	12.5
ARG162	10.38	11.04	9.87	10.19	12.5
ARG205	12.19	12.00	11.61	11.05	12.5
ARG208	14.90	16.13	14.99	15.25	12.5
ARG211	9.04	9.39	11.89	9.02	12.5
ARG223	10.69	10.52	10.49	10.48	12.5
ARG226	9.60	10.93	10.91	10.78	12.5
ARG230	11.89	14.32	11.10	10.94	12.5
ASP112	5.45	4.80	4.79	6.90	3.8
ASP123	7.49	7.93	10.05	8.09	3.8
ASP130	6.21	5.94	5.82	6.11	3.8
ASP174	3.88	4.62	2.32	2.64	3.8
ASP185	7.54	6.53	N/A	N/A	3.8
CYS107	12.76	12.88	12.85	12.61	9
GLU119	10.22	N/A	8.83	N/A	4.5
GLU153	6.20	4.07	3.63	6.55	4.5
GLU164	5.79	4.11	4.50	6.15	4.5
GLU171	4.80	5.13	6.36	2.95	4.5
GLU192	6.88	7.09	7.15	7.03	4.5
GLU196	6.85	7.39	7.02	7.41	4.5
GLU225	2.36	4.35	1.00	3.39	4.5
HIS140	3.56	3.54	3.39	3.35	6.5
HIS167	1.33	3.99	3.31	2.71	6.5
HIS168	2.65	2.01	1.42	3.51	6.5
HIS193	4.46	4.36	4.17	3.98	6.5
HIS99	3.39	2.64	2.67	1.79	6.5
LYS125	6.98	7.46	6.94	7.04	10.5
LYS131	7.35	7.84	7.58	7.61	10.5
LYS157	10.43	11.24	10.96	12.59	10.5
LYS169	6.86	6.77	6.99	7.41	10.5
LYS221	12.52	8.71	11.89	9.43	10.5
SER98	3.62	5.24	5.47	4.92	8
TYR134	14.35	13.02	13.85	13.82	10
TYR141	13.78	13.65	13.58	13.68	10

Hv1F VSD WT PROPKA3.1 pK_a Covariance

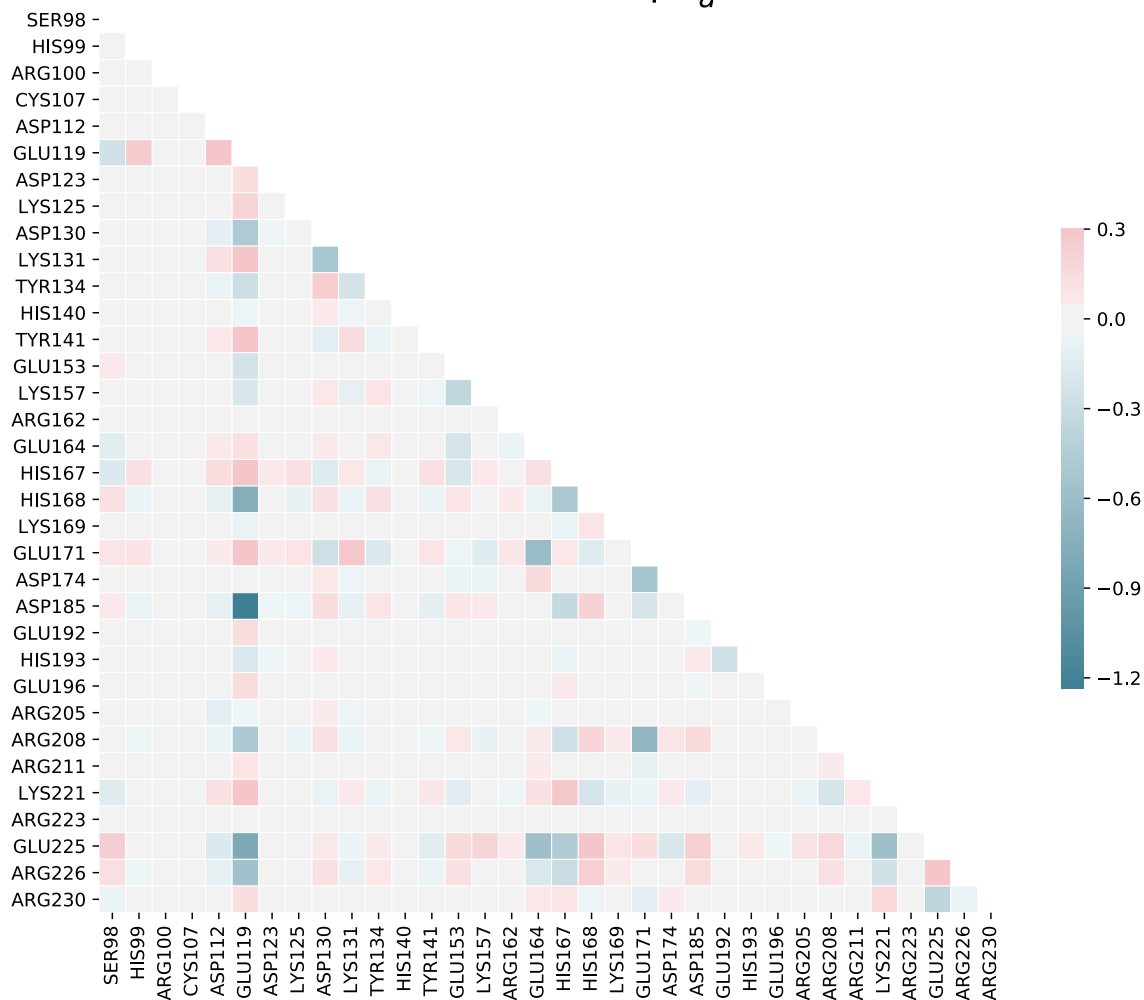


Figure 4.14: pK_a Covariance in Hv1F WT MD

Covariance results are plotted as a heat map for easier visualization of residues with larger covariance values. As indicated by the legend on the right, the more saturated the color, the larger the covariance, with pink residue pairs having positive covariance and blue residue pairs having negative covariance. A mask is applied so that the self-covariance and duplicate covariance values are not depicted.

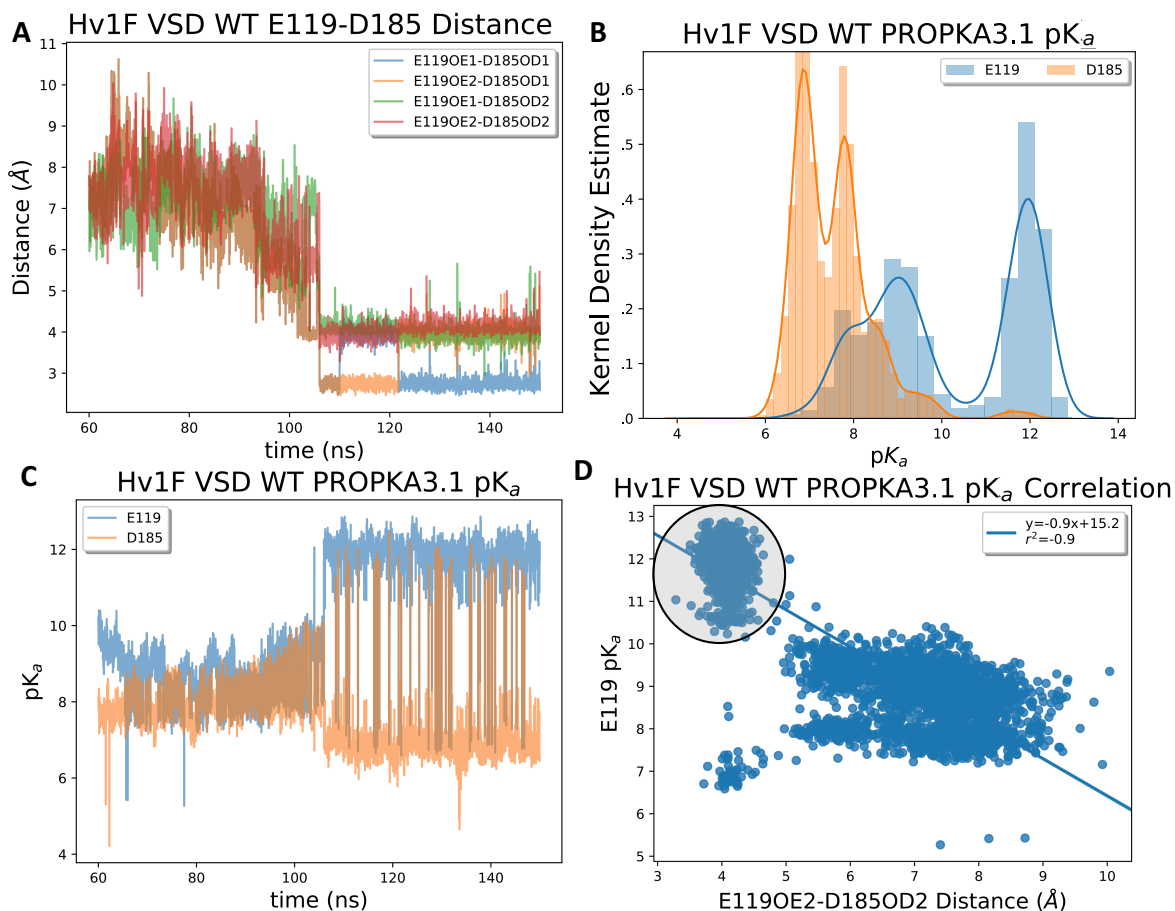


Figure 4.15: E119 and D185 Coupling in Hv1F WT MD

A: The distance between E119OE1-D185OD1 (blue), E119OE2-D185OD1 (orange), E119OE1-D185OD2 (green), and E119OE2-D185OD2 (red) terminal oxygen atoms, during the equilibrium phase of Hv1F WT MD trajectory. Around 110 ns the terminal oxygen atoms come within range to engage in repulsive Coulombic interactions.

B: Histograms of PROPKA3.1 pK_a predictions for indicate that both E119 (blue) and D185 (orange) have pK_a values much higher than the typical solution value for these residues with a bimodal distribution. Histograms were constructed using the Seaborn distplot function in Python (<https://seaborn.pydata.org/generated/seaborn.distplot.html>).

C: The time series of E119 pK_a (blue) and D185 pK_a (orange) reveals coupling between the two, which results in simultaneous pK_a fluctuations.

D: Linear regression performed in using Seaborn (<https://seaborn.pydata.org/generated/seaborn.regplot.html>). There is a strong correlation between E119 pK_a and the E119OE2-D185OD2 distances in Hv1F WT MD ($y = 0.9x + 15.2$; $r^2 = -0.9$). The grey circle highlights a population of points demonstrating that the pK_a of E119 only takes value over 11 when the E119-D185 distance is less than 5 Å.

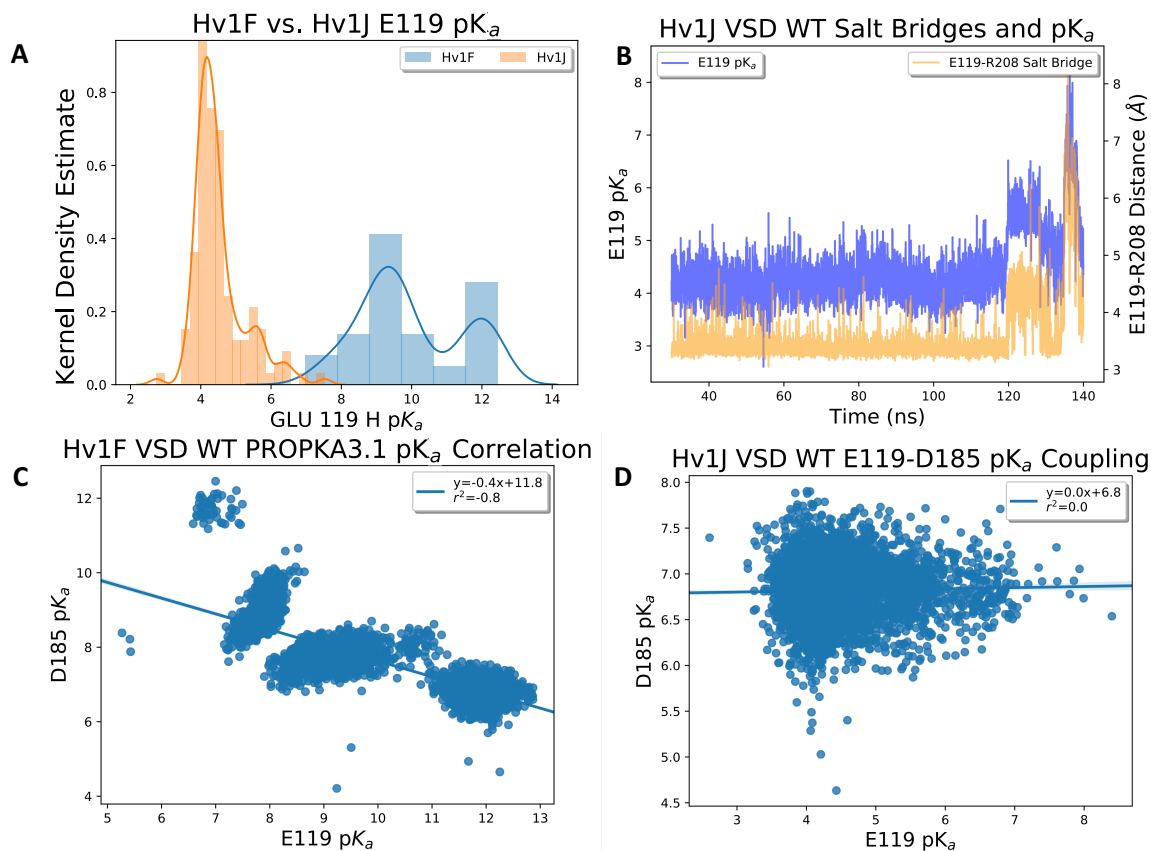


Figure 4.16: E119 pK_a is Largely Influenced by Coulombic Interactions

A: The distribution of pK_a values for E119 during the course of Hv1F WT (blue) and Hv1J WT (orange) MD. Calculations were performed using seaborn distplot (<https://seaborn.pydata.org/generated/seaborn.distplot.html>) and the kernel density estimate is plotted on the y-axis.

B: Overlay of E119 pK_a (violet) and E119-R208 (orange) salt bridge time series made using Pyplot (https://matplotlib.org/api/pyplot_api.html) in Python3.16.

C: Linear regression analysis performed in Python3.6 using Seaborn (<https://seaborn.pydata.org/generated/seaborn.regplot.html>) shows that indeed E119 and D185 pK_a values are strongly correlated in the Hv1F WT MD system ($y = 0.4x + 11.8$; $r^2 = -0.8$).

D: Linear regression analysis performed in Python3.6 using Seaborn (<https://seaborn.pydata.org/generated/seaborn.regplot.html>) shows that indeed E119 and D185 pK_a values are not correlated in the Hv1J WT MD system ($y = 0.0x + 6.8$; $r^2 = 0.0$).

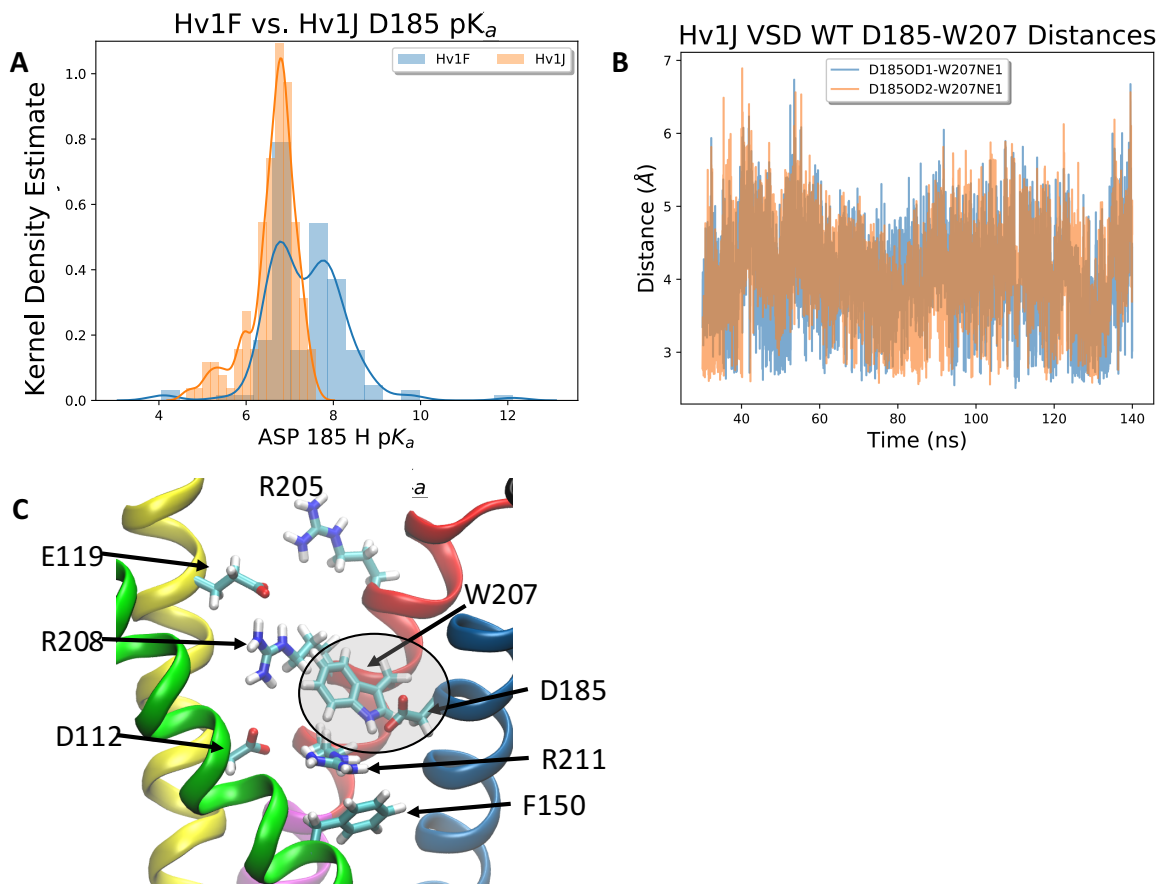


Figure 4.17: D185 Interacts with W207 in Hv1J WT MD

A: The distribution of pK_a values for D185 during the course of Hv1F WT (blue) and Hv1J WT (orange) MD. Calculations were performed using seaborn distplot and the kernel density estimate is plotted on the y-axis. Histograms were constructed using the Seaborn distplot function of Python (https://seaborn.pydata.org/generated/seaborn_distplot.html).

B: Time series plot of the distances between the terminal oxygen atoms of D185 and the nitrogen atom of W207 during the course of the Hv1J WT MD simulation. D185 remains close to W207 throughout the entire trajectory, shielding D185 from interacting with other residues (D), and thus causing the D185 pK_a to shift to a more neutral value in order to keep D185 charge neutral. Plots were made using Pyplot (https://matplotlib.org/api/pyplot_api.html) in Python 3.16.

C: Snapshot taken from the last frame of the 140 ns trajectory of Hv1J WT MD. The same coloring scheme as used in [Figure 4.5](#) is used here and the relevant residues are indicated. The shielding of D185 by W207 is highlighted by the grey circle.

CHAPTER 5: EXPERIMENTAL MEASUREMENT OF Hv1 FUNCTION IN ECEN MUTANTS

During whole-cell voltage clamp experiments, the pH of the internal solution (pH_i) was held constant at 5.5 while the pH of the EC solution (pH_o) was switched to pH values in the range from 4.5 to 7.5 by gravity-fed bath superfusion ([Figure 5.1A](#)). I-V curves were constructed by plotting I_{tail} in function of the applied step voltage ([Figure 5.1B](#)); V_{thr}, the potential at which I_{tail} is first observable, was determined at each pH_o value ([Table 5.1](#)). The difference between V_{thr} (ΔV_{thr}) at the measured ΔpH and at ΔpH = +1, which is pH_i = 6.5 and pH_o = 7.5 was calculated as $\Delta V_{thr} = V_{thr} - \overline{V_{thr}(\Delta pH = +1)}$ where $\overline{V_{thr}(\Delta pH = +1)}$ is the average V_{thr} at ΔpH = +1 ([Table 5.2](#)). This process normalizes V_{thr} to the value at ΔpH = 1 is necessary because V_{thr} is expected to shift ~40 mv/pH unit in WT Hv1, and normalization permits unambiguous comparisons between mutants and WT Hv1. The slope of a linear regression analysis of the ΔV_{thr} vs. pH_o plot is indicative of the steepness of ΔpH sensitivity in Hv1, and changes in the slopes of ΔV_{thr}-pH_o plots can help identify which mutations alter ΔpH-dependent gating.

5.1: ECEN Single Mutants

Δ pH-dependent gating in several neutralizing mutations of Hv1 acidic residues in the ECEN was measured as describe above in E119A and D185A mutants ([Figure 5.2](#)), which showed promise in PROPKA3.1 pKa covariance analyses ([Figure 4.14](#); [Figure 4.15](#)). D123A and D130A were also tested because they are in close proximity to E119 and D185 in the Hv1F model structure and could therefore serve as negative controls for E 119 and D185 ([Figure 4.1](#)). The slopes of the $V_{\text{thr}}\text{-pH}_0$ plots in E119A, D123A, D130A, and D185A single mutants are not obviously different from that of WT ([Figure 5.2](#)), indicating no change in Δ pH sensitivity. A post-hoc t-test comparing interpolated ΔV_{thr} values confirmed that E119A, D123A and D130A overall do not affect the Δ pH sensitivity of Hv1 ([Table 5.2](#)). However, the t-test shows that Δ pH sensitivity in D185A is slightly different ($\alpha=0.01$) from WT at extreme EC pH values ([Table 5.2](#)). This finding is different from a previous study in which pH_0 sensitivity was unchanged in D185A ([Ramsey et al., 2010](#)) because the current study tested responses at more acidic pH_0 than the previous work, and D185A is different from WT Hv1 only at the most acidic pH_0 tested ([Table 5.2](#)). Because pH_0 sensitivity was not dramatically altered at pH_0 7.5-5.5 in any of the single mutants tested here, we next sought to test the function of double-mutant Hv1 proteins.

5.2: ECEN Double Mutants

Δ pH-dependent gating does not appear to be obviously different from WT Hv1 in E119A-D123A and D123A-D130A mutants (Figure 5.3). Post-hoc t-tests comparing ΔV_{thr} values confirm that Δ pH sensitivity is unaltered in D123A-D130A, but does appear to be different from WT Hv1 at acidic EC pH in E119A-D123A (Figure 5.3). In contrast, the E119A-D185A double mutant showed a dramatic decrease in Δ pH-dependent gating (Figure 5.3). Post-hoc t-tests confirm ΔV_{thr} differences from WT Hv1 at pHo 4.5, 5.5, and 6.5 (Figure 5.3). The experimental data therefore suggest that E119 and D185 are both necessary for Δ pH-dependent gating in Hv1 at acidic pHo, as suggested by PROPKA3.1 analyses. The identification of E119 and D185 as crucial contributors to Δ pH-dependent gating in Hv1 is consistent with the results of our pKa covariance analysis method for identifying functionally relevant residues, and suggests that these side chains may interact with one another to form a functionally important EC H⁺ binding site within the ECEN.

5.3: ECEN Triple Mutants

Surprisingly, the triple mutant E119A-D123A-D185A did not appear to be different from the E119A-D185A double mutant, but was still drastically altered from WT ([Figure 5.4A](#); [Table 5.2](#)). Fits of third-order polynomials to the ΔV_{thr} vs. pH_o data reveal apparent differences in ΔpH sensitivities of certain mutant Hv1 proteins ([Figure 5.4B](#)). Polynomial fits indicate that E119-D185 mutant has WT-like ΔpH sensitivity at EC pH 6.5-7.5, but the ΔpH sensitivity is lost between EC pH 4.5-5.5 ([Figure 5.4B](#)). This result highlights how different mutants and mutant combinations may have different effects on pH_o sensitivity depending on the range of pH that is tested, complicating efforts to identify pH-sensing residues in Hv1. Our analysis of single, double, and triple ECEN candidate mutations suggests that no single side chain is sufficient to constitute the EC pH sensor, and is consistent with a previous study ([Ramsey et al., 2010](#)). Instead, we interpret the data to mean that interactions between identified ECEN acidic groups are necessary for ΔpH -dependent gating in Hv1. Because ΔpH -dependent gating was only perturbed in the pH_o 4.5-6.5 range, but remained intact at pH_o 6.5-7.5 ([Figure 5.3](#); [Figure 5.4](#)), we infer that other, as yet unidentified, residues must also contribute to ΔpH -dependent gating at neutral pH_o .

5.4: MD on Hv1J and Hv1F ECEN Mutants

To investigate how ENs may change in response mutations in ECEN, MD simulations on Hv1J E119A, D185A, and E119A-D185A mutants were performed in an identical manner to those for the WT system. The same mutations were made and simulated in the background of the resting state Hv1F model as well. The same salt bridge and PROPKA3.1 pK_a analysis described for the WT simulations was carried out on these Hv1J ([Table 4.1](#)) and Hv1F ([Table 4.2](#)) mutant simulations as well.

5.4.1: Hv1J ECEN Mutant MD

The salt bridge analysis of Hv1J reveals that the D112-R211 selectivity filter remains intact in all mutants ([Figure 5.5A](#); [Figure 5.6A-D](#)), however E_{rev} of the mutants were not directly measured here so no comparisons to the experimental data can yet be made regarding selectivity. In the Hv1J E119A-D185A double mutant MD, a D123-R208 salt bridge forms, which is not present in any of the other systems ([Figure 5.5B](#)). Interestingly, the formation of the D123-R208 salt bridge in the E119A-D185A mutant is associated with a substantial drop in the pK_a of D123 in this mutant, but not in WT or either single mutant MD ([Figure 5.7B](#)), another indication that electrostatic interactions are important in determining the pK_a values of Hv1 residues. D123-R208 interactions have not been explored with experimental methods, but here serves as an example of a compensating interaction that may occur in Hv1 mutants. In fact, this D123-R208 salt bridge in the Hv1J E119A-D185A structure appears to take the place of the WT E119-R208 salt bridge ([Figure 5.5B, E](#); [Figure 5.6A, D](#)).

Importantly, the loss of the E119-R208 salt bridge appears to be a major modulator of E119 pK_a in the Hv1J structure. In the D185A mutant, the E119-R208 salt bridge distance about

doubles ([Figure 5.5E](#); [Figure 5.6C](#)) and is associated with a substantial increase in the E119 pK_a in the D185A mutant ([Figure 5.7A](#)), which is consistent with the hypothesis that a lack of strong electrostatic interactions with positive countercharges in the ECEN causes dramatic shifts in the pK_a values of E119 and D185. Conversely, the E119-R205 interaction, which is already weak in WT, is slightly weakened, but otherwise does not change much in the presence of the D185A mutation ([Figure 5.5D](#); [Figure 5.6C](#)). The E119-R205 interaction appears to contribute less than the E119-R208 interaction in the Hv1J structure, which is consistent with the mutant cycle analysis and GIA, indicating that the E119-R208 interaction is indeed stronger than the E119-R205 interaction ([Table 1.1](#)).

The only salt bridge that D130 forms in Hv1J is with K131 ([Figure 4.8B](#)), and this salt bridge does not change much when ECEN neutralizing mutations are introduced ([Figure 5.5F](#); [Figure 5.6](#)). Likewise, the pK_a of D130 does not change much in the various ECEN mutant MD simulations ([Figure 5.7C](#)). These salt bridge and pK_a analyses are consistent with the idea that electrostatic interactions are important factors in determining residue pK_a and are consistent with experimental data indicating that D130 is not a primary contributor of the EC pH sensor.

As was previously discussed, D185 is shielding by W207 from participating strong electrostatic interactions in Hv1J ([Figure 4.17](#)). However, when the E119A mutation is introduced into the ECEN, a salt bridge not present in the WT simulation forms between D185 and R211 ([Figure 5.5C](#); [Figure 5.6B](#)). The D185-W207 interaction is not perturbed by the formation of the D185-R211 salt bridge (not shown), but rather the S4 arginine side chains reorient upwards, such that R208 interacts with D123 and R211 with D185 in the Hv1 E119A mutant ([Figure 5.5B-C](#); [Figure 5.6B](#)). The formation of the D185-R211 salt bridge in the Hv1J E119A mutant is associated with a drop in the pK_a value of D185 ([Figure 5.7D](#)). The summation

of the Hv1J computational data, when interpreted in light of the voltage clamp experiments presented here, strongly argues that electrostatic interactions are critically important in determining residue pK_a values, which are in turn important in determining the ΔpH -dependent gating of Hv1.

5.4.2: Hv1F ECEN Mutant MD

PROPKA3.1 analysis was performed in Hv1F E119A, D185A, and E119A-D185A MD simulations to see how these ECEN mutations influence the pK_a values of acidic residues in the ECEN ([Table 4.2](#); [Figure 5.8](#)). The PROPKA3.1 analysis of Hv1F WT suggested that the pK_a of E119 is shifted so high in part because of its close interaction with D185, and, as expected, the pK_a value of E119 in the Hv1F D185A mutant MD, while still high relative to the solution pK_a of a free glutamate residue, shifted down significantly relative to its value in WT ([Table 4.2](#); [Figure 5.8A](#)). Interestingly, the pK_a of E119 in the Hv1F D185A MD takes on a value of about 9 ([Table 4.2](#); [Figure 5.8A](#)), which is approximately the same value that E119 took in the WT simulations prior to the decrease in E119-D185 distance ([Figure 4.15A,C](#); [Figure 5.8A](#)). This finding further supports the idea that the electrostatic interaction between E119 and D185 in the WT Hv1F model is, in part, responsible for the large shift of E119 pK_a .

Consistent with the lack of ΔpH -dependent gating effect of the D123A single or double mutants, the pK_a of D123 is not affected by the ECEN mutations ([Figure 5.8B](#)). Similarly, the D130 pK_a is not affected by any of ECEN mutations ([Figure 5.8C](#)). These PROPKA3.1 results are consistent with the lack of an effect in the D123A, D130A, and D123A-D130A ECEN mutant voltage clamp experiments ([Table 5.1](#); [Table 5.2](#); [Figure 5.2](#); [Figure 5.3](#)). The consistency between the Hv1F ECEN mutant MD and voltage clamp studies helps to validate the

Hv1F model as well as the PROPKA3.1 pK_a fluctuation analysis method for identifying experimentally interesting candidates.

Comparing the PROPKA3.1 results of Hv1F WT and Hv1J WT simulations reveals that the pK_a of D185 is not as strongly influenced by electrostatic interactions due to being shielded by W207 ([Figure 4.17C](#)). E119A mutations in the background of Hv1F resting state model did not drastically alter the pK_a of D185 ([Figure 5.8D](#)). D185A mutations did not alter the closed-state H⁺ conduction without altering the open-state H⁺ conduction in the Hv1 R205H mutant, which suggests that D185 selectively stabilizes the active state relative to the resting-state (Randolph et al., 2016). Consistent with the D185A-R205A voltage clamp experiments, the PROPKA3.1 results demonstrate that, in the Hv1F resting state model, D185 is not engaged in stabilizing salt bridges ([Figure 4.12](#)), resulting in a stable pK_a across various Hv1F mutants, whereas in the Hv1J activated state model, D185 engages in weak but stabilizing salt bridges with S4 arginine residues ([Figure 4.8B](#)). These results highlight the importance of strong electrostatic interactions in influencing pK_a and, because the results of the PROPKA3.1 analysis on mutant MD correspond exceedingly well with the voltage clamp experiments, the results strongly argue that PROPKA3.1 analysis on MD trajectories can help to identify pK_a fluctuations with functional relevance and further validates the method for future use.

Similar to the WT analysis, the salt bridge analysis of Hv1F E119A, D185A, and E119A-D185A mutants revealed that no salt bridges formed in the ECEN ([Figure 5.9](#)). Only the D112-R205 salt bridge is significantly altered by the double mutant Hv1F E119A-D185A ([Figure 5.9A](#); [Figure 5.10D](#)). Unfortunately, this interaction has not been explored experimentally so comparisons can not yet be made.

Surprisingly, the Hv1F ECEN mutant salt bridge analysis revealed that, in the presence of ECEN mutants, there are slight alterations in the ICEN, about 20 Å away from the mutation site ([Figure 5.10](#)). Salt bridges are typically thought of as short range interactions happening when the participating atoms are less than 4.0 Å away from one another, and so mutations causing rearrangements in salt bridges 20 Å away is completely unexpected. However, electrostatic interactions can actually have effects over a long range beyond 4 Å ([Essmann et al., 1995](#)). Furthermore, Hv1 is known to be sensitive to the ΔpH as opposed to absolute EC or IC pH but, apparently, has independent EC and IC pH sensors located about 20 Å apart from one another (data presented in [Chapter 5.1-5.3](#)), and so the question of how the IC and EC sensors communicate and emerge as ΔpH -dependent gating still remains. The salt bridge analysis on Hv1F suggests that it is possible for changes in the one EN to be associated with rearrangements in the other EN and perhaps, through these rearrangements of electrostatic interactions throughout the pore of the Hv1 channel, is how the IC and EC pH sensors communicate. If these two networks can indeed talk, then making mutations in the ICEN should perturb Hv1 ability to sense EC stimuli such as H^+ or Zn^{2+} .

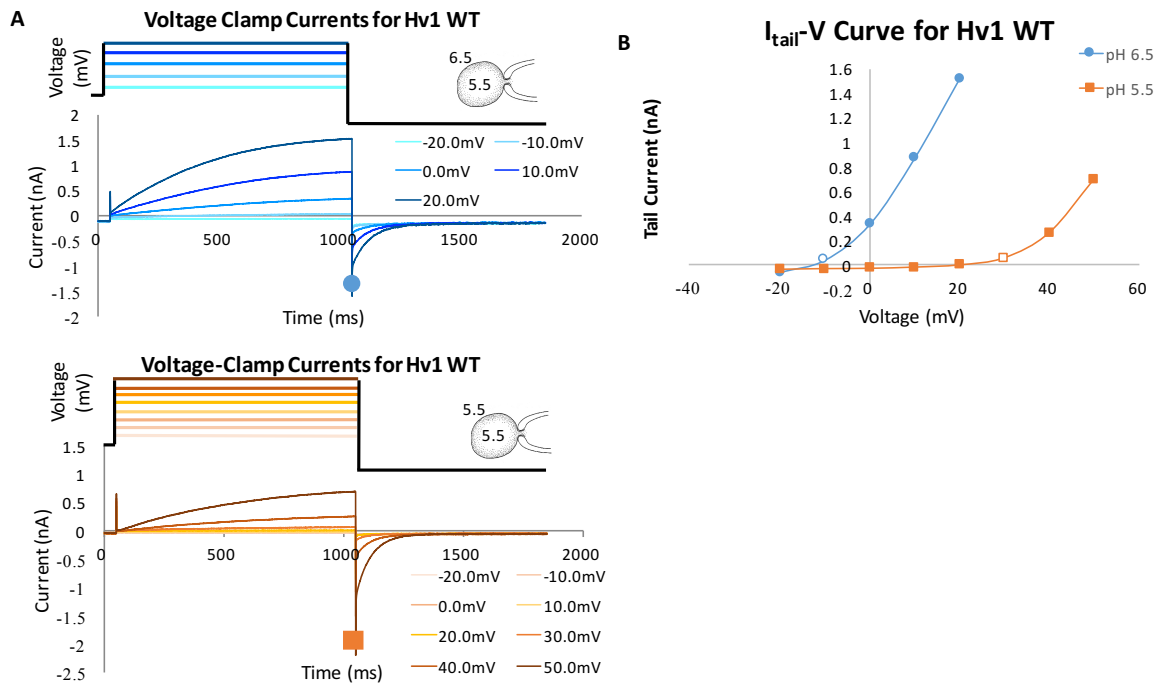


Figure 5.1: Raw Voltage Clamp Data for Hv1 WT

A: Raw current traces of Hv1 WT at $\text{pH}_i/\text{pH}_o = 5.5/6.5$ (top) and $\text{pH}_i/\text{pH}_o = 5.5/5.5$ (bottom). Similar recordings were obtained for all ECEN mutants. The cell was held at the holding potential of -50 mV for 50 ms and then the depolarizing pulse was delivered for 1000 ms, and then returned to a polarized potential at -80 mV for 800 ms to elicit tail currents. The voltage-step protocol is shown above the raw current traces. Tail current was used as the current measurement in (B) as depicted by the blue circle (top) and orange square (bottom).

B: Current-Voltage ($I_{\text{tail}}-V$) curves of the tail current of the raw traces for $\text{pH}_o = 6.5$ (blue circles) and $\text{pH}_o = 5.5$ (orange squares) shown in A. The open circle ($\text{pH}_o = 6.5$) and open square ($\text{pH}_o = 5.5$) represent the threshold potential (V_{thr}), the voltage at which current is first observable in a voltage-step protocol.

Table 5.1: Average Raw V_{thr} of Hv1 WT and ECEN Mutants

ΔV_{thr} values are measured from raw current traces and I_{tail} -V curves from voltage clamp experiments ([Figure 5.1](#)).

*Indicates values that are statistically different from WT at $\alpha = 0.05$.

**Indicates values that are statistically different from WT at $\alpha = 0.01$.

Table 5.1: Average Raw V_{thr} of Hv1 WT and ECEN Mutants								
pH _i	pH _o	V_{thr} (mV)	SD	SEM	n	p vs WT	ΔV_{thr} vs WT	$\Delta(\Delta V_{thr})$ vs WT
917 WT								
5.5	7.5	-68.9	8.5	2.6	11	1.0	0.0	0.0
5.5	6.5	-27.7	8.9	2.6	12	1.0	0.0	0.0
5.5	5.5	15.3	9.4	3.3	8	1.0	0.0	0.0
5.5	4.5	60.0	10.5	4.0	7	1.0	0.0	0.0
60 E119A								
5.5	7.5	-58.9	6.3	2.6	6	0.010*	10.0	-11.5
5.5	6.5	-6.1	4.9	2.0	6	0.00000649**	21.6	0.0
5.5	5.5	39.7	3.4	1.5	5	0.0000747**	24.3	2.8
5.5	4.5	85.0	8.4	3.4	6	0.000591**	25.0	3.4
69 D123A								
5.5	7.5	-47.2	3.9	1.6	6	0.0000034**	21.7	1.1
5.5	6.5	-7.1	5.2	1.8	8	0.00000405**	20.6	0.0
5.5	5.5	29.5	8.2	3.1	7	0.0083**	14.2	-6.4
5.5	4.5	64.2	8.6	3.5	6	0.45	4.2	-16.5
62 D130A								
5.5	7.5	-72.5	5.0	2.5	4	0.34	-3.6	-9.9
5.5	6.5	-21.3	3.0	1.3	5	0.04*	6.3	0.0
5.5	5.5	32.7	3.7	1.6	5	9.47E-04**	17.3	11.0
5.5	4.5	74.0	5.5	2.4	5	0.010*	14.0	7.6
95 D185A								
5.5	7.5	-28.6	6.9	1.7	17	9.2E-11**	40.3	-11.3
5.5	6.5	23.9	6.8	1.7	17	3.51E-13**	51.6	0.0
5.5	5.5	62.5	7.2	1.8	16	6.41E-08**	47.2	-4.4
5.5	4.5	92.0	8.4	3.7	5	0.000173**	32.0	-19.6
61 D123A-D130A								
5.5	7.5	-45.0	8.3	4.8	3	9.65E-04**	0.0	0.0
5.5	6.5	-0.6	3.9	1.6	6	0.000000126**	0.0	0.0
5.5	5.5	50.6	8.5	3.5	6	0.0000123**	0.0	0.0
5.5	4.5	86.7	9.4	4.7	4	0.00345**	0.0	0.0

pH _i	pH _o	V _{thr} (mV)	SD	SEM	n	p vs WT	ΔV _{thr} vs WT	Δ(ΔV _{thr}) vs WT
1206 E119A-D123A								
5.5	7.5	-38.6	9.6	2.6	13	4.38E-08**	30.3	-3.6
5.5	6.5	6.3	7.6	2.1	16	1.73E-11**	34.0	0.0
5.5	5.5	43.9	9.4	2.7	15	3.31E-07**	28.6	-5.4
5.5	4.5	76.8	5.1	0.5	11	3.19E-04**	16.8	-17.2
1256 E119A-D185A								
5.5	7.5	33.0	8.7	2.6	11	1.91E-17**	102.0	-4.8
5.5	6.5	79.0	7.7	0.3	28	4.30E-33**	106.7	0.0
5.5	5.5	98.4	7.5	0.4	26	4.00E-24**	83.1	-23.7
5.5	4.5	106.7	5.8	1.9	3	1.05E-04	46.7	-60.1
1257 D123A-D130A-D185A								
5.5	7.5	46.1	12.0	4.3	8	2.8E-11**	115.0	6.8
5.5	6.5	80.5	10.9	3.5	10	4.5E-15**	108.2	0.0
5.5	5.5	100.6	8.1	2.7	9	1.31E-11**	85.2	-23.0
5.5	4.5	115	7.07107	5	2	0.00641**	55.0	-53.2
1258 E119A-D123A-D185A								
5.5	7.5	29.7	10.2	3.9	7	2.20E-10**	98.7	5.8
5.5	6.5	65.2	6.6	2.0	11	8.67E-18**	92.8	0.0
5.5	5.5	86.7	4.6	1.6	8	2.56E-09**	71.3	-21.5
5.5	4.5	102.5	5.0	2.5	4	8.87E-06**	42.5	-50.4

Table 5.2: Average ΔV_{thr} of Hv1 WT and ECEN Mutants

ΔV_{thr} values are calculated as $V_{thr} - V_{thr}(\Delta pH = +1)$ where $V_{thr}(\Delta pH = +1)$ is the V_{thr} measured at $pH_o/pH_i = 6.5/5.5$.

*Indicates values that are statistically different from WT at $\alpha = 0.05$.

**Indicates values that are statistically different from WT at $\alpha = 0.01$.

Table 5.2: Average ΔV_{thr} of Hv1 WT and ECEN Mutants								
pHi	pHo	ΔV_{thr} (mV)	SD	SEM	n	p vs WT	ΔV_{thr} vs WT	$\Delta(\Delta V_{thr})$ vs WT
917 WT								
5.5	7.5	-42.6	11.4	1.1	10	1.0	0.0	0.0
5.5	6.5	0.0	0.0	0.0	12	1.0	0.0	0.0
5.5	5.5	42.8	6.8	0.8	8	1.0	0.0	0.0
5.5	4.5	84.6	8.8	1.1	8	1.0	0.0	0.0
E119A								
5.5	7.5	-52.8	7.4	1.2	6	0.07292	-10.2	-10.2
5.5	6.5	0.0	0.0	0.0	6	ND	0.0	0.0
5.5	5.5	48.6	4.3	0.7	6	0.09042	5.8	5.8
5.5	4.5	91.1	6.9	1.1	6	0.16437	6.5	6.5
D123A								
5.5	7.5	-41.7	4.1	0.7	6	0.85	0.9	0.9
5.5	6.5	0.0	0.0	0.0	8	ND	0.0	0.0
5.5	5.5	37.1	5.9	0.8	7	0.111	-5.6	-5.6
5.5	4.5	73.1	6.8	1.1	6	0.021*	-11.6	-11.6
D130A								
5.5	7.5	-50.8	1.7	0.4	4	0.19	-8.2	-8.2
5.5	6.5	0.0	0.0	0.0	5	ND	0.0	0.0
5.5	5.5	54.0	3.7	0.7	5	6.19E-03**	11.2	11.2
5.5	4.5	95.3	5.1	1.0	5	0.033*	10.7	10.7

pHi	pHo	ΔV_{thr} (mV)	SD	SEM	n	p vs WT	ΔV_{thr} vs WT	$\Delta(\Delta V_{thr})$ vs WT
D185A								
5.5	7.5	-52.2	4.9	0.3	17	0.00546**	-9.6	-9.6
5.5	6.5	0.0	0.0	0.0	17	ND	0.0	0.0
5.5	5.5	38.5	4.8	0.3	16	0.08893	-4.3	-4.3
5.5	4.5	67.7	4.0	0.8	5	0.00211**	-17.0	-17.0
D123A-D130A								
5.5	7.5	-43.9	8.6	2.9	3	0.86304	-1.3	-1.3
5.5	6.5	0.0	0.0	0.0	5	ND	0.0	0.0
5.5	5.5	51.9	8.9	1.5	6	0.04979*	9.1	9.1
5.5	4.5	86.7	9.0	2.3	4	0.71842	2.0	2.0
E119A-D123A								
5.5	7.5	-44.7	9.2	1.2	13	0.63645	-2.1	-2.1
5.5	6.5	0.0	0.0	0.0	16	ND	0.0	0.0
5.5	5.5	37.0	5.7	0.8	15	3.00E-02**	-5.8	-5.8
5.5	4.5	68.5	4.1	0.4	11	5.21E-05**	-16.2	-16.2
E119A-D185A								
5.5	7.5	-43.0	8.3	0.8	11	0.92487	-0.4	-0.4
5.5	6.5	0.0	0.0	0.0	28	ND	0.0	0.0
5.5	5.5	20.1	5.3	0.3	26	3.61E-12**	-22.7	-22.7
5.5	4.5	31.1	7.7	2.6	3	7.16E-06**	-53.5	-53.5

pHi	pHo	ΔV_{thr} (mV)	SD	SEM	n	p vs WT	ΔV_{thr} vs WT	$\Delta(\Delta V_{thr})$ vs WT
D123A-D130A-D185A								
5.5	7.5	-34.6	6.2	0.8	8	0.09341	8.0	-13.5
5.5	6.5	0.0	0.0	0.0	10	ND	0.0	-21.6
5.5	5.5	20.0	6.7	0.7	9	4.35E-06**	-22.8	-44.4
5.5	4.5	32.5	3.5	1.8	2.0	0.000048**	-52.1	-73.7
E119A-D123A-D185A								
5.5	7.5	-34.1	10.6	1.5	7	1.40E-01*	8.5	-13.0
5.5	6.5	0.0	0.0	0.0	11	ND	0.0	-21.6
5.5	5.5	21.9	4.4	0.5	8	3.63E-06**	-20.9	-42.5
5.5	4.5	36.7	4.7	1.2	4	1.59E-06**	-48.0	-69.5

ΔpH-Dependent Gating in Hv1 ECEN Single Mutants

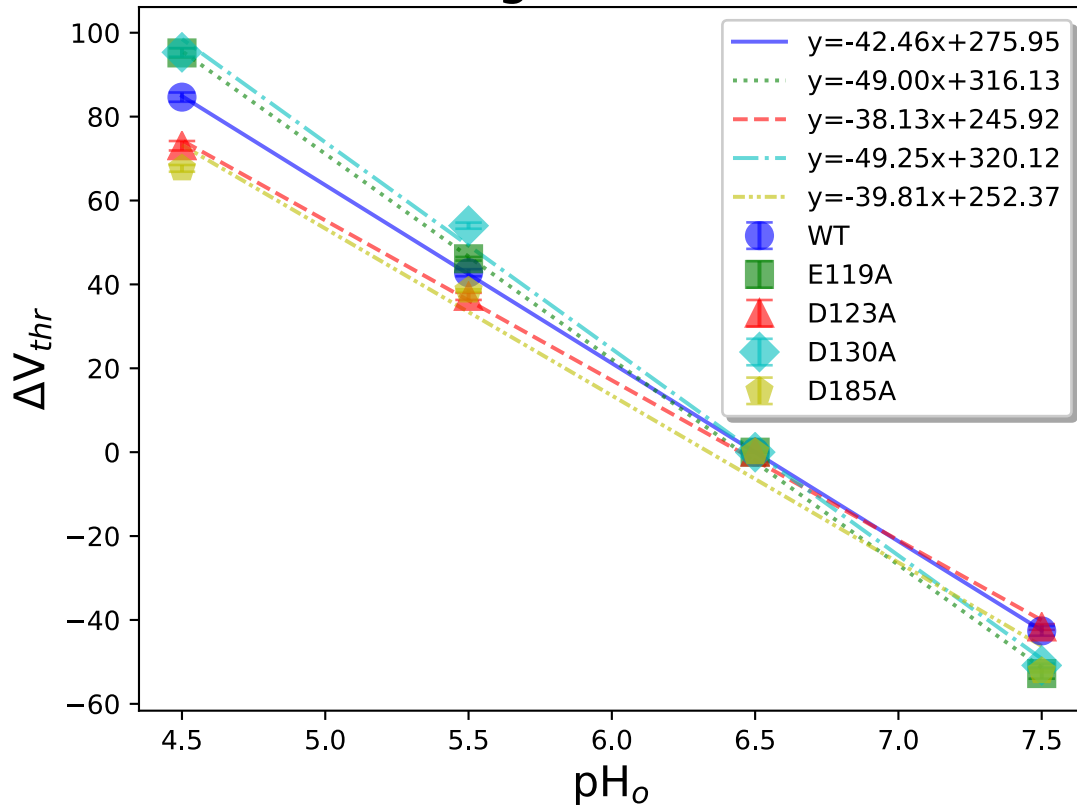


Figure 5.2: Hv1 EC pH Sensitivity of Voltage-Dependent Gating in ECEN Single Mutants

The mean \pm SEM of the threshold potential difference (ΔV_{thr}) between the measured ΔpH and that at $\Delta pH = +1$, from n experiments (Table 5.2) is plotted as a function of the EC pH for WT (blue circles), E119A (green squares), D123A (red triangles), D130A (cyan diamonds), and D185A (yellow pentagons). The IC pH was held constant at 5.5 for all experiments. Most error bars are smaller than the markers and are difficult to see, but in some cases are visible as faint lines within the marker, and in a few cases the error bars are exceeded marker size and are more easily seen. Linear regressions, calculated using Scipy (<https://docs.scipy.org/doc/scipy/reference/generated/scipy.stats.linregress.html>), between mean ΔV_{thr} and pH_o for WT (blue solid line; $-42.46x + 275.95$), E119A (green dotted line; $y = -49.00x + 316.13$), D123A (red dashed line; $y = -38.13x + 245.92$), D130A (cyan dash-dotted line; $y = -49.25x + 320.12$) and D185A (yellow densely dash-dotted line; $y = -39.81x + 252.37$) are plotted with the regression equations shown in the legend.

ΔpH-Dependent Gating in Hv1 ECEN Double Mutants

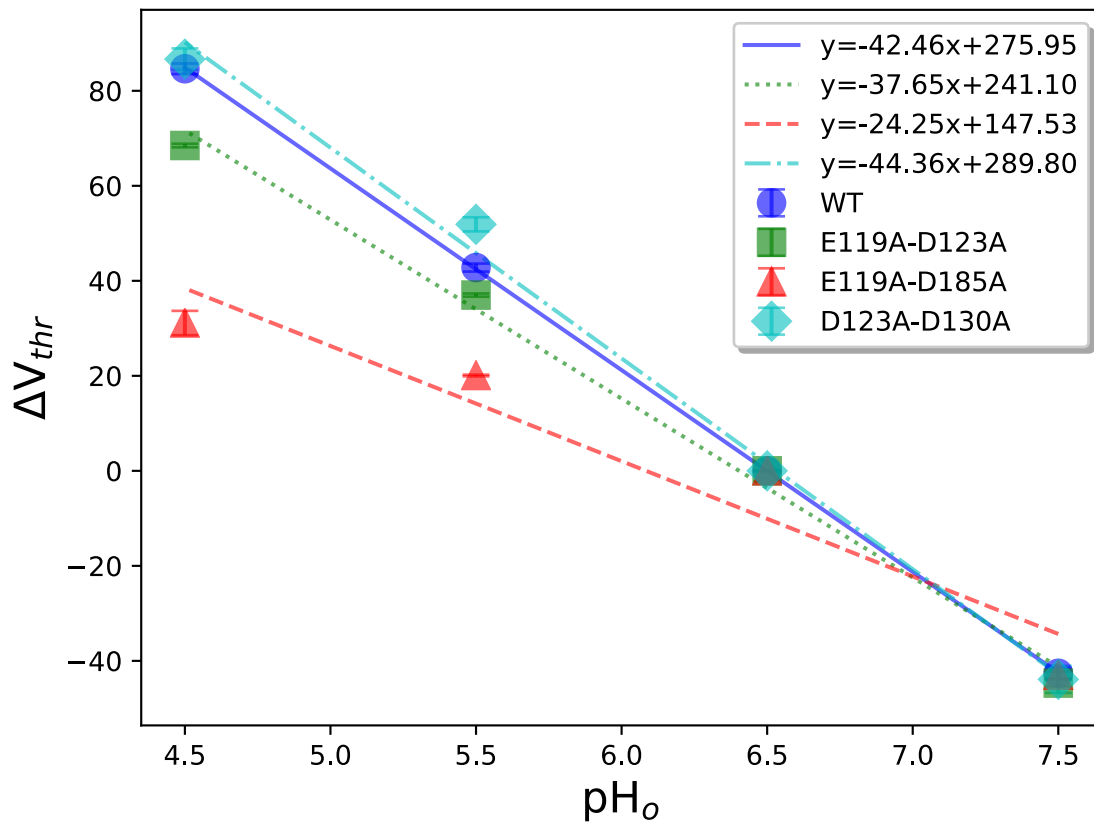


Figure 5.3: Hv1 EC pH Sensitivity of Voltage-Dependent Gating in ECEN Double Mutants

The mean \pm SEM of the threshold potential difference (ΔV_{thr}) between the measured ΔpH and that at $\Delta pH = +1$, from n experiments (Table 5.2) is plotted as a function of the EC pH for WT (blue circles), E119A-D123A (green squares), E119A-D185A (red triangles), and D123A-D130A (cyan diamonds). The IC pH was held constant at 5.5 for all experiments. Most error bars are smaller than the markers and are difficult to see, but in some cases are visible as faint lines within the marker, and in a few cases the error bars exceed marker size and are more easily seen. Linear regressions, calculated using Scipy (<https://docs.scipy.org/doc/scipy/reference/generated/scipy.stats.linregress.html>), between mean ΔV_{thr} and pH_o for WT (blue solid line; $y = -42.46x + 275.95$), E119A-D123A (green dotted line; $-37.65x + 241.10$), E119A-D185A (red dashed line; $-24.25x + 147.53$), and D123A-D130A (cyan dash-dotted line; $-44.36x + 289.80$) are plotted with the regression equations shown in the legend.

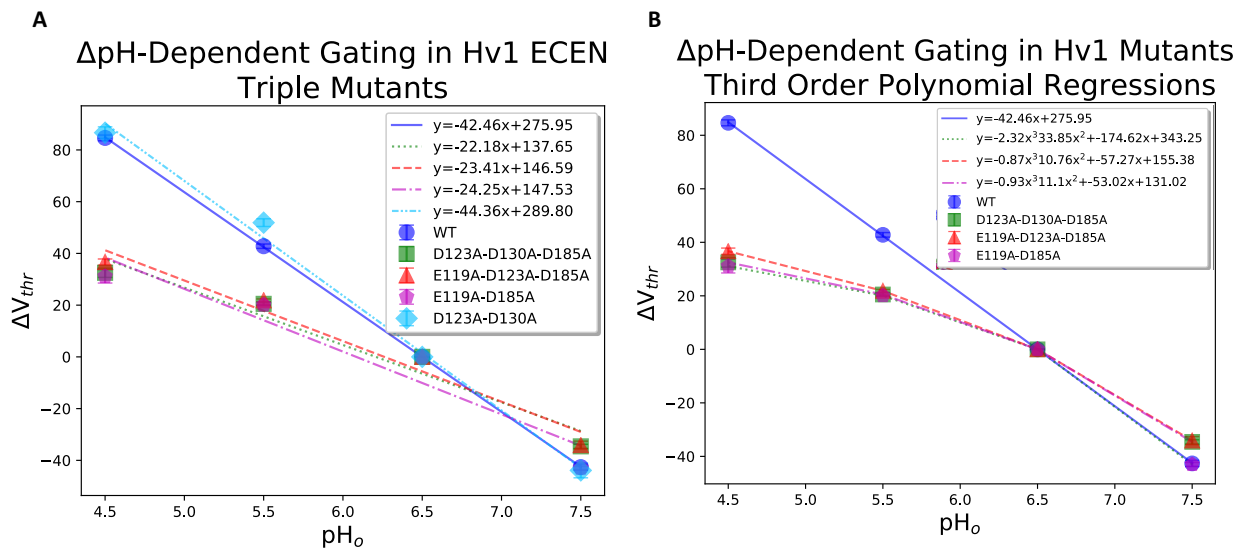


Figure 5.4: Hv1 EC pH Sensitivity of Voltage-Dependent Gating in ECEN Triple Mutants

A: The mean \pm SEM of the threshold potential difference (ΔV_{thr}) between the measured Δ pH and that at Δ pH = +1, from n experiments (Table 5.2) is plotted as a function of the EC pH for WT (dark blue circles), D123A-D130A-D185A (green squares), and E119A-D123A-D185A (red triangles). The IC pH was held constant at 5.5 for all experiments. The data for double mutants E119A-D185A (magenta pentagons) and D123A-D130A (light blue diamonds) are plotted for comparison. Most error bars are smaller than the markers and are difficult to see, but in some cases are visible as faint lines within the marker, and in a few cases the error bars are exceed marker size and are more easily seen. Linear regressions, calculated using Scipy (<https://docs.scipy.org/doc/scipy/reference/generated/scipy.stats.linregress.html>), between mean ΔV_{thr} and pH_o for WT (dark blue line; $-42.46x + 275.95$), D123A-D130A-D185A (green line; $-22.18x + 137.65$), and E119A-D123A-D185A (red line; $-23.41x + 147.53$) along with the double mutants E119A-D185A (dashed magenta line; $y = -24.25x + 147.53$) and D123A-D130A (dashed light blue line; $y = -44.36x + 289.80$) are plotted with the regression equations shown in the legend.

B: The same data as plotted in (A) but without D123-D130 an fit to a third-order polynomial equation calculated by Scipy (<https://docs.scipy.org/doc/numpy/reference/generated/numpy.polyfit.html>) instead of a linear fit for WT (blue circles and solide line; $y = -42.46x + 275.95$), D123A-D130A-D185A (green squares and dotted line; $y = -2.32x^3 + 33.85x^2 + 174.62x + 343.25$), E119A-D123A-D185A (red triangles and densely dashed line; $y = -0.87x^3 + 10.76x^2 - 57.27x + 155.38$), and E119A-D185A (magenta pentagons and dashed line; $y = -0.93x^3 + 11.1x^2 - 53.02x + 131.02$).

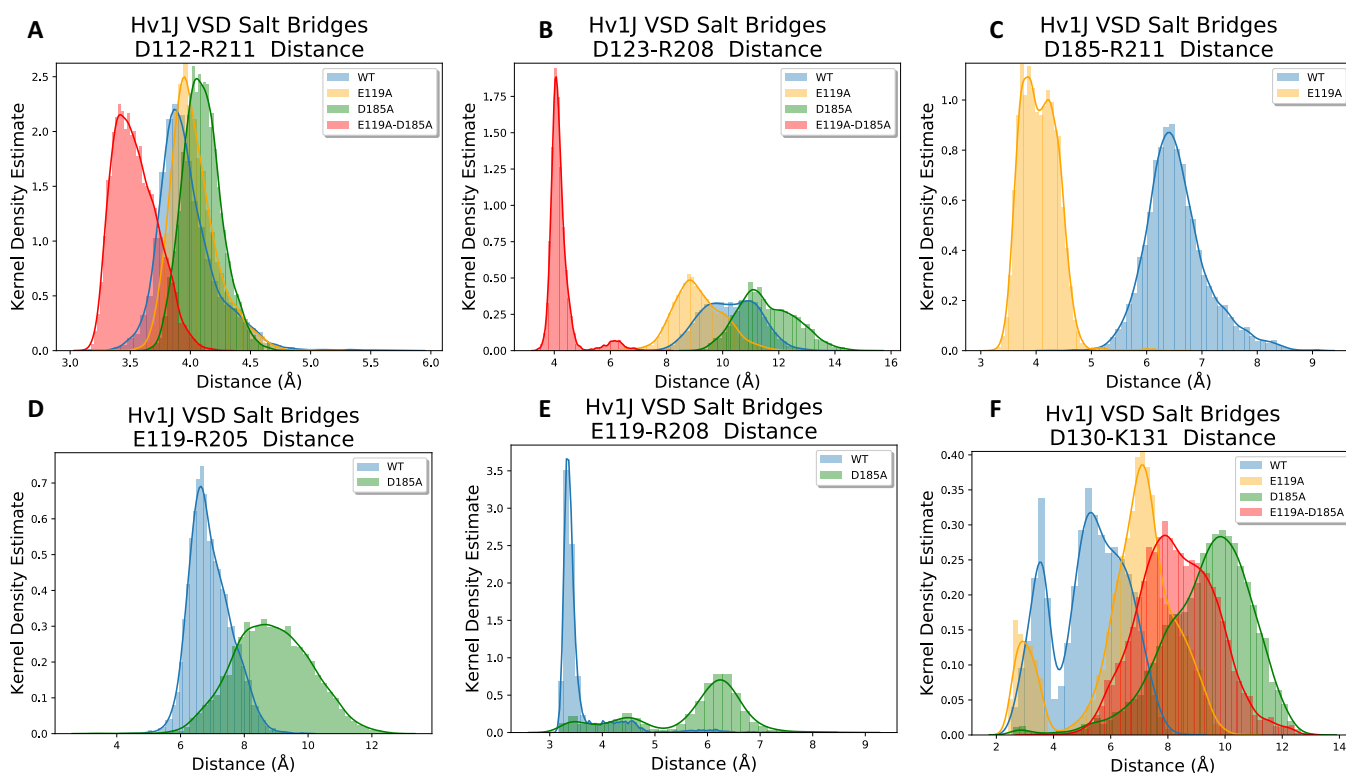


Figure 5.5: Salt Bridges in Hv1J ECEN Mutant Simulations

The VMD Salt Bridges plugin with default settings was used to calculate salt bridges every 2 fs in Hv1J WT (blue), E119A (yellow), D185A (green), and E119A-D185A (red). Histograms were made using the distplot function of Seaborn in Python3.16

(<https://seaborn.pydata.org/generated/seaborn.distplot.html>).

A: Distribution of D112-R211 salt bridge distances in Hv1J WT and mutant MD.

B: Distribution of D123-R208 salt bridge distances in Hv1J WT and mutant MD.

C: Distribution of D185-R211 salt bridge distances in Hv1J WT and mutant MD.

D: Distribution of E119-R205 salt bridge distances in Hv1J WT and mutant MD.

E: Distribution of E119-R208 salt bridge distances in Hv1J WT and mutant MD.

F: Distribution of D130-K131 salt bridge distances in Hv1J WT and mutant MD.

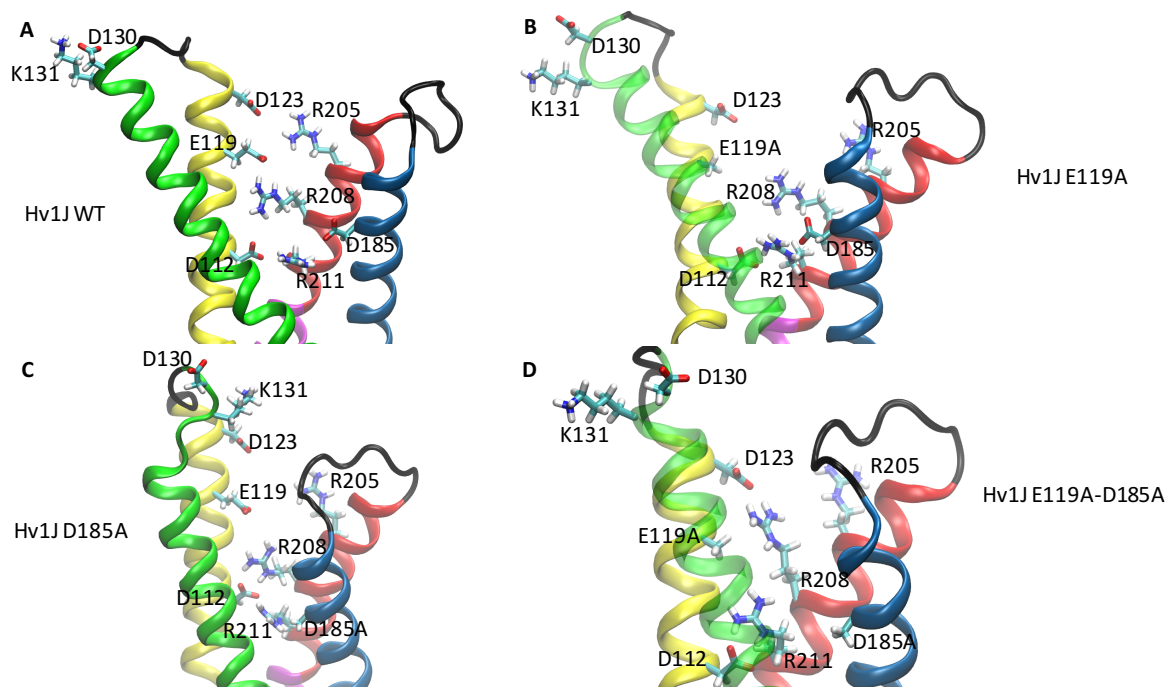


Figure 5.6: ECEN Structure in Hv1J WT and ECEN Mutant MD

The final coordinates from each simulation are depicted using the same coloring schemes described in [Figure 4.6](#) with the relevant residues indicated. The position of W207 does not change much as a result of the ECEN mutations and so is omitted for clarity.

A: The structure of the ECEN after 140 ns of Hv1J WT MD.

B: The structure of the ECEN after 150 ns of Hv1J E119A MD.

C: The final structure of the ECEN after 150 ns of Hv1J D185A MD.

D: The final structure of the ECEN after 220 ns of Hv1J E119A-D185A MD.

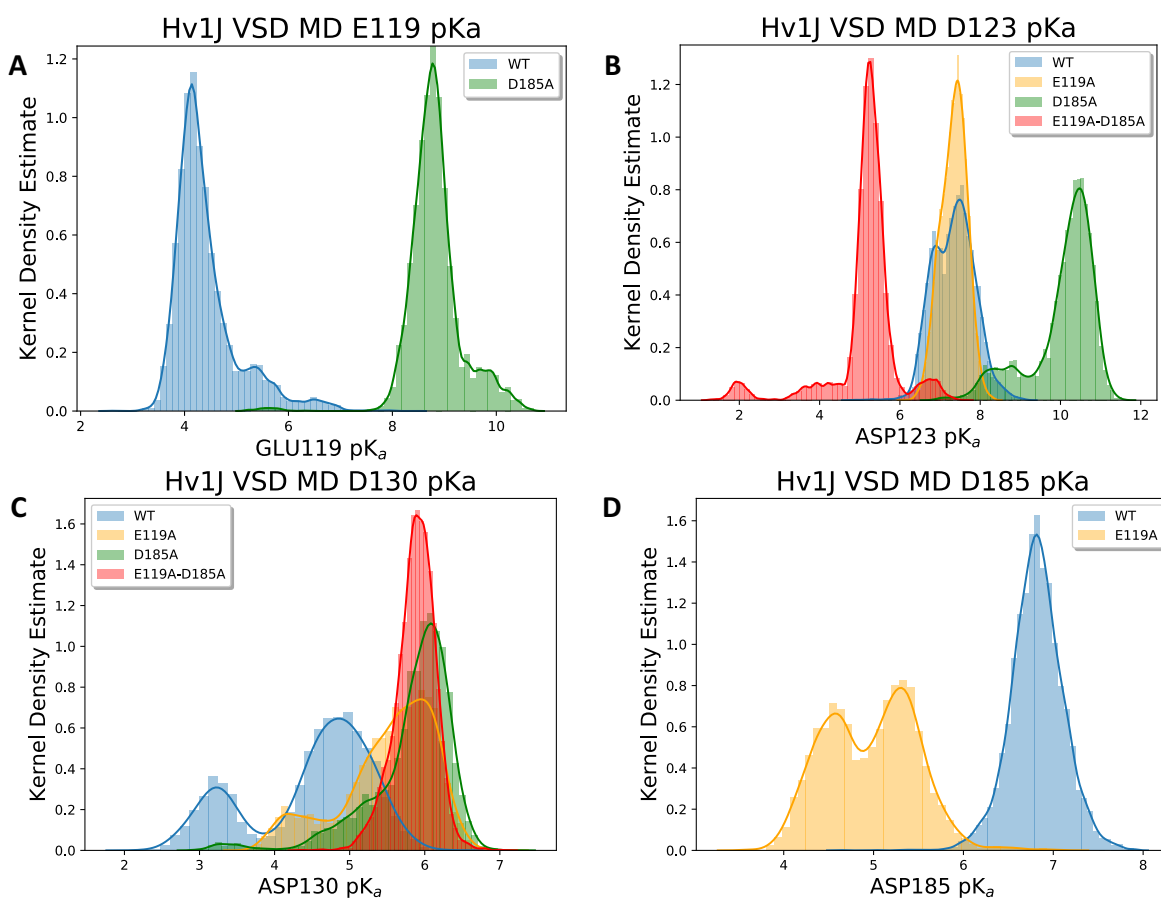


Figure 5.7: ECEN pK_a Values in Hv1J ECEN Mutant MD

PROPKA3.1 was used to calculate the pK_a values every 2 fs for Hv1J WT (blue), E119A (yellow), D185A (green), and E119A-D185A (red). [Table 4.1](#) shows the average pK_a values for ionizable residues in the Hv1J WT and mutant models. Histograms were made using the distplot function of Seaborn (<https://seaborn.pydata.org/generated/seaborn.distplot.html>) in Python3.16

A: Distribution of E119 pK_a in Hv1J WT and mutant MD.

B: Distribution of D123 pK_a in Hv1J WT and mutant MD.

C: Distribution of D130 pK_a in Hv1J WT and mutant MD.

D: Distribution of D185 pK_a in Hv1J WT and mutant MD.

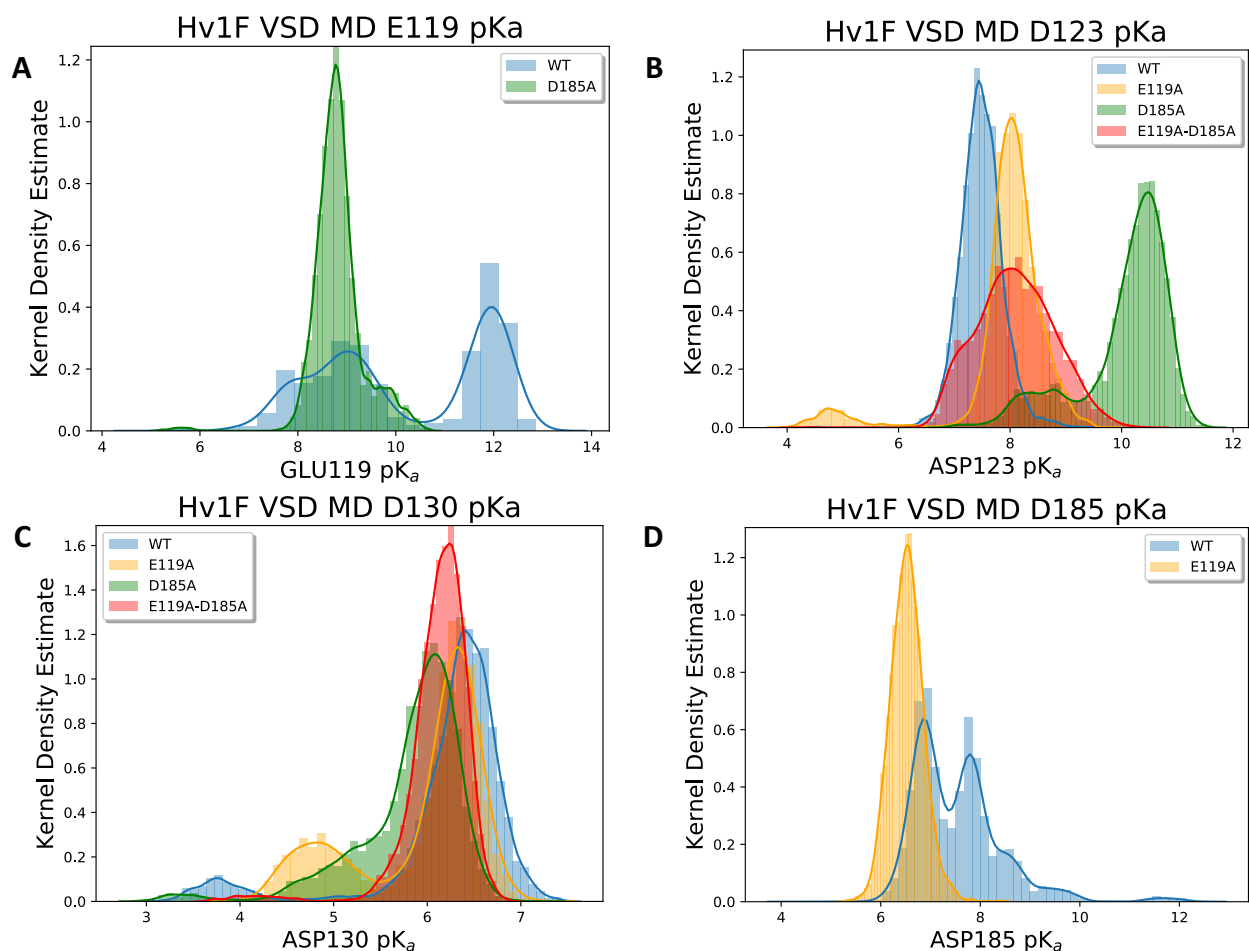


Figure 5.8: ECEN pK_a Values in Hv1F ECEN Mutant MD

PROPKA3.1 was used to calculate the pK_a values every 2 fs for Hv1F WT (blue), E119A (yellow), D185A (green), and E119A-D185A (red). [Table 4.2](#) shows the average pK_a values for ionizable residues in the Hv1F WT and mutant models. Histograms were made using the distplot function of Seaborn (<https://seaborn.pydata.org/generated/seaborn.distplot.html>) in Python3.16

A: Distribution of E119 pK_a in Hv1F WT and mutant MD.

B: Distribution of D123 pK_a in Hv1F WT and mutant MD.

C: Distribution of D130 pK_a in Hv1F WT and mutant MD.

D: Distribution of D185 pK_a in Hv1F WT and mutant MD.

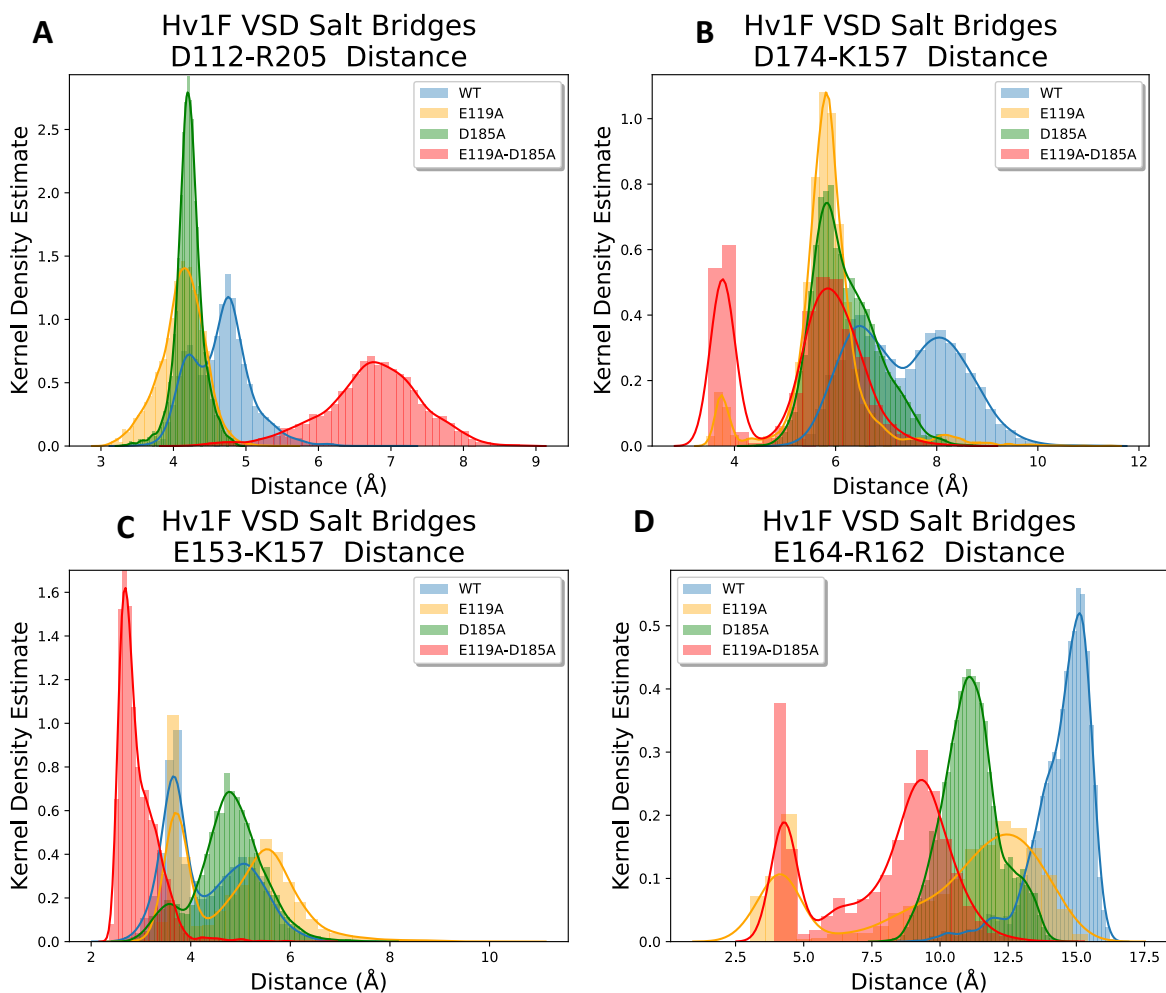


Figure 5.9: Salt Bridges in Hv1F ECEN Mutant Simulations

The VMD Salt Bridges plugin with default settings was used to calculate salt bridges in Hv1F WT (blue), E119A (yellow), D185A (green), and E119A-D185A (red). Histograms were made using the distplot function of Seaborn

(<https://seaborn.pydata.org/generated/seaborn.distplot.html>) in Python3.16

A: Distribution of D112-R205 salt bridge distances in Hv1J WT and mutant MD.

B: Distribution of D174-K157 salt bridge distances in Hv1J WT and mutant MD.

C: Distribution of E153-K157 salt bridge distances in Hv1J WT and mutant MD.

D: Distribution of E164-R162 salt bridge distances in Hv1J WT and mutant MD.

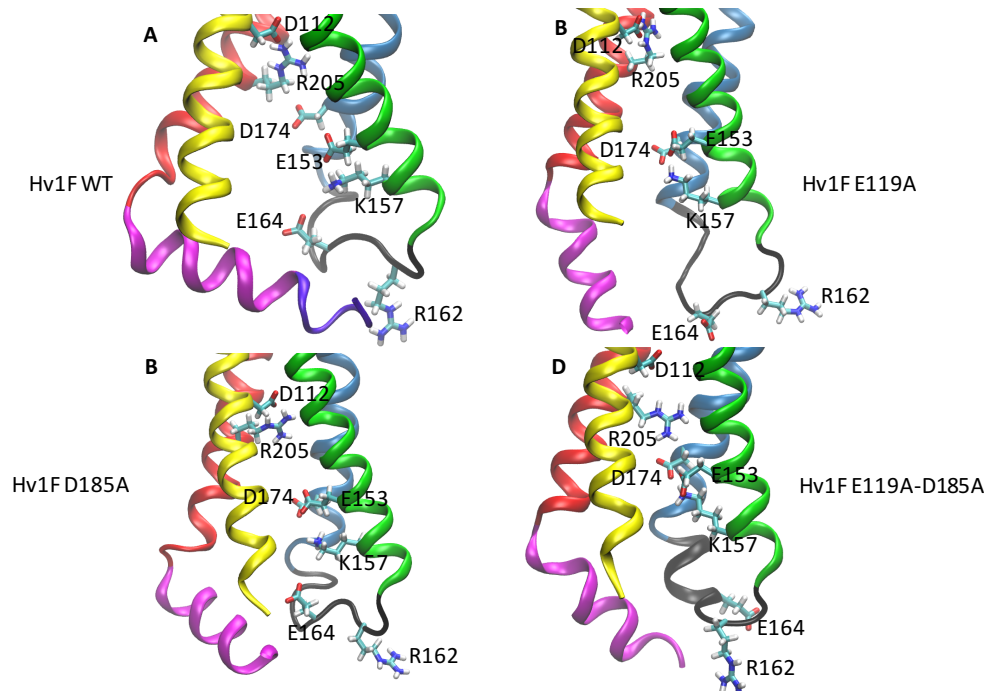


Figure 5.10: ICEN Structure in Hv1F WT and ECEN Mutant MD

The final coordinates from each Hv1F simulation are depicted using the same coloring schemes described in [Figure 4.1](#) with the relevant residues indicated.

A: The structure of the ICEN after 150 ns of Hv1F WT MD.

B: The structure of the ICEN after 150 ns of Hv1F E119A MD.

C: The final structure of the ICEN after 155 ns of Hv1F D185A MD.

D: The final structure of the ICEN after 150 ns of Hv1F E119A-D185A MD.

CHAPTER 6: Hv1 ALLOSTERY BETWEEN ECEN AND ICEN

In order to verify if that there is communication between the ICEN and the ECEN, ICEN mutants were constructed and EC Zn^{2+} potency in these ICEN mutants was measured. E153 was chosen for mutation to alanine (E153A) because it has previously been shown to be extremely important in stabilizing the closed state of the channel (Ramsey et al., 2010), it interacts with S4 arginine charges ([Table 1.1](#); Chamberlin et al., 2014), and the E153-K157 salt bridge was slightly altered by various ECEN mutants ([Figure 5.7B](#)). Additionally, in previously published simulations of Hv1F investigating structural effects of Zn^{2+} binding in the ECEN, the E153-R208 salt bridge distance was found to be highly correlated with the Zn^{2+} -H140 and Zn^{2+} -H193 distances in the ECEN Zn^{2+} binding site (De La Rosa et al., 2018), which is particularly interesting because the E119-R208 salt bridge is important in stabilizing the activated state of the channel ([Table 1.1](#); Chamberlin et al., 2014). Furthermore, The E119-R208 salt bridge is an important determinant of E119 pK_a and keeps the E119 pK_a in the activated state ([Figure 4.16B](#)) whereas E119 pK_a shifts up to higher values in the resting state Hv1F model when R208 leaves the ECEN and the E119-R208 salt bridge is broken ([Figure 4.16A](#)). All these factors together make E153 a good candidate for experiments on allostery between the ECEN and ICEN and also suggest that allosteric communication between the ECEN and ICEN may occur via movement of the S4 helix during gating.

As ΔpH -dependent gating experiments have recently revealed ([Chapter 5](#); Cherny et al., 2018), the ΔpH sensitivity of Hv1 is rather robust and it is difficult to investigate because a large range of pH_o and pH_i must be tested. Fortunately, inhibition of Hv1 voltage-dependent gating by Zn^{2+} binding provides an opportunity to more easily study the possibility of allostery between the ICEN and ECEN. Zn^{2+} , like H^+ , when applied to the EC side of Hv1, causes a rightward shift

towards depolarizing potentials of the $P_{\text{OPEN}}-V$ relationship, showing that Zn^{2+} and H^+ have similar effects on Hv1 voltage-dependent gating. Additionally, Zn^{2+} binds in the ECEN and the Zn^{2+} binding site includes at least two residues, E119 and D185, now known to be important for ΔpH -dependent gating (De La Rosa et al., 2018), showing that mechanisms of H^+ and Zn^{2+} sensing share similar structural components and mechanisms of channel inhibition. Previous MD simulations on Hv1F complexed to Zn^{2+} demonstrated that binding of Zn^{2+} in the ECEN causes rearrangements of the ICEN interactions, suggesting that there may be allosteric communication between the ICEN and ECEN (De La Rosa et al., 2018). To test for allostery between ICEN and ECEN, E153, an ICEN residue, was mutated to alanine and EC Zn^{2+} potency was measured.

Voltage clamp experiments on Hv1 E153A were performed exactly as done before except that, instead of superfusing EC solutions with different pH, EC solutions maintained a constant pH but with increasing Zn^{2+} concentration. When E153 is mutated to alanine in Hv1, the Zn^{2+} potency is reduced ([Figure 6.1](#)). The reduction of EC Zn^{2+} potency in the presence of ICEN neutralizing mutations supports the hypothesis that the ICEN and ECEN can communicate. This data shows that the mechanism for Hv1 Zn^{2+} sensitivity is more complicated than a simply tying the top of S4 to S2, as previously thought (Ramsey et al., 2006), and that Zn^{2+} also helps to stabilize the electrostatic interactions stabilizing the resting state of the channel. This result clearly indicates that information about the arrangement of the ICEN can be communicated over 20 Å away to the ECEN, emerging as allostery between the ICEN and ECEN.

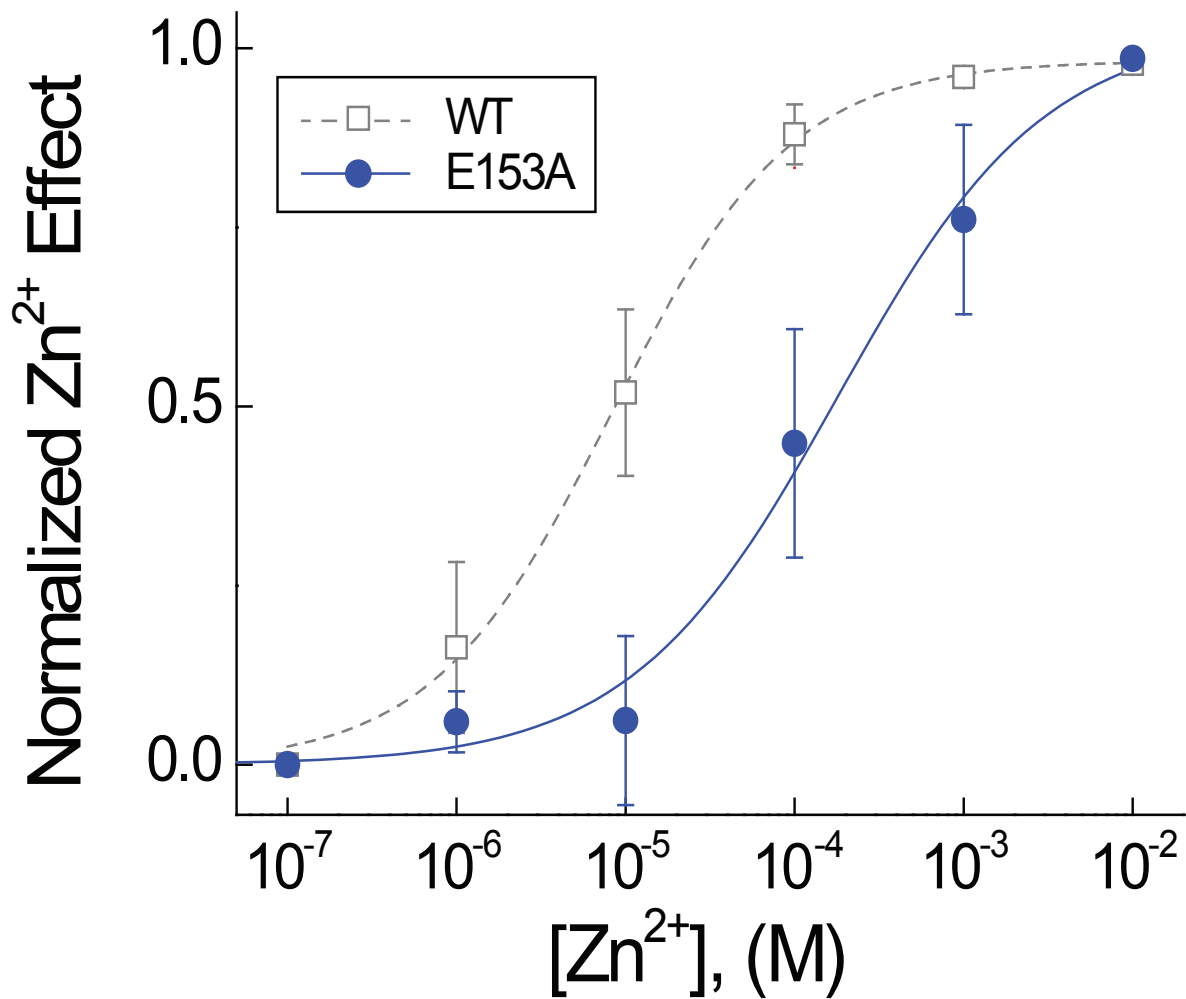


Figure 6.1: Zn²⁺ Potency is Reduced by E153A

Zn²⁺ potency in Hv1 E153A (blue filled circles) is compared with Hv1 WT (grey open squares). Lines represent Hill fits to the data for WT (grey dashed line; IC₅₀ = 3.6 μM, n_H = 0.8) and E153A (blue solid line; IC₅₀ = 241.2 μM; n_H = 0.87). This figure is reprinted from De La Rosa et al., 2018.

CHAPTER 7: DISCUSSION

The structure of Hv1, which is formed by a VSD in the absence of a canonical pore domain, is unique among voltage-gated ion channels. Hv1 also exhibits evidently unique functional properties, including exquisite H⁺ selectivity and steeply Δ pH-dependent gating. The structural bases for these biophysical properties are only just beginning to be understood. The paucity of experimentally-determined high resolution Hv1 structures has confounded efforts to understand the relationships between structure and function in Hv1 in atomic detail.

Computationally-generated Hv1 model structures have been described, but each model is in some way inconsistent with results of functional studies. Here, we pursued a combined experimental and computational approach to explore the structure of Hv1 and to investigate the mechanism of Δ pH-dependent gating. We first developed a new resting-state (Hv1F) and activated-state (Hv1J) model structures using restraints derived from voltage clamp electrophysiological experiments. Classical MD simulations in the presence of membrane lipids and explicit water were carried out on the new models, and we developed new methods for analyzing side chain pK_a values at each time step (i.e., every 2 fs) of the MD trajectories. pK_a analysis of Hv1J identified candidate pH_o-sensing residues in an intracellular network in Hv1, and our predictions are consistent with a recently published experimental study (Cherny et al., 2018). Analysis of Hv1F identified candidate EC pH sensors (E119 and D185), and subsequent experimental studies in E119A, D185A, and E119-D185A mutant Hv1 proteins confirmed that these residues are both required for pH_o sensitivity in Hv1. Together, our studies lead to the development of a new model for Δ pH-dependent gating in Hv1 that invokes state-dependent variable side chain pK_as as a central feature of the gating mechanism. Our results provide an

important proof-of-concept for the combined computational/experimental approach and set the stage for further work that will be necessary to achieve a more complete understanding of the structural basis for ΔpH -dependent gating in Hv1.

7.1: Hv1J Homology Model and Molecular Dynamics

7.1.1: Hv1J Homology Model

A new activated state model of Hv1 (Hv1J) was built using structural restraints derived from experimental data ([Table 1.1](#)). Selectivity data in Hv1 clearly demonstrates that D112 and R211 intimately interact in the activated-state conformation ([Berger and Isacoff, 2011](#); [Musset et al., 2011](#)). While mutant cycle analysis and GIA both indicate E119-R205, E119-R208, and D185-R208 interactions, the two analytic methods do not agree on which interactions make the largest energetic contributions to gating in Hv1. The mutant cycle analysis suggests that the D185-R208 interaction makes the most significant contribution, followed by the E119-R208, and then E119-R205 interaction, whereas GIA indicates that E119-R205 makes the most significant contribution, followed by D185-R208 and then E119-R208.

We pursued a conservative approach in applying D112-R211, D185-R208, and E119-R205 salt bridge structural restraints ([Table 3.2](#)) to build Hv1J, and added additional helical restraints to ensure the backbone structure was maintained. This strategy was successful in producing a model that is consistent with the most important experimental data ([Figure 4.5](#)). The D112-R211 salt bridge that forms the selectivity filter in Hv1 ([Berger and Isacoff, 2011](#)) is a necessary feature of any reasonable Hv1 activated state model and is clearly evident in the Hv1J model ([Figure 4.6A](#)). The Hv1J model also includes E119-R205, E119-R208, and D185-R208 salt bridges ([Figure 4.6B](#)), consistent with the mutant cycle analysis and GIA data ([Table 1.1](#); [Chamberlin et al., 2014](#)) and structural restraints used to build Hv1J ([Table 3.2](#)). Additional interactions between E119-R205 and D185-R211 are also apparent ([Figure 4.6B, C](#)), which is consistent with E119 and D185 selectively stabilizing the activated state of the Hv1 channel ([Ramsey et al., 2010](#); [Randolph et al., 2016](#)). These interactions help to hold the position of S4

such that N214 is in register with F150 ([Figure 4.5A](#)) as indicated by the N214R block voltage clamp experiments (Randolph et al., 2016).

Interestingly, we find that W207 is in the ECEN in Hv1J ([Figure 4.6C](#)) despite this residue not having been included in the structural restraints. This feature is consistent with voltage clamp data indicating that W207 modulates the H⁺ selectivity and EC pH sensing properties of Hv1 (Cherny et al., 2015). Hv1J is the only activated state model of Hv1 that includes W207 in the ECEN, and the Hv1J structure may therefore help to provide a structural explanation for experimental data that previously defied mechanistic explanation. Because Hv1J is the only Hv1 activated-state model that is consistent with all the currently known experimental data, it represents a good candidate model structure for investigating activated-state structure-function relationships.

7.1.2: Hv1J Molecular dynamics

The Hv1J VSD model was successfully simulated in the MD environment for 140 ns. Uncertainty and RMSD analysis ([Figure 4.7A](#)) indicated that the system had stabilized and equilibrated by 30 ns, so trajectory time from 30-140 ns was used to analyze the Hv1J WT system. The stability of the Hv1J model in the MD environment helps to verify it as a thermodynamically feasible model. Importantly, during the course of the MD trajectory D112 and R211 maintained a strong and stable salt bridge ([Figure 4.8A](#)), which is necessary to satisfy the selectivity data (Berger and Isacoff, 2011). D112 is also in close proximity to R208 ([Figure 4.6C](#)), with which it forms a longer range, weaker electrostatic interaction ([Figure 4.8A](#)). Voltage clamp data on the application of IC Zn²⁺ in the Hv1 H140A-H193A double mutant suggests that R208 interacts with D112 to form the selectivity filter (Kulleperuma et al., 2013), but this finding

initially seemed to conflict with the more rigorous D112-R211 selectivity data (Berger and Isacoff, 2011). The formation of a weaker D112-R208 interaction reconciles the previously contradictory findings by showing that D112 may be capable of forming interactions with both R211 and R208.

The E119-R208 salt bridge structural restraint suggested by GIA and mutant cycle analysis ([Table 1.1](#); Chamberlin et al., 2014) is maintained throughout the entirety of the MD trajectory ([Figure 4.8B](#)). E119 also forms an electrostatic interaction with R205 throughout the Hv1J WT simulation ([Figure 4.8B](#)) as is indicated by both the GIA and mutant cycle analysis ([Table 1.1](#)). The E119-R205 interaction is longer range and presumably weaker than the E119-R208 interaction, which is consistent with the GIA, but contradictory with the mutant cycle analysis ([Table 1.1](#)). Experiments to specifically probe the extent of E119-S4 arginine interactions will be necessary to better understand exactly which interactions are present in the activated state of Hv1.

Oddly, D185 never forms any interaction with R208, as is indicated by the GIA and mutant cycle analysis data ([Table 1.1](#)). Instead, D185 forms an electrostatic interaction with R211 ([Figure 4.8B](#)), and, while this D185-R211 interaction has not been tested experimentally, the formation of the D185-R211 interaction is consistent with D185 selectively stabilizing the open state of the Hv1J channel relative to the closed state (Ramsey et al., 2010; Randolph et al., 2016). It is possible that there may be more than one ‘correct’ interacting partner for D185, as seems to be the case for D112 and E119, leaving potential for a D185-R211 interaction. Experiments designed to specifically test which S4 arginine residues interact with D185 are needed to discriminate among activated-state models. Nonetheless, we are optimistic that Hv1J (or refined variants thereof) will be useful for probing the energetics of conformational dynamics

involving Coulombic interactions between and among E119, D185, R205, R208 and other nearby side chains. Indeed, in light of experimental results indicating complexity in the activation gating process ([Mony et al., 2015](#); [Villalba-Galea, 2014](#)), it seems plausible that Hv1 may sample >1 different conformation with distinct ECEN architectures.

Although there is no experimental data specifically identifying a D123-R205 interaction, we observe a stable association throughout the Hv1J MD trajectory ([Figure 4.8B](#)). The D123-R205 interaction during Hv1J MD is consistent with the voltage clamp data indicating that D123 contributes moderately to stabilization of the activated state in Hv1 (Ramsey et al., 2010). A highly dynamic D130-K131 interaction is also evident in the ECEN during Hv1J WT MD ([Figure 4.8B](#)), however there is virtually no data to compare this interaction to, and experimental studies are needed to probe this potential interaction. Although the ECEN structure observed in Hv1J is consistent with the majority of the available experimental data, one big discrepancy is the lack of a stable D185-R208 in the Hv1J MD ([Figure 4.8](#)).

During the course of the Hv1J WT MD simulation, the W207 side chain rotates and pushes the side chain of R208 away from D185 and towards E119 (compare initial coordinates in [Figure 4.6C](#) to final coordinates in [Figure 4.17C](#)). This results in a strong and stable E119-R208 interaction ([Figure 4.8B](#)), but W207 blocks strong and direct interactions between D185 and R208. W207 does not shield D185 from R211 because R211 is below both D185 and W207, allowing for the electrostatic interaction between D185 and R211 to form during MD ([Figure 4.8B](#)). The presence of W207 is consistent with the mutagenesis and voltage clamp data suggesting that W207 works to modify EC pH sensing and H⁺ selectivity (Cherny et al., 2015), and the effect of W207 to prevent a D185-R208 interaction is also consistent with some experimental data ([Table 1.1](#); Chamberlin et al., 2014). Interestingly, W207X mutants have fast

activation and deactivation kinetics, similar to Hv1- Δ C channels (Koch et al., 2008; Tombola et al., 2008). W207 was proposed as a contributor to the Hv1 dimer interface (Okuda et al., 2016). However, the hypothesis that W207 side chains from adjacent protomers interact in a lipid environment (Okuda et al., 2016) is difficult to reconcile with the demonstration that W207X mutations affect EC pH sensing, presumably by interacting with H⁺ (and possibly other side chains) in a well-solvated environment (Cherny et al., 2015). One potential resolution to the apparent discrepancy is that W207 undergoes a switch between a lipid-exposed environment (where it is involved in inter-subunit interactions), and solvent-exposed environment (where it modulates EC pH sensing) during Hv1 gating. Such a change in solvent accessibility to W207 could potentially be accomplished by a rotation of the S4 helix, as has been postulated in the helix-screw model (Tombola et al., 2006), or conversion between alpha and 3-10 S4 backbone helical structure, as has been suggested for other VS domain proteins (Infield et al., 2018; Kubota et al., 2014; Long et al., 2005; Payandeh et al., 2011; Schwaiger et al., 2011; Vieira-Pires and Morais-Cabral, 2010; Villalba-Galea et al., 2008). The hypothesis that movement of W207 during gating involves a substantial thermodynamic barrier is consistent with the experimental data showing faster gating kinetics in W207X mutants (Cherny et al., 2015; De La Rosa and Ramsey, 2018). An alternative (but not mutually exclusive) hypothesis is that the amphipathic W207 side chain lies at a solvent-lipid interface throughout the gating cycle. Experiments designed to identify interacting partners (i.e., side chains, water, and lipids) and pinpoint the mechanism of functional perturbations resulting from W207 mutation are needed to further constrain Hv1 model structures.

Three salt bridges and one electrostatic interaction contribute to ICEN structure in the Hv1J WT MD simulation (Figure 4.8C): strong and stable salt bridge pairs D174-K157, D174-

K221, and E153-K157 and a weaker E171-K221 electrostatic interaction ([Figure 4.8C](#)).

Preliminary data indicates that while K157A and K221A mutations do not appear to alter gating (Ramsey et al., 2010), K157A-K221A causes a negative V_{THR} shift, consistent with the hypothesis that these residues normally interact to stabilize the resting-state conformation ([Figure 4.4A](#)). Because K157 and K221 both interact with D174 in the Hv1J MD trajectory, they could potentially compensate for one another's loss in single-mutant constructs. An intriguing structural hypothesis for the unexpected effect of K157A-K221A is suggested by the Hv1J model structure: that D174-K157 and D174-K221 salt bridges bring the terminal nitrogen atoms of K157 and K221 close enough to produce a moderate repulsive interaction. Mutagenesis data also indicates that E153 and D174 individually contribute to interactions that help to stabilize the closed state (Ramsey et al., 2010) and GIA analysis indicates that these residues directly interact with S4 arginine gating charges ([Table 1.1](#)). Further, the D174E mutation has a larger effect on V_{THR} position than E153D, consistent with our observation that the ECEN network in Hv1J includes two strong S4 Arg salt bridges to D174 but only one to E153 ([Figure 4.8C](#)). E153 and D174 both interact closely with K157 ([Figure 4.8C](#)), potentially allowing the terminal oxygen atoms of E153 and D174 to engage in repulsive interactions in the open state; a repulsive interaction is expected to have the apparent effect of stabilizing the closed state relative to the open state. Our analysis of the ICEN in Hv1J strongly suggests that although Hv1J is compatible with available experimental data, more studies are needed to test specific side chain interactions seen in the ICEN and ECEN structures.

7.1.3: Hv1J PROPKA3.1 pK_a Calculations

pK_a values of residues in Hv1 are hypothesized to be a critical component of ΔpH-dependent gating ([Cherny et al., 1995](#); [DeCoursey, 2018](#); [Ramsey et al., 2010](#)). Unfortunately, it is not yet feasible to measure pK_a values in a functioning Hv1 ion channel, so alternative approaches must be used to investigate this possibility. PROPKA3.1 ([Bas et al., 2008](#); [Li et al., 2005](#); [Olsson et al., 2011](#); [Søndergaard et al., 2011](#)) is an empirical algorithm that has been shown to accurately calculate side chain pK_a values in protein environments ([Alexov et al., 2011](#)). PROPKA3.1 is typically used to determine the ionization state for ionizable residues prior to MD simulations, but here we developed new Python scripts to calculate the pK_a values of all ionizable residues at every step (2 fs intervals) during the equilibrated Hv1J MD simulation. Continuous calculation of pK_a values during an MD run is a novel application of the PROPKA3.1 algorithm, so we sought to validate its use for the purpose of examining pK_a fluctuations during a classical MD simulation.

The determined average pK_a values of Hv1J WT MD were surprising because many of the ionizable residues took values shifted away from the expected solution value ([Figure 4.9](#); [Table 4.1](#)). Because the average pK_a values did not clearly indicate any candidates, an alternative approach to examine residue-residue pK_a correlations was used to search for residues that may interact in ways that influence the pK_a values of the interacting residues.

A covariance analysis of pK_a values calculated during the Hv1J MD trajectory reveals that the H168 exhibits strong covariance with E171 (-0.98) and E164 (-1.01; [Figure 4.10](#); [Figure 4.11A, B](#)). A time course shows that the pK_a values of these residues covary in time in such a way that when the H168 pK_a increases, the E164 pK_a decreases and the pK_a values are inversely correlated ([Figure 4.11A](#)). We interpret correlated changes in pK_a values to reflect side chain pK_a

coupling and coupling predictions made by PROPKA3.1 on Hv1J also indicate that E164 and E171 are coupled residues (data not shown), validating our interpretation of pK_a covariance as pK_a coupling. PROPKA3.1 failed to predict H168 as a coupled residue, as the covariance analysis did, and it is unclear what causes the discrepancy. In any model analyzed using PROPKA3.1 no histidine residue is ever predicted to be coupled (data not shown), so it is possible that the PROPKA3.1 algorithm ignored histidine residues when determining coupled-residue patterns. H168 pK_a is less strongly coupled to K221 (0.55) and D174 (0.17) as well ([Figure 4.11A](#)). H168 was previously identified as being necessary for IC pH sensing (Cherny et al., 2018), and our observation that the pK_a of H168 is highly coupled with the pK_a values of several ICEN residues that are known to contribute to voltage-dependent gating (K157, K221, D174) suggests that our *in silico* methods are useful for *a priori* identification of functionally important residues.

Because H168 is insufficient to reconstitute hHv1-like responses to changes in pH_i when introduced into the background of a species orthologue that naturally exhibits weak pH_i sensitivity, H168 is inferred to interact with partner side chains that have not yet been identified (Cherny et al., 2018). The results of PROPKA3.1 covariance analysis in Hv1J suggests potential H168-interacting partners: D174, K157, K221, E171, and E164 ([Figure 4.10](#)). Among these, D174 is perhaps the most interesting to test because this residue is already known to be critical in voltage-dependent gating and ΔpH -dependent gating is coupled to voltage-dependent gating in Hv1. Having the same residue(s) involved in both voltage- and ΔpH -dependent gating would provide a structural explanation for how this coupling between voltage and ΔpH is achieved. K157 and K221 are also interesting experimental candidates because mutations at these sites shift voltage-dependent gating ([Figure 4.4A](#)). Experimental data are ambiguous about the roles

of E171 and E164 in ΔpH -dependent gating, and additional studies are needed to validate these candidate IC pH sensors.

Electrostatic interactions between residues in proteins are expected to contribute significantly to the residue pK_a values (Pace et al., 2009). Consistent with this hypothesis, we find that the H168 pK_a is correlated with the distance between the terminal oxygen atoms of E164 and the $\text{N}\delta$ atom of H168 (Figure 4.11C, D). This result is consistent with the model proposed here (Figure 7.1) in which electrostatic interactions are important determinates of residue pK_a values in Hv1, and pK_a values in turn influence ΔpH -dependent gating. Due to technical limitations, it is currently not feasible to experimentally measure individual residue pK_a values in the functional Hv1 channel, so direct comparisons between calculated pK_a values represent a promising new alternative technique. *In silico* approaches described here will be used to identify potential interacting partners of residues like H168 that are known to be necessary for ΔpH -dependent gating, and the effects of mutation(s) at newly identified candidate side chains will be evaluated using voltage clamp electrophysiology, as presented previously.

7.2: Hv1F Homology Model and Molecular Dynamics

7.2.1: Hv1F Homology Model

We employed a novel modeling method to refine an existing Hv1 VS domain homology model (Hv1D; [\(Randolph et al., 2016\)](#)) by applying spatial restraints derived from experimental data using Modeller9.16 to develop Hv1F ([De La Rosa et al., 2018](#)). Hv1D was chosen as the template for Hv1F because the register of S4 places R1/R205 across the pore from F150 and a continuous water pathway leads from R1/R205 to both the bulk IC and EC solution, consistent with the H⁺ conductance measured in R1H ([Randolph et al., 2016](#)). Slight modifications of the ECEN Zn²⁺ binding site in Hv1D were needed to make the H140 and H193 histidine residues closer to each other ([Figure 4.2A](#)), and additional refinements added the K157-K221 interaction that is indicated by the voltage clamp data ([Figure 4.4](#)).

Recent publications from our laboratory ([De La Rosa et al., 2018](#)) reinforce the notion that iterative refinement of Hv1 homology models using experimentally-derived structural constraints is a successful approach. Hv1F exhibits the core features expected for a resting-state Hv1 VSD structure ([Figure 4.1](#)), including S4 positioned such that R1/R205 is adjacent to hydrophobic constriction side chains ([Banh et al., 2019](#); [Randolph et al., 2016](#)), deeply hydrated EC and IC vestibules ([Figure 4.3C](#); [Berger and Isacoff, 2011](#); [Hong et al., 2013](#); [Ramsey et al., 2010](#); [Randolph et al., 2016](#)), a Zn²⁺ binding site formed by H140, H193, E119, and D185 ([Figure 4.2](#); [De La Rosa et al., 2018](#); [Ramsey et al., 2006](#)), and a K157-K221 ICEN interaction ([Figure 4.4](#)). The ability of the Hv1F model to predict residues important in ΔpH-dependent gating suggests that the structure is likely to be physiologically relevant and validates our iterative model refinement/experiment method.

7.2.2: Molecular Dynamics on Hv1F WT

The Hv1F model was subjected to 150 ns of classical MD to allow the model to equilibrate before structural properties were assessed. RMSD ([Figure 4.7B](#)) and uncertainty analysis (data not shown) indicates that the Hv1F WT structure reaches an equilibrium state after 60 ns of MD, and so the time range from 60 ns to 150 ns was used to analyze system properties of Hv1F WT. The Hv1F system takes twice as long to equilibrate as the Hv1J system. While no reason can definitively be attributed to explain why Hv1F takes longer to reach equilibrium, one possibility is that spontaneous interactions with Zn^{2+} , which spontaneously diffuses from the bulk solution to transiently interact with ECEN residues in Hv1, introduces additional structural complexity that requires more time to reach equilibrium (data not shown). During the Hv1F MD trajectory, the D174-R208 interaction engineered into the model, which is indicated by the voltage clamp data ([Table 1.1](#); Chamberlin et al., 2014), remained stable ([Figure 4.12A](#)). Furthermore, when harmonic constraints are applied to the Zn^{2+} binding site, the H140-N δ and H193-N δ atoms remain in the first coordination shell of Zn^{2+} (De La Rosa and Ramsey, 2018). Forming a histidine- Zn^{2+} first shell coordination in an MD environment is no trivial feat, and the demonstration that this can be accomplished in the Hv1F model is not only surprising, it further validates the Hv1F model. Unfortunately, several discrepancies between the Hv1F structure and voltage clamp data emerge during the MD simulation.

Even though the E153-R205 and E153-R208 interactions appear in the initial coordinates for Hv1F ([Figure 4.1A, C](#)), these interactions never form during the course of MD ([Figure 4.12A, B](#)) as the experimental data indicates they should ([Table 1.1](#); Chamberlin et al., 2014). A closer look at the experimental restraints used to build the Hv1F model reveals that, while the D174-R208 interaction was included, the E153-R205 and D174-R205 interactions were not

included as restraints. The restraint used for the E153-R208 interaction has mean of 5 Å ([Table 3.1](#)), which may be too high, and could be addressed by refining the Hv1F model using similar spatial restraints on interactions between E153, D174, R1/R205, and R2/R208. The GIA and mutant cycle analysis do not entirely agree, and determining which putative ICEN interactions contribute the most energy to resting-state VSD stabilization remains difficult ([Table 1.1](#)). However, the mutant cycle analysis and GIA do agree that E153-R208 and D174-R208 interactions are stronger than the E153-R205 and D174-R205 interactions ([Table 1.1](#)), so both the E153-R205 and D174 R205 interactions could be added using an average restraint of 5 Å and the E153-R208 and D174-R208 interactions could be restrained using an average of 3 Å. These more robust structural restraints to build a model would likely result in more stable interactions in the Hv1F resting state that better reflect the experimental data.

Instead of forming an interaction with R205 and/or R208 as expected, E153 forms a strong interaction with K157, which in turn has several electrostatic interaction partners ([Figure 4.12B](#)). E153-K157 interactions, along with all the salt bridges involving either K157 or K221 ([Figure 4.12B, C](#)), have not been tested experimentally and so no conclusions can be made about the validity of these interactions in Hv1F MD. Mutagenesis of these residues should help tease out a better understanding of the interacting partners in the ICEN, which can then be used to further refine the Hv1F model.

Despite the discrepancies in the Hv1F model relative to the experimental data suggesting that additional refinement is warranted, Hv1F was useful for identifying residues that are necessary for pH_o sensitivity. We find that two acidic side chains (E119 and D185) directly interact with one another in the resting-state Hv1F model, suggesting that they could exhibit pK_a coupling *in vivo*. Two other nearby acidic groups (D123 and D130) appear likely to modulate

electrostatic interactions between E119 and D185. In good agreement with model predictions, experimental data show that E119A-D185A and D123A-D130A-D185A are nearly pH_o-insensitive under acidic EC conditions ([Figure 5.3](#); [Figure 5.4](#)). The ability to identify functionally important residues *in silico* demonstrates that even an ‘imperfect’ model structure can be useful. We hypothesize that fluctuations in salt bridge distances and calculated pK_a values, may be less strongly dependent on initial input than are average pK_a values during an MD run, and covariance analyses may have allowed us to identify key interactions that might otherwise have been missed.

7.2.3: PROPKA3.1 pK_a Calculations on Hv1F

Because side chain pK_a is directly related to ionization status, understanding pK_a values for ICEN and ECEN residues in Hv1 is essential to a mechanistic understanding of ΔpH-dependent gating. Because the technology to measure the pK_a values of individual residues in Hv1 under voltage clamp is not yet available, we reasoned that the use of computational algorithms to predict pK_a values would allow us to correlate pK_a predictions with experimental data. Electrostatic interactions strongly influence the effective pK_as of residues in the protein environment ([Pace et al., 2009](#)). Strong attractive electrostatic interactions like salt bridges tend to lower acidic residue pK_a values and raise basic residue pK_a values ([Pace et al., 2009](#)). pK_a shifts thus have the effect of stabilizing Coulombic interactions. Conversely, repulsive electrostatic interactions, such as those between two negatively charged residues, causes the pK_a values of interacting residues with shift away from one another. Repulsive electrostatic interactions thus increase the probability that ionizable side chains will adopt their neutral forms,

and may help to mitigate the effect of such repulsive electrostatic interactions to destabilize protein structure.

Salt bridge analyses of Hv1F MD showed that the ECEN lacks stable salt bridges ([Figure 4.12](#)) because there are no positively charged basic residues in proximity to the acidic residues ([Figure 4.1B](#)). The only basic residues in the ECEN are the two histidine residues comprising the Zn²⁺ binding site, H140 and H193 ([Figure 4.1B](#); [Figure 4.2A](#)), but in the MD simulations these His residues are neutral, so H140 and H193 cannot form salt bridges with acidic residues in the ECEN. Consistent with this structural constraint, experimental data show that H140 and H193 are not required for pH_o sensitivity in Hv1. Given the potentially close physical proximity of E119, D123, D130, and D185, ionized side chains could result in a high density of uncompensated negative charge in the ECEN. We therefore hypothesize that pK_as at one or more of these acidic residues may be substantially elevated in the resting-state conformation of the Hv1 VSD.

Similar to Hv1J, PROPK3.1 calculations performed on the Hv1F MD trajectory revealed numerous residues, both basic and acidic, with pK_a values that are substantially different from their default solution values ([Figure 4.13](#); [Table 4.2](#)). A boxplot shows that E119, H168 and D185 pK_as vary widely during the Hv1F MD ([Figure 4.13](#)). In contrast to E119, much of the range in pK_a variation at H168 and D185 is due to the presence of outlier data points ([Figure 4.9](#)). Experimental data indicate that all three of these residues are necessary for pH sensing in Hv1, and it remains unclear whether pK_a fluctuation during an individual MD trajectory is predictive of functional contributions to Hv1 ΔpH-dependent gating. Model refinements to address remaining discrepancies with experimental data could help to address this question. More work is needed to determine how average pK_a values are related to channel function.

Analysis of pK_a covariance in Hv1J successfully identified H168, which appears to function as an IC pH sensor. To identify residues that may function as EC pH sensors, we subsequently analyzed pK_a covariance in Hv1F. E119 and D185 pK_as are highly coupled during Hv1F MD ([Figure 4.14](#); [Figure 4.15C](#)), but this coupling does not begin until around 110 ns ([Figure 4.15C](#)), when E119 and D185 terminal oxygen distances come within range for strong repulsive electrostatic interactions ([Figure 4.15A](#)). Comparing pK_a dynamics before and after the formation of the E119-D185 interaction in the Hv1F MD trajectory is internally controlled, and caveats normally associated with the comparison of two different MD trajectories are mitigated.

The coupling between E119 and D185 is associated with pK_a shifts in both residues, and results in bimodal pK_a distributions for E119 and D185 in Hv1F ([Figure 4.15B](#)). Prior to interacting with D185, E119 pK_a is about 8 ([Figure 4.15C](#)), as evidenced by a peak in the E119 pK_a distribution ([Figure 4.15B](#)). At t=110 ns, when the E119-D185 interaction forms ([Figure 4.15A](#)), the E119 pK_a shifts upward to a value of about 12, and a similar pattern is observed for the distribution of D185 pK_a values ([Figure 4.15B, C](#)). The close interaction between E119 and D185 ([Figure 4.15A](#)) causes the D185 and E119 pK_a values to become coupled, and their pK_a values are highly correlated ([Figure 4.15D](#)). The analysis of E119-D185 pK_a coupling behavior in Hv1F WT provides further evidence that short range electrostatic interactions are significant determinants for residue pK_a values in a protein environment.

The close proximity of E119-D185, which would normally not be stable in the classical MD environment, is facilitated by the presence of Zn²⁺ that diffuses into the binding site at about 110 ns ([Supplementary Figure 1A](#)). The coordinates of the Zn²⁺ were not input into the PROPKA3.1 calculations and so the presence of Zn²⁺ in the ECEN does not directly influence the pK_a of the ECEN residues. A supplementary MD simulation on Hv1F in the presence of 150

mM NaCl instead of ZnCl₂ confirmed that the presence of Zn²⁺ does not alter the calculated pK_a values ([Supplementary Figure 1C-D](#)). There were small differences in the frequency of certain values in the distribution of E119 pK_a in the presence of ZnCl₂ vs. NaCl ([Supplementary Figure 1C-D](#)). The NaCl condition was simulated only briefly (60 ns total) and the Hv1F ZnCl₂ system took until about 60 ns to equilibrate, so it may be that the NaCl system is not fully equilibrated, causing the discrepancies in the E119 pK_a distribution. Importantly, the range of the E119 pK_a values is not altered by the presence of Zn²⁺ ([Supplementary Figure 1C-D](#)).

If the repulsive E119-D185 interaction is indeed a cause of shifted E119 and D185 pK_a values, then the pK_a value of E119 and D185 should not be shifted in Hv1J, where E119-D185 is replaced with E119-R208 and D185-R211 interactions in Hv1J WT ([Figure 4.8B](#)). This is indeed the case for E119, where the pK_a maintains a solution value around 4.5 throughout most of the Hv1J WT MD ([Figure 4.16B](#)), resulting in a peak in the Hv1J E119 pK_a distribution centered at about 4.5 ([Figure 4.16A](#)). Towards the end of the Hv1J WT MD, after 120 ns, the E119-R208 salt bridge begins to dissociate, with the E119-R208 distance increasing ([Figure 4.16B](#)). At the same time, the E119 pK_a shifts up slightly ([Figure 4.16B](#)), as is expected for a negative residue lacking a stable counter charge. The coupling between E119 and D185 ([Figure 4.16C](#)) is disrupted by the replacement of E119-D185 interaction in Hv1F with E119-R208 and D185-R211 interactions in Hv1J ([Figure 4.16D](#)), as would be expected if the E119-D185 interactions is the cause of E119-D185 pK_a coupling, and subsequent pK_a shifts. This analysis suggests that the movement of S4 from the resting to the activated state may actually cause changes in pK_a values of the residues in the ECEN and provides a structural explanation for the coupling between voltage-dependent gating and ΔpH-dependent gating in Hv1.

The pK_a of D185, unexpectedly, did not change much in Hv1J WT MD when compared to Hv1F WT MD ([Figure 4.17A](#)). The D185-R211 interaction, the only electrostatic interaction D185 forms, is too long range to be a strong salt bridge ([Figure 4.8B](#)) and therefore this interaction does not exert much influence on the pK_a value of D185. The D185 pK_a distribution in Hv1J is more narrow than that in Hv1F, with only one peak centered at about 7 ([Figure 4.17A](#)), which is the pK_a value that D185 took during the Hv1F simulation after the formation of the E119-D185 interaction ([Figure 4.15A, C](#)). This is not what would be expected if the E119-D185 interaction was indeed causing the shift of D185 pK_a in the Hv1F MD, as suggested. Just as D185 formed a repulsive interaction in the Hv1F WT simulation that caused downward shift in pK_a , D185 forms a slightly repulsive interaction with the indole nitrogen in the W207 side chain (W207NE1; [Figure 4.17B,C](#)) in the Hv1J WT MD. The close proximity of the D185 terminal oxygen atoms and W207NE1 explains why D185 pK_a behaves in a manner similar to that in the Hv1F MD after the formation of the E119-D185 interaction. Furthermore, D185 is not coupled to any residues in the Hv1J WT structure according to the PROPKA3.1 pK_a covariance analysis ([Figure 4.10](#)), which is reflected as a narrowing of the pK_a distribution of D185 in Hv1J ([Figure 4.17A](#)).

While the analysis on the electrostatic interactions and pK_a values in Hv1F and Hv1J WT simulations presented here can never show a cause and effect relationship, cumulatively the data strongly suggests that electrostatic interactions, both attractive and repulsive, are strong modulators of residue pK_a values in the Hv1 channel environment. It seems likely that these results will also generalize to other protein environments as well. Validation of the pK_a values presented here remains to be determined experimentally, but this data is not likely to become available any time soon.

7.3: Structure of the Δ pH Sensor in Hv1

Early mutagenesis studies to identify the putative pH sensor in Hv1 concluded that no single ionizable residue was alone responsible for Δ pH-dependent gating (Ramsey et al., 2010). A t-test on the early mutagenesis experiments suggested that some single mutants may have Δ pH sensitivity only slightly different than WT ([Table 1.2](#)). Here, it was determined that ENs, formed in part by E119 and D185, are necessary for Δ pH-dependent gating. This is a novel perspective, as it is the first time that explicit interactions between ionizable residues in Hv1 have been confirmed to be responsible for Δ pH-dependent gating properties in Hv1.

7.3.1: There are Two Distinct pH Sensors in Hv1

Previously, H168, a residue in the ICEN, was identified as an IC pH sensor that does not sense EC pH (Cherny et al., 2018). This finding shows that, because H168 cannot sense the EC pH, the earliest mutagenesis studies failed to identify altered Δ pH-dependent gating in H168V mutants because only the EC was changed during voltage clamp experiments (Ramsey et al., 2010). This finding is consistent with the charge-compensation model, the earliest model proposed for Δ pH-dependent gating in Hv1 (DeCoursey, 2018). In the charge-compensation model there are two pH sensors and H^+ occupancy in the two sensors is mutually exclusive, making this an alternating axis model of Δ pH-dependent gating in Hv1. The identification of an ECEN interaction, E119-D185, that is necessary for Δ pH-dependent gating, for the first time provides a structural component of the EC pH sensor and is consistent with the charge compensation model.

It remains to be seen if the E119A-D185A double mutant also has perturbed IC pH sensitivity, but no matter the results of those experiments, it is definitive that there are at least

two distinct pH sensors, one accessible to the EC solution and one accessible to the IC solution. Furthermore, it appears that each pH sensor is composed of a minimum of two residues each. The voltage clamp experiments identifying H168 as an IC pH sensor suggested that other residues interact to produce the IC pH sensing of WT Hv1 (DeCoursey, 2018). While these other IC residues have not yet been identified, the pK_a covariance analysis on Hv1J WT MD reported here suggests that E164, E171, D174, and K221 as interesting experimental candidates ([Figure 4.10](#)). The voltage clamp experiments revealed that E119A and D185A single mutants did not have a robust effect on the Δ pH-dependent gating of Hv1 ([Figure 5.2](#)), while the E119A-D185A double mutant lost Δ pH-dependent gating at EC pH lower than 6.5 ([Figure 5.3](#)), demonstrating that both E119 and D185 are necessary for EC pH sensing in Hv1.

It is of note that E119 is well conserved in VSD sequences and, based on sequence alignments alone, wouldn't necessarily stand out as a residue with functional contributions in Hv1 Δ pH-dependent gating ([Figure 1.2](#)). Interestingly, D185 is conserved only in Hv1 VSD. It is a hydrophobic residue in most other VSDs ([Figure 1.2](#)). The Hv1F pK_a fluctuation calculations suggested that E119 and D185 interact in way that shifts the pK_a of E119 in the resting state ([Figure 4.15](#)), showing that the local electrostatic environment needs to be considered when trying to understand the effects of various substitutions observed in sequence alignments. In the case of Hv1, it seems like the non-conserved D185 residue, rather than providing a new function directly, is responsible for shifting the pK_a of the conserved residue E119, allowing it to take on a new function in the Hv1 VSD not available in other VSD structures. This finding demonstrates analyzing sequences for differences may not be sufficient to identify functionally relevant residues in VSD proteins. Interpreting sequence differences in homologous proteins will require

not only identifying the differences in proteins, but also considering how these substitutions interact with other, conserved residues in the structure.

7.3.2: Coupling Between Voltage-Dependent Gating and Δ pH-Dependent Gating

Voltage-dependent gating and Δ pH-dependent gating are intimately coupled in Hv1 and whether these two properties can be decoupled remains to be determined. Comparison of Hv1F WT and Hv1J WT pK_a calculations suggests a simple mechanism for the coupling between voltage and Δ pH. In the resting state Hv1F model, the pK_a of E119 was shifted significantly upward by a repulsive interaction with D185 ([Figure 4.15](#)), but in the active state model Hv1J, the pK_a of E119 is the expected solution value of 4.5 because of the formation of a stable salt bridge with R208 ([Figure 4.16](#)). The S4 gating charges, including R208, are the known voltage-sensors in Hv1 (Gonzalez et al., 2013; Ramsey et al., 2006; Sasaki et al., 2006) and interpreting the MD results in this light suggests that voltage-dependent gating is coupled to Δ pH-dependent gating by the interactions of S4 gating charges with acidic countercharges in the ICEN and ECEN. When S4 moves between the ICEN and ECEN during gating, the pK_a of the ECEN residues change because of changes in the electrostatic interactions and structure of the ECEN, emerging as Δ pH-dependent gating that is coupled to voltage-dependent gating.

The S4 movement mechanism of coupling between voltage-dependent gating and Δ pH-dependent gating is compatible with the charge compensation model of Δ pH-dependent gating in Hv1. When Hv1 is closed as in Hv1F, S4 is in the down state and occupies the ICEN ([Figure 4.1](#)). Because S4 occupies the ICEN, the IC pH sensing residues interact with S4 arginine gating charges, and therefore H^+ cannot occupy the IC sensor. When Hv1 is open as in Hv1J, S4 is in the up position and occupies the ECEN where the S4 gating charges interact with the EC pH

sensing residues E119 and D185 ([Figure 4.5A-B](#); [Figure 4.6A-C](#); [Figure 4.8B](#); [Table 1.1](#); (Chamberlin et al., 2014). When S4 gating charges are interacting with the ECEN, no H⁺ can occupy the ECEN. Mutual exclusivity of H⁺ occupancy in the IC pH sensor and EC pH sensor, as suggested by the charge compensation model, emerges as a property of the S4 movement mechanism of voltage- and ΔpH-dependent gating coupling

7.3.3: Structure of the Hv1 EC pH Sensor

Consistent with previously published work, the E119A, D123A, D130A, and D185 single mutants did not show a ΔpH sensitivity noticeably different from the WT channel ([Figure 5.2](#)). There is a general trend observed in the ΔV_{thr}-pH_o plots that, as the EC pH becomes more acidic, ΔV_{thr} of the single mutants seems to become more perturbed from WT ([Figure 5.1A](#)). t-tests comparing the ΔV_{thr} values suggest that the effect of E119A, D123A, D130A, and D185A single mutants may not be so straightforward to interpret. However, MD on Hv1F and Hv1J ECEN mutants helps to provide some context for the voltage clamp results.

The t-tests show that at all measured ΔpH, E119A has ΔV_{thr} comparable to that of WT ([Table 5.2](#)), indicating that ΔpH sensitivity is not perturbed in the Hv1 E119A single mutant. In both the Hv1F and Hv1J E119A mutant MD systems, none of the measured salt bridges or pK_a values are altered much by the E119A mutation ([Figure 5.5](#); [Figure 5.7](#); [Figure 5.8](#); [Figure 5.9](#)), consistent with the lack of effect of E119A on ΔpH-dependent gating. Additionally, the mutant MD simulations hint that D123 may actually help compensate for E119A mutations. In the Hv1J E119A-D185A double mutant MD, the pK_a of D123 drops to be close to that of E119 in the Hv1J WT simulation ([Figure 5.7A-B](#)) and a salt bridge between D123 and R208 forms, taking the place of the Hv1J WT E119-R208 salt bridge ([Figure 5.5B](#); [Figure 5.6D](#)). This MD analysis

suggests that D123 is able to compensate for E119A mutations, resulting in no effect on Δ pH-dependent gating in Hv1 E119A, consistent with the voltage clamp data ([Table 5.2](#); [Figure 5.2](#)). D123 compensation for loss of E119 could also explain why there is a robust effect on Hv1 Δ pH-dependent gating in the D123A-D130A-D185A despite there being no effect in the D123A-D130A double mutant ([Figure 5.4A](#); [Table 5.2](#)). When D123 is mutated in the background of the D185A mutant, there is no longer any compensating interactions for E119, resulting in the robust Δ pH-dependent gating effect seen in the D123A-D130A-D185A triple mutant. If D123 is close enough to E119 to compensate for the loss of this residue, then it may be close enough in the WT channel to modulate the EC pH sensor activity.

The concept of EC pH sensor modulators in Hv1 is not new, and W207 has been previously suggested to have a similar role in Hv1 (Cherny et al., 2015). D185, part of the EC pH sensor in Hv1, forms an interaction with the indole nitrogen of W207 in the Hv1J WT MD ([Figure 4.17B-C](#)), which is consistent with the role of W207 as a EC pH sensor modulator. Similarly, the distance between the terminal oxygen atoms of E119 and D123 in the Hv1J WT simulation remain under 8 Å ([Supplementary Figure 2](#)), which may be close enough to modulate the EC pH sensing of E119 and D185. The t-tests suggest that the Δ pH sensitivity in D123A and E119A-D123A mutants may be perturbed at acidic EC pH ([Table 5.2](#)). The D123A and E119A-D123A effect on Hv1 Δ pH-dependent gating is not robust and needs further confirmation, but is consistent with D123 serving as a EC pH modulator. Curiously, the E119A-D123A-D185A triple mutant, while showing significantly perturbed Δ pH-dependent gating relative to WT, exhibited Δ pH-dependent gating virtually identical to that seen in the E119A-D185A double mutant ([Figure 5.4](#)). The data clearly indicates that E119-D185 forms the core of the EC pH sensor in Hv1. If both of these residues are removed, there is no EC pH sensor to modulate. The presence

of D123 makes no difference. The integration of the voltage clamp data and Hv1J MD suggests that D123 may be able to compensate for the loss of E119 in Hv1, resulting in a mild, if any at all, disturbance of Hv1 Δ pH-dependent gating.

t-tests comparing ΔV_{thr} imply that D130A may have altered Δ pH-dependent gating at EC pH lower than 6.5 ([Table 5.2](#)). It is not entirely clear how to interpret this result. No MD simulations on Hv1J D130A mutants were conducted and so no direct comparisons to structural changes in mutants can be made. Comparing the D130-K131 salt bridge in Hv1J WT, E119A, D185A, and E119A-D185A simulations indicates that this interaction occurs over a broad range of distances for all mutants ([Figure 5.5F](#)) and E119A, D185A, and E119A-D185 mutations slightly increase the distance of this D130-K131 interaction, breaking up the salt bridge ([Figure 5.6](#)). The mutations slightly increase the pK_a of D130, suggesting that D130 may interact with, and therefore be a modulator of, the E119-D185 EC pH sensor, in a similar manner to D123, which is consistent with the t-test results. D130 doesn't appear to be very close to the EC pH sensor in Hv1J ([Figure 5.6A](#)) so it is unclear how the ECEN mutations can affect D130 pK_a . It is possible that some kind of long-range electrostatic interaction, such as that shown for Hv1 Zn^{2+} ([Figure 6.1](#)), could also be at play within the ECEN. Confidence in the position of D130 in Hv1J is not high and it is also possible that the Hv1J model needs to be refined so that D130 is closer to E119 and D185, which could probably be accomplished by extending S2 to include D130 at the very top.

t-tests show that the D123A-D130A double mutant has a ΔV_{thr} different from WT at EC pH 5.5, but ΔV_{thr} was not perturbed at any other EC pH value tested ([Table 5.2](#)). This result is unexpected and the MD simulations do not provide any insight into how to interpret the D123A-D130A mutant. More mutant combinations in both voltage clamp experiments and MD

simulations are needed to gain insight into the effects of D123A-D130A on Hv1 structure and Δ pH-dependent gating. Refinements of the Hv1J model and a more thorough analysis of attractive and repulsive electrostatic interactions and residue pK_a fluctuations may also be necessary to gain a comprehensive understanding of structural effects of D123A-D130A mutations in Hv1.

In D185A mutations, the t-tests shows that the ΔV_{thr} values at EC pH 7.5 and 4.5 are both different than WT, suggesting that Δ pH-dependent gating is slightly perturbed from WT, but there was no difference at EC pH 6.5 and 5.5 ([Table 5.2](#)). MD on the D185A mutant showed that the D185A mutation disrupted the E119-R208 salt bridge ([Figure 5.5E](#); [5.6C](#)). This finding is consistent with the rightward shifts in P_{open}-V curves in Hv1 D185A mutants (Ramsey et al., 2010). Previously, the rightward shifts in P_{open}-V curves in D185A mutants were interpreted to mean that D185 interacts with the S4 gating charges to stabilize the Hv1 open state ([Table 1.1](#); [Chamberlin et al., 2014](#); [Ramsey et al., 2010](#); [Randolph et al., 2016](#)), but in the Hv1J WT simulation presented here, D185 never forms strong interaction with S4 arginine residues because of shielding by W207 ([Figure 4.17B-C](#)), which initially seemed inconsistent with the voltage clamp data. However, the Hv1J D185A mutant MD shows that the D185A mutations disrupts the salt bridge between E119-R208, suggesting that D185 may have a strong influence on the ability of E119 to form salt bridges with S4 arginine residues. If D185 influences E119-S4 arginine interactions then, even if there were no D185-S4 arginine interactions, the D185A mutations would still destabilize the open state and result in the observed rightward shifts in P_{open}-V curves as is reported ([Chamberlin et al., 2014](#); [Ramsey et al., 2010](#)). This finding indicates that the Hv1J model may not conflict with the data as much as initially thought, and emphasizes the difficulty in deciphering structural information from voltage clamp experiments.

High resolution structures determined by experimental methods will be necessary to fully comprehend the structure of the Hv1 channel.

Additionally, the D185A mutation causes the E119 pK_a to increase from a solution value of around 4.5 in Hv1J WT MD to around 9 in Hv1J D185A MD ([Figure 5.7A](#)). This finding suggests that the D185A mutation causes the pK_a of E119 to shift so much that it no longer senses EC pH in the same range as WT. E119 pK_a deviations from a value of 4.5 would explain why the D185A mutation appears to have altered ΔpH-sensitivity at EC pH 4.5 as the t-tests indicate ([Table 5.2](#)). The Hv1J D185A mutation is also associated with an increase in D123 pK_a from around 7.5 to around 11 and an increase in D130 pK_a from 5 to around 6, which could potentially explain the altered ΔpH-dependent gating at EC pH 7.5 ([Table 5.2](#)). The changes in the ECEN structure and function caused by ECEN mutations are nuanced, further highlighting the necessity for high resolution experimental structures.

While the integration of published, experimental, and computational data seems to support the hypothesis that compensatory interactions in Hv1 ECEN allow for more than one way to build a ΔpH sensor in Hv1 and some specific interactions can be identified as candidates, no definitive conclusions can be made about what interactions may compensate for one another in the various mutants. Voltage clamp experiments on more double and triple mutant combinations will be necessary to understand the specific interactions and their compensating interactions in mutants in any detail. It will also be necessary to identify residues that are necessary versus sufficient versus residues that serve as modulators instead of sensors, which cannot be teased out with the current experimental data. This will necessitate defining and standardizing what distinguishes a sensor from a modulator. Preliminarily, it seems as if pH

sensors, when mutated, result in a flattening of the $\Delta V_{\text{thr-pH}_o}$ curves and pH sensor modulators result in a change in slope of the $\Delta V_{\text{thr-pH}_o}$ curve when mutated.

The finding that no mutant tested had altered ΔpH -dependent gating at EC pH 6.5-7.5 suggests that there are other residues, which remain to be identified, responsible for sensing the pH in this range. Mutations of E119 and D185, two acidic residues, resulted in disturbance of Hv1 ΔpH -dependent gating at acidic EC pH. Perhaps basic residues are responsible for ΔpH -dependent gating when EC pH is above 6.5. There are no obvious candidates that stand out from the analysis presented here. However, H140 and H193 presumably both have a pK_a in the 6.5-7.5 range and both are in the ECEN and so these two residues may be good starting points to investigate residues responsible for Hv1 ΔpH -dependent gating from EC pH range 6.5-7.5. W207X mutants have been shown to lose pH_o sensitivity at pH_o over 7.5 and, therefore, W207 is an excellent candidate to mutate in combination with E119 and D185 to produce a completely flat $\Delta V_{\text{thr-pH}_o}$ relationship.

It's clear that the active state of Hv1 is ΔpH sensitive (Cherny et al., 1995; Ramsey et al., 2006; Sasaki et al., 2006), but the question of whether the resting state, or both the resting and activated state, is the state capable of sensing ΔpH remains. Previously published data suggests that both the open and closed state are ΔpH sensitive (Cherny et al., 1995; Ramsey et al., 2006; Randolph et al., 2016; Sasaki et al., 2006) and the results of the Hv1F and Hv1J MD are in agreement with these experiments. However, no experiments were done here to explicitly test how the closed-state H^+ conductance may be affected by the ECEN mutation. This hypothesis could be tested by engineering E119A-D185A mutations into the background of R205H-N214R mutants. This experiment could prove to be incredibly difficult as four mutations are required. E119A-D185A measurements could also be made on gating charges, but these would also

require simultaneous mutations W207A and N214R (De La Rosa and Ramsey, 2018). These experiments are not trivial, but understanding if Hv1 closed state H^+ conductance is also ΔpH sensitive as the active state conductance is crucial to development of a complete picture of ΔpH -dependent gating in Hv1.

The combined experimental and computational approach used here proved to be quite successful at identifying pH sensors in Hv1. Moving forward, more advanced computational methods could be applied to better understand the intricacies of the structural effects of ECEN mutations. Solvation properties, water accessibility, and hydrogen bonds are also determinants of protein residue pK_a values and, therefore, assessing the dynamics and structure of water and hydrogen bonds during the MD simulations will be critical to understanding the structural and functional effects of various mutations. The structure of Hv1 itself is not well understood and so trying to understand the structure and dynamics of water and hydrogen bonds within the Hv1 channel seems unobtainable, and so water and hydrogen bond analysis was avoided in this study. Additionally, it is much harder to correlate these MD properties to experimental data in Hv1, as there is no currently available method that can study the structure of water in a channel under voltage clamp. To avoid complications in interpreting water and hydrogen bond analysis data, the focus was kept on understanding the structure of ENs in Hv1 for this project.

Recent developments in MD force fields provide more rigorous alternatives than classical MD to study water structure, dynamics, and hydrogen bonds in Hv1. Protein electrostatic interactions are influenced by water-water and water-protein interactions within the Hv1 channel, and polarizable force fields could allow for a more realistic representation of the electrostatic interactions, including hydrogen bonds, during the course of MD simulations. Polarizable force fields like Drude (Lemkul et al., 2016) better account for dipole moments in polar molecules

such as water. The Hv1 coordinates could then be fed into the PROPKA3.1 pK_a calculation algorithm in a manner similar to that presented here. This approach would be straightforward, however application of polarizable force fields is relatively new so extra care in ensuring convergence, which can be difficult to achieve, is necessary. The polarizable force fields will likely be a better tool than classical MD for investigations of how water structure, dynamics, and hydrogens bonds influence Hv1 structure and function.

Constant pH MD is a newer and more robust method that could be used to investigate residue pK_a values in Hv1. In constant pH MD, the pH of the solution is held constant and a specified group of residues is allowed to titrate so that explicit titration curves for specific residues can be calculated (Wallace and Shen, 2009). While constant pH MD can be an extremely powerful method for studying ΔpH -dependent gating in Hv1, it is computationally demanding, taking up a large amount of time for a single simulation. Because of the computational cost, the system has to be reduced and does not model explicit water, which, as discussed, is important in determining electrostatic interactions and, subsequently, pK_a values. Furthermore, achieving convergence is also an issue, making this a technically demanding MD method. To date, the constant MD method has not been successful at identifying pH sensors in Hv1. However, with advances in computer science constant pH MD will become more accessible and easier to run.

Quantum mechanics simulations (QM) may also be useful for investigating mechanisms of Hv1 ΔpH -dependent gating. In fact, QM has already been successfully applied to Hv1 to investigate the mechanism of the D112-R211 H^+ selectivity filter (Dudev et al., 2015). Although the model used in this published QM is not consistent with the experimental data, it does demonstrate that QM can be applied to Hv1 to study electrostatic interactions and their

associated functions. The results of QM are highly dependent on the input coordinates so more rigorous, experimentally-determined structures would be preferred before performing QM simulations. Furthermore, QM can currently only be applied to a partial Hv1 system, with only a few residues represented. Consequently, QM simulations would not be capable of studying allostery between ECEN and ICEN, which is possible with classical MD. However, system size in QM may also improve with the development of new hardware and better algorithms. Regardless, QM will remain useful for understanding the chemistry of electrostatic interactions, which will further our understanding of the mechanisms of H⁺ selectivity, ΔpH-dependent gating, and H⁺ conduction mechanisms.

While these alternative methods are likely to be more rigorous MD methods for investigating Hv1 ΔpH-dependent gating, the PROPKA3.1 pK_a fluctuation and covariance analysis was successful in identifying H168, E119, and D185 as pH sensors. This method is also easy to apply and is not as computationally demanding as other MD methods, making it more accessible to both low-budget labs and novices trying to learn the MD method. Because classical MD is less computationally demanding, these simulations and the pK_a calculations take less time than would be required for one constant pH MD or QM simulation. The pK_a fluctuation and covariance analysis technique developed here proves to be a good compromise between utility in identifying experimental candidates, accessibility, and quick turnover from model building to MD analysis to experiment.

7.4: Allosteric Communication Between ICEN and ECEN

The existence of two electrostatic networks was proposed upon the first extensive mutagenesis experiments on Hv1 (Ramsey et al., 2010) and has since been confirmed by mutant cycle analysis experiments ([Table 1.1](#); [Chamberlin et al., 2014](#)). The counter charge model of ΔpH -dependent gating (DeCoursey, 2018) invokes two pH sensors, one EC sensor and one IC sensor, which the data indicates are formed by electrostatic interactions between at least two residues, rather than single residues. The voltage-dependence of Hv1 gating is dependent on ΔpH gradient, rather than the absolute pH in either the EC or IC solution (Cherny et al., 1995), so it seems as if the IC and EC pH sensor must communicate to emerge as ΔpH -dependent gating.

The results of ΔpH -dependent gating experiments are not always easy to interpret. Some mutations produce seemingly small changes in ΔpH sensitivity, which the MD suggested was associated with changes in electrostatic network organization and residue pK_a values, but the relevance of these changes remains to be determined. A more robust assay than changes in the ΔpH sensitivity are necessary to assess communication between the ECEN and ICEN. The Zn^{2+} binding site includes residues E119 and D185 that were confirmed in this study to also be EC pH sensors ([CHAPTER 5](#); [Figure 5.3](#)) and EC Zn^{2+} has the same effect as H^+ on voltage-dependent gating in Hv1 (Cherny and DeCoursey, 1999; Ramsey et al., 2006; Sasaki et al., 2006). This suggests that Zn^{2+} and EC H^+ potency are intimately linked and likely share a mechanism in modulating voltage-dependent gating in Hv1 and therefore, measuring Zn^{2+} potency in Hv1 is a good alternative to measuring ΔpH -dependent gating to assess communication between ECEN and ICEN.

7.4.1: Correlation Between ICEN Salt Bridge Distances and ECEN Histidine-Zn²⁺

Distances

In a previous publication, a computational approach to simulate histidine-Zn²⁺ interactions was devised to investigate the possible structural changes associated with Zn²⁺ binding (De La Rosa et al., 2018). During the course of the Zn²⁺ binding MD, harmonic constraints between the H140 and Zn²⁺ and H193 and Zn²⁺ were gradually reduced until H140 and H193 could coordinate Zn²⁺ in the first shell without any constraints. Eventually, Zn²⁺ was allowed to dissociate from the ECEN binding site and the changes in the organization of electrostatic networks were assessed. Surprisingly, it was found that the E153-R208 salt bridge distance is highly correlated with histidine-Zn²⁺ distances in the ECEN. This is similar to the effect of ECEN mutations on the organization of the ICEN observed in the Hv1F simulations reported here ([CHAPTER 5](#)), in which the ECEN mutations were associated with the slight strengthening of several ICEN electrostatic networks. These observations further support the close link between ΔpH and Zn²⁺ effects on Hv1 voltage-dependent gating. This MD data also supports the hypothesis that the ECEN and ICEN can communicate on the status of the network.

7.4.2: Mutations in the ECEN Diminish EC Zn²⁺ Potency

If there is indeed communication between the ECEN and ICEN, the mutations in the ICEN should influence Hv1 ability to sense EC H⁺ or Zn²⁺. Mutating E153 in the ICEN to alanine and measuring EC Zn²⁺ demonstrated that, as expected if the ECEN and ICEN networks communicate, the E153A mutant showed a diminished EC Zn²⁺ potency ([Figure 6.1](#)). This result supports the hypothesis that the ECEN and ICEN communicate to influence Zn²⁺ potency. The exact mechanisms of this phenomenon are still unclear. It could be the E153A mutation disrupts

the E153-R208 interaction that is an important stabilizer of the closed-state Hv1 channel (Chamberlin et al., 2014; Ramsey et al., 2010) and therefore hinders the ability of Zn^{2+} to stabilize the closed-state of Hv1. Alternatively, as suggested by MD, mutating the ICEN may cause rearrangements in the ECEN that make Zn^{2+} less potent. These two mechanisms are not mutually exclusive, so there is also a possibility that both coupling via S4 interactions as well as EN rearrangement are possible for the coupling between ECEN and ICEN. More work is necessary to further clarify the nature of coupling between ECEN and ICEN in Hv1, however, it seems likely that this result will also apply to pH sensing.

To verify that this result also extends to Δ pH-dependent gating in Hv1, the E153A mutant should be measured under different EC pH gradients, as was done for the ECEN mutations presented in [CHAPTER 5](#). Mutating E153 to alanine should cause a change in the EC pH sensitivity if the ECEN and ICEN can communicate, as was demonstrated for EC Zn^{2+} ([Figure 6.1](#)). The extent of change in EC pH sensitivity is difficult to predict. The mutations could change the slope, and hence the Δ pH sensitivity, of the ΔV_{thr-pH_i} curves, knock out the Δ pH sensitivity in the same pH range or a different pH range than the E119A-D185A mutant. It may also be necessary to mutate more than one ICEN residue at a time to elicit a response, as was necessary in the EC pH experiments presented here for E119A-D185A Hv1 double mutants. The salt bridge- Zn^{2+} -histidine correlation analysis suggest that D174, like E153, may also be a good experimental candidate because the D174-S4 arginine salt bridges distances are also highly correlated with H140- and H193- Zn^{2+} distances (De La Rosa et al., 2018). Furthermore, just as was the case for E153, D174 has also known to interact with S4 arginine charges to stabilize the resting state of the channel (Chamberlin et al., 2014; Ramsey et al., 2010). Additionally, D174E, like E153A, mutations were shown to have slightly perturbed Δ pH sensitivity in preliminary t-

tests to compare ΔpH sensitivity in various mutants ([Table 1.2](#)). The pK_a covariance analysis has proven to be successful at identifying pH sensors in Hv1 and the pK_a covariance analysis on Hv1J WT showed that the pK_a of H168 is highly correlated to D174 pK_a . Together these data identify D174 as an interesting experimental candidate for both Zn^{2+} as well as IC pH sensor.

Another necessary experiment is to examine if the E119A-D185A double mutant has altered IC pH sensitivity. The H168 IC pH sensor was determined not to be able to sense the EC pH (Cherny et al., 2018) so, presumably, the E119-D185 EC pH sensor will not sense the IC pH. However, no experiments were done to explicitly test this hypothesis and the data presented in this work can neither support nor refute the hypothesis that E119-D185 EC pH sensor does not sense the IC pH. This hypothesis could be easily tested by performing the same E119A-D185A double mutant voltage clamp experiments in the inside-out patch configuration instead of whole cell configuration. This slight change in experimental set up would allow for the IC pH to be changed during the course of a single experiment while the EC pH is held constant.

7.5: A Refined Mechanism of Δ pH-Dependent Gating in Hv1

Aggregation of all the available data suggests a model of gating that requires a minimum of two steps, a voltage-dependent step and Δ pH-dependent step ([Figure 7.1](#)). A two-step gating model is consistent with previous voltage clamp data indicating that a voltage-independent transition precedes opening of the H^+ conduction pathway (Villalba-Galea, 2014). The Hv1F MD pK_a calculations suggest that E119 has a high pK_a in the resting state and thus is protonated, carrying a neutral charge. The protonation of Hv1 in the resting state helps to mitigate the destabilizing effects caused by the close proximity of the terminal oxygen atoms of E119 and D185. Based on the Hv1J MD pK_a calculations it appears that after voltage sensor activation, replacement of E119-D185 interactions with E119-R208 interactions causes the pK_a of E119 to shift back down to value for a glutamate residue in solution. This downward shift in the pK_a of E119 caused by the movement of S4 would result in deprotonation of E119, which is consistent with the kinetic ([Villalba-Galea, 2014](#)) and VCF (Mony et al., 2015) data demonstrating a voltage independent movement in the EC end of S1, which is the location of E119, preceding channel opening. Deprotonation of E119 is the first structural explanation provided for the voltage-independent movements in S1 measured under voltage clamp conditions. Whether H^+ occupancy is localized to E119 alone or delocalized through other residues in the network like D185 and W207 remains to be determined and will be nontrivial to determine experimentally. The E119-D185 interaction, with and without W207 present, would be a good candidate for DFT calculations to further explore the functional effects of this interaction.

In the previously proposed countercharge model of Δ pH-dependent gating, the movement of S4 causes the gating charge arginine residues to transition from interactions in the ICEN to interactions in the ECEN, or vice versa during gating ([Figure 7.1A](#); [DeCoursey, 2018](#)).

Protonation events in the ICEN or ECEN can modulate the strength of electrostatic interactions that stabilize the resting/closed or activated/open state, respectively. H^+ binding events at acidic residues compete for interactions with S4 arginine gating charges, and thus the pK_a and protonation states of acidic countercharges in S1-S3 influence the strength of electrostatic interactions between these countercharges and S4 gating charges, which can subsequently modulate voltage-dependent gating. When the ICEN-S4 arginine interactions are disrupted during gating from closed-state to open state, the ICEN pK_a shifts to higher values ([Figure 7.1A, left](#)). Similarly, disruption of ECEN-S4 arginine interactions during open state to closed-state gating causes the ECEN pK_a to shift high ([Figure 7.1A, right](#)).

Experimental data show that E119 and D185 are activated-state S4 Arg ‘counter-charge’ side chains and are primary structural determinants of the EC pH sensor, whereas D123, D130, and W207 serve secondary or modulatory roles. H168 is a necessary component of the IC pH sensor, but the other ICEN residues remain to be identified. Structural models and experimental data show that E153 and D174 are resting-state S4 Arg ‘counter-charges’, and we hypothesize that these residues are likely candidates for primary pH sensing sites in the ICEN. pK_a calculations show that E153 and D174 are coupled to H168 in the Hv1J activated-state model ([Figure 4.10](#)) and to E119 and D185 in the Hv1F resting-state model ([Figure 4.14](#)). Together, experimental and computational studies suggest that coupling between ΔpH -dependent gating and voltage-dependent gating requires that acidic ‘counter-charges’ in the ECEN (E119 and D185) or ICEN (E153 and D174) interact with S4 Arg gating charge side chains in a mutually exclusive fashion to stabilize activated- and resting-state VSD conformations, respectively ([Table 1.1](#); Chamberlin et al., 2014; Ramsey et al., 2010). The precise contributions of putative secondary ICEN (K157, E164, E171, E225, and K221) and ECEN (D123, D130, and W207) side

chains to network structures remains less clear, but we hypothesize that these residues are involved in pK_a tuning at primary sites. In summary, voltage-dependent translation of S4 drives conformational changes in the ECEN and ICEN that result in large pK_a shifts at primary pH-sensing sites, and changes in charge status secondarily affect the resting- vs. activated-state equilibrium by altering the strength of Coulombic interactions with S4 Arg gating charge side chains. ECEN and ICEN side chain pK_a s are also influenced by interactions with secondary groups and may allow for allosteric coupling between ECEN and ICEN residues.

Alternative mechanistic models to explain coupling between Δ pH- and voltage-dependent gating are possible. One possibility is that coupling between voltage- and Δ pH-dependent gating is achieved entirely by the movement of the S4 helix, and allosteric interactions between ECEN and ICEN are not required. Here, a change in pH_o or pH_i results in differential H^+ occupancy at ECEN or ICEN proton binding sites, respectively, and thereby directly modulates the strength of S4 Arg-to-acidic counter charge Coulombic interactions to alter the Hv1 activated- (open) to resting- (closed)-state equilibrium ([Figure 7.1B](#)). We model the effect of changes voltage-dependent S4 position on H^+ occupancy in the ECEN and ICEN by invoking coupling coefficients M and L , respectively ([Figure 7.1C](#)). Mutations that alter pH_o or pH_i sensitivity could therefore achieve their effects by either altering ECEN or ICEN pK_a s or by changing the values of M or L ([Figure 7.1C](#)).

A third coupling coefficient (N) may be postulated to represent free energy changes associated with allosteric coupling between the ECEN and ICEN ([Figure 7.1D](#)). The necessity for N is suggested by our finding that EC Zn^{2+} potency is modulated by neutralization of the ICEN residue E153 ([Figure 6.1](#)). Voltage clamp experiments may be able to measure the Δ pH-dependent Hv1 function without provoking voltage-dependent movement of S4, and could be

used to measure the effects of mutations on N independent of M and L . Experiments like those presented in [CHAPTER 5](#) (i.e., resting-state H^+ currents in R205H) also hold promise as a method for measuring the pH dependence of the resting- (closed)-state conformation. Indeed, gating of the resting-state H^+ conductance in R205H is modulated by changes in pH_o (Randolph et al., 2016). It should therefore be possible to determine whether mutations primarily alter ΔpH -dependent gating by altering ECEN or ICEN pK_a s or coupling coefficients, and future studies may allow us to discriminate between direct and indirect coupling mechanisms.

Our new model allows us, for the first time, to predict how changes in pH_o or pH_i will simultaneously alter ECEN and ICEN side chain titration curves and the P_{open} - V relation in Hv1 ([Figure 7.2](#)). We hypothesize that mutually exclusive H^+ occupancy at ECEN and ICEN sites could explain why ΔpH -dependent gating of Hv1 appears to be linear (~ 40 mv/pH unit) rather than saturable ([Figure 7.2, left](#)). H^+ binding to monoprotic site(s) is expected to manifest a sigmoidal dependence on pH_o or pH_i , as illustrated by the Henderson-Hasselbach equation ([Pou and Senozan, 2001](#)). Hv1J pK_a analysis suggests that the E119A-D185A mutations cause an increase in the ECEN pK_a , resulting in a leftward shift in the voltage-dependent gating titration curve that brings saturation of Hv1 ΔpH -dependent gating into the experimentally-measurable ΔpH range ([Figure 7.2, left](#)). We therefore predict that pH_o responses in WT saturate at acidic pH values that are difficult or impossible to measure in intact cells under physiological conditions. Glu and Asp exhibit solution pK_a values of 3.8 and 4.5, respectively, and the apparent loss of EC pH sensitivity at acidic EC pH (i.e., $pH_o \leq 5.5$) in E119A-D185A is consistent with the idea that the mutations cause an upward shift in the ECEN pK_a , resulting in saturation of ΔpH -dependent gating at less acidic pH_o and therefore within in the measurable range ([Figure 7.2](#)).

Previously published data suggest that WT Hv1 saturates at high IC and EC pH (i.e., $\text{pH}_{i/o} \geq 8.5$), which is within the measurable range ([Figure 7.2, middle; Cherny et al., 2015](#)). However, reversal potential analyses also indicate that the H^+ gradient is unlikely to remain intact at high pH due to a nonspecific transmembrane H^+ shuttling mechanism, raising the possibility that deviations in the slope of the V_{THR} vs. ΔpH relation at high pH_i are influenced by experimental conditions, and may not be adequately controlled even by the inclusion of 100 mM pH buffer in recording solutions ([Cherny et al., 1995, 2015](#)). Even if the reported effects of $\text{pH}_{i/o} > 8.5$ on V_{THR} shifts in WT Hv1 are not influenced by experimental artefacts, W207 mutations do appear to allow saturation to be observed at less alkaline pH_o ([Cherny et al., 2015](#)), suggesting that similar effects of other candidate EC pH-sensing residues may also be experimentally measurable. If EC and IC saturation only occurs at unmeasurably low pH_o or high pH_i the full titration curve for WT Hv1 channel remains undetermined ([Figure 7.2, right](#)). At intermediate (i.e., experimentally-measurable) pH_o and pH_i values, ΔpH -dependent gating may therefore appear to be quasi-linear (~ 40 mV/pH unit) at all measurable ΔpH ([Figure 7.2, right](#)).

Still, the apparently linear slope of V_{thr} shifts (~ 40 mV/pH unit) measured over a wide range (i.e., pH 3.5 – 8.5) is substantially shallower than ionization of a monoprotic H^+ binding site (i.e., Henderson-Hasselbach behavior) seems to predict. We hypothesize that the inclusion of >1 anionic side chain in ECEN and ICEN structures results in polyprotic H^+ binding sites. The multiple titration sites of polyprotic acids and/or negative cooperativity resulting from repulsive electrostatic interactions between acidic side chains may at least partially explain the shallow V_{thr} vs. ΔpH relations measured in WT and mutant Hv1 channels. Having the ability to predict these titration curves and the effects of mutations in an empirical model of voltage- and ΔpH -dependent gating is likely to result in new hypotheses and experiments that further our

understanding of Hv1 gating mechanisms. Our current work therefore represents an important advance in the understanding of the relationships between VSD structure and H⁺ channel gating.

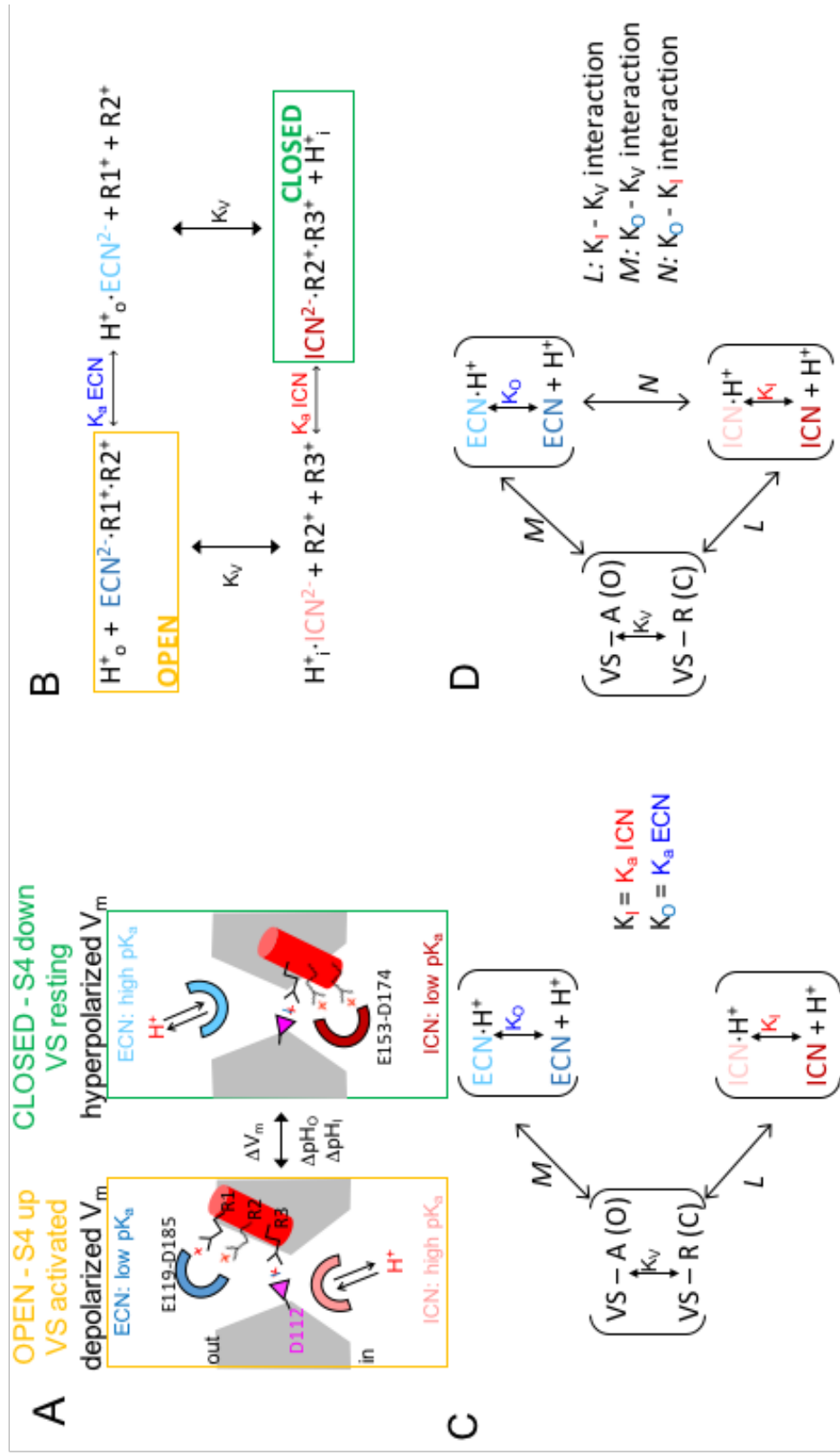


Figure 7.1: Model of ΔpH -Dependent Gating in Hv1

A: A cartoon representation of ΔpH -dependent gating in Hv1 with the EC side of the cell shown at the top and IC side at the bottom. The open state is shown on the left outlined in yellow while the closed state is shown on the right outlined in green. The red cylinder represents the S4 helix with the S4 arginine gating charges, represented as sticks with '+' signs. The pink triangle represents D112 and the grey blocks represent the rest of the Hv1 protein. The ECEN is represented by the blue horseshoe and labeled ECN, while the ICEN is shown by a red horseshoe and labeled ICN.

B: A kinetic model of Hv1 voltage-dependent gating in Hv1. H_0^+ represents a proton on the EC side of the cell and H_i^+ represents a proton on the IC side of the cell. R1^+ and R2^+ represent the first and second S4 gating charges R205 and R208, respectively. The state outlined in yellow represents the activated open state of the channel and corresponds to the cartoon representation outline in yellow in (A). The state outlined in green corresponds to the resting closed state depicted in the cartoon representation outlined in green in (A). The titration of the ECEN, labeled ECN^{2-} , results in activated-closed to activated-open transitions represented on the top and has a rate of $K_a\text{ECN}$. Titration of the ICEN, labeled ICN^{2-} , causes a transition between resting and closed states with rate $K_a\text{ICN}$, represented on the bottom. The vertical transition with rate $K_{(V)}$ is the voltage-dependent gating transition.

C: A model of how voltage-dependent gating could be coupled to ΔpH -dependent gating. The voltage-dependent gating model represented in (B) is collapsed into the transition represented as VS-A(O) to VS-R(C). In this model voltage-dependent gating is coupled to both the titration reaction in the ECEN and in the ICEN with a coupling coefficient of M and L, respectively. $K_a\text{ECN}$ and $K_a\text{ICN}$ from (A) are renamed as K_o and K_i , respectively.

D: An alternative model of coupling between voltage- and ΔpH -dependent gating. The model is very similar to that depicted in (C) with the only difference being a third coupling parameter, N, introduced to represent the potential for direct coupling between the ECEN and ICEN.

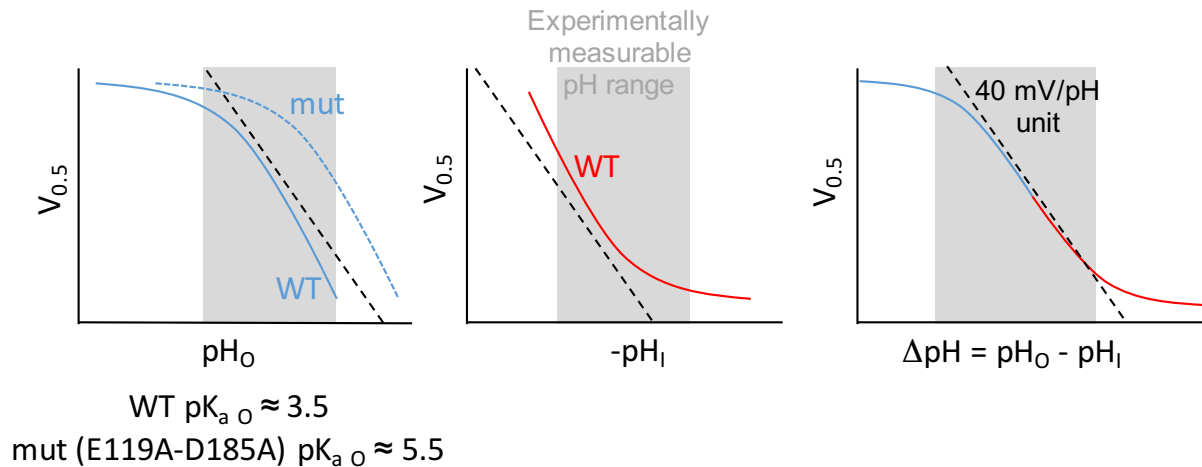


Figure 7.2: Predicted Titration Curves of Hv1

Predicted titration curves for Hv1 based on Δ pH-dependent gating mutagenesis experiments. At all experimentally measurable pH values in the voltage clamp set up, represented by the grey box, the Δ pH sensitivity is linear, shifting about 40 mV/pH unit change, represented by the black dashed line. The plot on the left represents the relationship between voltage-dependent gating of Hv1 WT and E119A-D185A changing EC pH (pH_0). The plot in the middle shows the relationship between changing IC pH (pH_i) and the voltage-dependent gating. The plot on the right combines the effects of pH_i and pH_0 on voltage-dependent gating in WT Hv1 to show how sensing both EC pH and IC pH emerges as Δ pH-dependent gating, with a linear relationship at all measurable pH ranges.

BIBLIOGRAPHY

- Ackers, G.K., and Smith, F.R. (1985). Effects of site-specific amino acid modification on protein interactions and biological function. *Annu. Rev. Biochem.* *54*, 597–629.
- Aggarwal, S.K., and MacKinnon, R. (1996). Contribution of the S4 segment to gating charge in the Shaker K⁺ channel. *Neuron* *16*, 1169–1177.
- Alexov, E., Mehler, E.L., Baker, N., Baptista, A.M., Huang, Y., Milletti, F., Nielsen, J.E., Farrell, D., Carstensen, T., Olsson, M.H.M., et al. (2011). Progress in the prediction of pK_a values in proteins. *Proteins* *79*, 3260–3275.
- Bánfi, B., Schrenzel, J., Nüsse, O., Lew, D.P., Ligeti, E., Krause, K.H., and Demaurex, N. (1999). A novel H⁽⁺⁾ conductance in eosinophils: unique characteristics and absence in chronic granulomatous disease. *J. Exp. Med.* *190*, 183–194.
- Banh, R., Cherny, V.V., Morgan, D., Musset, B., Thomas, S., Kulleperuma, K., Smith, S.M.E., Pomès, R., and DeCoursey, T.E. (2019). Hydrophobic gasket mutation produces gating pore currents in closed human voltage-gated proton channels. *Proc. Natl. Acad. Sci. U.S.A.* *116*, 18951–18961.
- Bas, D.C., Rogers, D.M., and Jensen, J.H. (2008). Very fast prediction and rationalization of pK_a values for protein-ligand complexes. *Proteins* *73*, 765–783.
- Bayless-Edwards, L., Winston, V., Lehmann-Horn, F., Arinze, P., Groome, J.R., and Jurkat-Rott, K. (2018). NaV1.4 DI-S4 periodic paralysis mutation R222W enhances inactivation and promotes leak current to attenuate action potentials and depolarize muscle fibers. *Sci Rep* *8*, 10372.
- Bennett, A.L., and Ramsey, I.S. (2017a). CrossTalk opposing view: proton transfer in Hv1 utilizes a water wire, and does not require transient protonation of a conserved aspartate in the S1 transmembrane helix. *J. Physiol. (Lond.)*.
- Bennett, A.L., and Ramsey, I.S. (2017b). Rebuttal from Ashley L. Bennett and Ian Scott Ramsey. *J. Physiol. (Lond.)* *595*, 6803.
- Berger, T.K., and Isacoff, E.Y. (2011). The pore of the voltage-gated proton channel. *Neuron* *72*, 991–1000.
- Best, R.B., Zhu, X., Shim, J., Lopes, P.E.M., Mittal, J., Feig, M., and Mackerell, A.D. (2012). Optimization of the additive CHARMM all-atom protein force field targeting improved sampling of the backbone ϕ , ψ and side-chain $\chi(1)$ and $\chi(2)$ dihedral angles. *J Chem Theory Comput* *8*, 3257–3273.

- Bezanilla, F. (2008). How membrane proteins sense voltage. *Nat. Rev. Mol. Cell Biol.* *9*, 323–332.
- Boyd, R.S., Jukes-Jones, R., Walewska, R., Brown, D., Dyer, M.J.S., and Cain, K. (2009). Protein profiling of plasma membranes defines aberrant signaling pathways in mantle cell lymphoma. *Mol. Cell Proteomics* *8*, 1501–1515.
- Capasso, M., Bhamrah, M.K., Henley, T., Boyd, R.S., Langlais, C., Cain, K., Dinsdale, D., Pulford, K., Khan, M., Musset, B., et al. (2010). HVCN1 modulates BCR signal strength via regulation of BCR-dependent generation of reactive oxygen species. *Nat. Immunol.* *11*, 265–272.
- Capasso, M., DeCoursey, T.E., and Dyer, M.J.S. (2011). pH regulation and beyond: unanticipated functions for the voltage-gated proton channel, HVCN1. *Trends Cell Biol.* *21*, 20–28.
- Carmona, E.M., Larsson, H.P., Neely, A., Alvarez, O., Latorre, R., and Gonzalez, C. (2018). Gating charge displacement in a monomeric voltage-gated proton (Hv1) channel. *Proc. Natl. Acad. Sci. U.S.A.* *115*, 9240–9245.
- Chamberlin, A., Qiu, F., Rebolledo, S., Wang, Y., Noskov, S.Y., and Larsson, H.P. (2014). Hydrophobic plug functions as a gate in voltage-gated proton channels. *Proc. Natl. Acad. Sci. U.S.A.* *111*, E273-282.
- Chanda, B., and Bezanilla, F. (2008). A common pathway for charge transport through voltage-sensing domains. *Neuron* *57*, 345–351.
- Chen, X., Wang, Q., Ni, F., and Ma, J. (2010). Structure of the full-length Shaker potassium channel Kv1.2 by normal-mode-based X-ray crystallographic refinement. *Proc. Natl. Acad. Sci. U.S.A.* *107*, 11352–11357.
- Cherny, V.V., and DeCoursey, T.E. (1999). pH-dependent inhibition of voltage-gated H(+) currents in rat alveolar epithelial cells by Zn(2+) and other divalent cations. *J. Gen. Physiol.* *114*, 819–838.
- Cherny, V.V., Markin, V.S., and DeCoursey, T.E. (1995). The voltage-activated hydrogen ion conductance in rat alveolar epithelial cells is determined by the pH gradient. *J. Gen. Physiol.* *105*, 861–896.
- Cherny, V.V., Morgan, D., Musset, B., Chaves, G., Smith, S.M.E., and DeCoursey, T.E. (2015). Tryptophan 207 is crucial to the unique properties of the human voltage-gated proton channel, hHV1. *J. Gen. Physiol.* *146*, 343–356.
- Cherny, V.V., Morgan, D., Thomas, S., Smith, S.M.E., and DeCoursey, T.E. (2018). Histidine168 is crucial for ΔpH-dependent gating of the human voltage-gated proton channel, hHV1. *J. Gen. Physiol.*

- Cho, D.-Y., Hajighasemi, M., Hwang, P.H., Illek, B., and Fischer, H. (2009). Proton secretion in freshly excised sinonasal mucosa from asthma and sinusitis patients. *Am J Rhinol Allergy* 23, e10-13.
- Chowdhury, S., and Chanda, B. (2012). Estimating the voltage-dependent free energy change of ion channels using the median voltage for activation. *J. Gen. Physiol.* 139, 3–17.
- Chowdhury, S., Haehnel, B.M., and Chanda, B. (2014a). A self-consistent approach for determining pairwise interactions that underlie channel activation. *J. Gen. Physiol.* 144, 441–455.
- Chowdhury, S., Jarecki, B.W., and Chanda, B. (2014b). A molecular framework for temperature-dependent gating of ion channels. *Cell* 158, 1148–1158.
- Cramer, C.J. (2004). *Essentials of computational chemistry: theories and models* (Chichester, West Sussex, England ; Hoboken, NJ: Wiley).
- Cukierman, S. (2003). The transfer of protons in water wires inside proteins. *Front. Biosci.* 8, s1118-1139.
- Cukierman, S. (2006). Et tu, Grotthuss! and other unfinished stories. *Biochim. Biophys. Acta* 1757, 876–885.
- De La Rosa, V., and Ramsey, I.S. (2018). Gating Currents in the Hv1 Proton Channel. *Biophys. J.* 114, 2844–2854.
- De La Rosa, V., Bennett, A.L., and Ramsey, I.S. (2018). Coupling between an electrostatic network and the Zn²⁺ binding site modulates Hv1 activation. *J. Gen. Physiol.* 150, 863–881.
- Decoursey, T.E. (2003). Voltage-gated proton channels and other proton transfer pathways. *Physiol. Rev.* 83, 475–579.
- DeCoursey, T.E. (2010). Voltage-gated proton channels find their dream job managing the respiratory burst in phagocytes. *Physiology (Bethesda)* 25, 27–40.
- DeCoursey, T.E. (2013). Voltage-Gated Proton Channels: Molecular Biology, Physiology, and Pathophysiology of the H_v Family. *Physiological Reviews* 93, 599–652.
- DeCoursey, T.E. (2015). The Voltage-Gated Proton Channel: A Riddle, Wrapped in a Mystery, inside an Enigma. *Biochemistry* 54, 3250–3268.
- DeCoursey, T.E. (2017). CrossTalk proposal: Proton permeation through HV 1 requires transient protonation of a conserved aspartate in the S1 transmembrane helix. *J. Physiol. (Lond.)*.
- DeCoursey, T.E. (2018). Voltage and pH sensing by the voltage-gated proton channel, HV1. *J R Soc Interface* 15.

- DeCoursey, T.E., and Cherny, V.V. (1997). Deuterium isotope effects on permeation and gating of proton channels in rat alveolar epithelium. *J. Gen. Physiol.* *109*, 415–434.
- DeCoursey, T.E., Morgan, D., and Cherny, V.V. (2003). The voltage dependence of NADPH oxidase reveals why phagocytes need proton channels. *Nature* *422*, 531–534.
- Delemotte, L., Tarek, M., Klein, M.L., Amaral, C., and Treptow, W. (2011). Intermediate states of the Kv1.2 voltage sensor from atomistic molecular dynamics simulations. *Proc. Natl. Acad. Sci. U.S.A.* *108*, 6109–6114.
- Di Cera, E. (1998). Site-Specific Thermodynamics: Understanding Cooperativity in Molecular Recognition. *Chem. Rev.* *98*, 1563–1592.
- Dinauer, M.C., Orkin, S.H., Brown, R., Jesaitis, A.J., and Parkos, C.A. (1987). The glycoprotein encoded by the X-linked chronic granulomatous disease locus is a component of the neutrophil cytochrome b complex. *Nature* *327*, 717–720.
- Dudev, T., Musset, B., Morgan, D., Cherny, V.V., Smith, S.M.E., Mazmanian, K., DeCoursey, T.E., and Lim, C. (2015). Selectivity Mechanism of the Voltage-gated Proton Channel, Hv1. *Sci Rep* *5*, 10320.
- Eder, C., and DeCoursey, T.E. (2001). Voltage-gated proton channels in microglia. *Prog. Neurobiol.* *64*, 277–305.
- El Chemaly, A., Okochi, Y., Sasaki, M., Arnaudeau, S., Okamura, Y., and Demaurex, N. (2010). VSOP/Hv1 proton channels sustain calcium entry, neutrophil migration, and superoxide production by limiting cell depolarization and acidification. *J. Exp. Med.* *207*, 129–139.
- Essmann, U., Perera, L., Berkowitz, M.L., Darden, T., Lee, H., and Pedersen, L.G. (1995). A smooth particle mesh Ewald method. *The Journal of Chemical Physics* *103*, 8577–8593.
- Fischer, H. (2012). Function of Proton Channels in Lung Epithelia. *Wiley Interdiscip Rev Membr Transp Signal* *1*, 247–258.
- Fischer, H., Widdicombe, J.H., and Illek, B. (2002). Acid secretion and proton conductance in human airway epithelium. *Am. J. Physiol., Cell Physiol.* *282*, C736–743.
- Fiser, A., Do, R.K., and Sali, A. (2000). Modeling of loops in protein structures. *Protein Sci.* *9*, 1753–1773.
- Fogel, M., and Hastings, J.W. (1972). Bioluminescence: mechanism and mode of control of scintillon activity. *Proc. Natl. Acad. Sci. U.S.A.* *69*, 690–693.
- Fujiwara, Y., Kurokawa, T., Takeshita, K., Kobayashi, M., Okochi, Y., Nakagawa, A., and Okamura, Y. (2012). The cytoplasmic coiled-coil mediates cooperative gating temperature sensitivity in the voltage-gated H(+) channel Hv1. *Nat Commun* *3*, 816.

- Fujiwara, Y., Kurokawa, T., and Okamura, Y. (2014). Long α helices projecting from the membrane as the dimer interface in the voltage-gated H(+) channel. *J. Gen. Physiol.* *143*, 377–386.
- Gonzalez, C., Koch, H.P., Drum, B.M., and Larsson, H.P. (2010). Strong cooperativity between subunits in voltage-gated proton channels. *Nat. Struct. Mol. Biol.* *17*, 51–56.
- Gonzalez, C., Rebolledo, S., Perez, M.E., and Larsson, H.P. (2013). Molecular mechanism of voltage sensing in voltage-gated proton channels. *J. Gen. Physiol.* *141*, 275–285.
- Gosselin-Badaroudine, P., Delemotte, L., Moreau, A., Klein, M.L., and Chahine, M. (2012). Gating pore currents and the resting state of Nav1.4 voltage sensor domains. *Proc. Natl. Acad. Sci. U.S.A.* *109*, 19250–19255.
- Gowers, R.J., Linke, M., Barnoud, J., Reddy, T.J.E., Melo, M.N., Seyler, S.L., Domański, J., Dotson, D.L., Buchoux, S., Kenney, I.M., et al. (2016). MDAAnalysis: A Python Package for the Rapid Analysis of Molecular Dynamics Simulations. In *Proceedings of the 15th Python in Science Conference*, S. Benthall, and S. Rostrup, eds. pp. 98–105.
- Hamill, O.P., Marty, A., Neher, E., Sakmann, B., and Sigworth, F.J. (1981). Improved patch-clamp techniques for high-resolution current recording from cells and cell-free membrane patches. *Pflugers Arch.* *391*, 85–100.
- Haynes, W.M. (2014). *CRC handbook of chemistry and physics: a ready-reference book of chemical and physical data* (Boca Raton; London; New York: CRC Press).
- Henderson, L.M., Chappell, J.B., and Jones, O.T. (1987). The superoxide-generating NADPH oxidase of human neutrophils is electrogenic and associated with an H⁺ channel. *Biochem. J.* *246*, 325–329.
- Henderson, L.M., Chappell, J.B., and Jones, O.T. (1988a). Internal pH changes associated with the activity of NADPH oxidase of human neutrophils. Further evidence for the presence of an H⁺ conducting channel. *Biochem. J.* *251*, 563–567.
- Henderson, L.M., Chappell, J.B., and Jones, O.T. (1988b). Superoxide generation by the electrogenic NADPH oxidase of human neutrophils is limited by the movement of a compensating charge. *Biochem. J.* *255*, 285–290.
- Hille, B. (2001). *Ion Channels of Excitable Membranes* (Sunderland Massachusetts, USA: Sinauer Associates).
- Hondares, E., Brown, M.A., Musset, B., Morgan, D., Cherny, V.V., Taubert, C., Bhamrah, M.K., Coe, D., Marelli-Berg, F., Gribben, J.G., et al. (2014). Enhanced activation of an amino-terminally truncated isoform of the voltage-gated proton channel HVCN1 enriched in malignant B cells. *Proc. Natl. Acad. Sci. U.S.A.* *111*, 18078–18083.

- Hong, L., Pathak, M.M., Kim, I.H., Ta, D., and Tombola, F. (2013). Voltage-sensing domain of voltage-gated proton channel Hv1 shares mechanism of block with pore domains. *Neuron* 77, 274–287.
- Horovitz, A., and Fersht, A.R. (1990). Strategy for analysing the co-operativity of intramolecular interactions in peptides and proteins. *J. Mol. Biol.* 214, 613–617.
- Horovitz, A., Bochkareva, E.S., Yifrach, O., and Girshovich, A.S. (1994). Prediction of an inter-residue interaction in the chaperonin GroEL from multiple sequence alignment is confirmed by double-mutant cycle analysis. *J. Mol. Biol.* 238, 133–138.
- Humphrey, W., Dalke, A., and Schulten, K. (1996). VMD: visual molecular dynamics. *J Mol Graph* 14, 33–38, 27–28.
- Infield, D.T., Matulef, K., Galpin, J.D., Lam, K., Tajkhorshid, E., Ahern, C.A., and Valiyaveetil, F.I. (2018). Main-chain mutagenesis reveals intrahelical coupling in an ion channel voltage-sensor. *Nat Commun* 9, 5055.
- Isgro, T., Phillips, J., Sotomayor, M., Villa, E., Yu, H., Tanner, D., Liu, Y., Wu, Z., and Hardy, D. (2017). NAMD Tutorial.
- Jensen, M.Ø., Jogini, V., Borhani, D.W., Leffler, A.E., Dror, R.O., and Shaw, D.E. (2012). Mechanism of voltage gating in potassium channels. *Science* 336, 229–233.
- Jiang, Y., Lee, A., Chen, J., Ruta, V., Cadene, M., Chait, B.T., and MacKinnon, R. (2003). X-ray structure of a voltage-dependent K⁺ channel. *Nature* 423, 33–41.
- Jorgensen, W.L., Chandrasekhar, J., Madura, J.D., Impey, R.W., and Klein, M.L. (1983). Comparison of simple potential functions for simulating liquid water. *The Journal of Chemical Physics* 79, 926–935.
- Klauda, J.B., Venable, R.M., Freites, J.A., O'Connor, J.W., Tobias, D.J., Mondragon-Ramirez, C., Vorobyov, I., MacKerell, A.D., and Pastor, R.W. (2010). Update of the CHARMM all-atom additive force field for lipids: validation on six lipid types. *J Phys Chem B* 114, 7830–7843.
- Klauda, J.B., Monje, V., Kim, T., and Im, W. (2012). Improving the CHARMM force field for polyunsaturated fatty acid chains. *J Phys Chem B* 116, 9424–9431.
- Koch, H.P., Kurokawa, T., Okochi, Y., Sasaki, M., Okamura, Y., and Larsson, H.P. (2008). Multimeric nature of voltage-gated proton channels. *Proc. Natl. Acad. Sci. U.S.A.* 105, 9111–9116.
- Kubota, T., Lacroix, J.J., Bezanilla, F., and Correa, A.M. (2014). Probing α -3(10) transitions in a voltage-sensing S4 helix. *Biophys. J.* 107, 1117–1128.

- Kulleperuma, K., Smith, S.M.E., Morgan, D., Musset, B., Holyoake, J., Chakrabarti, N., Cherny, V.V., DeCoursey, T.E., and Pomès, R. (2013). Construction and validation of a homology model of the human voltage-gated proton channel hHv1. *J. Gen. Physiol.* *141*, 445–465.
- Larsson, H.P., Baker, O.S., Dhillon, D.S., and Isacoff, E.Y. (1996). Transmembrane movement of the shaker K⁺ channel S4. *Neuron* *16*, 387–397.
- Lee, S.-Y., Letts, J.A., and Mackinnon, R. (2008). Dimeric subunit stoichiometry of the human voltage-dependent proton channel Hv1. *Proc. Natl. Acad. Sci. U.S.A.* *105*, 7692–7695.
- Lee, S.-Y., Letts, J.A., and MacKinnon, R. (2009). Functional reconstitution of purified human Hv1 H⁺ channels. *J. Mol. Biol.* *387*, 1055–1060.
- Lehninger, A.L., Nelson, D.L., and Cox, M.M. (2013). *Lehninger principles of biochemistry* (New York: W.H. Freeman).
- Lemkul, J.A., Huang, J., Roux, B., and MacKerell, A.D. (2016). An Empirical Polarizable Force Field Based on the Classical Drude Oscillator Model: Development History and Recent Applications. *Chem. Rev.* *116*, 4983–5013.
- Li, H., Robertson, A.D., and Jensen, J.H. (2005). Very fast empirical prediction and rationalization of protein pKa values. *Proteins* *61*, 704–721.
- Li, Q., Wanderling, S., Paduch, M., Medovoy, D., Singharoy, A., McGreevy, R., Villalba-Galea, C.A., Hulse, R.E., Roux, B., Schulten, K., et al. (2014). Structural mechanism of voltage-dependent gating in an isolated voltage-sensing domain. *Nat. Struct. Mol. Biol.* *21*, 244–252.
- Li, Q., Shen, R., Treger, J.S., Wanderling, S.S., Milewski, W., Siwowska, K., Bezanilla, F., and Perozo, E. (2015). Resting state of the human proton channel dimer in a lipid bilayer. *Proc. Natl. Acad. Sci. U.S.A.* *112*, E5926–5935.
- Li, S.J., Zhao, Q., Zhou, Q., Unno, H., Zhai, Y., and Sun, F. (2010). The role and structure of the carboxyl-terminal domain of the human voltage-gated proton channel Hv1. *J. Biol. Chem.* *285*, 12047–12054.
- Lishko, P.V., and Kirichok, Y. (2010). The role of Hv1 and CatSper channels in sperm activation. *J. Physiol. (Lond.)* *588*, 4667–4672.
- Long, S.B., Campbell, E.B., and Mackinnon, R. (2005). Voltage sensor of Kv1.2: structural basis of electromechanical coupling. *Science* *309*, 903–908.
- Long, S.B., Tao, X., Campbell, E.B., and MacKinnon, R. (2007). Atomic structure of a voltage-dependent K⁺ channel in a lipid membrane-like environment. *Nature* *450*, 376–382.

- MackKerell, A.D., Bashford, D., Bellott, M., Dunbrack, R.L., Evanseck, J.D., Field, M.J., Fischer, S., Gao, J., Guo, H., Ha, S., et al. (1998). All-atom empirical potential for molecular modeling and dynamics studies of proteins. *J Phys Chem B* *102*, 3586–3616.
- MackKerell, A.D., Feig, M., and Brooks, C.L. (2004). Improved treatment of the protein backbone in empirical force fields. *J. Am. Chem. Soc.* *126*, 698–699.
- Mannuzzu, L.M., Moronne, M.M., and Isacoff, E.Y. (1996). Direct physical measure of conformational rearrangement underlying potassium channel gating. *Science* *271*, 213–216.
- Martí-Renom, M.A., Stuart, A.C., Fiser, A., Sánchez, R., Melo, F., and Sali, A. (2000). Comparative protein structure modeling of genes and genomes. *Annu Rev Biophys Biomol Struct* *29*, 291–325.
- Mason, P.E., Neilson, G.W., Dempsey, C.E., Barnes, A.C., and Cruickshank, J.M. (2003). The hydration structure of guanidinium and thiocyanate ions: implications for protein stability in aqueous solution. *Proc. Natl. Acad. Sci. U.S.A.* *100*, 4557–4561.
- Michaud-Agrawal, N., Denning, E.J., Woolf, T.B., and Beckstein, O. (2011). MDAAnalysis: A toolkit for the analysis of molecular dynamics simulations. *Journal of Computational Chemistry* *32*, 2319–2327.
- Mony, L., Berger, T.K., and Isacoff, E.Y. (2015). A specialized molecular motion opens the Hv1 voltage-gated proton channel. *Nat. Struct. Mol. Biol.* *22*, 283–290.
- Morgan, D., Capasso, M., Musset, B., Cherny, V.V., Ríos, E., Dyer, M.J.S., and DeCoursey, T.E. (2009). Voltage-gated proton channels maintain pH in human neutrophils during phagocytosis. *Proc. Natl. Acad. Sci. U.S.A.* *106*, 18022–18027.
- Morgan, D., Musset, B., Kulleperuma, K., Smith, S.M.E., Rajan, S., Cherny, V.V., Pomès, R., and DeCoursey, T.E. (2013). Peregrination of the selectivity filter delineates the pore of the human voltage-gated proton channel hHV1. *J. Gen. Physiol.* *142*, 625–640.
- Morihata, H., Nakamura, F., Tsutada, T., and Kuno, M. (2000). Potentiation of a voltage-gated proton current in acidosis-induced swelling of rat microglia. *J. Neurosci.* *20*, 7220–7227.
- Murata, Y., Iwasaki, H., Sasaki, M., Inaba, K., and Okamura, Y. (2005). Phosphoinositide phosphatase activity coupled to an intrinsic voltage sensor. *Nature* *435*, 1239–1243.
- Musset, B., Morgan, D., Cherny, V.V., MacGlashan, D.W., Thomas, L.L., Ríos, E., and DeCoursey, T.E. (2008a). A pH-stabilizing role of voltage-gated proton channels in IgE-mediated activation of human basophils. *Proc. Natl. Acad. Sci. U.S.A.* *105*, 11020–11025.
- Musset, B., Cherny, V.V., Morgan, D., Okamura, Y., Ramsey, I.S., Clapham, D.E., and DeCoursey, T.E. (2008b). Detailed comparison of expressed and native voltage-gated proton channel currents. *J. Physiol. (Lond.)* *586*, 2477–2486.

- Musset, B., Smith, S.M.E., Rajan, S., Cherny, V.V., Sujai, S., Morgan, D., and DeCoursey, T.E. (2010a). Zinc inhibition of monomeric and dimeric proton channels suggests cooperative gating. *J. Physiol. (Lond.)* 588, 1435–1449.
- Musset, B., Smith, S.M.E., Rajan, S., Cherny, V.V., Morgan, D., and DeCoursey, T.E. (2010b). Oligomerization of the voltage-gated proton channel. *Channels (Austin)* 4, 260–265.
- Musset, B., Capasso, M., Cherny, V.V., Morgan, D., Bhamrah, M., Dyer, M.J.S., and DeCoursey, T.E. (2010c). Identification of Thr29 as a critical phosphorylation site that activates the human proton channel Hvcn1 in leukocytes. *J. Biol. Chem.* 285, 5117–5121.
- Musset, B., Smith, S.M.E., Rajan, S., Morgan, D., Cherny, V.V., and Decoursey, T.E. (2011). Aspartate 112 is the selectivity filter of the human voltage-gated proton channel. *Nature* 480, 273–277.
- Nagle, J.F., and Morowitz, H.J. (1978). Molecular mechanisms for proton transport in membranes. *Proc. Natl. Acad. Sci. U.S.A.* 75, 298–302.
- Okuda, H., Yonezawa, Y., Takano, Y., Okamura, Y., and Fujiwara, Y. (2016). Direct Interaction between the Voltage Sensors Produces Cooperative Sustained Deactivation in Voltage-gated H⁺ Channel Dimers. *J. Biol. Chem.* 291, 5935–5947.
- Olsson, M.H.M., Søndergaard, C.R., Rostkowski, M., and Jensen, J.H. (2011). PROPKA3: Consistent Treatment of Internal and Surface Residues in Empirical pKa Predictions. *J Chem Theory Comput* 7, 525–537.
- Pace, C.N., Grimsley, G.R., and Scholtz, J.M. (2009). Protein ionizable groups: pK values and their contribution to protein stability and solubility. *J. Biol. Chem.* 284, 13285–13289.
- Pahari, S., Sun, L., and Alexov, E. (2019). PKAD: a database of experimentally measured pKa values of ionizable groups in proteins. *Database (Oxford)* 2019.
- Pathak, M.M., Yarov-Yarovoy, V., Agarwal, G., Roux, B., Barth, P., Kohout, S., Tombola, F., and Isacoff, E.Y. (2007). Closing in on the resting state of the Shaker K(+) channel. *Neuron* 56, 124–140.
- Pathak, M.M., Tran, T., Hong, L., Joós, B., Morris, C.E., and Tombola, F. (2016). The Hv1 proton channel responds to mechanical stimuli. *J. Gen. Physiol.* 148, 405–418.
- Payandeh, J., Scheuer, T., Zheng, N., and Catterall, W.A. (2011). The crystal structure of a voltage-gated sodium channel. *Nature* 475, 353–358.
- Phillips, J.C., Braun, R., Wang, W., Gumbart, J., Tajkhorshid, E., Villa, E., Chipot, C., Skeel, R.D., Kalé, L., and Schulten, K. (2005). Scalable molecular dynamics with NAMD. *J Comput Chem* 26, 1781–1802.

- Po, H.N., and Senozan, N.M. (2001). The Henderson-Hasselbalch Equation: Its History and Limitations. *Journal of Chemical Education* 78, 1499.
- Pomès, R., and Yu, C.-H. (2003). Relay and blockage of protons in water chains. *Front. Biosci.* 8, d1288-1297.
- Qiu, F., Rebolledo, S., Gonzalez, C., and Larsson, H.P. (2013). Subunit interactions during cooperative opening of voltage-gated proton channels. *Neuron* 77, 288–298.
- Qiu, F., Chamberlin, A., Watkins, B.M., Ionescu, A., Perez, M.E., Barro-Soria, R., González, C., Noskov, S.Y., and Larsson, H.P. (2016). Molecular mechanism of Zn²⁺ inhibition of a voltage-gated proton channel. *Proc. Natl. Acad. Sci. U.S.A.* 113, E5962–E5971.
- Radak, B., K., Roux, B., and Chipot, C. (2018). Simulating Biomolecules with Variable Protonation State: A Tutorial for Constant-pH Molecular Dynamics.
- Ramsey, I.S., Moran, M.M., Chong, J.A., and Clapham, D.E. (2006). A voltage-gated proton-selective channel lacking the pore domain. *Nature* 440, 1213–1216.
- Ramsey, I.S., Ruchti, E., Kaczmarek, J.S., and Clapham, D.E. (2009). Hv1 proton channels are required for high-level NADPH oxidase-dependent superoxide production during the phagocyte respiratory burst. *Proc. Natl. Acad. Sci. U.S.A.* 106, 7642–7647.
- Ramsey, I.S., Mokrab, Y., Carvacho, I., Sands, Z.A., Sansom, M.S.P., and Clapham, D.E. (2010). An aqueous H⁺ permeation pathway in the voltage-gated proton channel Hv1. *Nat. Struct. Mol. Biol.* 17, 869–875.
- Randolph, A.L., Mokrab, Y., Bennett, A.L., Sansom, M.S., and Ramsey, I.S. (2016). Proton currents constrain structural models of voltage sensor activation. *Elife* 5.
- Rodriguez, J.D., Haq, S., Bachvaroff, T., Nowak, K.F., Nowak, S.J., Morgan, D., Cherny, V.V., Sapp, M.M., Bernstein, S., Bolt, A., et al. (2017). Identification of a vacuolar proton channel that triggers the bioluminescent flash in dinoflagellates. *PLoS ONE* 12, e0171594.
- Sakata, S., Kurokawa, T., Nørholm, M.H.H., Takagi, M., Okochi, Y., von Heijne, G., and Okamura, Y. (2010). Functionality of the voltage-gated proton channel truncated in S4. *Proc. Natl. Acad. Sci. U.S.A.* 107, 2313–2318.
- Sakata, S., Miyawaki, N., McCormack, T.J., Arima, H., Kawanabe, A., Özkucur, N., Kurokawa, T., Jinno, Y., Fujiwara, Y., and Okamura, Y. (2016). Comparison between mouse and sea urchin orthologs of voltage-gated proton channel suggests role of S3 segment in activation gating. *Biochim. Biophys. Acta* 1858, 2972–2983.
- Sali, A., and Blundell, T.L. (1993). Comparative protein modelling by satisfaction of spatial restraints. *J. Mol. Biol.* 234, 779–815.

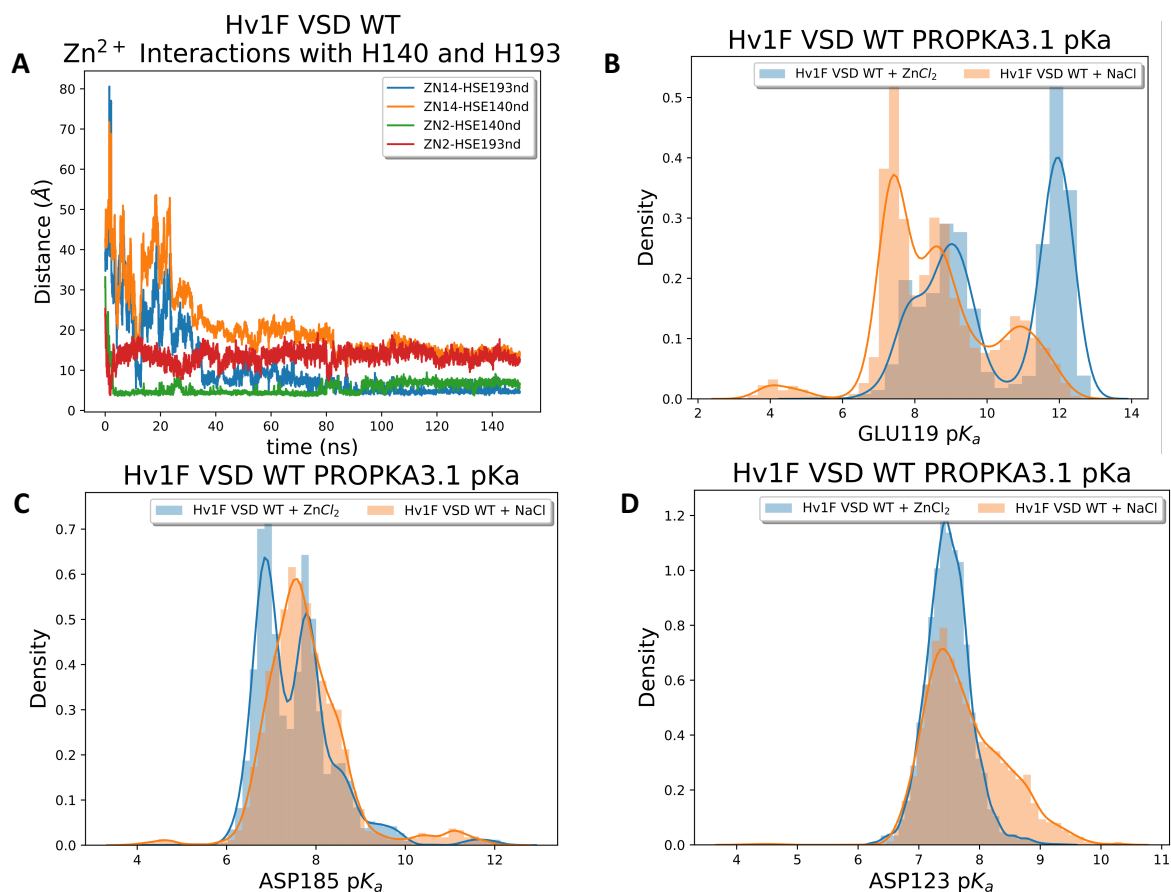
- Sali, A., Webb, B., Madhusudhan, M.S., Shen, M.-Y., Dong, G., Marti-Renom, M.A., Eswar, N., Alber, F., Topf, M., Oliva, B., et al. (2016). MODELLER A Program for Protein Structure.
- Sasaki, A. (2017). Microglia and brain macrophages: An update. *Neuropathology* 37, 452–464.
- Sasaki, M., Takagi, M., and Okamura, Y. (2006). A voltage sensor-domain protein is a voltage-gated proton channel. *Science* 312, 589–592.
- Schilling, T., Gratopp, A., DeCoursey, T.E., and Eder, C. (2002). Voltage-activated proton currents in human lymphocytes. *J. Physiol. (Lond.)* 545, 93–105.
- Schwaiger, C.S., Bjelkmar, P., Hess, B., and Lindahl, E. (2011). 3_{10} -helix conformation facilitates the transition of a voltage sensor S4 segment toward the down state. *Biophys. J.* 100, 1446–1454.
- Seoh, S.A., Sigg, D., Papazian, D.M., and Bezanilla, F. (1996). Voltage-sensing residues in the S2 and S4 segments of the Shaker K⁺ channel. *Neuron* 16, 1159–1167.
- Smith, S.M.E., Morgan, D., Musset, B., Cherny, V.V., Place, A.R., Hastings, J.W., and Decoursey, T.E. (2011). Voltage-gated proton channel in a dinoflagellate. *Proc. Natl. Acad. Sci. U.S.A.* 108, 18162–18167.
- Søndergaard, C.R., Olsson, M.H.M., Rostkowski, M., and Jensen, J.H. (2011). Improved Treatment of Ligands and Coupling Effects in Empirical Calculation and Rationalization of pK_a Values. *J Chem Theory Comput* 7, 2284–2295.
- Starace, D.M., and Bezanilla, F. (2001). Histidine scanning mutagenesis of basic residues of the S4 segment of the shaker k⁺ channel. *J. Gen. Physiol.* 117, 469–490.
- Starace, D.M., and Bezanilla, F. (2004). A proton pore in a potassium channel voltage sensor reveals a focused electric field. *Nature* 427, 548–553.
- Starace, D.M., Stefani, E., and Bezanilla, F. (1997). Voltage-dependent proton transport by the voltage sensor of the Shaker K⁺ channel. *Neuron* 19, 1319–1327.
- Stote, R.H., and Karplus, M. (1995). Zinc binding in proteins and solution: a simple but accurate nonbonded representation. *Proteins* 23, 12–31.
- Struyk, A.F., and Cannon, S.C. (2007). A Na⁺ channel mutation linked to hypokalemic periodic paralysis exposes a proton-selective gating pore. *J. Gen. Physiol.* 130, 11–20.
- Struyk, A.F., Scoggan, K.A., Bulman, D.E., and Cannon, S.C. (2000). The human skeletal muscle Na channel mutation R669H associated with hypokalemic periodic paralysis enhances slow inactivation. *J. Neurosci.* 20, 8610–8617.
- Swartz, K.J. (2008). Sensing voltage across lipid membranes. *Nature* 456, 891–897.

- Takeshita, K., Sakata, S., Yamashita, E., Fujiwara, Y., Kawanabe, A., Kurokawa, T., Okochi, Y., Matsuda, M., Narita, H., Okamura, Y., et al. (2014). X-ray crystal structure of voltage-gated proton channel. *Nat. Struct. Mol. Biol.* *21*, 352–357.
- Tao, X., Lee, A., Limapichat, W., Dougherty, D.A., and MacKinnon, R. (2010). A gating charge transfer center in voltage sensors. *Science* *328*, 67–73.
- Taylor, A.R., Chrachri, A., Wheeler, G., Goddard, H., and Brownlee, C. (2011). A voltage-gated H⁺ channel underlying pH homeostasis in calcifying coccolithophores. *PLoS Biol.* *9*, e1001085.
- Thannickal, V.J., and Fanburg, B.L. (2000). Reactive oxygen species in cell signaling. *Am. J. Physiol. Lung Cell Mol. Physiol.* *279*, L1005-1028.
- Thomas, R.C., and Meech, R.W. (1982). Hydrogen ion currents and intracellular pH in depolarized voltage-clamped snail neurones. *Nature* *299*, 826–828.
- Thomas, S., Cherny, V.V., Morgan, D., Artinian, L.R., Rehder, V., Smith, S.M.E., and DeCoursey, T.E. (2018). Exotic properties of a voltage-gated proton channel from the snail *Helisoma trivolvis*. *J. Gen. Physiol.*
- Tian, D.-S., Li, C.-Y., Qin, C., Murugan, M., Wu, L.-J., and Liu, J.-L. (2016). Deficiency in the voltage-gated proton channel Hv1 increases M2 polarization of microglia and attenuates brain damage from photothrombotic ischemic stroke. *J. Neurochem.* *139*, 96–105.
- Tombola, F., Pathak, M.M., and Isacoff, E.Y. (2005). Voltage-sensing arginines in a potassium channel permeate and occlude cation-selective pores. *Neuron* *45*, 379–388.
- Tombola, F., Pathak, M.M., and Isacoff, E.Y. (2006). How does voltage open an ion channel? *Annu. Rev. Cell Dev. Biol.* *22*, 23–52.
- Tombola, F., Ulbrich, M.H., and Isacoff, E.Y. (2008). The voltage-gated proton channel Hv1 has two pores, each controlled by one voltage sensor. *Neuron* *58*, 546–556.
- Tombola, F., Ulbrich, M.H., Kohout, S.C., and Isacoff, E.Y. (2010). The opening of the two pores of the Hv1 voltage-gated proton channel is tuned by cooperativity. *Nat. Struct. Mol. Biol.* *17*, 44–50.
- Vargas, E., Yarov-Yarovoy, V., Khalili-Araghi, F., Catterall, W.A., Klein, M.L., Tarek, M., Lindahl, E., Schulten, K., Perozo, E., Bezanilla, F., et al. (2012). An emerging consensus on voltage-dependent gating from computational modeling and molecular dynamics simulations. *J. Gen. Physiol.* *140*, 587–594.
- Vieira-Pires, R.S., and Morais-Cabral, J.H. (2010). 3(10) helices in channels and other membrane proteins. *J. Gen. Physiol.* *136*, 585–592.

- Villalba-Galea, C.A. (2014). Hv1 proton channel opening is preceded by a voltage-independent transition. *Biophys. J.* *107*, 1564–1572.
- Villalba-Galea, C.A., Sandtner, W., Starace, D.M., and Bezanilla, F. (2008). S4-based voltage sensors have three major conformations. *Proc. Natl. Acad. Sci. U.S.A.* *105*, 17600–17607.
- Villalba-Galea, C.A., Frezza, L., Sandtner, W., and Bezanilla, F. (2013). Sensing charges of the *Ciona intestinalis* voltage-sensing phosphatase. *J. Gen. Physiol.* *142*, 543–555.
- Wallace, J.A., and Shen, J.K. (2009). Predicting pKa values with continuous constant pH molecular dynamics. *Meth. Enzymol.* *466*, 455–475.
- Wallace, J.A., and Shen, J.K. (2011). Continuous Constant pH Molecular Dynamics in Explicit Solvent with pH-Based Replica Exchange. *J Chem Theory Comput* *7*, 2617–2629.
- Wang, Y., Li, S.J., Pan, J., Che, Y., Yin, J., and Zhao, Q. (2011). Specific expression of the human voltage-gated proton channel Hv1 in highly metastatic breast cancer cells, promotes tumor progression and metastasis. *Biochem. Biophys. Res. Commun.* *412*, 353–359.
- Wang, Y., Li, S.J., Wu, X., Che, Y., and Li, Q. (2012). Clinicopathological and biological significance of human voltage-gated proton channel Hv1 protein overexpression in breast cancer. *J. Biol. Chem.* *287*, 13877–13888.
- Webb, B., and Sali, A. (2014). Comparative Protein Structure Modeling Using MODELLER. *Curr Protoc Bioinformatics* *47*, 5.6.1-32.
- Wood, M.L., Schow, E.V., Freites, J.A., White, S.H., Tombola, F., and Tobias, D.J. (2012). Water wires in atomistic models of the Hv1 proton channel. *Biochim. Biophys. Acta* *1818*, 286–293.
- Wu, L.-J., Wu, G., Akhavan Sharif, M.R., Baker, A., Jia, Y., Fahey, F.H., Luo, H.R., Feener, E.P., and Clapham, D.E. (2012). The voltage-gated proton channel Hv1 enhances brain damage from ischemic stroke. *Nat. Neurosci.* *15*, 565–573.
- Yu, Y., Yu, Z., Xie, M., Wang, W., and Luo, X. (2018). Hv1 proton channel facilitates production of ROS and pro-inflammatory cytokines in microglia and enhances oligodendrocyte progenitor cells damage from oxygen-glucose deprivation in vitro. *Biochem. Biophys. Res. Commun.* *498*, 1–8.
- Yusaf, S.P., Wray, D., and Sivaprasadarao, A. (1996). Measurement of the movement of the S4 segment during the activation of a voltage-gated potassium channel. *Pflugers Arch.* *433*, 91–97.
- Zhou, Y., Xia, X.-M., and Lingle, C.J. (2018). BK channel inhibition by strong extracellular acidification. *ELife* *7*.

APPENDIX A

Supplementary Figures



Supplementary Figure 1: E119 pK_a in the Presence of Zn²⁺ vs. in the Presence of Na⁺ in Hv1F WT MD

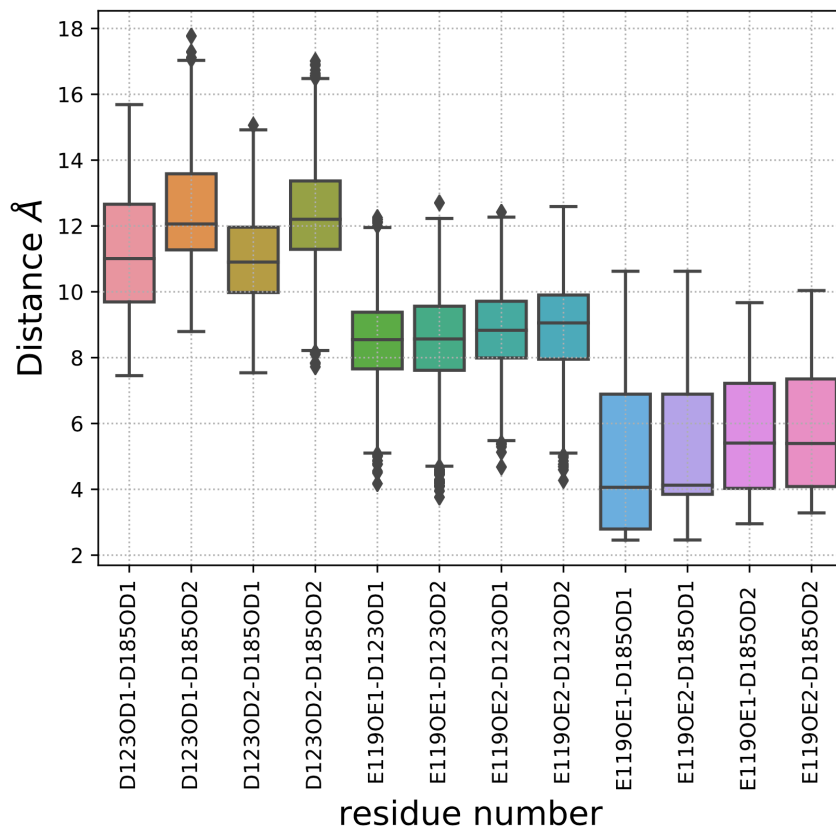
A: Distance in angstroms (Å) between H140 and Zn²⁺ ion ID 14 (orange), Zn²⁺ ion ID 14 and H193 (blue), Zn²⁺ ID 2 and H140 (green), and Zn²⁺ ID 2 and H193 (red). All distances are measured from the center of the Zn²⁺ ion to the Nδ of H140 or H193. Plot was made using Pyplot in Python3.16.

B: Overlapping histograms of Hv1F WT E119 pK_a in the presence of ZnCl₂ (blue) and NaCl (orange) show that the range of pK_a values accessible to E119 is slightly altered by the presence of Zn²⁺, the distributions of pK_a values are largely overlapping, indicating that the E119 pK_a is slightly, but not largely affected by the presence of Zn²⁺ in the ECEN. Histograms were made using the distplot function of Seaborn in Python3.16.

C: Overlapping histograms of Hv1F WT D185 pK_a in the presence of ZnCl₂ (blue) and NaCl (orange) show that the pK_a of D185 is unaffected by the presence of Zn²⁺ in the ECEN. Histograms were made using the distplot function of Seaborn in Python3.16.

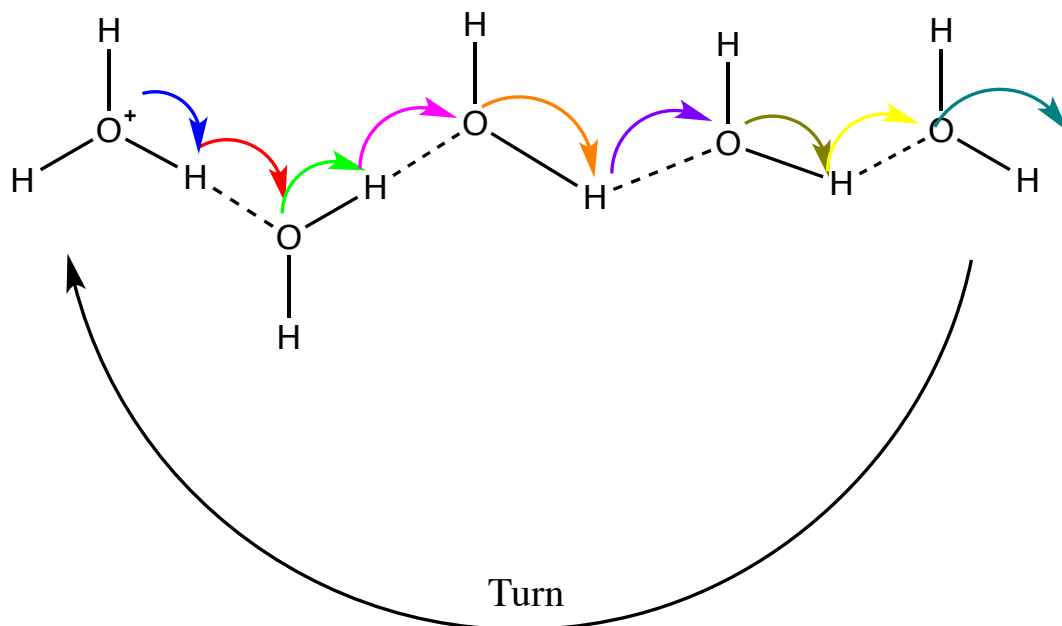
D: Overlapping histograms of Hv1F WT D123 pK_a in the presence of ZnCl₂ (blue) and NaCl (orange) show that the pK_a of D123 is unaffected by the presence of Na⁺ in the ECEN. Histograms were made using the distplot function of Seaborn in Python3.16.

Hv1F VSD WT ECEN Distance Statistics



Supplementary Figure 2: Hv1F WT D123 Distances

Distances were measured using VMD. Boxplots were made using Seaborn boxplot function in Python.



Supplementary Figure 3 Grotthuss proton transfer

A series of water molecules forms a HBC via hydrogen bonds (dashed lines) and allows a proton to be virtually transferred from one place to another. Colored arrows represent sequential steps of rearrangements in the HBC to permit proton conduction. Adapted from Pomès and Yu, 2003 Figure 1.

APPENDIX B

Workstation Information

1. GPU Workstation (Proton)
 - HP Z800
 - Two 3.33 GHz Intel W5590 CPUs
 - 1 NVIDIA Quadro 2000
 - 2 NVIDIA Tesla C2075
 - CentOS 7.6
 - Cuda 10.0
 - NAMD2.11.

2. GPU Server (Kraftwerk)
 - Head node
 - One 8-core 64-bit Intel Xeon CPU
 - 4 GB RAM
 - Shared 11 TB RAID 6 storage
 - Compute nodes
 - Three 12-core Intel Xeon CPUs
 - 2-3 GB RAM
 - Three NVIDIA Tesla M2075 GPUs
 - One 32-core Intel Xeon CPU with 4GB RAM
 - 2 NVIDIA Tesla K80 GPUs
 - Infiniband architecture.
 - NAMD 2.9

3. CPU server (Teal)
 - (<https://rampages.us/chipc/research/facilities/>)
 - 5040 64-bit Intel and AMD compute cores, each with:
 - 2–4 GB RAM/core
 - 10.2 TB of total RAM
 - 180 TB of home space
 - tmp space of between 360 and 787 GB per node.
 - 20 Gb/second Infiniband architecture.
 - NAMD2.10

VITA

Ashley L. Bennett

9000 Old Mayland Way
Henrico, Virginia 23294

919.815.6971

bennettal2@vcu.edu

[hwww.researchgate.net/profile/
Ashley_Bennett15](http://www.researchgate.net/profile/Ashley_Bennett15)

[www.linkedin.com/in/ashley-
bennett-115669b8/](http://www.linkedin.com/in/ashley-bennett-115669b8/)

Language(s): English

Primary Specialization	Molecular dynamics and biophysics of voltage sensor domains and ion channels
Expertise and Interests	Voltage sensor domain structure Voltage sensor domain gating mechanisms Proton transfer mechanisms in ion channels Voltage sensor pH sensing mechanisms Structure and function of complex electrostatic networks in voltage sensor domains Allosteric communication between separated electrostatic networks in voltage sensor domains
Education	Department of Physiology and Biophysics, School of Medicine, Virginia Commonwealth University, Richmond, Virginia – PhD 2019 Department of Chemistry and Biochemistry, University of North Carolina at Wilmington, Wilmington, North Carolina – B.S. 2014 Department of Biology, University of North Carolina at Wilmington, Wilmington, North Carolina – B.S. 2014

Department of Mathematics and Statistics, University of North Carolina at Wilmington, Wilmington, North Carolina – Minor 2014

Department of Psychology, University of North Carolina at Wilmington, Wilmington, North Carolina – Minor 2014

Honors and Awards VCU Charles C. Clayton Scholarship for outstanding PhD Student in School of Medicine. Virginia Commonwealth University, School of Medicine. May 2019.

Department of Physiology and Biophysics Ramsey Award for outstanding PhD Student in Department of Physiology and Biophysics. Virginia Commonwealth University, School of Medicine. May 2018.

Hypercube Scholar for academic excellence in computational research. Department of Chemistry and Biochemistry, University of North Carolina at Wilmington May 2014.

Organizations Women in Science Member, Virginia Commonwealth University, School of Medicine. 2015-present
Living with Autism, Inc. Fundraising Volunteer. 2011-present
Chemistry Club Vice President, University of North Carolina at Wilmington. 2011
Chemistry Club Vice President, University of North Carolina at Wilmington. 2012

Society Memberships Biophysical Society Member. 2017-present
American Chemical Society Member. 2011-2016
The Autism Society of North Carolina Member. 2010

Research Experience **PhD Candidate, Department of Physiology and Biophysics, Virginia Commonwealth University, School of Medicine; Richmond, Virginia – August 2014-present**
Principal Investigator: I. Scott Ramsey
Research Topic: Gating mechanics of voltage-gated proton channel Hv1
Lab duties:

- Constructing homology models of Hv1
- Conducting molecular dynamics simulations on Hv1 on GPU workstations and CPU servers with NAMD
- Setting up GPU workstation

- Maintaining GPU workstation
- Writing Python analysis programs
- Analyzing modeling and molecular dynamics data
- Carrying out PCR mutagenesis in Hv1
- Performing whole cell patch clamp experiments
- Culturing HEK293 cells

**Student Researcher, Department of Chemistry and Biochemistry,
University of North Carolina at Wilmington; Wilmington, North Carolina –
January 2013-July 2014**

Principal Investigator: Hee-Seung Lee

Research Topic: Membrane insertion mechanisms of antimicrobial peptide δ -lysin

Lab duties:

- Conducting molecular dynamics simulations of δ -lysin on CPU workstation with GROMACS

**Summer Intern, Intracellular Regulation Group, National Institutes of
Environmental Health Sciences; Research Triangle Park, North Carolina
– May 2012-August 2012**

Principal Investigator: David Miller

Research Topic: Glucocorticoid receptor-induced changes in ABC transport protein expression and activity at the blood-brain barrier

Lab duties:

- Extracted endothelial cells from the brain and spinal cord of rats and mice
- Quantified ABC transporter proteins using Bradford protein quantification assay
- Performed Western blot experiments
- Carried out confocal microscopy on brain and spinal cord endothelial cells
- Analyzed and quantified fluorescence from confocal images
- Analyzed and quantified Western blot experiments

**Student Researcher, Department of Biology, University of North Carolina
at Wilmington; Wilmington, North Carolina – August 2011-December
2011**

Principal Investigator: Arthur Frampton

Research Topic: Screening compounds extracted from marine algae for equine herpes antiviral properties

Lab duties:

- Cultured equine pulmonary endothelial cells
- Infected equine pulmonary endothelial cells with equine herpes virus

- Treated infected endothelial cells with control or marine algae compounds with potential antiviral properties
- Performed absorption spectroscopy on equine pulmonary endothelial cells

Summer Intern, Intracellular Regulation Group, National Institutes of Environmental Health Sciences; Research Triangle Park, North Carolina – May 2011-August 2011

Principal Investigator: David Miller

Research Topic: Determining ABC transport proteins changes in expression and transport activity at the blood-brain barrier induced by dioxin

Lab duties:

- Extracted endothelial cells from the brain and spinal cord of rats and mice
- Quantified ABC transporter proteins using Bradford protein quantification assay
- Performed Western blot experiments
- Carried out confocal microscopy on brain and spinal cord endothelial cells
- Analyzed and quantified fluorescence from confocal images
- Analyzed and quantified Western blot experiments

Summer Intern, Performance Physical Therapy; Cary, North Carolina – May 2007-August 2007

Principal Investigator: Brandon Young

Research Topic: Biomechanics of the rotator cuff muscles in baseball pitchers age 8 -12 years

Lab duties:

- Write informed consent

Teaching Experience

Teaching Assistant for PHIZ 206, Department of Physiology and Biophysics, Virginia Commonwealth University; Richmond, Virginia – August 2017-December 2017

Course Instructor: Ramzi Ockaili

Course Description: Lab component for VCU's undergraduate introductory human physiology class.

Teaching duties:

- Instructed about 60 students
- Graded homework assignments
- Graded quizzes
- Calculated final grade
- Evaluated attendance
- Set and clean up lab equipment

	<ul style="list-style-type: none"> ▸ Conducting experiment prior to lab ▸ Lectured for 6 class meetings ▸ Answer questions for students
Leadership Experience	<p>Founding Member of Chemistry Club. University of North Carolina at Wilmington 2011</p> <p>Vice President of Chemistry Club. University of North Carolina at Wilmington 2011</p> <p>President of Chemistry Club. University of North Carolina at Wilmington 2012</p>
Service to University	<p>Biomedical Science Doctoral Portal Recruiter. Virginia Commonwealth University, School of Medicine. 2017-present</p> <p>Website redesign committee. Department of Physiology and Biophysics, Virginia Commonwealth University, School of Medicine. 2016-present</p>
Volunteer Service	<p>Living with Autism, Inc. Golf Tournament Fundraiser Volunteer 2014</p> <p>Living with Autism, Inc. Golf Tournament Fundraiser Volunteer 2013</p> <p>Living with Autism, Inc. Golf Tournament Fundraiser Volunteer 2012</p>
Laboratory Skills	<p>Computational Research</p> <ul style="list-style-type: none"> Molecular dynamics (NAMD, GROMACS) Homology modeling (MODELLER) Molecular modeling and visualization (VMD, PyMol, Chimera, Phenix) Electronic structure calculations (Titan, HyperChem, Spartan) <p>Experimental Research</p> <ul style="list-style-type: none"> Whole-cell voltage clamp PCR mutagenesis cDNA extraction and purification Mammalian cell culture Gel electrophoresis Confocal microscopy Absorption spectroscopy
Computer Skills	<p>Operating System</p> <ul style="list-style-type: none"> Linux operating system Windows operating system Mac OS X <p>Programming Languages</p> <ul style="list-style-type: none"> Python Tcl Bash

Miscellaneous Software

Microsoft Office Suite
Apple iWorks Suite
ImageJ
Just Acquire
ProLaw

Publications

V De La Rosa, **AL Bennett**, and IS Ramsey (2018). Coupling between an electrostatic network and the Zn²⁺ binding site modulates Hv1 activation. *Journal of General Physiology* 150(6):863-881. PMID: 29743298

AL Bennett and IS Ramsey (2017). Rebuttal from Ashley L. Bennett and Ian Scott Ramsey. *Journal of Physiology* 595(22):6803. PMID: 29023729

AL Bennett and IS Ramsey (2017). CrossTalk opposing view: proton transfer in Hv1 utilizes a water wire, and does not require transient protonation of a conserved aspartate in the S1 transmembrane helix. *Journal of Physiology* 595(22):6797-6799. PMID: 29023730

MJ King, **AL Bennett**, PF Almeida, and H-S Lee (2016). Coarse-grained simulations of hemolytic peptide δ -lysin interacting with a POPC bilayer. *Biochimica et Biophysica Acta*. 1858(12):3182-3194. PMID: 27720634

AL Randolph, Y Mokrab, **AL Bennett**, MS Sansom, and IS Ramsey (2016). Proton currents constrain structural models of voltage sensor activation. *Elife* 5. pii: e18017. PMID: 27572256

Poster Presentations

"Zn²⁺ Modulates Hv1 Proton Channel Gating via Conformational Coupling to an Intracellular Coulombic Network". V De La Rosa, **AL Bennett** and IS Ramsey. Biophysical Society Annual Meeting, San Francisco, California. February 2018.

"Gating Currents in Hv1 Proton Channels Reveal a Voltage Sensor Mode Shift/Relaxation". V De La Rosa, **AL Bennett** and IS Ramsey. Biophysical Society Annual Meeting, New Orleans, Louisiana. February 2017.

"Electrodynamic networks in closed-state voltage-gated proton channel Hv1". **AL Bennett** and IS Ramsey. Department of Physiology and Biophysics Summer Retreat, Virginia Commonwealth University, Medical College of Virginia, Richmond, Virginia. August 2016.

"Extracellular Zn²⁺ coordination in the Hv1 proton channel constrains resting-state voltage sensor domain structure". V De La Rosa, **AL Bennett** and IS

Ramsey. Ion Channels Gordon Research Conference, Mount Holyoke College, South Hadley, MA. Poster presentation. July 2016

"Hv1 Proton Channel Resting-State Voltage Sensor Model Structures are Refined by Experimental Mapping of Zinc-Coordinating Residues". V De La Rosa, **AL Bennett** and IS Ramsey. Biophysical Society Annual Meeting, Los Angeles, CA. Poster presentation. February 2016

"An Experimentally-Validated Model Structure of the Hv1 Proton Channel Voltage Sensor in its Resting State". Y Mokrab, **AL Bennett**, Mark SP Sansom and IS Ramsey. Biophysical Society Annual Meeting, Baltimore, Maryland. February 2015.

"How does a proton cross a membrane". **AL Bennett** and IS Ramsey. Biomedical Sciences Doctoral Portal Third Colloquium, Virginia Commonwealth University, Medical College of Virginia. May 2015.

"A new role for a conserved phenylalanine residue in H⁺-selective voltage-sensor domain". **AL Bennett**, IS Ramsey, and JC Hackett. Biomedical Sciences Doctoral Portal Second Colloquium, Virginia Commonwealth University, Medical College of Virginia Campus. March 2015.

"Glucocorticoid Receptor Regulation of P-glycoprotein at the Blood-Brain and Blood-Spinal Cord Barriers". **AL Bennett**, L Smith, C Campos, and D Miller. Summers of Discovery Poster Presentations, National Institute of Environmental Health Sciences, Research Triangle Park. August 2012.

"Blood-brain barrier efflux transporter regulation through NF- κ B". **AL Bennett**, J Bonni, X Wang, C Campos, R Cannon, J Peart, L Smith, and D Miller. Summers of Discovery Poster Presentations, National Institute of Environmental Health Sciences, Research Triangle Park. August 2011.

Oral Presentations

"A new perspective on Hv1 voltage-sensor modulation by Zn²⁺". Forbes Day Colloquium, Virginia Commonwealth University, Medical College of Virginia. March 2018.

"How did the proton cross the membrane?". MEDCHM 670 Mini-Symposium, Virginia Commonwealth University, Medical College of Virginia. May 2016.

"Why did the proton cross the membrane: In silico investigation of the Hv1 proton channel". Biomedical Sciences Doctoral Portal First Colloquium, Virginia Commonwealth University, Medical College of Virginia Campus. November 2014.